SAPIENZA
UNIVERSITÀ DI ROMA

Hydrogen production through steam electrolysis in molten carbonate cells

Doctoral School in Science and Technologies for the Industrial Innovation
Ph.D. in Chemical Processes for Industry and Environment (XXXVII cycle)

Silvia Lo Conte
ID number 1761344

Advisor
Prof. Maria Cristina Annesini

Academic Year 2024/2025

Hydrogen production through steam electrolysis in molten carbonate cells
PhDthesis. Sapienza University of Rome

This thesis has been typeset by LaTeX and the Sapthesis class.

Author's email: silvia.loconte@uniroma1.it

Abstract

Molten carbonate cells, widely used industrially as fuel cells (MCFC), can also operate in reverse mode (MCEC), representing a valid solution for large-scale power-to-gas applications and H_2 or syngas production. Since a molten carbonate cell can operate in both electrolysis and fuel cell modes, it provides a cost-effective solution for integrating this technology into existing energy infrastructures. However, the study of MCECs is still relatively recent, and several aspects require further investigation and optimization before industrial application can be fully realized.

This thesis aims to analyze the electrochemical performance, operational stability, and hydrogen production efficiency of MCECs under varying conditions through experimental and numerical approaches.

For the experimental campaign, two different setups were used: i) a button cell, with an active area of approximately 3 cm^2, and ii) a planar single cell, square-shaped with an active area of 100 cm^2. The effects of systematic variations in temperature and hydrogen electrode composition were evaluated in both setups. On the one hand, the button cell was employed to investigate the hydrogen (Ni) electrode kinetics, as this setup allows for individual electrode measurements. On the other hand, the planar single cell was used to assess electrochemical performance and to carry out gas analysis of the hydrogen electrode output.

Polarization curves and impedance spectra obtained from the button cell were analyzed to investigate the hydrogen production mechanism occurring at the Ni electrode. Notably, the impedance data were deconvoluted using the Distribution of Relaxation Times, marking a novel approach in MCEC research. By combining these findings with the overpotential measurements, the potential rate-determining step of the reaction was identified, indicating that water reduction at the Ni electrode is under mixed kinetic-diffusion control.

As for the planar cell, both experimental and numerical results, including a 2D model used to evaluate thermal effects, have demonstrated that by carefully adjusting the gas composition and operating temperature, the output gas can be tailored to produce either pure hydrogen or syngas. Under certain conditions, a significant amount of CO is produced, underscoring the need for further investigation into CO_2 electrolysis. Additionally, a second experimental campaign conducted using this setup demonstrated the stable operation of an MCEC coupled with a variable power supply. This result highlights the feasibility of using such technology for large-scale applications in which the electrolyzer can be directly integrated with renewable energy sources. Furthermore, the study includes an analysis of process integration, assessing how molten carbonate electrolyzers could be incorporated within an industrial framework for hydrogen production.

Finally, fuel-assisted electrolysis mode has been tested on a molten carbonate button cell, demonstrating its feasibility. However, further investigation is needed to validate these findings and identify the most suitable fuel to achieve energy savings for the electrolyzer.

The obtained results provide an in-depth picture of the main factors affecting the performance of MCECs, highlighting the significance of optimizing operational conditions and electrode kinetics to facilitate their industrial applications.

Contents

Chapter 1

Introduction

The European Union has set an ambitious target to achieve climate neutrality by 2050, with an interim goal of reducing net greenhouse gas emissions by at least 55% by 2030 [1]. A fundamental pillar of this strategy is the expansion of renewable energy sources, as more than 75% of the EU's total emissions are attributed to energy production and consumption. In line with this, the European Commission revised the Renewable Energy Directive in 2022, raising the target for the share of renewable energy from 32% in 2018 to 45% by 2030 [1]. However, the large-scale integration of renewable energy into the electricity grid presents significant challenges, particularly due to the intermittency and variability of these energy sources. Ensuring a stable balance between electricity generation and demand, as well as strengthening transmission and distribution networks, will be critical. Therefore, the development of advanced energy storage solutions and a resilient grid infrastructure is essential to support the growing share of renewables and ensure the reliability of the energy system.

Energy storage systems are currently under active investigation, development, and implementation to uphold the increasing share of renewable energy in the grid. To effectively support the integration of renewable energy, energy storage systems must fulfill specific requirements, such as high storage capacity and the ability to store energy for extended periods. Energy can be stored in four primary forms: mechanical, electrical, thermal, and chemical. Among the various storage technologies, chemical storage via Power-to-Gas (PtG) systems has demonstrated the highest potential, with storage capacities ranging from 100 GWh to 10 TWh and the capability for long-term energy storage [2]. PtG processes convert surplus electrical energy into chemical energy in the form of chemical products, including hydrogen and, potentially, synthetic methane. As a highly efficient fuel, hydrogen offers promising applications as a substitute for conventional fuels in power generation, heating, and sustainable mobility, including large-scale transportation and industrial applications. There are several methods to store electrical energy in the form of gas, but the most direct and efficient way to achieve this conversion is through electrolysis. Water electrolysis is a promising and extensively studied process for hydrogen production.

Likewise fuel cells, electrolyzers can be categorized according to the operating temperature in low and high-temperature processes. Increasing the temperature

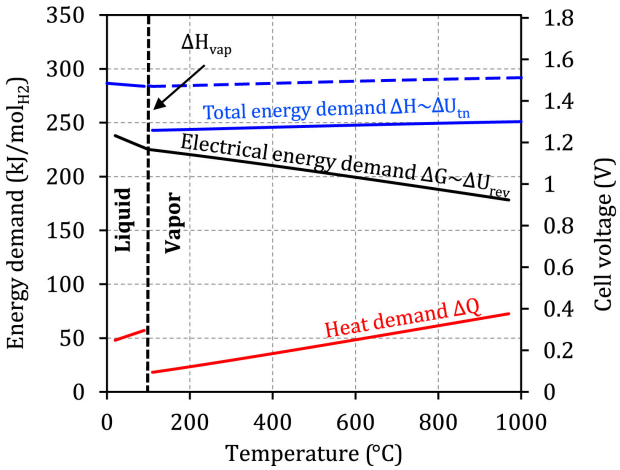

Figure 1.1. Total (ΔH), thermal (Q) and electrical (ΔG) energy demand of an ideal electrolysis process as function of the temperature [3].

in electrolysis processes is highly advantageous for two primary reasons. Firstly, high-temperature electrolysis often exhibits superior performance compared to low-temperature methods, primarily due to reduced losses, such as ohmic resistance, at elevated temperatures. Secondly, from a thermodynamic perspective, in steam electrolysis processes a portion of the energy required to drive the water-splitting reaction is provided in the form of heat, thereby reducing the demand of electricity of the process (see Fig. 1.1). This combination significantly decreases the overall energy requirements for steam electrolysis compared to water electrolysis. Consequently, high-temperature electrolyzers can function near thermoneutral voltage, which represents the theoretical operating point that reaches maximum efficiency.

Low-temperature electrolyzers, so-called water electrolyzers, are based on alkaline and polymer electrolyte membrane (PEM) technologies. Alkaline electrolyzer is the most mature and diffused technology. The standard alkaline electrolysis cell employs a liquid electrolyte, typically potassium or sodium hydroxides, and two electrodes separated by a diaphram to prevent gas mixing. It normally operates in the range $70 - 90$ °C but with low power densities, around 400 mA/cm^2 under efficiencies in the range $60 - 80\%$. One of the issues related to the alkaline cells is that they have limited responsiveness to fluctuations in electrical input, which can be problematic when integrating with renewable energy sources like wind or solar power. Rapid changes in current can result in excessive gas production, potentially causing the electrolyte solution to be expelled from the cell and reducing system efficiency. Moreover, the electrolyte mixture, containing 20-30% potassium/sodium hydroxide, is highly corrosive, necessitating the use of corrosion-resistant materials for all cell components, including the electrodes [3]. Recently, a new alkaline technology called Anion Exchange Membrane (AEM) electrolysis was introduced, in which the liquid electrolyte is replaced by a membrane that transports OH^-. While it offers the advantage of avoiding the use of corrosive liquids and having a potentially more compact design, it faces challenges related to membrane durability and cost. The long-term stability and economic feasibility of AEM cells are areas of ongoing research and development [4].

Among low-temperature electrolysis technologies, Proton Exchange Membrane (PEM) electrolyzers are particularly promising. Derived from fuel cell technology, PEM electrolyzers operate at high current densities of up to 2000 mA/cm² and achieve efficiencies around 80%, producing hydrogen at high pressures, up to 80 bar. However, PEM technology is still in the early stages of commercialization and is characterized by high costs due to the use of noble metals and fluorinated membranes. Additionally, PEM systems require high operating pressures and pure water, contributing to their complexity. They also have a shorter lifespan compared to alkaline electrolyzers. To make PEM electrolyzers more cost-effective, ongoing research is focused on replacing expensive platinum-based electrocatalysts with non-noble metals and improving overall system efficiency [3].

High-temperature electrolyzers (steam electrolyzers) are solid oxide electrolysis cells (SOECs) and, as proposed in this thesis, molten carbonate electrolysis cells (MCECs). The recent development of high-temperature fuel cells and the high theoretical efficiency of steam electrolysis brought an increasing interest on SOEC and MCEC technologies, which are based on fuel cells operated in reverse mode. Solid oxide cells operate at high temperatures, between 700 and 900 °C, which contributes to their higher efficiency compared to more mature technologies. The high efficiency is mainly due to favorable kinetics and thermodynamics at these operating temperatures. However, special materials are required to withstand these extreme conditions, which is why this technology is still under development. Typically, SOECs employ composite materials where the electrochemically active phase is mixed within the ceramic phase of the electrolyte. This approach aims to maximize the length of the triple-phase interface, thereby enhancing catalytic activity, and to improve mechanical stability, ensuring strong adhesion between the electrolyte and the electrode. For the anode, perovskite oxides are commonly used due to their high catalytic activity, good thermal compatibility with the electrolyte composite, and high electrical conductivity. For the cathode, nickel-based composites are generally employed. However, due to the presence of O_2^- anions as charge carriers, nickel-based composites experience rapid deactivation, prompting ongoing research into alternative cathode materials. SOECs operate at pressures below 30 bar and require lower applied potentials compared to low-temperature technologies, ranging from 0.7 to 1.5 V [5]. Despite this, they are characterized by high concentration overpotentials related to steam transport limitations and significant ohmic overpotentials, which are more pronounced when the cells are connected in a stack. Consequently, current densities generally do not exceed 1 A/cm^2. Because of the high temperatures, co-electrolysis can occur in the SOEC, simultaneously converting CO_2 to CO and H_2O to H_2, resulting in the production of syngas. This syngas can serve as a feedstock for the CO_2-neutral production of various hydrocarbons in the chemical industry. For example, it can be utilized in the Fischer-Tropsch synthesis process to produce synthetic fuels, including diesel or gasoline. Additionally, syngas can be converted into methanol, which is a versatile chemical used for fuels, solvents, and as a precursor for high-value chemicals such as formaldehyde and acetic acid.

Since this technology is still at an early development stage, many characteristics have to be investigated and improved, such as total system development, part-load behavior and long-term stability. In general, typical applications for SOECs are seen in combination with processes which can provide the required heat for the reaction.

Additionally, constant operation is preferable, since ceramics are susceptible to thermal stress. This will be a critical issue when the SOEC is used for power-to-gas, since the necessary flexible mode of operation requires numerous start-up and shut-down processes [3].

Molten Carbonate Electrolysis Cells (MCEC) are another high-temperature electrolysis technology that, like SOEC, operates by reversing the corresponding fuel cell process. However, MCEC technology is relatively new and has been studied primarily at the laboratory scale. Compared to SOECs, which have seen broader development and industrial attention, research on MCECs is still in its early stages. These cells are also supplied with water vapor, but operate at $550 - 700$ °C, lowering the demands of the constructive materials. This technology utilizes a molten carbonate electrolyte in a porous, chemically inert ceramic matrix. The hydrogen electrode is usually made of Ni-based alloys while Ni oxide is frequently used as oxygen electrode. The minimum operating temperature is constrained by the electrolyte's melting point, which ranges between 400 and 500 °C, depending on its composition. So far, the MCEC literature is not extensive, mainly focusing on lab-scale experiments, simple numerical models, or analyses of the process's integration with other energy conversion systems.

Still, the technology is of extreme interest due to the high development stage of molten carbonate fuel cell (MCFC) technology that is the only that accounts, between all the fuel cell technologies, power plants in the multimegawatt power scale. MCFCs are commercially available for stationary power generation with installations around the world, with power from 300 kW to 60 MW (Baran Industrial Complex Fuel Cell Facility, Korea). Historically, several companies produced demonstration MCFC devices (e.g., MC-Power and ERC in the United States, Ansaldo in Italy, ECN in the Netherlands, MTU in Germany, and IHI and Toshiba in Japan). Nevertheless, most of them have dropped this activity and, nowadays, the leading global developer is the U.S.-based company Fuel Cell Energy (FCE), which produces stationary systems ranging from 300 kW to 2.8 MW [6]. Research interest in MCFCs has also surged due to their potential for the sequestration and capture of CO_2. This technology is able to achieve simultaneous CO_2 capture and power generation because of its unique chemistry, and has broad applicability to a wide variety of CO_2 sources. Major companies have recognized this potential and made significant investments in the development of MCFC technology for carbon capture and utilization. ExxonMobil, in particular, has partnered with Fuel Cell Energy to commercialize a novel MCFC-based process for capture CO_2 emissions from industrial sources [7–9]. They plan to build a pilot plant at Esso Nederland BV's Rotterdam Manufacturing Complex, where CO_2 will be captured directly from the industrial flue gases before it can be released into the atmosphere. In this process, CO_2-containing flue streams, such as those from combustion exhaust, will be directed to the molten carbonate fuel cell. There, electrochemical reactions will generate electricity and hydrogen while capturing and concentrating the CO_2 for either utilization or permanent sequestration.

Molten carbonate fuel cells' electrical efficiency varies from 47% to 48% with the potential to reach up to 57%. When combining heat and power, the overall efficiency can exceed 80% [6]. This should be enough to ensure their place in the market, but the cost of this type of installation is still high. To compete with conventional

power generation systems, a generally agreed target life span for MCFCs is 40,000 h and the system is allowed to be shut down after this period. To reach the required lifetime and reduce costs, the MCFC component materials need to be modified or new materials need to be developed. Besides, investigating the various electrode processes in MCFC, such as cathodic oxygen reduction, the effect of carbonate melt wetting properties on the materials, and the corrosion mechanisms of cell components, is critical to achieving this goal. Also investigation of the various MCFC electrode processes such as the cathodic oxygen reduction, the effect of carbonate melt wetting properties on MCFC materials and the mechanisms of corrosion of cell components are critical to achieve this goal. Apart from the materials' stability, the cost of the MCFC system needs to be lowered for mass commercialization. At present, the average installed cost for a commercially available MCFC module is around $4,000 per kW. The high costs of MCFC stacks are attributed to relatively lower power densities (120 mW cm^2) of MCFC systems, and a 20% improvement in power densities can substantially reduce the cost of power from MCFC. If the installed cost of MCFC can be reduced to $2,000 per kW, it could be the preferred choice for stationary power generators above 400 kW range [10].

Building on the well-established technology of MCFC, it becomes essential to investigate their application as electrolyzers to address the growing challenges related to clean hydrogen production and the decarbonization of industrial processes. Molten Carbonate Electrolysis Cells present a promising opportunity, because of the high efficiency inherent in high-temperature operations and their potential to convert carbon dioxide, alongside water vapor, into synthetic fuels or chemical feedstocks. Note that it is necessary to feed the hydrogen electrode with both CO_2 and steam to produce the carbonate ions required for the electrochemical reaction. Unlike more mature electrolysis technologies, the high operating temperatures allow MCECs to harness additional thermal energy, making them advantageous for utilizing residual heat from industrial processes. However, the novelty of this technology poses several challenges, such as the durability of materials and the electrolyte losses. J.R. Selman, a renowned expert in the field of electrochemical engineering, has extensively studied molten carbonate fuel cells and identified three critical pillars that govern their long-term performance [11]. These are (i) reaction kinetics, (ii) interfacial wetting, and (iii) corrosion. Selman highlighted that these processes all occur at key interfaces within the fuel cell. The first two processes, reaction kinetics, and interfacial wetting, take place at the "active" interfaces, where electrochemical and chemical reactions occur, specifically at solid/liquid and solid/liquid/gas junctions. The third, corrosion, directly impacts the cell's longevity, limiting its useful life. Although these principles were developed in the context of MCFCs, they are equally relevant for molten carbonate electrolysis cells, as both technologies share nearly identical hardware. The electrochemical environment, material choices, and interface dynamics that affect MCFC performance will similarly influence MCEC systems. This is why improving the understanding and management of these three factors is not only crucial for enhancing MCFCs but also for advancing MCEC technology, as it will help address challenges like electrode degradation and electrolyte stability. Despite promising laboratory-scale results, large-scale applications of MCEC remain limited. Current research focuses on optimizing electrode and electrolyte materials, as well as gaining a deeper understanding of the electrochemical mechanisms that govern

the electrolysis process.

1.1 Goals of this work

The primary objectives of this thesis are twofold: firstly, to conduct a detailed and systematic study of the chemical-physical phenomena occurring in molten carbonate electrolysis cells (MCEC), to acquire fundamental insights for the development and enhancement of hydrogen production technology; secondly, to develop and apply a numerical approach to describe and understand the complexity of these phenomena within electrochemical cells.

Regarding the first objective, experimental testing was performed using two different setups, which facilitated a thorough examination of the cells' behavior under various conditions. These experimental activities were primarily conducted at the ENEA research center in Casaccia (Rome) and, to a lesser extent, at the Royal Institute of Technology (KTH) in Stockholm. Conventional characterization techniques, such as polarization curves and Electrochemical Impedance Spectroscopy (EIS), were employed to gain insights into the cells' performance. Various operational conditions, including gas composition and temperature changes, were tested to explore the reaction kinetics and to quantitatively assess hydrogen production through chromatographic analysis. This analysis aimed to quantify the contributions of the reverse Water Gas Shift (rWGS) reaction and electrolysis to hydrogen production under different conditions. Additionally, the thesis investigates the performance of MCECs under dynamic loading conditions to evaluate their feasibility for integration with renewable energy sources, which are inherently intermittent. This includes analyzing how the cells respond when powered by variable electrical power throughout the day.

A significant part of the work involved the development of a 2D model to predict the performance of the cells. This model, validated against experimental data, provides valuable insights into the main contributions to the MCEC overpotential and the thermal effects of an adiabatic cell. Furthermore, a preliminary analysis was conducted on integrating MCEC technology into a process for producing pure hydrogen, to assess the primary energy consumption involved and evaluate the process efficiency. Through this multifaceted approach, this work aims to advance the understanding of MCEC technology and evaluate its practical applications in hydrogen production. The contents of this doctoral thesis are summarized in the following section.

1.2 Thesis outline

In this work, Chapter 2 illustrates the operating principles of molten carbonate cells functioning as fuel cells and electrolyzers, along with general aspects related to the materials, designs, and recent advancements in MCEC research.

In Chapter 3 a description of the principal characterization techniques employed in this work is provided, with particular attention dedicated to the DRT methodology and all its useful implications in the analysis of the EIS measurements.

Chapter 4 outlines the experimental campaigns, testing procedures, material characteristics, and the experimental apparatus used, detailing the tests carried out in the laboratories of the ENEA research center with both button cell and single cell setups.

Chapter 5 extensively presents the experimental results obtained from the button cell setup, with a particular focus on the hydrogen electrode. The first part discusses the polarization curves and analyzes the exchange current density dependencies on the partial pressure of the reactants and temperature, fitting the data with the Butler-Volmer equation. In the second part, the DRT analysis of the EIS measurements for the hydrogen electrode is presented, allowing the qualitative distinction between the different processes contributing to the electrode's polarization.

Chapter 6 is dedicated to the analysis of the planar single MCEC performance. The first part focuses on the 2D model, developed based on literature data and validated with experimental results. This model was used to predict thermal effects under adiabatic conditions, showing that, in the absence of temperature control, the cell temperature could rise significantly, with chemical reactions alongside electrochemical processes substantially influencing cell behavior. The second part of the chapter focuses on the experimental data obtained from the single cell during the experimental campaign carried out for this work, with special attention given to the gas chromatographic analysis for quantifying hydrogen production under different operating conditions.

Chapter 7 explores the integration of MCEC technology into industrial processes, focusing on two key aspects. On the power supply side, the coupling of MCEC with renewable energy sources is analyzed, presenting experimental data obtained during the third experimental campaign of this thesis, where a planar single cell was powered by a dynamic source simulating a photovoltaic plant. On the product side, a process analysis is provided for a plant scheme focused on hydrogen production using MCEC.

Chapter 8 provides a brief introduction to fuel-assisted electrolysis, a recently innovation in high-temperature electrochemical cells. It then presents experimental results from the Royal Institute of Technology (KTH), where preliminary tests on a button cell were conducted as part of the broader experimental campaign for this thesis, aimed at evaluating the feasibility of this novel operating mode.

Finally in Chapter 9, the results obtained from the experimental investigations and the numerical analysis are resumed and some conclusions are provided.

Chapter 2

Fundamentals

This chapter provides an overview of the molten carbonate fuel cell (MCFC) and molten carbonate electrolysis cell (MCEC) technologies. The working principles, state-of-the-art materials, and design of these systems will be described. Notably, the components of MCEC are made from the same materials used in MCFCs. The primary difference between them lies in the current direction, as the electrolyzer operating principle is the reverse of that of the fuel cell. Special emphasis will be placed on the advancements and research specific to MCECs, including investigations into electrochemical performance, durability, kinetic mechanisms, and modeling activities.

2.1 The molten carbonate fuel cell

Molten carbonate fuel cells (MCFCs) are electrochemical devices that directly convert the energy content of a fuel, most commonly hydrogen, into electrical and thermal energy. These high-temperature fuel cells operate with a molten carbonate electrolyte within a temperature range of $550-700$ °C. The electrolyte melting point determines the minimum operating temperature, i.e. $400-500$ °C depending on the carbonate composition [12, 13]. Limited electrolyte conductivity at lower temperatures and accelerated corrosion along with electrolyte vaporization at higher temperatures define the operating temperature range.

Fig. 2.1 shows a schematic overview of the main operating mechanism of an MCFC. In this scheme, it is considered that only pure H_2 is supplied to the anode (Ni electrode), while a CO_2-O_2 mixture is fed to the cathode (NiO electrode). The fuel (H_2) reaches the electrode-electrolyte interface diffusing through the porous structure of the anode. The hydrogen oxidation reaction occurs at the triple phase boundary (TPB), where the gas, the electronic conducting phase (metal electrode), and the ionic conducting phase meet, facilitated by carbonate ions (CO_3^{2-}) from the electrolyte. This reaction produces water and carbon dioxide while releasing two electrons (e^-) to the external circuit. These electrons are subsequently transferred to the cathode, where they reduce oxygen and carbon dioxide to form carbonate ions. What is explained above can be easily summarized considering the electrochemical semi-reactions occurring at the anode and the cathode side:

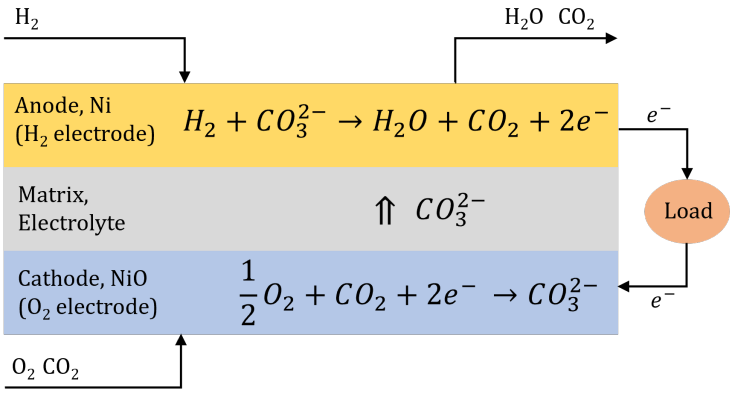

Figure 2.1. The working principle of the molten carbonate fuel cell.

$$\mathrm{H_2 + CO_3^{2-} \rightarrow H_2O + CO_2 + 2e^-} \tag{2.1}$$

$$\mathrm{CO_2 + \frac{1}{2}O_2 + 2e^- \rightarrow CO_3^{2-}} \tag{2.2}$$

So that the overall cell reaction is

$$\mathrm{H_2 + \frac{1}{2}O_2 + CO_{2,NiO} \rightarrow H_2O + CO_{2,Ni}} \tag{2.3}$$

where it is underlined that carbon dioxide must be supplied to the cathode to produce the $\mathrm{CO_3^{2-}}$ ion conductor, and it is released to the anode as a consequence of $\mathrm{H_2}$ oxidation.

One significant advantage of high-temperature fuel cells is their resistance to carbon monoxide poisoning. Instead of being harmful, carbon monoxide can serve as a fuel in MCFCs through the following reaction occurring at the anode:

$$\mathrm{CO + CO_3^{2-} \rightarrow 2CO_2 + 2e^-} \tag{2.4}$$

although this reaction is regarded to be slow [14–16].

Alongside the electrochemical reactions, the reverse water-gas shift (rWGS) reaction takes place at the anode (Ni electrode),

$$\mathrm{H_2 + CO_2 \leftrightarrow H_2O + CO} \tag{2.5}$$

The presence of nickel as a catalyst, combined with the operating temperature, allows this reaction to reach equilibrium rapidly [17, 18]. Consequently, this can affect the gas composition within the Ni electrode, which may influence the electrode's performance.

Thanks to the high operating temperature MCFCs can utilize a wide range of fuels, such as methane and other higher hydrocarbons, which can be converted into hydrogen through steam reforming, (reactions 2.6 and 2.7). This reaction can take place either directly within the fuel cell (internal reforming) or in a separate reformer (external reforming). In the former case, the endothermic steam reforming reaction is powered by the heat produced by the exothermic hydrogen

oxidation. This integration of reactions within the cell simplifies the stack's thermal management, as the heat produced by hydrogen oxidation is efficiently absorbed by the reforming process. By implementing internal reforming, the overall cooling load of the system can be significantly reduced—by as much as 50% according to [19]. This reduction occurs because the heat generated by the exothermic H_2 oxidation is effectively consumed within the system, minimizing the need for external cooling and improving overall thermal efficiency. Moreover, the consumption of hydrogen due to the electrochemical reaction enhances steam conversion during internal reforming, resulting in higher fuel utilization and overall efficiency.

$$CH_4 + H_2O \leftrightarrow 3H_2 + CO \tag{2.6}$$

$$C_nH_m + H_2O \leftrightarrow \left(n + \frac{m}{2}\right) H_2 + nCO \tag{2.7}$$

MCFCs are typically used for large stationary power generation due to their significant efficiency, regardless of the type of fuel employed. They can achieve up to 55% efficiency for fuel-to-electricity conversion, and the total efficiency can exceed 90% when integrating combined heat and power (CHP) or combined cooling and power (CCP) applications [20]. Fig. 2.2 provides an example of the integration between an MCFC and a gas turbine power plant, while Fig. 2.3 illustrates a possible integration of MCFC technology in a cooling system.

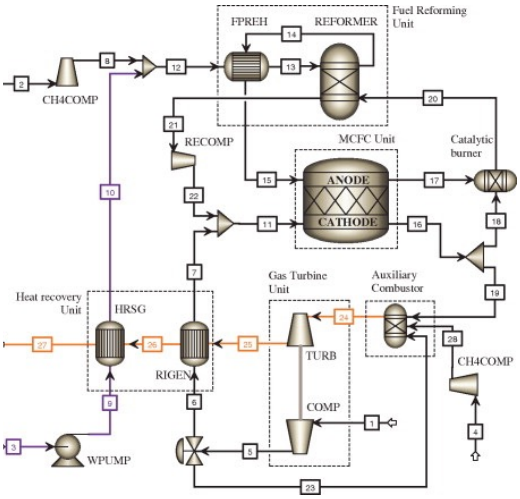

Figure 2.2. Layout diagram of the hybrid MCFC–Gas Turbine power plant studied in [21].

MCFC technology has been commercially deployed in various countries including the USA, South Korea, Germany, Italy, and Japan, with over 300 MW of power generation capacity installed across more than 50 locations worldwide [20, 23, 24]. Thus, even though the MCFC technology is already commercialized to some extent, there is always a demand for better and cheaper materials to improve the performance and make MCFC an effective replacement for traditional power generation. The highly corrosive and mobile electrolyte necessitates the exclusive use of nickel and high-quality steel for the various components of MCFCs [25–27], resulting in significant costs. Similarly, the elevated temperatures pose a challenge

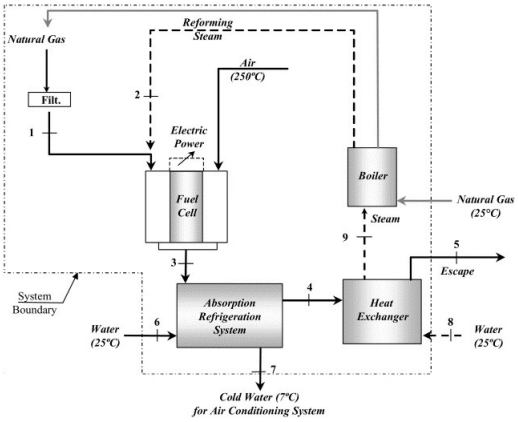

Figure 2.3. MCFC associated with an absorption refrigeration system [22].

to mechanical stability and negatively affect the lifespan of the stack. Throughout the lifetime of MCFCs, a slow but steady loss of electrolyte occurs, which tends to cause gradual performance decay [28]. The dissolution of the oxygen electrode is also a major factor limiting the lifespan of MCFCs. The current state-of-the-art oxygen electrode (described in Sec. 2.2.4), nickel oxide, slowly dissolves into the electrolyte, creating metal particles that precipitate across the electrolyte tile. This process can eventually lead to short-circuiting between the fuel electrode and the oxygen electrode. Since the mid-1970s, the materials for the electrodes and electrolyte have remained essentially unchanged [10, 29] and they will be described in detail in the following sections.

2.2 Materials and Design

In molten carbonate fuel cells the electrolyte mixture (molten carbonate salts) is held in a porous ceramic matrix between a porous anode and a porous cathode. The matrix also facilitates the conduction of carbonate ions between the electrodes and acts as a barrier to separate the fuel and oxidant gases.

In earlier stages of MCFC development important improvements of cell performance were obtained by a design strategy which assumed that the filling and wetting of porous cell components (electrodes and electrolyte matrix) satisfies capillary equilibrium [11]. The condition for capillary equilibrium - equal capillary pressure among all three porous bodies - is expressed by the following equation [30]:

$$\frac{\sigma_{\mathrm{c}} \cos\theta_{\mathrm{c}}}{D_{\mathrm{c}}} = \frac{\sigma_{\mathrm{m}} \cos\theta_{\mathrm{m}}}{D_{\mathrm{m}}} = \frac{\sigma_{\mathrm{a}} \cos\theta_{\mathrm{a}}}{D_{\mathrm{a}}} \tag{2.8}$$

where D is the diameter of the largest flooded pores, σ is the superficial tension and θ is the contact angle of the electrolyte, while the subscripts a, c and m refer to anode, cathode and matrix respectively. If Eq.2.8 is satisfied, all matrix pores, being smaller in diameter as compared to electrode pores, are filled with electrolyte, while electrode pores are partially filled permitting diffusion of gaseous species. Thus, at equilibrium, the distribution of a small amount of molten carbonate among the

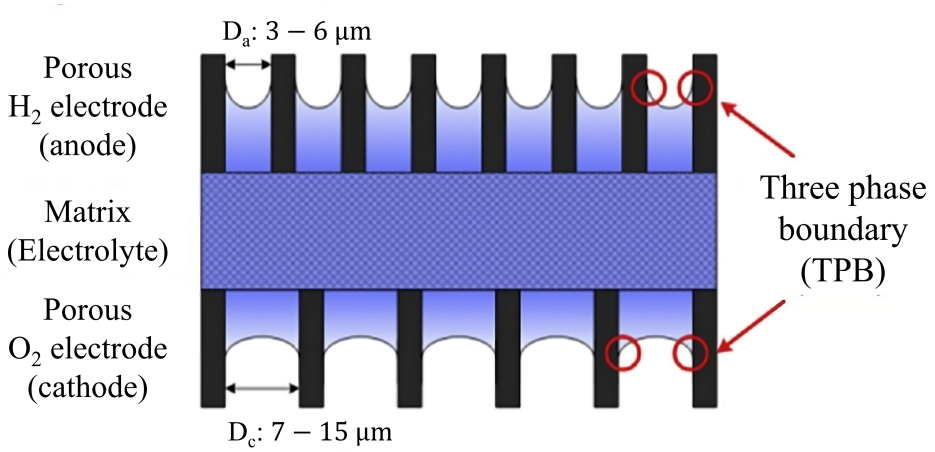

Figure 2.4. Schematic representation of constant volume capillary equilibrium of melt among molten carbonate cell porous electrodes and matrix support, showing in-pore meniscus formation and wetting [11].

three porous components will be fixed, given a certain total volume of melt in the cell. The partially filled pores in electrodes provide triple-phase boundaries (solid electrode, reactant gas and liquid electrolyte) for redox reactions (Fig. 2.4).

The constant-volume capillary equilibrium assumption is a relatively simple tool to help design a well-working MCFC cell, because it allows some control of the relatively complicated three-way interaction in such a cell. This three-way interaction involves (i) porous-electrode geometry (fixing pore size distribution and electrode thickness), (ii) choice of electrode materials and carbonate composition (which govern wetting parameters such as surface tension σ and contact angle θ), and (iii) operational parameters (such as gas flow rate, utilization, and current load) which, in large cells, strongly affect the distribution of local reaction rate and temperature, and thereby kinetics and wetting. Additionally, when individual cells are arranged in series to create a stack that meets the target power output, interconnect layers, or bipolar plates, are also required. Significant efforts have been dedicated over the past few decades to create corrosion-resistant cell components and fabrication techniques that ensure both stability and performance. In the following sections, a concise overview will be provided of the key types and properties of materials used in state-of-the-art MCFCs and their stack components, along with the various kinds of cells.

2.2.1 Electrolyte

The electrolyte plays a crucial role by transporting dissolved reactants (fuel and oxidant) to the catalytic surface, where electrons are released and recombined, and by conducting ionic charge between the electrodes, thus completing the cell's electrical circuit. In MCFCs, carbonate ions serve as the charge carriers, generated through the oxidation reaction at the oxygen electrode – see Eq. 2.2. The electrolyte also acts as a physical barrier to separate the fuel and oxidant gas streams from mixing directly. Finally, the molten carbonates ensure gas sealing between the separator plates, which separate individual cells within a stack configuration (more about this

in Sec. 2.2.5).

The electrolyte can be a binary (Li/K, Li/Na) or a ternary (Li/Na/K) eutectic mixtures of carbonates. The composition affects (i) ionic conductivity, (ii) solubility of reactants and reaction products, (iii) the diffusion coefficients of reactants and products, (iv) the rate of the anodic and cathodic reactions, (v) electrolyte vapor pressure, and (vi) stability of the lithium-aluminate matrix.

Since about 1980, the standard electrolyte composition has been $Li_2CO_3{-}K_2CO_3$ (62:38 mol%) [31, 32]. However, in the early 1990s it was found that, due to the different mobility of cations (Li^+, K^+) within the eutectic mixture, electrolyte segregation (i.e. separation of the Li and K carbonates) can occur within the matrix. This phenomenon leads to the non-uniformity of composition dependent physical properties such as melting point, basicity, and wetting properties. Besides, as it will be discussed in Sec. 2.2.4, the segregation increases the potassium concentration near the oxygen electrode and this leads to increased NiO solubility and a decline in performance [33–35]. These observations, particularly the issue of NiO dissolution in the electrolyte, caused several developers in the late 1990s to investigate alternative electrolyte materials.

An early study by Ang and Sammells [36] suggested that Li/Na carbonate exhibits higher ionic conductivity compared with other mixtures. This was confirmed by subsequent researches [31, 37, 38]. Additionally, the Li–Na electrolyte offers improved NiO electrode (O_2 electrode) stability [39, 40] and reduced electrolyte evaporation [27, 36] compared with the Li-K mixture. These properties make Li–Na a better choice for high-pressure operation, improving the long-term performance of the cell [29, 37]. Nevertheless, Li–Na cells are more sensitive to temperature changes under atmospheric conditions due to lower oxygen solubility in the Li–Na carbonate. As a result, operating Li–Na cells at lower temperatures (< 650 °C) leads to larger voltage drops than in Li–K cells at equal conditions [31, 37].

To address the issues with binary electrolytes, several research groups in the early 2000s began studying the ternary Li/Na/K carbonate system [36, 41–46]. This system offers the advantage of having the lowest melting point among molten carbonates mixtures (397 °C). The research aimed to optimize the composition of the ternary electrolyte to achieve low oxygen electrode (NiO) solubility, low vapor pressure, low reactivity with stainless steel, and high chemical oxygen solubility. However, the reduced ionic conductivity at lower operating temperatures (i.e. $500 - 550\,°C$) remains a significant challenge to their broader application.

Of course, "alternative electrolytes" may be created by adding small amounts of alkaline earth carbonates or rare-earth oxides to state-of-the-art eutectics [38, 44, 47]. Although these alternative electrolyte formulations promise benefits, a decrease in conductivity with alkaline earth addition has been observed [38, 48]. Therefore, optimization of electrolyte composition remains a complex task, requiring thorough investigation of additives' effects on long-term cell performance. Adopting a new electrolyte composition demands careful compatibility checks with structural and electroactive components and may necessitate fine-tuning or even a complete overhaul of material choices.

However, improvements can also be achieved through a system-based approach. Due to practical considerations, such as non-uniform temperature distribution in large-scale cells, the minimum operating temperature of an MCFC is typically

about 100 °C above the electrolyte's melting point. By making possible operation at temperatures lower than $600 - 650$ °C, "alternative electrolytes" could mitigate corrosion of structural materials, thereby extending the MCFC's lifespan.

2.2.2 Matrix

The MCFC matrix acts as a separator between the anode and cathode holding the electrolyte. It is sandwiched between the anode and cathode, and the carbonate melt is immobilised by capillary pressure (typically > 0.2 MPa) [10]. A sufficient capillary force for the electrolyte uptake and retention inside the matrix is obtained by keeping the pore diameters of the matrix smaller than those of the electrodes [49, 50] and by having a good wettability [51]. Optimal performance is achieved when the electrolyte only partially fills the pores in the electrodes but completely saturates the matrix. Typically, the electrolyte content in the matrix should exceed 50 vol% [51], compared to a maximum of 30 vol% within the electrodes [52, 53]. In terms of the cell pore to filling ratio, which is the ratio of electrolyte volume to total pore volume, the lowest polarization resistances are observed when this ratio is between 50–80%, with an exponential increase for lower and higher values [54]. For acceptable cell performance, the matrix should generally have a porosity of 50 to 70% [50, 55, 56] and a pore size below 1 µm [49], with an optimal average pore size distribution of $0.1 - 0.3$ µm [50, 54]. While increasing the porosity can enhance ionic conductivity, it may also compromise the matrix's structural integrity, leading to premature degradation. Conversely, smaller pore sizes can strengthen the matrix and reduce the risk of cracks, improving stability under high-pressure conditions, though this might penalize the electrochemical performance [53, 57].

Another crucial characteristic of the matrix is its Specific Surface Area (SSA), which significantly influences both the average pore size and porosity [54]. For MCFCs, a SSA of around 10 m^2/g [54, 58] is typically used, although high-performance matrices can achieve up to approximately 12 m^2/g [53]. Given the highly reactive nature of the retained alkaline-based carbonate electrolytes (see Sec. 2.2.1), the matrix must be chemically stable and inert to ensure the cell's long-term operation. Additionally, the mechanical strength of the MCFC matrix should be at least 90–100 gf/mm^2 [59].

To meet these requirements, the state-of-the-art material used is lithium aluminate ($LiAlO_2$), reinforced with aluminum agents. Among its three allotropic forms — α-$LiAlO_2$ (hexagonal structure), β-$LiAlO_2$ (monoclinic structure), and γ-$LiAlO_2$ (tetragonal structure) [60] — the α-phase [61, 62] and γ-phase [54, 63–65] are mainly used as MCFC matrices. In the early 1980s, based on short-term testing, γ-$LiAlO_2$ was chosen as the matrix support material due to its high corrosion resistance to molten carbonates [66]. However, this material faces challenges such as particle growth, pore coarsening, and allotropic transformation from the γ-phase to the α-phase. Since the α-phase is denser (3.4 g/cm^3) than the γ-phase (2.6 g/cm^3), this transformation increases the pore volume thus resulting in the electrolyte depletion within the matrix [10]. The loss of electrolyte reduces ionic transport and causes fuel crossover resulting in polarization losses. Generally, matrix stability is compromised at higher temperatures, in low CO_2 gas atmospheres, and in strongly basic carbonate melts [67, 68]. Conversely, α-$LiAlO_2$ exhibits a higher stability under

MCFC operation [68], remaining stable in both H_2/CO_2 and air/CO_2 environments at 650°C, unlike γ-$LiAlO_2$. Although the α-phase offers better microstructural stability, it is inferior to γ-phase in terms of mechanical strength, requiring additional reinforcement [62, 69].

2.2.3 Anode

In an MCFC, the anode is where the fuel (e.g. H_2) is electrochemically oxidized. It is typically made from a porous sintered Ni base with a thickness of $0.6-0.8$ mm and a porosity of $55-70\%$, with a mean pore diameter of $3-5$ mm. This porosity provides adequate interconnected pores for mass transfer of gaseous reactants and adequate surface area for the electrochemical reactions [52, 70]. To maintain an allowable ohmic loss during the drawing of current in fuel cell operation, the electrical conductivity should be larger than about 100 S/m [29]. Therefore, the anode thickness should be kept as low as possible to improve conductivity, as long as this does not compromise mechanical strength.

Nickel in the form of sintered powders of a nickel-based alloy containing small amounts of Cr or Al is currently used as the anode material. The main problem with pure nickel is that it does not sufficiently resist creeping and sintering under the compressive force required to minimize contact resistance between cell components [20]. The micro-dispersed oxide particles formed in Ni-10 wt% Cr anodes and Ni-$(5-10)$ wt% Al anodes have proved to maintain adequate stability of the electroactive microstructure in the anode [71, 72]. These alloys are now almost exclusively used in commercially produced stacks. However, the electrolyte can easily lithiate the Cr electrode to produce $LiCrO_2$. Since this reaction consumes the electrolyte, it creates micropores inside the electrode, leading to cell instability and performance decline during long-term operation [73]. On the other hand, the Ni-Al alloy anode shows higher creep resistance than the Ni-Cr anode, with minimum electrolyte loss. The low creep rate with this alloy is attributed to the formation of $LiAlO_2$ particles that are finely dispersed in the Ni-Al network structure, but remain electrochemically inert [72, 74].

Although the current additives to the anode base material, when added in the right proportions and following careful dispersion procedures, have largely solved the problem of creep, the susceptibility to this phenomenon could still be improved. Additionally, since MCFC operation relies on the ionic exchange between the melt and solid electrodes, the wettability of the electrodes (the wetting angle) especially on the anode side is an important parameter determining the MCFC performance. The wetting angle for standard MCFC anodic gas composition is around 50° with $(Li/Na)_2CO_3$ and 31° with $(Li/K)_2CO_3$ [52]. Hence efforts are being made to improve the anode wettability through the coatings or additives. Composite anodes made of ceramic oxides, such as those using oxides of lanthanum (La_2O_3) and samarium (Sm_2O_3) with titanium powder (to provide electronic conductivity) have shown good performance [75, 76]. Ceramic-based or ceramic-coated anodes also improve sulphur tolerance, possibly by an order of magnitude [77], and wettability, while being morphologically stable during cell operation. The main drawback of these additives is that they increase the ohmic resistance of the anode, and their addition can impede the conducting path even if used in relatively smaller amounts [10].

2.2.4 Cathode

General requirements for MCFC cathode materials, besides sufficient electrical conductivity, are limited solubility in carbonate electrolyte at the operating temperature, sufficient porosity ($70 - 80\%$, with a mean pore diameter of $7 - 12$ µm [10]) to allow the diffusion of reacting species and stability in oxidizing atmosphere. The currently used cathode material is lithiated NiO, formed from porous Ni by oxidation and lithiation of porous nickel in contact with lithium carbonate under an oxidizing atmosphere. This process generates its characteristic dual pore size distribution, required for proper functioning of the three-phase interface: small pores are filled with electrolyte and are responsible for transport of ions, while larger pores provide access for the gaseous species.

Although NiO fulfills the performance requirements such as catalytic activity and electrical conductivity, its dissolution in carbonate electrolyte is one of the issues that limits MCFC lifetime [28, 35, 78]. NiO dissolution from the cathode into the carbonate electrolyte occurs according to one of the following mechanisms [20]:

$$\mathrm{NiO} + \mathrm{CO_2} \rightarrow \mathrm{Ni^{2+}} + \mathrm{CO_3^{2-}} \tag{2.9}$$

or

$$\mathrm{NiO} \rightarrow \mathrm{Ni^{2+}} + \mathrm{O^{2-}} \tag{2.10}$$

Therefore, the driving force for the dissolution depends on CO_2 partial pressure and the acid–base properties of the molten carbonate. The dissolution rate increases with CO_2 partial pressures [79], whereas higher activity of O^{2-} in the melt retards dissolution [80]. The dissolution of NiO leads to increased cathodic polarization due to structural changes, possible phase transformation and Ni shortening. The shortening takes place when Ni^{2+} ions formed in the cathode side diffuse through the matrix to the anode, where they are reduced by fuel (hydrogen) to form solid nickel particles:

$$\mathrm{Ni^{2+}} + \mathrm{H_2} + \mathrm{CO_3^{2-}} \rightarrow \mathrm{Ni} + \mathrm{CO_2} + \mathrm{H_2O} \tag{2.11}$$

The deposited Ni particles move across the matrix under the influence of the electric field. Since the reduction reaction (2.11) continues, a string of Ni particles is thereby created that tends to stretch from cathode to anode. The particles may agglomerate, forming a metallic dendrite that grows out of the NiO substrate of the cathode toward the anode. Eventually, shorting between anode and cathode occurs and causes a rapid decline in cell voltage and performance [28, 33].

Nowadays, NiO–composite cathode materials are considered the most promising approach to reducing the dissolution rate of NiO. This applies especially to coating or doping the NiO surface with lower solubility elements, possibly in combination with additives that enhance basicity in the carbonate electrolyte. Adding rare-earth elements [81–83] such as CeO_2, La_2O_3, Pr_2O_3, Nd_2O_3, Dy_2O_3, and $La_{0.8}Sr_{0.2}CoO_3$ to a NiO cathode lowers the dissolution rate of NiO by an order of magnitude. ZnO and $MgFe_2O_4$ [84, 85] composited with NiO have been studied as alternative cathode materials. These composite materials show promising stability under cathode environments, but long-term in-cell tests are required to confirm their practical suitability.

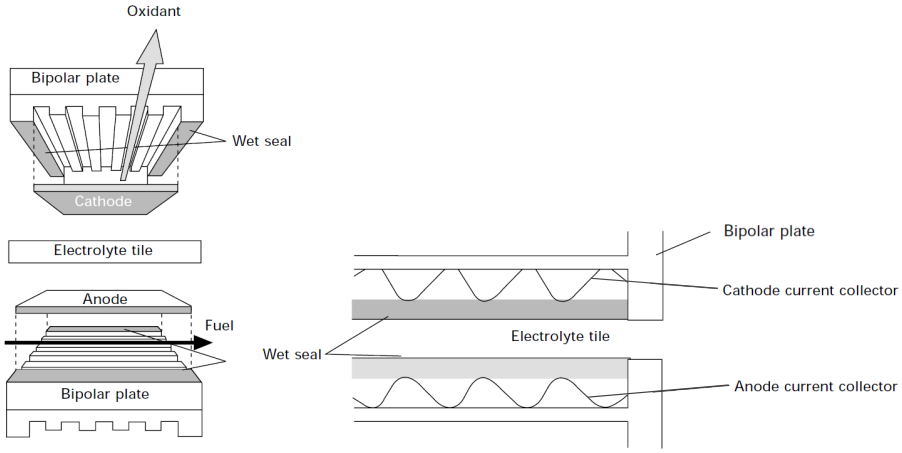

Figure 2.5. Schematic of single planar cell assembly and location of the wet seal [32].

2.2.5 Bipolar plates

The bipolar plate separates individual planar cells within a stack, as illustrated in Fig. 2.5. Although it is not an active component, it is perhaps the most critical non-active metallic part, subjected to harsher operational conditions than the active components. This is due to its location between the reducing environment of the fuel and the oxidizing environment of air, both in the presence of the corrosive molten carbonates. Since it is not involved in the catalytic reactions, the bipolar plate can consist of less specialized materials than the electrodes and matrix, and is usually made of stainless steel alloys, which nevertheless must have high corrosion resistance. Corrosion of the metal components, alongside with electrolyte loss, is the main factor contributing to the long-term voltage decay in MCFCs [86].

A bipolar plate generally consists of two metallic components: the separator plate and the current collector (see Fig. 2.5). These components must simultaneously satisfy various chemical, electrical and mechanical requirements and are therefore usually made of the same material, which is why they are consider as a whole under the terminology of bipolar plate. It is based on a corrugated design that has to fulfill the following functional requirements:

- separate fuel and oxidant streams between adjacent cells, while providing electrical contact;
- create flow channels to guide the gases from the manifolds to the electrodes;
- provide a leak-tight gas flange around the electrodes.

The last function is achieved by extending the electrolyte tile to the plate edges, where it is sandwiched between the two juxtaposing plates, creating what is known as the wet-seal, and is indicated in Fig. 2.5. Corrosion in this area is particularly critical and may lead to poor sealing, resulting in gas leakage, electrolyte loss and rapid decay of cell performance [87]. In addition to the corrosion resistance, another

important requirement for a bipolar plate is excellent electrical conductivity. Other mechanical requirements include fluid flow, high temperature resistance, proper contact between components, weldability, and easy formability.

Currently, no alloy has been found that combines all these desired properties. The most commonly used material for bipolar plates is Cr–Ni ferritic stainless steel. Alloys such as 310S and 316L are relatively inexpensive and perform well in the cathode area. They develop a thick, multi-layered oxide scale that offers good electrical conductivity and serves as an effective diffusion barrier [25]. On the anode side, it is required to apply a pure nickel coating that, being stable under reducing conditions, prevents the formation of the oxide layer [88]. With the protection provided by the Ni-clad coating, the anode-side bipolar plate shows virtually no corrosion attack for up to 10000 hours of operation [89].

2.2.6 Planar MCFCs

The state-of-the-art MCFC is invariably of planar construction and each of the porous components (i.e. anode, cathode, electrolyte, and matrix) is normally made by tape-casting [29, 35]. This has enabled significant scale-up of the manufacturing process of the planar components and cells of 1 m^2 are now routinely manufactured. The tape-casting process has also allowed to produce very thin electrolyte structures ($0.25 - 0.5$ mm). There is a strong incentive for making thinner electrolyte structures because their ohmic resistance significantly influences the operating voltage of MCFCs [90]. However, the minimum thickness is constrained by the need to maintain sufficient mechanical strength and to limit the formation of Ni dendrites, which can lead to short circuits between the electrodes (see Sec. 2.2.3).

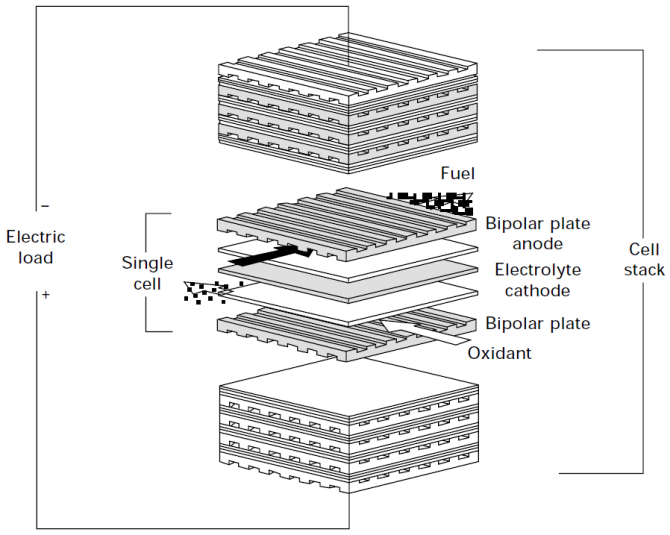

Figure 2.6. Assembly of cross-flow molten carbonate single cells to stack configuration [29].

Conventional MCFCs are characterized by square or rectangular geometry [92]. While square cells are used for cross-flow MCFC stacks (see Fig. 2.6), cells are usually rectangular in co-flow stacks with a shorter length in the gas flow direction and a

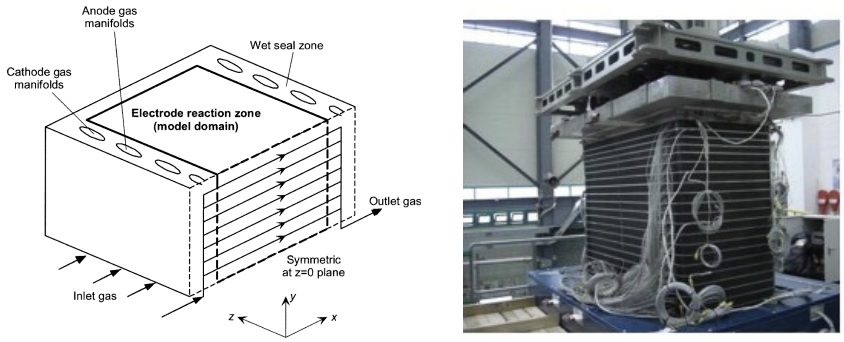

Figure 2.7. Schematic of a co-flow MCFC stack (left) and a picture of a 125-kW stack adapted from [91].

greater width to reduce the significant axial temperature rise [92, 93] (see Fig. 2.7).

From an economic and technical standpoint, square/rectangular MCFCs have been successfully developed for high-power applications, with outputs ranging from several hundred kW to tens of MW [11, 20]. However, the commercialization of MCFCs for the residential market, which requires smaller power outputs, faces several technical challenges. These include long start-up times, high thermal losses, limited lifespan due to gas crossover issues, and instability of materials (see previous sections).

To address these limitations, Nicolini et al. proposed a novel cylindrical cell geometries for small-size MCFCs, which was patented by IPASS [94–96]. This geometry, schematically represented in Fig. 2.8, offers several potential advantages over the traditional MCFC layout. These benefits include reduced construction time and costs thanks to the possibility of using an injection molding technique, minimized thermal dispersion, increased global efficiency, reduced gas tightness issues between the cell plates, and uniform compression strain on the contact surface. Nicolini et al. demonstrated the feasibility of these cylindrical cells, progressing from laboratory-scale cells of 3 cm^2 to the realization of a 1 kW stack comprising 15 single cells of 250 cm^2 [95]. Indeed, the optimum size for this geometry is in the 1 kW to 5 kW range: in this way, the mentioned benefits, thermal self-sustain conditions, cogeneration, and a compact design may be obtained [96]. This makes cylindrical MCFCs a promising alternative for overcoming the technical challenges that currently hinder the commercialization of MCFCs in the small-power market.

2.2.7 Tubular MCFCs

A recently proposed alternative to the planar electrode cell is the tubular cell, originally motivated by its lower thermal dispersion and greater ease of large-scale production, particularly when reducing the size of cells from industrial plants to potential domestic use. Besides, the state-of-the-art planar MCFC components require micrometer-scale precision in dimensional accuracy during manufacturing, accounting for over half of the production cost of a stack [97].

In a tubular cell complex separator plate would be unnecessary, which could

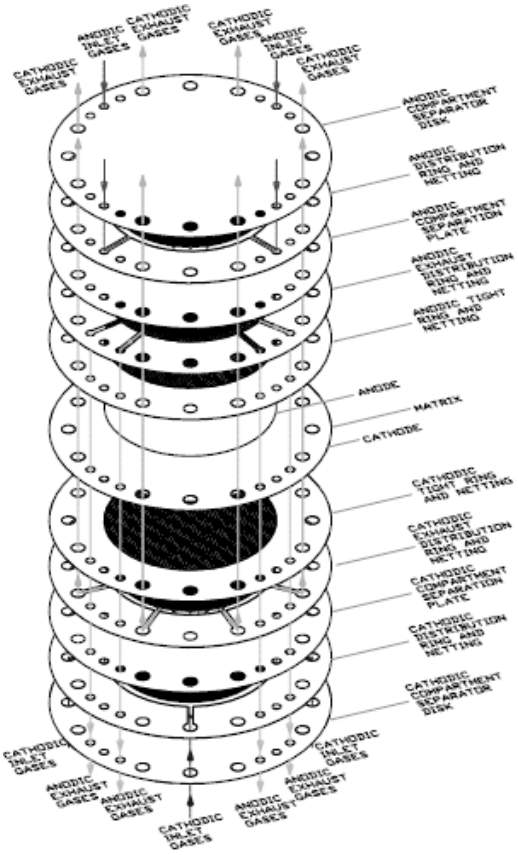

Figure 2.8. Exploded view of a cylindrical molten carbonate fuel cell in a stack [95].

greatly ease the dimensional accuracy requirements for the cell components, drastically increase the yield rate, and thereby significantly decrease manufacturing costs. Additionally, in a tubular MCFC, each cell is separated from the others, minimizing any mutual influence between cells. Therefore, a shorter start-up time can be expected in comparison with a planar MCFC stack. Furthermore, in a tubular cell assembly, it is possible to replace individual damaged cells.

Kawase developed a method of manufacturing a tubular MCFC [97]. The key feature of this method lies in the ability to exploit the natural shrinkage of the nickel electrode (which forms the outer cylinder of the assembly) during the sintering process from metal powder, thereby sealing the electrolyte and providing the cell with the necessary mechanical strength. The cell, represented in Fig. 2.9, was found to have a generation performance close to that of a planar MCFC, although there is room for improvement. It was furthermore found that the tubular MCFC can start from a cold-stopped condition in a few hours. In a subsequent work [98], he also evaluated the basic durability of tubular MCFCs fed with coal or biomass gasification product. The results showed almost no deterioration in voltage with increasing pressure over a continuous generation test of 5600 h, meaning that stable generation is possible with tubular MCFCs. It was also demonstrated that tubular MCFCs are durable against sudden changes in temperature (about 100 °C per hour) and the differential pressure between the anode and cathode (about 0.1 MPa) as

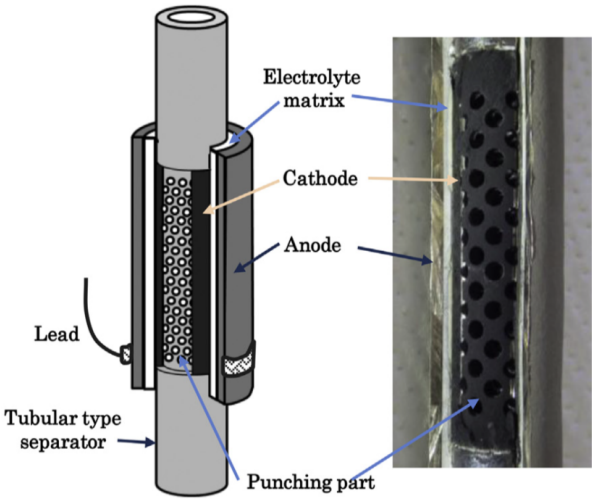

Figure 2.9. Schematic illustration of a tubular MCFC [97].

could be caused by system faults. The results also suggest that the properties of tubular MCFCs could be utilized for fast startup of power generation systems from the cold shutdown state.

2.3 The molten carbonate electrolysis cell

When the MCFC is run in reverse, it operates as a molten carbonate electrolysis cell (MCEC) to produce fuel gas, e.g. hydrogen or syngas (H_2+CO). As mentioned before, for the electrolyzer operation it still uses the state-of-the-art fuel cell components described above, including nickel-based porous electrodes and molten carbonate electrolyte. Fig. 2.10 shows the working principle of the molten carbonate electrolysis cell.

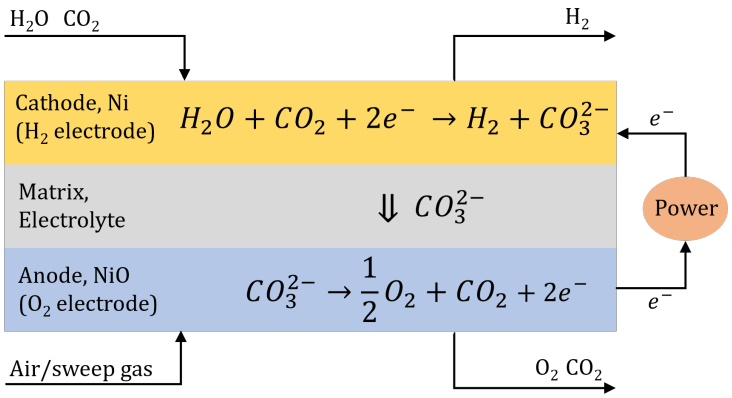

Figure 2.10. The working principle of the molten carbonate electrolysis cell.

The Ni electrode, as anode in the MCFC, works as cathode in the MCEC. Water

is reduced at the Ni electrode according to:

$$H_2O + CO_2 + 2e^- \rightarrow H_2 + CO_3^{2-} \tag{2.12}$$

The carbonate ions are conducted through the electrolyte to be oxidized at the oxygen electrode (i.e. anode in the MCEC), producing carbon dioxide and oxygen, according to

$$CO_3^{2-} \rightarrow CO_2 + \frac{1}{2}O_2 + 2e^- \tag{2.13}$$

No gas flow is strictly required at the oxygen electrode inlet for the electrochemical reaction to proceed. However, in practice, a mixture of air and a small amount of carbon dioxide is supplied as a sweep gas. This ensures an oxidizing atmosphere, which is necessary to maintain the stability of the NiO electrode (see Sec. 2.2.4), while the presence of CO_2 helps stabilize the carbonate electrolyte. So, the overall reaction in the MCEC is

$$H_2O + CO_{2,Ni} \rightarrow H_2 + \frac{1}{2}O_2 + CO_{2,NiO} \tag{2.14}$$

Due to the presence of carbon dioxide in the inlet fuel gas, direct CO_2 electrolysis generating CO may take place at the Ni electrode through the following reaction

$$2CO_2 + 2e^- \rightarrow CO + CO_3^{2-} \tag{2.15}$$

However, it has been reported that the kinetics of this reaction is much slower compared to water electrolysis on nickel-based electrodes [16, 99, 100]. Nevertheless, carbon monoxide could be generated at this electrode through the reverse water-gas shift reaction, i.e. Reaction 2.5.

The following sections will provide an overview of the studies conducted to investigate the performance and durability of MCEC, and the kinetics of the electrodes.

2.3.1 MCEC electrochemical performance

The reversibility of molten carbonate fuel cells was demonstrated in the last decade by Hu et al. [101], who successfully operated a lab-scale molten carbonate cell with state-of-the-art components in both fuel cell and electrolysis modes. Their work revealed improved electrochemical performance in MCEC mode compared to MCFC mode. Specifically, the results showed that the Ni hydrogen electrode exhibited higher polarization losses in electrolysis mode than in fuel cell mode, while the NiO oxygen electrode performed significantly better in MCEC mode. The authors also investigated the electrochemical performance degradation of the cell over time [102]. The MCEC durability test was performed galvanostatically by running a button cell with a 3 cm^2 active area under a constant electrolysis current density of 0.16 A/cm^2 for 2165 h. Although a decrease in the performance of the cell and electrodes is shown after the MCEC durability test, especially when performing measurements in fuel cell mode, the degradation was not permanent and the cell performance could be partially recovered by electrolyte refilling. Since conventional fuel cell materials were used in the MCEC durability test, the study also demonstrated that the cell could alternatively operate as an electrolysis cell for fuel gas production and as a

fuel cell for electricity generation, i.e., as a so-called reversible molten carbonate fuel cell (RMCFC). Notably, the results reveal that the cell performance improves after 1019 h of RMCFC operation.

Conversely, Pérez-Trujillo et al. [103] were the first to test a single molten carbonate cell with an 80 cm^2 active area in reversible mode. Thanks to their increased size and design, single cells give valuable information before progressing to a prototype or industrial stage. However, throughout the experimental campaign the molten carbonate cell presented a quite high degradation, contrary to previous findings of Hu [101, 102]. This result was confirmed in a subsequent work [104], where they operated a conventional molten carbonate cell as alternated fuel cell/electrolysis cell. Rapid cell degradation was recorded as soon as the cell began alternating operating modes, following an initial stable operation period of 650 h in fuel cell mode. A continuous and rapid increase in both internal resistance and electrode polarization was observed during about 400 h of alternated operation. Since partial recovery of cell performance was obtained by electrolyte refilling, electrolyte evaporation was assumed as one possible degradation factor of the cell performance. A detailed analysis with SEM/EDX and XRD was also conducted to evaluate degradation of the active cell materials. Although the electrolyte matrix appeared almost unaffected, clear signs of accelerated structural degradation in both fuel and oxygen electrodes were found as a result of the alternated mode of operations.

Finally, Audasso et al. [105] also conducted a study on the performance of MCECs using single cells. They investigated the behavior of the cell under different operating conditions in terms of temperature and fuel electrode gas composition. A series of long-term tests at -150 mA/cm^2 and 650 °C are performed to demonstrate long-term stability. In particular, before electrolyte loss made the performance unstable, different cells were operated for about 1000 h with an average voltage of about 1.14 V.

2.3.2 Water electrolysis reaction mechanisms and kinetics

Although extensive research has been conducted on the electrode reaction mechanisms in MCFCs [106–109], the same can not be said for MCEC electrodes. Hu et al. studied the kinetics of the NiO electrode [110] and Ni electrode [111] operated in electrolysis mode. They determined the dependency of the exchange current density on the reactant partial pressure to elucidate the mechanisms of the hydrogen and oxygen production reactions in the MCEC. They evaluated the current distribution along the depth of the electrode by a combination of its intrinsic activity, its specific surface area, the effective diffusion path lengths of the electroactive species, and the effective conductivities of the electrolyte and electrode.

For NiO electrode, they found that the reverse process of oxygen reduction in MCFC operation, based on a widely accepted mechanism [112], suitably describes oxygen production in the electrolyzer:

$$CO_3^{2-} \leftrightarrow O^{2-} + CO_2 \tag{2.16}$$

$$O^{2-} \leftrightarrow (O^-) + e^- \tag{2.17}$$

$$O^{2-} + (O^-) \leftrightarrow O_2^{2-} + e^- \tag{2.18}$$

$$O_2^{2-} \leftrightarrow O_2^- + e^- \tag{2.19}$$

$$O_2^{2-} \leftrightarrow O_2 + e^- \tag{2.20}$$

Assuming that reaction 2.20 of oxygen evolution is the rate-determining step, the reaction order for oxygen agrees with the partial pressure dependency obtained from the experimental data. The experimental results for the partial pressure dependency of carbon dioxide indicate a positive dependence at low CO_2 concentrations, with values between 0.09 and 0.30, and a negative dependence at high CO_2 concentrations, ranging from -0.26 to 0.01. These findings are compared with theoretical predictions based on the reaction mechanism. According to reaction 2.16, the coverage of oxide ions (O^{2-}) depends on the CO_2 concentration. Theoretically, a partial pressure dependency of -0.25 is expected under conditions of low O^{2-} coverage, while for high O^{2-} coverage, the dependency increases to 0.75 [110]. Hence, at low CO_2 concentrations, the experimental results agree with the theoretical predictions, as reducing the CO_2 partial pressure shifts the equilibrium of the homogeneous reaction 2.16 toward the formation of oxide ions. However, the theoretical value of 0.75 for elevated O^{2-} coverage is significantly higher than the experimental range $(0.09 - 0.30)$, suggesting that additional reaction mechanisms, potentially involving intermediate O^{2-} coverage and other steps, might influence oxygen production at the NiO porous electrode under these conditions.

As for the Ni electrode, the dependence on H_2, CO_2, and H_2O gas partial pressures on the exchange density was evaluated, and compared with the reaction orders obtained considering four different reaction mechanisms valid for hydrogen oxidation on a flag electrode in fuel cell operation. One of the mechanism studied by the authors was based on the inverse of an accepted reaction mechanism for the hydrogen oxidation, suggested by Lu and Selman [106]:

$$H_2 + 2M \leftrightarrow 2MH \tag{2.21}$$

$$MH + CO_3^{2-} \leftrightarrow OH^- + CO_2 + M + e^- \tag{2.22}$$

$$MH + OH^- \leftrightarrow H_2O + M + e^- \tag{2.23}$$

In their work it is assumed that reaction 2.22 is the rate-determining step, and thus the preceding and following steps are in quasi-equilibrium. The proposed mechanism is based on the assumption that the reaction steps occur in sequence, with no diffusion of intermediates toward or away from the electrode surface. However, to fully account for the significant presence of OH^- ions in carbonate melts [106], it is plausible that reactions 2.22 and 2.23 take place simultaneously, rather than as consecutive steps. In this case, the rate of reaction 2.23 would not be constrained by the supply of OH^- ions from reaction 2.22, and a more rigorous analysis would be required to capture this behavior.

The reaction orders that Hu et al. [111] obtained from experimental data do not reasonably satisfy neither this mechanism nor the other ones they suggested. However, the mechanisms were conceptualized starting from data obtained using flag electrodes. Thus the authors pointed out that the reaction kinetics could be affected by the different morphology and structure of a porous electrode. Additionally, the interpretation of experimental data and the evaluation of kinetic parameters were

based on the assumption that the reactive surface area and the effective electrolyte conductivity were independent on gas composition. The authors commented on the inconsistency of their results, stating that this assumption might not be valid, and suggesting to consider the dependence of electrolyte wetting properties of the hydrogen electrode on the gas composition. Although no agreement was found between the experimental data and the theoretical reaction mechanism, two key elements emerged from their work. First, the hydrolysis equilibrium plays a crucial role and should not be neglected:

$$H_2O + CO_3^{2-} \leftrightarrow 2OH^- + CO_2 \tag{2.24}$$

Second, the hydrogen production reaction involves two charge transfer steps, with at least one serving as the rate-determining step (RDS).

On the other hand, Frangini et al. [113] demonstrated that another reaction mechanism involving bicarbonate species is active at temperature below 600 °C. They investigated the molten carbonate electroreduction of water in the range $500 - 550$ °C, in a ternary carbonate eutectic electrolyte $Li_2CO_3{-}Na_2CO_3{-}K_2CO_3$ (43.5-31.5-25.0 mol%) by using cyclic voltammetry. The study identified a chemical-electrochemical-chemical mechanism, where the electro-reduction step of bicarbonate is preceded by acid-base buffering equilibria of CO_2 and H_2O with the melt, followed up by dimerization reactions of adsorbed hydrogen atoms or radical bicarbonate anions:

$$H_2O + CO_3^{2-} \leftrightarrow 2OH^- + HCO_3^- \tag{2.25}$$

$$OH^- + CO_2 \leftrightarrow HCO_3^- \tag{2.26}$$

$$2HCO_3^- + 2e^- \leftrightarrow H_2 + 2HCO_3^- \tag{2.27}$$

The results suggest that water electrolysis in molten carbonates may be conducted at around 500 °C, although the relatively low electrolysis current densities (20 mA/cm^2 at $-1.6V$) are not yest optimal for practical applications.

2.3.3 Carbon dioxide electrolysis

Apart from water reduction, significant research over the last decade has focused on CO_2 electrolysis, particularly in molten carbonate cells and solid oxide cells. The reactivity of CO_2 in molten carbonates, already well-understood from its application in mature MCFC technology [114, 115], offers potential pathways to convert CO_2 into valuable products like CO, C, or syngas (CO + H_2) when combined with steam. Studies have shown that while the direct one-step reduction of CO_2 into C in molten carbonates is challenging due to the unfavorable reduction potential, the reduction of CO_2 into CO at a moderate electrolysis potential is more feasible [15, 116]. Researchers have explored the optimal conditions for this process, finding that high temperature and high CO_2 partial pressure favor CO production. Cassir et al. [16] highlighted the complexity of the CO_2/CO reduction process, which involves multistep mechanisms and is influenced by various factors, including the composition of the molten carbonate, operating temperature, and gas pressures. They investigated the reaction mechanism using an inert Pt electrode in the state-of-the-art molten eutectic $Li_2CO_3K_2CO_3$ ($62 - 38$ mol%), at 650 °C, under different

partial pressure of CO_2. Their work demonstrated that the electroreduction of CO_2 into CO is feasible in oxo-acidic conditions ($P_{CO_2} > 0.1$ bar), involving a diffusion-limited quasi reversible system in a one electron-step. Finally, in a subsequent study [117], they showed that CO is electrochemically produced in MCECs, with the ratio of products depending on the electrolysis potential. Building on these findings, Monzer et al. [118, 119] developed models for both a laboratory-scale cell and a 1 MW stack, accounting for the simultaneous electrolysis of CO_2 and H_2O in molten carbonate systems. Their results reveal that during CO_2 electrolysis, the limiting current density can be reached at lower values, significantly impacting the cell's performance.

2.4 High-Temperature electrochemical cells modelling

Models describing electrochemical cells may be classified into (i) zero-dimensional models, which consist of correlations between potential and current density, (ii) one-dimensional models, and (iii) multi-dimensional models. For a more comprehensive understanding of the mathematical models developed for high-temperature electrochemical cells, the reader is referred to this review [120]. Below, the strengths and weaknesses of each model class will be discussed, along with examples from the literature specific to MCECs.

2.4.1 0D models

Zero-dimensional (0D) models describe the relationship between cell potential, current, and overpotentials through a relation of the type:

$$E_{cell} = E_N \pm \left(\sum_j \eta_j(i) \right) \tag{2.28}$$

where E_{cell} is the cell potential, the terms η_j are the different overpotentials contributions, which depend on the current density i, and E_N is the open circuit potential, known as Nernst potential:

$$E_N = \left| E^0 - \frac{RT}{n\mathcal{F}} ln \prod_i^{n_c} a_i^{\nu_i} \right| \tag{2.29}$$

The overpotentials can be classified into three categories: activation, ohmic, and concentration. Each of these contributions can be described using either empirical or semi-empirical relationships. While 0D models are computationally efficient and useful for identifying performance-limiting overpotentials, their main limitation is that they cannot be easily applied to cells operating under different conditions or geometries. This limitation arises because the parameters used to describe the various overpotentials are specific to the original setup, which restricts the model's ability to accurately predict improvements in cell performance.

Pérez-Trujillo et al. [103] analyzed five models for MCFCs proposed in the literature for describing a molten carbonate cell operating both as fuel cell and electrolyzer. They found that the fuel cell behavior could be accurately described

by a model accounting for activation overpotentials in both electrodes as well as an Ohmic overpotential. However, none of the models considered accurately describe the operation in electrolysis mode, especially at high current densities. The same group modified one of those models to extend its validity to conditions under which high reactant utilization factors are reached [121]. Nevertheless, the correlation between the numerical and experimental voltage in electrolysis mode was not as good as in fuel cell mode, requiring the improvement of the concentration overpotentials predictions.

Murmura et al. [122] developed a 0D model to analyze data from an MCEC employing a ternary electrolyte mixture and operated in a lower temperature range ($490 - 550$ °C). Their results, combined with those reported in [103] for a cell using a binary electrolyte and operated at higher temperatures, were evaluated with a model accounting for Ohmic and activation overpotentials. Ohmic overpotentials is related to the current density through Ohm's law,

$$\eta_{ohm}(T, i) = \frac{l}{\kappa(T)} \cdot i \tag{2.30}$$

wher l is a fitting parameter and $\kappa(T)$ is the electrolyte conductivity, whose temperature dependence was provided in [102] for high temperatures and [46] for low temperatures. The activation overpotentials was determined from the Butler-Volmer equation:

$$i = i_0 \left(\exp\left(\alpha_a \frac{n\mathcal{F}\eta_{act}}{RT} \right) - \exp\left(-\alpha_c \frac{n\mathcal{F}\eta_{act}}{RT} \right) \right) \tag{2.31}$$

in which the transfer coefficient, α, was considered to be equal to 0.5, from which the following dependence between measured current density, exchange current density (i_0), and temperature, was derived

$$i = 2i_0 \sinh\left(\frac{\mathcal{F}\eta_{act}}{RT} \right) \tag{2.32}$$

The total overpotentials was therefore given by

$$\eta = r(T) \cdot i + \frac{RT}{\mathcal{F}} \text{arcsinh}\left(\frac{i}{2i_0(T)} \right) \tag{2.33}$$

The values of i_0 and r at each temperature were obtained by fitting the experimental data. The agreement between modeled and experimental results was good. It was found that, while the dependence of Ohmic losses on temperatures is discontinuous when cell operation is switched from the lower to the higher temperature range, activation losses vary with continuity. These observations suggest that the electrochemical reaction mechanism does not depend on the electrolyte composition and that Ohmic losses play a significant role in the performance of MCECs.

2.4.2 1D models

Compared to the more simple 0D models, one-dimensional (1D) models could account for concentration, potential, current density, and temperature along the thickness of the electrolyte and electrodes. These models provide a more detailed description of

overpotential contributions, enabling the distinction between anodic and cathodic processes, and incorporating some information about the cell's geometry. The main limitation is that cells rarely have geometries that can be adequately described by a 1D model, making it difficult to accurately assess the different overpotential contributions. Most 1D models found in the literature are for fuel cells and account for concentration, potential, and current density gradients along the thickness of the electrodes and electrolyte [123, 124]. Fig. 2.11 provide an example of an MCFC

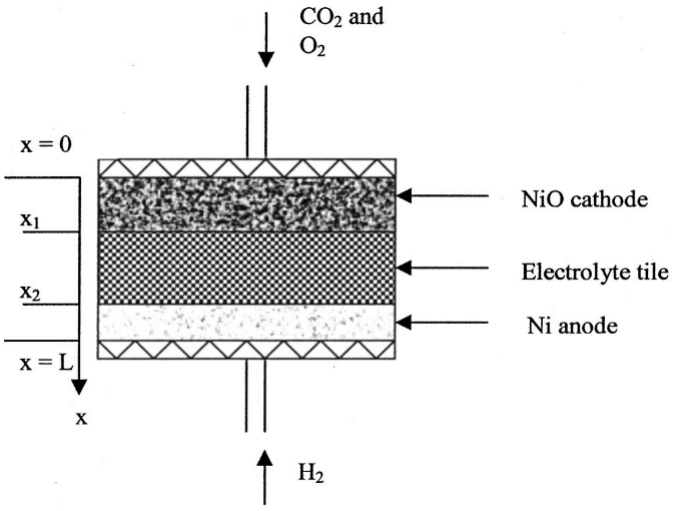

Figure 2.11. Schematic representation of the MCFC modeled by Subramanian et al. [124].

modelled by Subramanian et al. [124] Furthermore, many of these models are specific to either the anode or the cathode, are developed based on experimental data from lab-scale cells, and tend to be quite complex [107, 125].

The only example of a 1D model for MCECs is provided by the work of Hu et al. [126], who analyzed data obtained from a button cell. They developed a model for the porous Ni electrode, based on the Maxwell-Stefan transport equations for mass transfer in the gas phase combined with equations describing the current distribution in the electrolyte phase. It also includes the rWGS, assuming that the reaction mainly takes place in the electrode. A mass balance for gas species k in the electrode is given by

$$\frac{\partial c_k}{\partial t} = -\nabla \cdot N_k + \mathcal{R}_k \tag{2.34}$$

where $\mathcal{R}_k$ is the molar rate of production of k per unit volume, considering both the electrochemical reaction of hydrogen production and the water gas shift reaction. Since in the MCEC the effective conductivity for the solid phase of the Ni electrode is much higher than for the electrolyte phase, they have assumed that the potential change occurs only in the electrolyte phase, which follows the Ohm's law and is given by

$$\nabla \cdot i_l = \nabla \cdot (-\kappa_{\text{eff}} \nabla \Phi_l) = S \cdot j_{\text{loc}} \tag{2.35}$$

where i_l is the geometric current density in the electrolyte phase, κ_{eff} is the effective electrolyte conductivity, Φ_l is the potential in the electrolyte phase, S is the internal specific surface area, and j_{loc} is the local current density for the hydrogen production.

The latter is described through a Butler-Volmer kind expression, see Eq. 2.31. The model was fitted to experimental steady state polarization data for various inlet gas compositions of H_2O, CO_2 and H_2 between 10 and 40%. It was used to predict cell performance for a broad range of inlet gas compositions and to evaluate the effect of the rWGS reaction. The authors pointed out that the fitted kinetic coefficients and electrode porosity differed in the case when including the rWGS compared to when not including the rWGS. Therefore, more experimental data, especially at higher current densities, is needed to shed more light of the role of the rWGS reaction in the MCEC.

A 1D model describing a complete MCEC was developed as a preliminary analysis before creating a 2D model, which is part of the work reported in this thesis (see Section 6.1.2).

2.4.3 2D and 3D models

One-dimensional models allow for a greater degree of detail, although by definition, they only account for potential, concentration, and temperature gradients in one direction; however, electrochemical cells are inherently two- or three-dimensional. For instance, the main flow direction of the gases is generally perpendicular to that of the ion transfer, and more complex models are required for their complete characterization. Multi-dimensional models enable a more in-depth description of the phenomena occurring within an electrochemical cell. Specifically, by increasing the dimensions of the model it is possible to describe the change in gas composition along the direction of the flow of the gas itself. This aspect becomes crucial when chemical reactions take place within the gas channels. In addition, if the cell is not operated under isothermal conditions, the 2D models allow to describe temperature profiles arising within the cell as a consequence of Joule heating, heat effects accompanying the chemical and electrochemical reactions, and the possible application of external heating/cooling systems. On the other hand, it should be noted that in addition to an increased computational cost, multidimensional models require several parameters to be fully defined. Their accurate development therefore goes hand-in-hand with the availability of experimental data to determine the values of the model parameters from their correlation or to validate the use of literature parameters.

2D models have been suggested in the past to describe the behavior of molten carbonate cells in fuel cell mode [123, 127]. The 2D model developed by Bosio et al. [123] for MCFC enabled the identification of the effects of gas cross-over phenomena, which have to be carefully controlled to avoid material damage and losses of electrical efficiency. The model is two-dimensional in the horizontal plane of the cell, assuming no temperature variations along the vertical axis. It is designed for planar rectangular cells with a cross-flow gas feeding system. Based on this model, the authors developed and validated a 3D model for an MCFC stack, accounting for the heat transfer along the vertical coordinate of the stack. They found a good agreement between simulation and experimental results.

Verda and Sciacovelli developed a 3D model to describe a molten carbonate fuel cell (MCFC) stack consisting of disc-shaped cells [127]. Their simulation results highlighted the non-homogeneous distribution of temperature and gas composition at both the cell and stack levels. This non-uniformity was found to decrease

efficiencies and output power densities by increasing resistances and reducing cell lifetime. The latter issue was primarily attributed to the formation of hot spots and significant temperature differences within the cell, which negatively affected material resistance. Further analysis demonstrated that optimizing fluid distribution is crucial for improving cell design. Two different strategies were evaluated, which can be applied together to achieve better performance. It was shown that power density could be increased by about 20% through double-sided feeding. Additionally, the average temperature gradients in the axial direction were reduced by more than 70%. Significant reductions in temperature gradients, particularly in the transverse direction, can also be achieved by adjusting the mass flow rate of the cathodic gas supplied to various cells. This analysis exemplifies the insights that can only be gained by developing multi-dimensional models.

To the best of the author's knowledge, multi-dimensional numerical analyses focusing on MCEC performance are absent from the literature. A 2D model for an MCEC has been developed as part of this thesis, and the results are discussed in a scientific article [128]. These findings will be detailed in Section 6.1.2.

Chapter 3

Analysis tools and techniques

In this Chapter, a description of the basics of the principal and most renowned electrochemical characterization techniques employed in the study of electrochemical cells, namely Polarization Curves (or i-V curves) and Electrochemical Impedance Spectroscopy (EIS), is provided. Additionally, other characterization techniques employed in this study are briefly presented. The following Section will describe the advanced Distribution of Relaxation Times (DRT) method that relies on the EIS measurements. The combination of EIS-DRT will be the basis of the first part of results obtained in the experimental work of this thesis.

3.1 Polarization curves

The polarization curve (or i-V curve) is the most employed diagnostic technique used to characterize the overall immediate performance of electrochemical cells [129]. It consists in the measurement of the cell voltage with the varying of the current provided by an external power supply. It provides information about the general electrical response of the cell over the range of currents investigated, making it a valuable instrument for assessing the dependency of the cell performance on the operating conditions. Additionally, by examining different sections of the plot (see Fig. 3.1), it offers insight on the effects of the different overpotentials. The

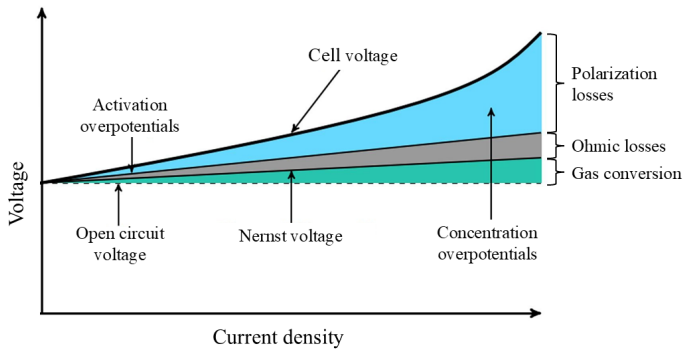

Figure 3.1. Polarization curve and overpotentials for a generic electrochemical cell (adapted from [121]).

Open Circuit Voltage (OCV) represents the inherent potential difference between the electrodes when no external current is supplied to the cell. The OCV can be estimated using the Nernst equation. However, to obtain the real OCV, it is essential to account for the energy losses due to gas conversion occurring inside the cell and any gas leakages. If the Nernst potential is calculated using the molar fractions of the feeding gases without considering these losses, the resulting OCV will be overestimated. In the case of MCEC, rWGS reaction can cause changes in the gas composition at the hydrogen electrode, thereby influencing the OCV value. Even when the gas composition is adjusted to account for the rWGS equilibrium, discrepancies of around 0.05 V between calculated and experimental OCVs have still been documented in several studies [117, 121].

Polarization curves can be divided into distinct regions that represent different electrochemical phenomena affecting the performance of the cell. The first region at low current densities is dominated by activation polarization, which is associated with the energy required to initiate the electrochemical reactions at the electrodes. This region is characterized by a steep rise in voltage as current begins to flow. Indeed, due to the fact that reactions at the electrodes are not infinitely fast, part of the potential is lost to sustain the reaction rate.

The linear trend that covers most of the plot is caused by the ohmic polarization due to the internal resistance of the cell, which is constant with respect to a change in the current density (see Eq. 2.30). As mentioned in Section 2.2.1, the conductivity of the electrolyte is a critical parameter that can limit cell's performance. In fact, in MCECs, the largest contribution to energy loss comes from the ohmic resistance associated with the electrolyte-matrix layer. From the slope of the central region of the curve, the physical quantity known as Area Specific Resistance (ASR), measured in $\Omega \cdot cm^2$, is typically estimated. This allows for a comparison of the overall performance of a cell under different operating conditions or a comparison of different cells under the same conditions.

Finally, at higher current values, the diffusion of chemical species at the electrolyte-electrode interfaces and within the electrodes themselves becomes a limiting factor. As a result, it becomes increasingly difficult to supply a sufficient amount of reactants to the reaction site interfaces. Consequently, there is a significant increase in potential, which in this case is referred to as concentration overpotential, η_{conc}, and can be viewed as an activation energy required to drive mass transfer at the rate needed to support the current. The limiting case for mass transport is when the reactant concentration at the reacting sites drops all the way to zero. Thus, the electrolyzer could never sustain a higher current density than that which causes the reactant concentration to fall to zero. This value is the limiting current density of the electrolyzer.

3.2 Electrochemical Impedance Spectroscopy

Electrochemical Impedance Spectroscopy (EIS) is a highly sensitive technique used to analyze the response of an electrochemical device to a small periodic AC signal applied across a range of frequencies. Unlike polarization curves, EIS can provide detailed insights into the various physicochemical processes occurring within the

cell's components. This is because each of these processes has associated a unique time constant (relaxation time) and, as a result, they each respond differently at different frequencies, allowing for their contributions to be isolated and studied.

3.2.1 Principle of EIS

The most common and standard approach to measure the impedance of an electrochemical system is by perturbing the system and measuring phase shift and amplitude of the system response via the measuring variables voltage and current. According to the way the sinusoidal perturbation signal is provided, the measuring techniques are categorized as galvanostatic and potentiostatic. Considering a potentiostatic measurement, for a generic sinusoidal voltage input signal $e(t) = E\cos(\omega t + \theta)$ the response is a current signal which can be expressed as $i(t) = I\cos(\omega t + \phi)$, where $\omega = 2\pi f$, f being the signal's frequency, E and I are the amplitude of the voltage and current signals respectively, while θ and ϕ are their initial phases. Rewriting both sinusoidal expressions as complex-form functions, $e^*(t)$ and $i^*(t)$, the complex impedance $Z^*(\omega)$ can be calculated as:

$$Z^*(\omega) = \frac{e^*(t)}{i^*(t)} = \frac{E}{I}\exp[j(\theta - \phi)] = \frac{E}{I}\left(\cos(\theta - \phi) + j\sin(\theta - \phi)\right) \tag{3.1}$$

which can be expressed as a complex number having its real and imaginary components expressed as follows:

$$Re[Z^*(\omega)] = Z_{\mathrm{Re}}(\omega) = \frac{E}{I}\cos(\theta - \phi) \tag{3.2}$$

$$Im[Z^*(\omega)] = Z_{\mathrm{Im}}(\omega) = \frac{E}{I}\sin(\theta - \phi) \tag{3.3}$$

It should be noted that an impedance is only defined for systems that satisfy the following conditions [129–131]:

- Causality: a system is causal, when the measured response signal at any point of time exclusively depends on the perturbation signal at this point of time and/or its evolution until this point of time.
- Linearity: the measured response is a linear function of the perturbation signal, i.e., the relation between output and input underlies the principles of superposition and amplification.
- Time-invariance: the output of a time-invariant system does not depend explicitly on time, i.e., the system response on a certain perturbation signal should be exactly the same for any shift of time.

Although many electrochemical systems, including the molten carbonate cells, are usually non-linear, linearity can be assumed when the magnitude of the applied signal is small enough to cause a linear response. In this work the fulfillment of the above mentioned preconditions was verified by applying the Kramers-Kronig relations [132],

$$Z_{\mathrm{Re}}(\omega) = \frac{2}{\pi}\cdot\int_0^\infty \frac{\omega'\cdot Z_{\mathrm{Im}}(\omega')}{\omega^2 - \omega'^2}d\omega' \tag{3.4}$$

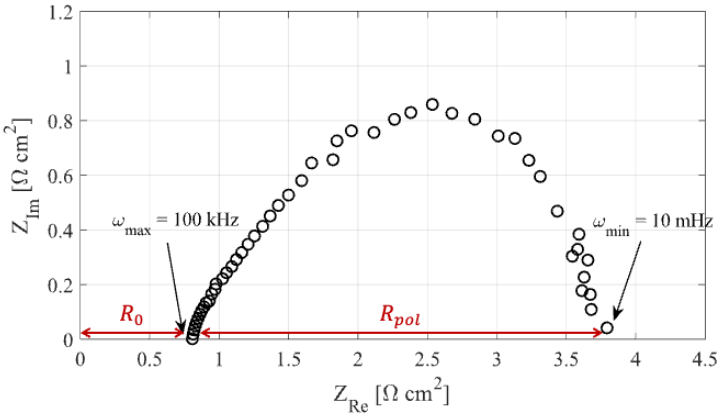

Figure 3.2. Typical Nyquist-plot of a complex electrochemical impedance spectrum recorded on an button MCEC (active surface 3 cm^2, employed in this work).

$$Z_{\mathrm{Im}}(\omega) = \frac{-2}{\pi} \cdot \int_0^{\infty} \frac{\omega \cdot Z_{\mathrm{Re}}(\omega')}{\omega^2 - \omega'^2} d\omega' \tag{3.5}$$

By applying Equations 3.4 or 3.5 to either the real or imaginary part of a measured spectrum, the other component can be computed. If the computed data shows good agreement with the measured values, it can be concluded that the system under investigation is linear, time-invariant, and causal, thereby validating any subsequent analysis based on the EIS data.

3.2.2 EIS measurement on MCECs

There are few studies on the impedance analysis of molten carbonate cells, with almost all conducted in fuel cell mode. However, regardless of the operating mode, molten carbonate cells couple very diverse mechanisms and processes making them non-linear systems. Nevertheless, if the excitation signal is small enough ($E < 10$ mV), the response can be assumed to be linear and time invariant [64]. An impedance measurement is generally performed for a discrete quantity of frequency values ω_n in a frequency range $\omega_{min} < \omega_n < \omega_{max}$ relevant to the analyzed system. For an MCEC a good interval range could be 10 mHz − 100 kHz. Expediently, the frequency range is swept in a logarithmic mode, i.e., the measuring frequencies are chosen in a way that every decade has the same amount of measuring frequencies. The recorded impedance values are usually plotted in the complex plane. This representation is also known as Nyquist plot. Fig. 3.2 gives an example for a Nyquist plot, reporting an experimental EIS spectrum measured from a sample tested in this work.

At very low frequencies, all electrochemical loss processes are excited and contribute to the measured impedance. Since the perturbation frequency is much lower than the relaxation frequencies of these individual loss processes, the voltage response remains in phase with the current perturbation, resulting in the imaginary part of the recorded impedance being zero. As the perturbation frequency is increased, the signal becomes faster than some of the excited loss processes. The slower loss processes start to lag behind the perturbation signal, leading to a decrease in the amplitude of their response. This introduces a phase shift between the excitation

current and the measured voltage response, causing the imaginary part of the impedance to become non-zero, while the real part decreases. When the excitation signal is much faster than the relaxation frequency of a particular physical process, that process is no longer excited and does not contribute to the measured impedance. Therefore, at very high frequencies, none of the physical loss processes are excited anymore, resulting in the voltage response being back in phase with the current perturbation. The high-frequency intercept with the real axis corresponds to the ohmic resistance R_0 of the cell. The difference between the low and high-frequency intercept is the so-called polarization resistance R_{pol} of the cell. R_{pol} is the sum of all single polarization resistances caused by the individual loss mechanisms.

EIS measurements applied on the MCECs enable a clear separation of the ohmic resistance and the polarization resistance of the cell [101, 121]. Further information can be given accepting the general assumption, considered valid for MCECs, that the small arc appearing in the high-frequency region is related to the fast charge transfer mechanism linked to the electrochemical reactions. Therefore, if the real part of the total impedance of this arc is extrapolated, it results in the resistance related to the charge transfer mechanisms responsible for the activation overpotential losses. By similar considerations, the bigger arc appearing in the low-frequency region is often associated with the diffusion resistance, which causes the voltage to rapidly drop at high current densities [101, 102, 133]. However, since the EIS response appears very broadened, it can be challenging to distinctly identify the contributions of individual physicochemical processes to the total polarization resistance. This makes it difficult to completely understand the evolution of these processes and their dependence on the cell's operating conditions. In Section 3.4, an alternative and reliable deconvolution methodology for the EIS spectra, the Distribution of Relaxation Times (DRT), will be extensively explained.

3.3 Other characterization techniques

The following Sections provide a brief overview of the additional characterization techniques used in the experimental portion of this study. In addition to Gas Chromatography (GC), SEM analysis was conducted to perform post-mortem examinations of the tested samples. As these techniques are not central to the focus of this work, further details can be found in more specialized literature.

Gas chromatography (GC)

Gas Chromatography is an essential analytical technique for determining the composition of gas mixtures. This method is based on the differing retention times of gas species as they pass through a stationary phase (solid phase) carried by a mobile phase (gas carrier). Each gas species moves through the stationary phase at varying rates depending on its molecular weight and physical properties, reaching the detector at distinct times, referred to as elution (or retention) times.

The analysis produces a gas chromatogram, which represents the intensity of peaks corresponding to detected gas species as a function of elution time. Qualitative information can be obtained by comparing the elution times to known references,

typically found in literature or stored in the instrument's analysis software. Quantitative analysis is achieved by comparing the peak areas, as the ratio of these areas directly reflects the concentration ratio of the gas species in the mixture.

Scanning Electron Microscopy (SEM) and Energy - Dispersive X-ray spectroscopy (EDX)

Electron microscopes operate on similar principles as light microscopes, but instead of photons, they use beams of energetic electrons to produce high-resolution images of a sample's surface. This ability to examine the microscopic characteristics of samples enables a thorough evaluation of morphological changes resulting from operational conditions and degradation phenomena. Additionally, when energetic electrons collide with the atoms in the sample, they excite the atoms' energy states, and the subsequent relaxation emits radiation in the X-ray spectrum. This phenomenon forms the basis of energy dispersive X-ray spectroscopy (EDS), which provides insights into the sample's chemical composition by identifying the concentrations of various elements. Scanning electron microscopy (SEM) enables detailed analysis of the sample at the micron and submicron scale, facilitating the estimation of geometric parameters such as pore sizes, particle radii, and layer thicknesses.

3.4 Distribution of Relaxation Times (DRT) method

MCECs are intricate electrochemical systems where multiple processes occur simultaneously, each characterized by its own relaxation time. When two or more processes have similar relaxation times, it becomes challenging to isolate their contributions to the total impedance of the cell. This difficulty arises because Electrochemical Impedance Spectroscopy (EIS) can only clearly differentiate processes that are separated by at least two orders of magnitude in the frequency domain.

A useful method to address this limitation is the Distribution of Relax- ation Times (DRT) analysis. DRT allows the representation of impedance as a differential sum of infinitesimally small RC elements, provided that the impedance function obeys the Kramers-Kronig relations, Eqs. 3.4 and 3.5 [134, 135]. Through the application of DRT, each electrochemical process is characterized by its intrinsic time constant τ, with the amplitude corresponding to a distinct contribution to the overall polarization resistance. This method provides a distribution of the magnitudes of individual processes in the frequency domain. The relationship between the impedance spectrum $Z(\omega)$ and the distribution function $\gamma(\tau)$ is expressed in Eq. 3.6:

$$Z(\omega) = R_0 + R_{pol} \int_0^\infty \frac{\gamma(\tau)}{1 + j\omega\tau} d\tau \tag{3.6}$$

Here, R_0 and R_{pol} represent the cell's or electrode's ohmic and polarization resistance, respectively, while ω denotes the angular frequency of the input signal, τ refers to the continuous relaxation time function, and $\gamma(\tau)$ the continuous relaxation time distribution function. The relaxation time distirbution function satisfies the normalization condition, as follows

$$\int_0^\infty \gamma(\tau) d\tau = 1 \tag{3.7}$$

Due to the impracticality of generating a continuous (and infinite) input signal for EIS measurements, the previous equations must be reformulated in discrete form to make the experimental data meaningful. The discrete representation of the relaxation time distribution function can be expressed as:

$$\gamma(\tau) = \sum_{k=1}^{N} \gamma_k \delta(\tau - \tau_k) \tag{3.8}$$

where γ_k is the k-th element of the distribution function and $\delta(\tau - \tau_k)$ is the Dirac delta function. In practice, the discrete function γ_k for N serial RC elements approximate the continuous function $\gamma(\tau)$. The predefined values of τ_k are distributed logarithmically.

As derived from Eq. 3.6 and Eq. 3.8, the impedance can now be described by Eq. 3.9 and Eq. 3.10 for a discrete and finite set of data:

$$Z_{\mathrm{Re}}(\omega) = R_0 + R_{pol} \sum_{k=1}^{N} \frac{1}{1 + (\omega\tau_k)^2} \gamma_k \tag{3.9}$$

$$Z_{\mathrm{Im}}(\omega) = R_{pol} \sum_{k=1}^{N} \frac{-\omega\tau_k}{1 + (\omega\tau_k)^2} \gamma_k \tag{3.10}$$

In this formulation, γ_k represents the contribution of the k-th RC element, characterized by the relaxation time τ_k, to the total polarization resistance. Based on the validity of the Kramers-Kronig equations [134, 136], the DRT function can be calculated either from Eq. 3.9 or Eq. 3.10. Considering the Eq. 3.10 expressed in its matrix form, and introducing the constant value of the polarization resistance into the distribution vector $b_k = R_{pol}\gamma_k$, it results:

$$\boldsymbol{Z}_{\mathrm{Im}} = \boldsymbol{K}\boldsymbol{b} \tag{3.11}$$

The calculation of $\boldsymbol{b}$ represents an inverse ill-posed problem. Although various methods exist to address such problems, the most widely recognized and reliable approach is the Tikhonov regularization algorithm [137]. This algorithm involves solving the following minimization problem:

$$\min_{b} \left\{ \|\boldsymbol{K}\boldsymbol{b} - \boldsymbol{Z}_{\mathrm{Im}}\|_2^2 + \lambda^2 \|\boldsymbol{b}\|_2^2 \right\} \tag{3.12}$$

where λ serves as self-consistent regularization parameter that controls the smoothness of $\boldsymbol{b}$.

The solution to this minimization problem is given by:

$$\boldsymbol{b} = \left(\boldsymbol{K}^T\boldsymbol{K} + \lambda^2 \boldsymbol{I} \right)^{-1} \boldsymbol{K}^T \boldsymbol{Z}_{\mathrm{Im}} \tag{3.13}$$

where $\boldsymbol{I}$ represents the identity matrix. The shape of the solution of Eq. 3.13 is strictly controlled by the value of λ, which must be carefully optimized: high values may obscure distinguishable features, while low values can lead to erroneous oscillations that are unrelated to the physicochemical processes within the system.

Among the several methods for selecting the optimal regularization parameter (e.g. Discrepancy principle, L-curve, Generalized cross validation method), the L-curve is the most widely used in applied mathematics due to to handle noise-induced perturbations [138–140]. The L-curve essentially represents a balance between two quantities that must be managed simultaneously: data fitting and the influence of data errors. On one side, if λ is too large, it over-smooths the solution curve, leading to a poor fit with the data and increasing the following residual: $|\boldsymbol{Kb} - \boldsymbol{Z}_{\mathrm{Im}}|_2$. Conversely, if λ is too small, the fit improves, but the solution shows artificial peaks due to the excessive influence of data errors, resulting in an overly large $|\boldsymbol{b}|_2$ (see Fig. 3.3). According to theory, the optimal value of λ corresponds to the corner of the L-shaped curve. In this work, the Tikhonov algorithm and the optimal regularization parameter value were determined using a custom MATLAB® program.

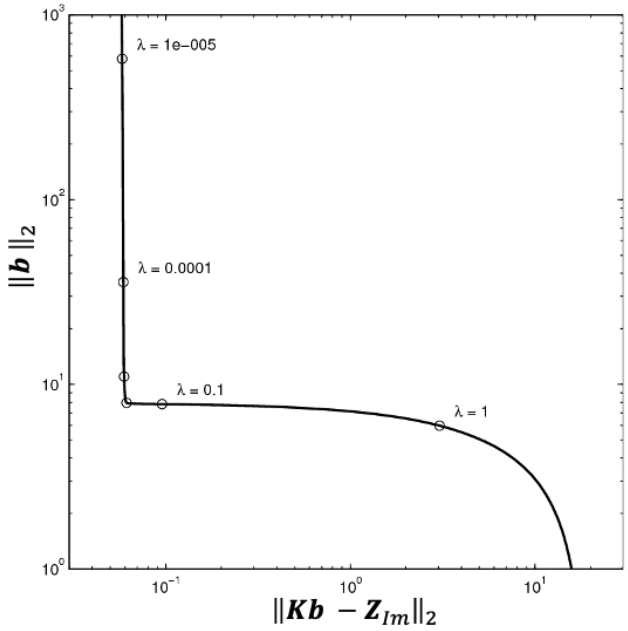

Figure 3.3. L-curves for the Tikhonov regularization (adapted from [139]).

As an example, Fig. 3.4 illustrates the distribution function (red line) obtained from the DRT analysis and the imaginary part of the impedance (black line) of the MCEC tested during the experimental work of this thesis. Although the distribution function shows a slight shift toward the high-frequency region compared to the experimental data, it reveals a clear series of peaks that stand out above the zero line. Each peak, or cluster of peaks, corresponds to the response of a particular physicochemical process, indicating distinct underlying mechanisms. The nature of these peaks will be assessed by means of a systematic experimental campaign, presented hereafter, to shed light on the nature of the process behind each peak.

The DRT method has been already successfully employed in the study of physicochemical processes occurring in both fuel cells [141, 142] and lithium-ion batteries [143]. Regarding molten carbonate cells, to the author's knowledge, there is only one study in the literature about DRT applied to a 100 cm^2 cell operated under fuel cell conditions [64], and nothing about MCECs. In [64] temperature

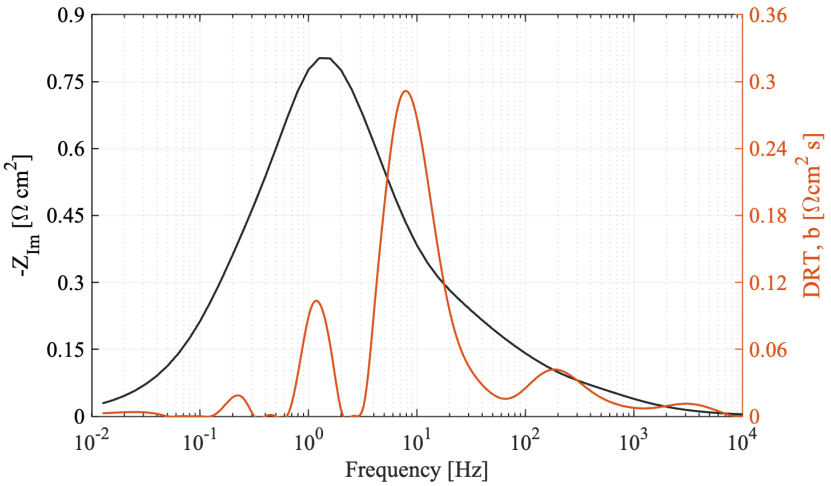

Figure 3.4. Imaginary component of the MCEC impedance and the DRT distribution function when the cell is operating at 650 °C, and fed with $O_2/CO_2/N_2$ (15/30/55 mol%) and $H_2/CO_2/H_2O/N_2$ (10/20/20/50 mol%) respectively on the anodic and cathodic side.

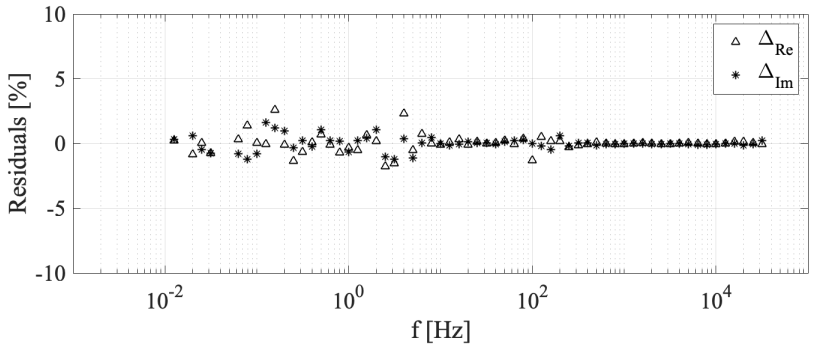

Figure 3.5. Computational residuals of Kramers-Kronig reconstruction as a function of frequency for the EIS measurement reported in Fig. 3.2.

and gas composition effects on the cell impedance have been investigated and five physicochemical processes have been identified: three charge transfer processes at high frequencies and two mass transfer phenomena at low frequencies.

Finally, it is important to underline that the quality of the experimental data plays a fundamental role in the interpretation of the DRT plots. If the experimental spectra are affected by instrumental interference that cause a loss in the linearity of the EIS response, scattered signals appear in the EIS spectra that will be converted into ghost peaks into the DRT plots, impeding a correct identification and analysis of the processes. A method to assess the quality of the experimental spectra is the so-called Kramers-Kronig test, which basically assess the validity of the Kramers-Kronig relationships through all the frequency range examined.

In this work, the Kramers-Kronig test was performed by means of the "Lin-KK Tool" software developed by Boukamp et al [132, 134, 135]. The residual errors plot of the aforementioned test is depicted in Fig. 3.5. To the best of the authors'

knowledge, there are no specific thresholds for KK residuals reported in the literature concerning molten carbonate button cells. In this study, the KK residuals remain relatively low (approximately below 3%) and, more importantly, exhibit no significant bias, with the residuals distributed randomly around zero. This random distribution satisfies key criteria for the validity of the KK relations, including time-invariance and causality of the system. While the spectrum contains noise, the lack of significant bias in the residuals supports the reliability of the DRT results. It must be noted that in some cases, especially when high water contents are fed to the cell, the low frequency region of the spectra is affected by a more significant error, but still acceptable.

Chapter 4

Experimental

In this chapter, the technical realization of the experiments performed in the thesis is addressed. For the experimental campaign, two setups were used: i) button cell, cylindrical in shape with an active area of approximately 3 cm^2, ii) planar single cell, square-shaped with an active area of 100 cm^2. In the first sections, the materials used for assembling the cells, as well as the characteristics of the two setups employed, are described. In the second part of this chapter, the testing procedures and conditions adopted for the realization of all the experiments described in this thesis are summarized.

The experimental work here presented was carried out at the Laboratory for Hydrogen and new Energy Vectors (TERIN-DEC-H2V) of the Department of Energy Technologies and Renewable Sources at ENEA (Rome, Italy).

4.1 Materials and equipment set-ups

The same materials were used for the main components (i.e., electrodes, matrix, and electrolyte) in both the button and single cell, all of which were provided by KIST Fuel Cell Research Centre laboratories in Seoul (South Korea). The electrodes consist, on the hydrogen side, of a Ni alloy with 5% Al, necessary to give mechanical stability, while the oxygen electrode is made of NiO. A porous $\gamma-LiAlO_2$ matrix separates the electrodes and also provides support for the electrolyte, which is an eutectic mixture of 62/38 mol% Li_2CO_3/K_2CO_3. All these components are made by tape-casting [29] and the main characteristics are summarized in Table 4.1. For the current collectors, nickel is used on the hydrogen side, while stainless steel SS316 is employed on the oxygen side.

The electrolyte layers are alternated with the matrix layers and then assembled between the hydrogen electrode (bottom) and the oxygen electrode (top). During the cell heating, when the melting point of the electrolyte is reached, it converts into liquid filling the hydrogen electrode and part of the matrix by gravity, while the oxygen electrode is filled due to capillary forces. As explained in Sec. 2.2, the electrolyte has to completely fill the matrix pores and partially fill the electrodes. Single cells and button cells have different active area, specifically 100 cm^2 and 3 cm^2, respectively. As a result, each cell type requires a different quantity of electrolyte and matrix layers to achieve the required filling degree (see Tab. 4.1).

Table 4.1. Characteristics of cell components used in the button and single cell set-ups.

Characteristics of unit cells components	Single cell	Button cell
Cell frame, size	Square 13 cm × 13 cm	Circular 3 cm^2
Cell frame, material	Aluminized SUS-316 L	Ceramic
H_2 electrode current collector, size	11 cm ×11 cm	3 cm^2
H_2 electrode current collector, material	Ni	Ni
O_2 electrode current collector, size	10 cm ×10 cm	3 cm^2
O_2 electrode current collector, material	SUS-316 L	SUS-316 L
H_2 electrode		
Thickness (mm)	0.69	
Porosity	$55 - 60\%$	
Material	Ni + $5\%_{wt}$ Al	
O_2 electrode		
Thickness (mm)	0.70	
Porosity	$60 - 65\%$	
Material	NiO	
Electrolyte	Li_2CO_3/K_2CO_3 (mol% 62:38)	
Matrix		
Material	γ-$LiAlO_2$	
Thickness [a] (mm)	5 × 0.3	2 × 0.3

[a] Each matrix sheet is about 0.3 mm thick, two and five sheets were employed for the button cell and the single cell, respectively.

Button cells were employed for the electrochemical characterization and evaluation of single physicochemical processes. Single cells were used in order to study the evolution of chemical and electrochemical reactions *in operando* and the direct coupling of MCECs with photovoltaic power. More details on the set-ups and the experimental procedures adopted in this work will be provided in the next sections.

4.1.1 Button cell test station

A schematic representation of the laboratory cell equipment is provided in Fig. 4.1. The set-up is equipped with reference electrodes (gold wires in equilibrium with a gas mixture containing 33/67% O_2/CO_2) for measurement on individual electrodes. The two identical reference electrodes are placed in separate chambers filled with the same electrolyte as in the cell. The setup features two separate chambers containing the electrolyte, each equipped with a reference electrode (gold wires in equilibrium with a gas mixture of 33/67% O_2/CO_2) for individual electrodes measurements. The small-scale cell, housed in a ceramic cell casing, was placed inside an oven. The cell

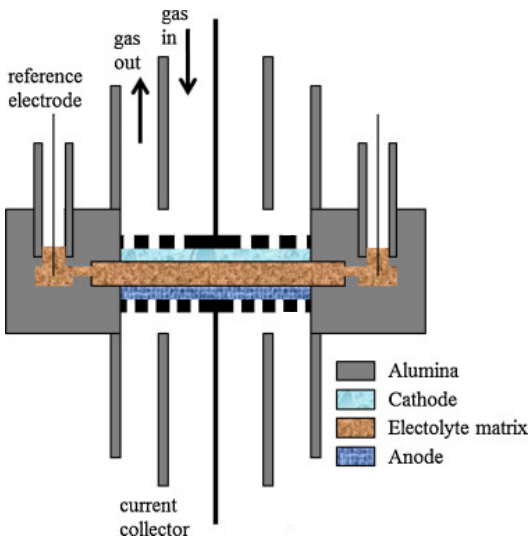

Figure 4.1. The button MCEC in cross-section, adapted from [65]. The terms "anode" and "cathode" refer to the fuel cell mode, specifically the H_2 electrode and the O_2 electrode, respectively.

temperature was kept constant throughout each experimental run and was monitored with two K-type thermocouples: one located within the furnace and another placed directly on the cell to detect any temperature discrepancies between the interior and exterior. Gas flow meters from Bronkhorst were used to regulate the flow of all gases, except for water, which was introduced via a Controlled Evaporation and Mixing (CEM) system. Additionally, two thermocouples were installed in the gas supply lines to both electrodes to monitor the gas temperatures. This was done to ensure that water in the lines remained in vapor form, preventing condensation and avoiding inaccurate measurements. All equipment and experimental parameters were managed and tracked through a custom software interface developed in the LabView environment.

4.1.2 Single cell test station

The cell is housed within two stainless steel SS316 casings, which are placed inside a heating furnace. A schematic representation of the casing-electrode-matrix-electrolyte assembly is reported in Fig. 4.2. The casings are equipped with conduits that serve the dual purpose of supplying gases to the electrodes and providing electrical connections. The single cell was tested in an MCFC Test Station produced by CNL Energy Co. Ltd. The test bench is equipped with Bronkhorst® EL-FLOW Classic mass flow meters for all the gases. A humidifier is employed to control water vapor content in the hydrogen electrode inlet gas stream. Five K thermocouples were used to monitor the thermal behavior of the system. Two thermocouples were placed in the lines supplying the gases (hydrogen and oxygen line), and another one in the humidifier. The last two thermocouples were placed in the furnace and the hydrogen electrode housing to monitor the cell temperature. All these components were

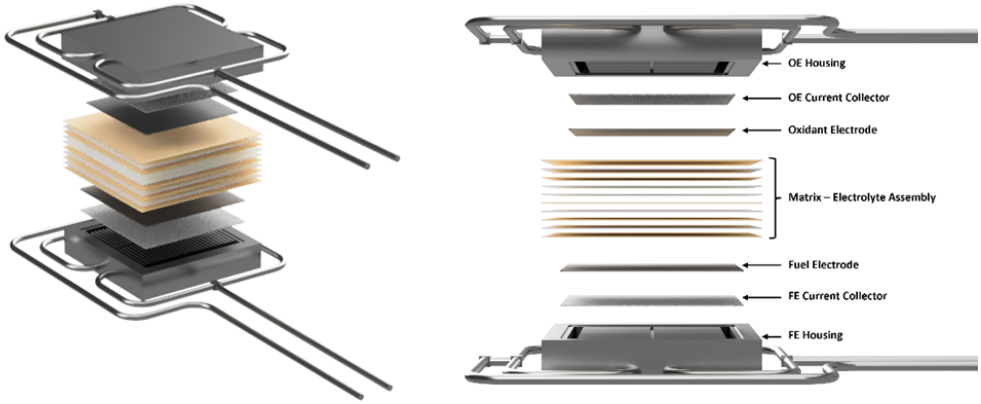

Figure 4.2. Single cell assembling for MCEC performance tests.

controlled and monitored through a software interface developed by CNL Energy Co. Ltd.

4.2 Experimental campaign

The experimental procedure and testing conditions are summarized hereafter. These include the start-up process, the identification and estimation of physicochemical processes, the study of the evolution of chemical and electrochemical reactions, and the investigation of the direct coupling of MCECs with photovoltaic power sources.

4.2.1 Button cells testing conditions

The start-up procedure of the button cell includes a temperature and gas profile. At first, the cell is under air and the temperature is gradually increased 450 °C in 4 h, in order to burn away binder materials and reach the carbonate melting point. Then the air is exchanged for CO_2 and the cell is kept at 450 °C for 2 h, until it is raised to the working temperature, i.e. 650 °C. Lastly, the gases are changed to the standard fuel and oxidant gases containing 64/16/20% $H_2/CO_2/H_2O$ and 15/30/55% $O_2/CO_2/N_2$, respectively. Meanwhile, a weight of approximately 2 kg is put on the top of the cell. In order to obtain a steady and good performance, the cell is run in fuel cell mode under a constant current load for almost one week. After that, the operating conditions, including gas compositions, temperatures, and operation modes (i.e., electrolysis cell, and fuel cell), can be changed for investigation.

To determine the mechanisms of the phenomena involved in the operation of an MCEC, an experimental campaign was decided upon to investigate only the dynamics of the hydrogen compartment. This choice was based on the results of previous studies [101, 103, 110, 121] which highlighted that the anodic dynamics in MCECs are substantially less relevant for the correct functioning of the electrolyzer. A gas consisting of 15/30/55% $O_2/CO_2/N_2$ was used for the NiO oxygen electrode during all the experiments. The reference composition for the Ni electrode is 10/20/20/50% $H_2/H_2O/CO_2/N_2$ (Test I in Tab. 4.2) to have the same CO_2 and H_2O content,

Table 4.2. Test matrix containing the molar percentages of the inlet gas for the hydrogen electrode of the button cell.

	Test	$\%H_2$	$\%H_2O$	$\%CO_2$	$\%N_2$
Reference composition	**I**	**10**	**20**	**20**	**50**
$\%H_2O$ variation	II	10	**10**	20	**60**
	III	10	**30**	20	**40**
	IV	10	**50**	20	**20**
	V	10	**70**	20	**0**
$\%CO_2$ variation	VI	10	20	**10**	**60**
	VII	10	20	**30**	**40**
	VII	10	20	**50**	**20**
	IX	10	20	**70**	**0**

reactants of the electrochemical reaction, and to ensure a reducing environment for the electrode stability with the presence of 10% hydrogen. Finally, the nitrogen is necessary to evaluate the effect of varying the molar fraction of the reactants while keeping the total flow rate constant. Starting from the reference composition, the molar fraction of the reactant gases at the hydrogen electrode was varied one at a time while keeping the other operating parameters constant (e.g., temperature, total flow rate, molar fraction of the other chemical species). Different gas mixtures of $H_2/H_2O/CO_2/N_2$ used for the Ni hydrogen electrode are shown in Tab. 4.2. The compositions to be analyzed were defined at 10%, 30%, 50%, and 70% molar fraction of water vapor (Test II-V in Tab. 4.2). The same values were then considered for carbon dioxide (Test VI-IX in Tab. 4.2). For each test the gas mixture is also modified in the N_2 partial pressure, allowing the molar fraction of the compound under study to be varied without altering the fractions of the other components. The total gas flow rates were maintained at a constant value of 200 mL/min and 20 mL/min for the electrodes and the reference electrodes, respectively.

The test matrix reported in Tab. 4.2 was repeated at three different temperatures, 620, 650 and 680 °C. The variation in operating temperature is particularly interesting for evaluating the chemical-physical phenomena occurring in a MCEC. Temperature influences the diffusion processes of the components within the device: an increase in temperature leads to greater molecular diffusion. Additionally, temperature affects the electrical conductivity properties of the electrodes: the resistance of the anodic and cathodic metallic materials increases with decreasing temperature. The impact of temperature on the electrolyte's liquefaction condition is also significant: higher temperatures increase ionic mobility within the matrix-electrolyte complex. Regarding the reactions occurring in the cell, in addition to the electrochemical reactions, the reverse water-gas shift (rWGS) reaction takes place, which is favored by high operating temperatures.

For each condition, the electrochemical performance of the cell and the individual electrodes were evaluated through the use of galvanostatic polarization curves and electrochemical impedance spectroscopy (EIS) tests. The former were carried out using a BK Precision 9201 Multi-Range DC Power Supply, to supply a specific current. Whereas the latter were carried out using a Solartron SI-1260 frequency

response analyzer module and a Solartron SI-1287 Impedance/Gain - Phase analyzer. ZView software for Windows from Scribner Associate Inc. is employed to process the EIS data. EIS measurements were performed at open circuit voltage (OCV) and in electrolysis mode in the frequency range 10 mHz - 10 kHz. OCV measurements were run potentiostatically with an amplitude of 10 mV, while in electrolysis mode the measurements were run galvanostatically applying a current of 100 mA/cm^2. Measuring EIS at OCV allows for the characterization of the system's inherent electrochemical properties without any external current. Conversely, the measurements in electrolysis mode can provide insight into the cell behavior in-operando. This helps in understanding how the system responds under load and identifies any potential performance limitations. Applying a current of 100 mA/cm^2 ensures that the cell is under a controlled and stable conditions (i.e. ohmic losses region of the polarization curve), and the value is chosen to be representative of typical operating conditions, enabling the study the system's behavior under realistic electrolysis scenarios.

Once the in-operando electrochemical measurements are completed, the polarization curves will be investigated to evaluate the effect of gas composition and temperature on the hydrogen electrode performance, while the impedance spectra will be processed using the DRT method. This method allows for the deconvolution of the impedance spectra, thereby separating the individual contributions of the processes occurring in the electrodes.

4.2.2 Single cells testing conditions

The start-up procedure for the single cell takes longer than for the button cell, i.e., about a week, but follows the same steps. First, the temperature is gradually increased until reaching the melting point of the carbonates, with air supplied to both electrodes. Then, the temperature is kept constant until the electrolyte is fully melted, switching air with pure CO_2. At this point, still supplying CO_2, the temperature is gradually increased again until reaching the operating temperature (650 °C). At the end of this procedure, the cell is fed with the same standard mixtures as the button cell, i.e., 64/16/20% $H_2/CO_2/H_2O$ and 15/30/55% $O_2/CO_2/N_2$, and a 2 kg load is applied to the cell, just like with the button cell. The cell is then run in fuel cell mode under a constant current load for almost two weeks until stable performance is achieved. Two experimental campaigns were carried out using this set-up, as described in the following paragraphs.

Systematic operating conditions variations

In line with the test performed on the button cell, the first experimental campaign on the single cell focused on the systematic variation of certain operating conditions at the hydrogen electrode (HE). The aim is to quantify the cell's performance in terms of both power consumption and hydrogen production, by varying the composition at the HE (%H_2O and %CO_2) and the temperature. The choice of these variables is motivated by their significant influence on the electrochemical reactions and the overall behavior of the cell during electrolysis. By analyzing these parameters, the study seeks to understand not only how they affect the efficiency of hydrogen production, but also how they influence secondary reactions, such as the rWGS

Table 4.3. Test matrix containing the molar percentages of the inlet gas for the hydrogen electrode of the single cell.

	Test	$\%H_2$	$\%H_2O$	$\%CO_2$	$\%N_2$
Reference composition	**I**	**10**	**20**	**20**	**50**
$\%H_2O$ variation	II	10	**10**	20	**60**
	III	10	**30**	20	**40**
	IV	10	**40**	20	**30**
$\%CO_2$ variation	V	10	20	**10**	**60**
	VI	10	20	**30**	**40**
	VII	10	20	**40**	**30**

reaction, which can lead to the formation of CO. This is particularly important because optimizing these variables is key to either minimizing CO formation for pure hydrogen production or maximizing syngas yield, depending on the desired application.

During all the experiments, the NiO oxygen electrode was supplied with a gas mixture of 15/30/55% $O_2/CO_2/N_2$. The reference composition for the Ni electrode was 10/20/20/50% $H_2/H_2O/CO_2/N_2$ (Test I in Tab. 4.3), which is the same as that used in the button cell test campaign. Starting from this reference composition, the molar fraction of the reactant gases at the hydrogen electrode was varied one at a time while keeping the other operating parameters constant (e.g., temperature, total flow rate, molar fraction of the other chemical species). The tested gas compositions at the HE are summarized in Tab. 4.3. The test matrix was repeated for three different temperatures: 620 °C, 650 °C, and 680 °C. An increase in temperature can enhance the kinetic energy of gas molecules, leading to improved mass transport and more uniform distribution of reactants within the inlet channels. This is particularly important in an industrial setting, where optimal gas flow is crucial for maximizing reaction efficiency. Additionally, higher temperatures can reduce the viscosity of the gas mixtures, further promoting better flow characteristics and reducing potential pressure drops across the system. However, it is essential to consider that while increased temperatures facilitate gas diffusion and improve reactant accessibility at the electrodes, they may also influence the reactions taking place, including the rWGS reaction, which is favored at elevated temperatures. Moreover, temperature significantly impacts the electrochemical performance of the cell, influencing parameters such as OCV and thermoneutral potential. Additionally, elevated temperatures typically reduce the ohmic resistance of the cell, allowing for more efficient electrolysis. Thus, understanding the thermal behavior and optimizing the temperature within the single cell is vital for achieving efficient performance and reliable operation.

The total gas flow rates were consistently maintained at 440 mL/min for both the electrodes. These values were selected to analyze the performance of the cell at significant current levels, thus ensuring meaningful conversion rates for the electrochemical reactions under investigation.

For each condition, polarization curves and impedance measurements in OCV were performed on the cell to evaluate its electrochemical performance across a range

of operating conditions. The polarization curves were obtained using an electronic ELS300Z from ELTO DC Electronics Co. integrated into the station, while the EIS measurements were carried out using a Solartron SI-1260 frequency response analyzer module and a Solartron SI-1287 Impedance/Gain - Phase analyzer.

After defining the polarization curve, measurements were taken at various current densities corresponding to different levels of conversion, to quantify the hydrogen production through electrolysis and the CO formation. Keeping the cell under the chosen load conditions, gas chromatographic analyses were conducted on the outgoing streams from the hydrogen electrode. A Clarus 680-Perkin Elmer gas chromatographer, outfitted with specific columns for the compound studied (Hayspe Q and Molecular Sieve 5A) and a thermal conductivity detector (TCD), was used to analyze the composition at the hydrogen electrode outlet. Gas chromatographic analysis allows for quantifying the productivity of chemical and electrochemical reactions and how they are influenced by operating conditions.

MCEC coupled with PV

The second part of the experimental tests conducted on the single cell will focus on studying the integration of molten carbonate electrolyzers in a real-world context, specifically with supply from non-programmable renewable sources (e.g., solar and wind). To this end, dynamic experimental campaigns have been designed to simulate typical days of the year and the corresponding electricity supply. These tests will focus on the dynamic response of MCEC devices when powered by variable electrical power throughout the day. The ambitious goal of this work is to perform a long-term test on a single MCC repeating unit that can mimic the direct coupling of the electrolyzer with photovoltaic (PV) systems over a typical meteorological year. The designed experimental campaign aims to continuously monitor the electrochemical performance of the MCEC in a load-following configuration, simulating twelve typical PV days distributed throughout the year.

The first step was to quantify the solar irradiation in a typical meteorological year (See Fig. 4.3) using the opens source tool from EU Photovoltaic Geographical Information System (PVGIS, [146]), geo-locating a hypothetical photovoltaic plant at ENEA Casaccia R.C., Rome. The choice of this location does not invalidate the generality of the work, as it is representative of the Italian climate and, more broadly, of a moderate climate with an annual solar yield of around 1500 kWh/m^2 [147, 148]. This allowed for the definition of monthly electricity production profiles throughout the typical meteorological year (TMY).

After obtained the monthly energy profiles, they were further broken down into hourly profiles for each month of the typical year under consideration. For each month, a representative day was selected by choosing the daily energy production profile with the highest root mean square deviation from the monthly average. By setting the peak power of the PV system under consideration to 1 kW, the percentage of power delivered on an hourly basis was calculated for the twelve typical days identified in the previous step. As an illustrative example, Fig. 4.4 shows the profile for the month of January along with the selected typical day. As the final step, the percentage of power delivered by the PV system was compared with the power that can be delivered by a single cell in electrolysis mode. To achieve this, a polarization

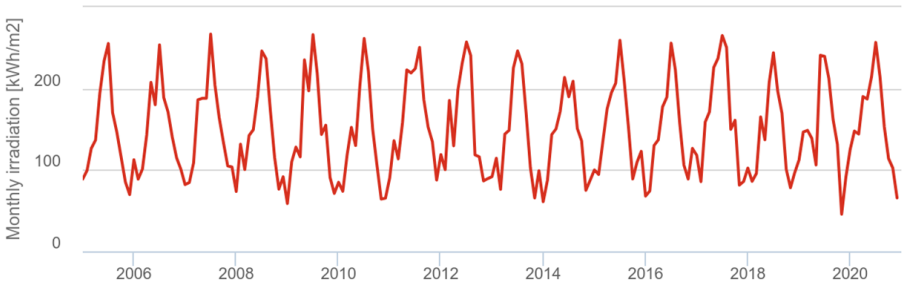

(a) *Monthly solar irradiation from 2005-2020.*

Month	Year
January	2008
February	2005
March	2016
April	2008
May	2008
June	2010
July	2007
August	2017
September	2012
October	2012
November	2015
December	2017

(b) *Selected months for the TMY.*

Figure 4.3. Typical meteorological year simulated by PVGIS tool [146], geo-locating an hypothetical PV plant at ENEA Casaccia (Rome).

curve under reference conditions was used as a model (i.e., using the same reference composition as in previous experimental campaigns, see Tab. 4.3). The maximum power deliverable by the single-cell MCEC was determined in the linear region of this curve.

Once the deliverable powers for the single cell were determined, two experimental campaigns were conducted to investigate the electrochemical behavior of MCECs over time, when the input power is variable. In the first experimental campaign, variable power profiles were applied to the cell terminals to simulate the 12 typical days described previously, while maintaining the same gas composition at the inlet. This yielded pairs of voltage-current values for each hour of each typical day. Subsequently, assuming a real operating scenario where the inlet gas flow rates can be adjusted to maintain constant reactant conversion based on the power available from the renewable source, a second experimental campaign was structured. This campaign used the currents absorbed by the cell from the previous experiment as input values. Based on these currents, the gas flow rates entering the MCEC were recalculated

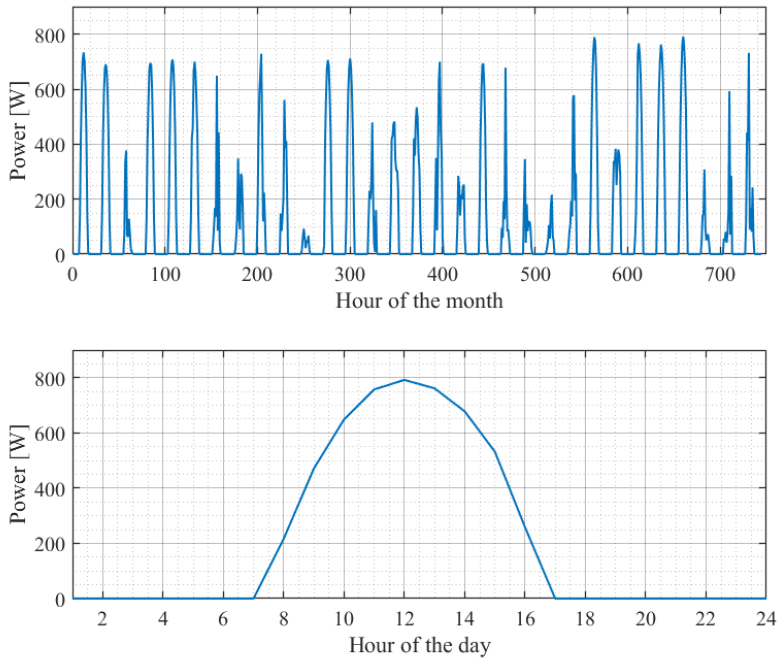

Figure 4.4. Top: monthly power profile for January with respect to the TMY in Fig. 4.3 considering a 1 kW PV plant; bottom: power profile of the typical day in January with the highest root mean square deviation from the monthly average.

hour by hour to ensure constant conversion of the reactants. Fig. 4.5 schematically summarizes the experimental procedure just described.

The aim of the experimental campaigns was to continuously monitor the electrochemical performance of the molten carbonate electrolyzer in a load-following configuration, simulating twelve typical days of PV energy distribution throughout the year. This approach can shed light on the dynamic behavior of molten carbonate electrolyzer, enabling the identification of degradation effects that occur during progressive increases and decreases in power load.

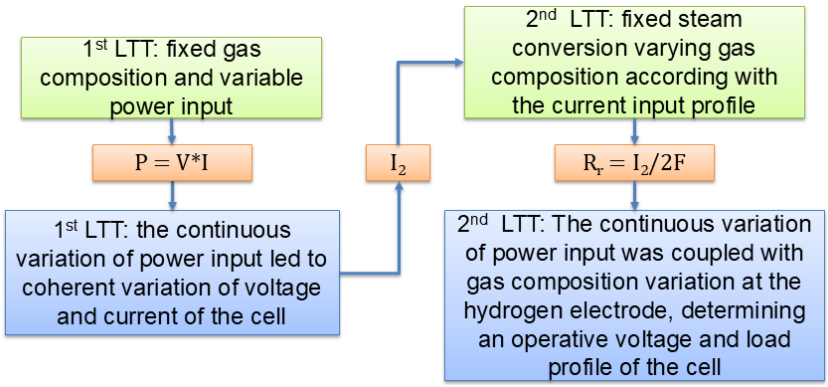

Figure 4.5. Experimental procedure to investigate the single MCEC behavior when coupled with a PV source. LTT stands for *long term test*.

Chapter 5

Electrochemical investigation of Nickel electrode in a button MCEC

In this chapter, the results of the experimental campaign conducted on the molten carbonate button cell, as described in Sec. 4.2.1, are presented. The analysis of the results focuses on investigating the electrochemical mechanisms occurring at the Ni hydrogen electrode, as this electrode appears to play a critical role in the molten carbonate cell's performance during electrolysis mode.

In the first part, the polarization curves obtained at the Ni electrode are presented. Since the hydrogen production reaction mechanism is not yet fully understood, a preliminary analysis of the kinetic parameters at the Ni electrode has been conducted in this work. The general approach for elucidating the reaction mechanism in the MCEC involves determining the dependency of the exchange current density on the partial pressures of the reactants. In this study, the exchange current density is estimated at the various tested conditions using the Butler-Volmer equation, focusing on polarization data at low overpotential to minimize the influence of mass-transfer limitations.

The second part of this chapter describes the DRT analysis conducted on the Ni electrode impedance spectra, which were evaluated across a broad measuring range of temperature and gas composition (see Tab. 4.2). To the best of the author's knowledge, this study is the first to apply the DRT approach to molten carbonate cells operating in electrolysis mode. This method enabled the separation of four different polarization loss mechanisms occurring inside the Ni electrode based on their characteristic time constants. The main process, at about 10 Hz, exhibits a systematic dependency on H_2O and CO_2 variation and thus it can be attributed to mass transport losses. Whereas, the observed trends at low frequencies underscore the potential influence of electrolyte wetting properties on electrode performance, even though uncertainties persist regarding the precise nature and consistency of these effects. The results presented in the second section of this chapter are also detailed in a manuscript that has been submitted for publication [149].

5.1 Evaluation of kinetic parameters

The work by Hu et al. [111] is the only systematic study aimed at investigating the reaction mechanisms characterizing the Ni electrode. For the estimation of exchange current density, i_0, they have analyzed iR-corrected[1] polarization curves at low overpotentials, using a model developed for porous electrodes, which was previously validated for a button cell in fuel cell mode [109, 150]. This model describes the iR-corrected overpotentials accounting for the current distribution along the thickness of the electrode, according to:

$$\frac{d\eta}{di} = \sqrt{\frac{RT}{n\mathcal{F}Si_0\kappa}} \tag{5.1}$$

where κ is the effective electrolyte conductivity in the electrolyte phase. S is the exterior surface area of the agglomerates, where the dominating part of the electrode reaction takes place. The value for both κ and S were taken from previous work conducted to study MCFC performance [125], and were considered constant for all gas compositions tested. The overpotential data were fitted using Eq. 5.1 to obtain the exchange current density i_0 for each set of experimental conditions. From the derived i_0 values, the partial pressure dependencies for hydrogen, carbon dioxide and water were determined through the following relationship:

$$i_0 = i_0^*(y_{\mathrm{H_2O}})^a(y_{\mathrm{CO_2}})^b(y_{\mathrm{H_2}})^c \tag{5.2}$$

where y_k indicates the molar fraction of the general component k, i_0^* is the standard exchange current density, and, a, b and c denote the reaction orders of water and carbon dioxide, and hydrogen, respectively.

The authors found that the experimentally evaluated parameters a, b, and c did not agree with the theoretical reaction orders predicted by the proposed reaction mechanisms. They have explained this discrepancy by referring to the assumptions made for estimating the surface area and effective conductivity.

In this thesis, the polarization curves where analyzed using a different approach, mainly due to two key factors. First, the material used for the hydrogen electrode is a Ni-Al alloy, while Hu et al. used Ni-Cr. The choice of different materials for the electrode can affect the electrochemical behavior, as Ni-Al and Ni-Cr have different structural characteristics (see Sec. 2.2.3). The porosity level and the pore distribution of the electrode impact the arrangement of the electrolyte within the electrode, and, as a result, influence both the effective conductivity and the surface area. To the author's knowledge, no studies in the literature specifically focus on evaluating these properties for the material used in this thesis, i.e. Ni + $5\%_{\mathrm{wt}}$ Al. Additionally, given the challenges in estimating these parameters solely from polarization and impedance spectroscopy data, a different modeling strategy was adopted in this work, which does not rely on assumptions about these properties.

The objective of this section is to evaluate the reaction orders of water and carbon dioxide for the electrolysis reaction based on the determination of exchange

[1]The term "iR" represents the product of the current (i) and the internal resistance (R) of the cell. An iR-corrected polarization curve removes this ohmic contribution, providing a more accurate representation of the intrinsic electrochemical performance of the electrodes.

current densities, adopting a different strategy from that of Hu et al. The evaluation of the reaction orders will enable speculation about the reaction mechanism and, therefore, gain a deeper understanding of the roles that these two reactants play in the kinetics of the electrode.

5.1.1 Methodology

The exchange current densities are obtained by analyzing iR-corrected polarization curves at low overpotentials. The curves for each operating condition were corrected for the internal resistance by subtracting the term $i \cdot R_0$ from the experimental overpotential value, where R_0 represents the internal resistance determined from EIS experimental data under the same operating conditions. In the low overpotentials region, the mass-transfer limitations are assumed to be negligible, meaning that the polarization losses can be attributed solely to the electrode reaction activation polarization. Therefore, the current-voltage relationship was described through the Butler-Volmer equation:

$$i = i_0 \left(\exp\left(\alpha_a \frac{n\mathcal{F}\eta_{act}}{RT} \right) - \exp\left(-\alpha_c \frac{n\mathcal{F}\eta_{act}}{RT} \right) \right) \tag{5.3}$$

Henceforth η_{act} will be indicated simply as η. The Butler Volmer equation rearrangement gives the Allen-Hickling equation [129]

$$\ln \frac{i}{\exp(\alpha_a + \alpha_c) n\mathcal{F}\eta - 1} = \ln i_0 - \frac{\alpha_c n\mathcal{F}\eta}{RT} \tag{5.4}$$

and the value of α_c and the exchange current density, i_0, can be evaluated fitting the experimental data. The transfer coefficient, α_c, gives an estimation of the fraction of the electrical energy that contributes to overcoming the activation energy of the electrochemical reaction. It indicates how the energy barrier is shared between the reactant and product sides of the reaction, and in most systems it turns out to lie between 0.3 and 0.7 [129].

The general procedure for elucidating the mechanisms of the hydrogen production reactions in the MCEC is to determine the dependency of the exchange current density on the reactant concentrations. It can be calculated from Eq. 5.2 written in logarithmic form

$$\ln(i_0) = \ln(i_0^*) + a \ln(y_{H_2O}) + b \ln(y_{CO_2}) \tag{5.5}$$

Hu et al. [133] demonstrated that H_2 content significantly affects the mass-transfer polarization, while it influences the Ni activation overpotential only when its concentration is very low, specifically less than $< 5\%$. Therefore, in this experimental campaign, the H_2 content is kept fixed at 10%, while the concentrations of water and carbon dioxide are varied (see Tab. 4.2) to specifically focus on their roles in electrochemical hydrogen production. Consequently, the dependence of the exchange current density has been evaluated exclusively based on these two reactants.

Additionally, it must be considered that due to different reactions possibly taking place at the Ni electrode, an essential problem is to know the actual gas composition inside the cell when determining the partial pressure dependencies. One such reaction is the reverse water-gas shift (rWGS):

$$H_2 + CO_2 \leftrightarrow H_2O + CO \tag{5.6}$$

Due to the operating temperature and the presence of nickel that act as a catalyst, the shift reaction could very rapidly establish the equilibrium [17, 18]. In addition to the rWGS, the methanation reaction could also occur, although it is much less favored under the operating conditions of the MCEC.

To account for all the species that could form between 620 and 680 °C from a $H_2/CO_2/H_2O$ mixture, equilibrium conditions of all the inlet compositions tested were directly evaluated from the minimization of total Gibbs free energy. At equilibrium, a system's Gibbs free energy reaches its minimum, meaning that no further spontaneous chemical reactions will occur. In practical terms, for a given set of reactants at a constant temperature and pressure, the system will naturally evolve toward a state where the total Gibbs free energy is as low as possible. This approach does not require prior knowledge of the system's chemistry or defined reaction stoichiometry. All chosen components are treated as reactants, and the calculation determines the distribution of components that minimizes the system's free energy, i.e., the distribution that can be achieved at the equilibrium established. An application of this method for chemical equilibrium evaluation in an MCFC is reported in [151]. For this work, the total Gibbs free energy minimization was performed using AVEVA PRO/II simulation software. In addition to H_2, H_2O, and CO_2, which constitute the inlet gas flow rate, also CO, CH_4, C_2H_6, C_3H_6, and CH_3OH were considered in the equilibrium calculations.

Once the values of i_0 and α_c are determined through the fitting of Eq. 5.4, the dependence of i_0 on the partial pressures of the reactants will be investigated under two scenarios, considering the uncertainty of the actual composition within the electrode. The first scenario assumes that no reactions occur other than electrolysis, meaning that the composition within the cell remains as set at the inlet (see Tab. 4.2). The second scenario scenario assumes that additional chemical reaction can occur and that the system reaches equilibrium conditions, using the results obtained from the Gibbs free energy minimization. The objective of this dual approach is to estimate the extent to which non-electrochemical reactions, such as the rWGS, may impact the reaction orders of the electrochemical process. Finally, the dependence of i_0 will be evaluated as a function of temperature,allowing for an estimation of the impact that temperature variations can have on the kinetics of the electrochemical process and, consequently, on the activation overpotential. In the next section, the experimental data, fitting results and the analysis of reaction orders will be presented and discussed.

5.1.2 Results

The performance of the Ni electrode has been investigated in a broad range of operating conditions to obtain kinetic data for the hydrogen production reaction (see Tab. 4.2). Fig. 5.1 and Fig. 5.2 illustrate the iR-corrected polarization curves at 620, 650, and 680 °C for $\%H_2O$ variations and $\%CO_2$ variation, respectively. Regardless of the temperature, the overpotential at high current densities increases when either the CO_2 or H_2O molar fraction is lower. This is attributed to mass transfer limitations, as CO_2 and H_2O are reactants in the electrolysis cell. In general, concentration polarization appears to be more significant when the CO_2 concentration is lower compared to a reduction in H_2O. This observation can be explained by the reverse

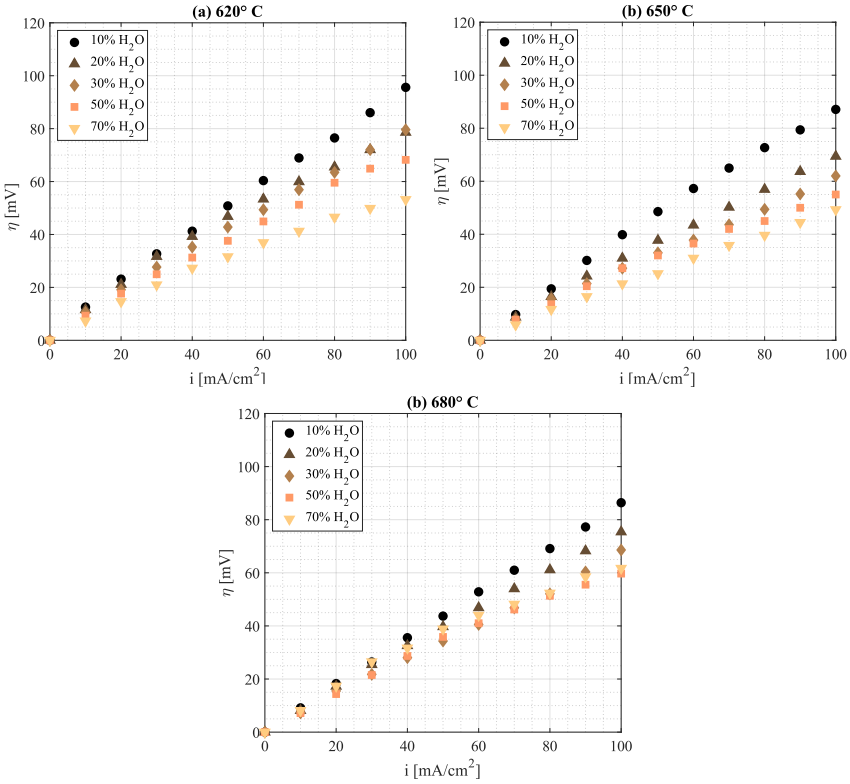

Figure 5.1. IR-corrected polarization curves for the Ni electrode at 620 °C (a), 650 °C (b), and 680 °C (c) varying H_2O percentages. The H_2 and CO_2 percentages were kept constant at 10% and 20%, respectively, while N_2 was used to balance the composition to maintain a constant flow rate.

water-gas shift (rWGS) reaction, which consumes CO_2 and produces H_2O, thereby further lowering the CO_2 content in the system.

The effect of the operating temperature was also investigated, with an example shown for the reference composition 10/20/20/50% $H_2/H_2O/CO_2/N_2$ in Fig. 5.3. A noticeable improvement in electrode performance is observed when increasing the temperature from 620 to 650 °C, while the polarization curves at 650 and 680 °C almost overlap. This result aligns with the findings of Hu et al. [111], who reported that the performance improved more significantly going from 600 to 625 °C than between 625 and 650 °C.

The hydrogen electrode gas composition, calculated at equilibrium for temperatures between 620 and 680°C, is shown in Tab. 5.1. The simulations revealed that CO is the only component formed in significant quantities, i.e. $> 0.1\%$, at equilibrium. This result holds true under all conditions in which the button cell was tested during the experimental campaign. Moreover, it demonstrates that the rWGS reaction plays a significant role in determining the composition within the cell.

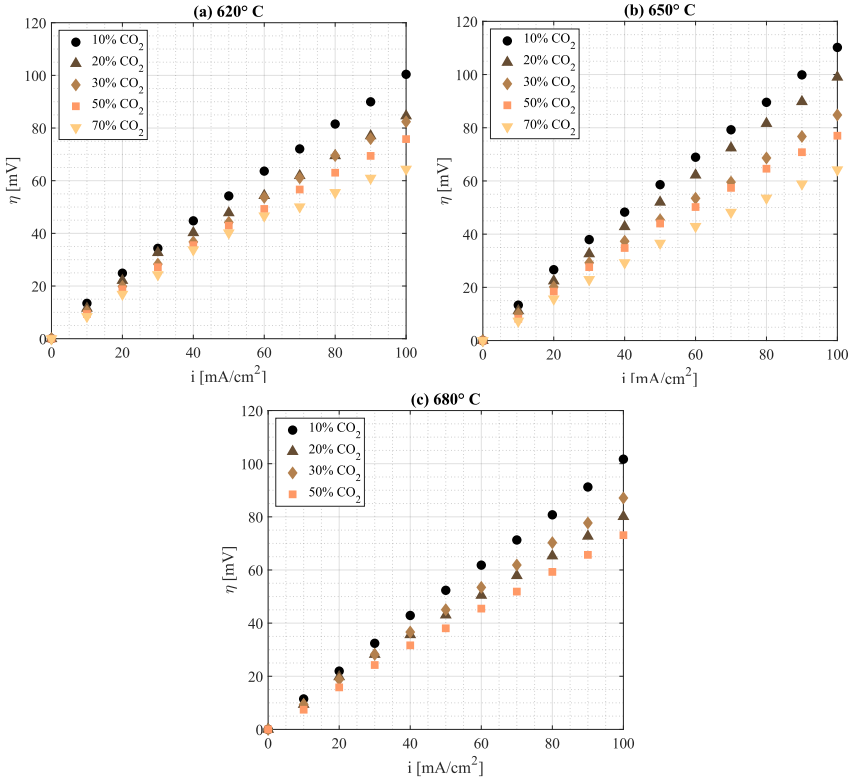

Figure 5.2. IR-corrected polarization curves for the Ni electrode at 620 °C (a), 650 °C (b), and 680 °C (c) varying CO_2 percentages. The H_2 and H_2O percentages were kept constant at 10% and 20%, respectively, while N_2 was used to balance the composition to maintain a constant flow rate.

Table 5.1. Gas composition calculated at equilibrium at 620 – 680 °C, using as inlet compositions the ones reported in Tab. 4.2

620 °C				650 °C				680 °C				
H_2	CO_2	H_2O	CO	H_2	CO_2	H_2O	CO	H_2	CO_2	H_2O	CO	N_2
7.61	17.62	22.39	2.38	7.36	17.36	22.64	2.64	7.12	17.12	22.88	2.88	50
Test II-V: Variation of H_2O												
6.65	16.67	13.33	3.32	6.39	16.40	13.60	3.61	6.14	16.14	13.86	3.86	60
8.14	18.15	31.86	1.85	7.93	17.93	32.07	2.07	7.71	17.71	32.29	2.29	40
8.72	18.73	51.28	1.27	8.56	18.56	51.44	1.44	8.38	18.38	51.62	1.62	20
9.03	19.03	70.97	0.97	8.89	18.90	71.11	1.10	8.75	18.75	71.25	1.25	0
Test VI-IX: Variation of CO_2												
8.61	8.61	21.39	1.39	8.45	8.45	21.55	1.55	8.29	8.29	21.71	1.71	60
6.83	26.84	23.17	3.16	6.54	26.54	23.46	3.46	6.26	26.26	23.74	3.74	40
5.71	45.72	24.29	4.28	5.38	45.38	24.62	4.62	5.06	45.06	24.94	4.94	20
4.92	64.92	25.08	5.08	4.58	64.58	25.42	5.42	4.26	64.26	25.74	5.74	0

Estimate of i_0 and α_c

The exchange current density i_0 was determined from Eq. 5.4 by linear regression analysis. Only the data obtained up to a current density of 60 mA/cm^2 were

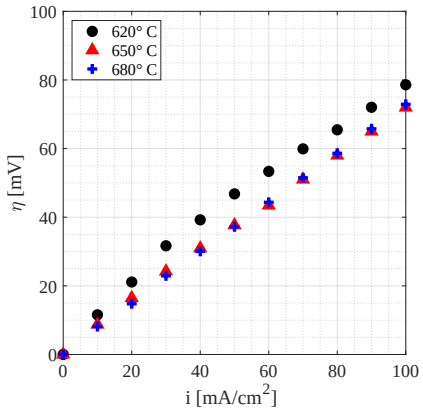

Figure 5.3. IR-corrected polarization curves for the Ni electrode in the MCEC fed with the gas 10/20/20/50% $H_2/H_2O/CO_2/N_2$ at operating temperatures from 620 to 680 °C.

used for the calculation, to minimize the effect of concentration polarization. Since the electrochemical reduction of water is a two-electron transfer process, the term $(\alpha_a + \alpha_c)n$ in Eq. 5.4 assumes the value of 2. For each set of data i_0 was evaluated from the intercept of the Allen-Hickling plot (Eq. 5.4)

$$\ln \frac{i}{\exp(2F\eta) - 1} \quad vs. \quad \eta \tag{5.7}$$

The Allen-Hickling plots at 620, 650, and 680 °C for the different gas composition tested are compared in Fig. 5.4. The transfer coefficients α_c, obtained from the

Table 5.2. Transfer coefficients, α_c, obtained as slopes of the Allen-Hickling plots in Fig. 5.4. The value range from 0.25 to 0.55, in agreement with the fact that the electrochemical water reduction is less favored energetically compared to the oxidation reaction.

	Molar fraction [%]					
T [°C]	10	20	30	50	70	
620	0.3478	0.3494	0.3165	0.2499	0.3210	H_2O variation
650	0.5592	0.3508	0.2419	0.2540	0.2916	$\%CO_2/H_2/N_2$
680	0.5205	0.4821	0.4164	0.5106	0.4086	20/10/balance
620	0.4028	0.3518	0.4191	0.4348	0.4889	CO_2 variation
650	0.4639	0.5056	0.4383	0.5565	0.4982	$\%H_2O/H_2/N_2$
680	0.4935	0.4142	0.5061	0.5535	-	20/10/balance

slopes of the Allen-Hickling plots in Fig. 5.4 (see Eq. 5.4), are reported in Tab. 5.2. The α_c values ranges from 0.25 to 0.55, indicating that the reaction rate is more sensitive to changes in the applied potential for the hydrogen production process. In practical terms, since α_c is either equal to or less than 0.5 for all the conditions, this agrees with the fact that the water reduction reaction is less energetically favored compared to the hydrogen oxidation reaction.

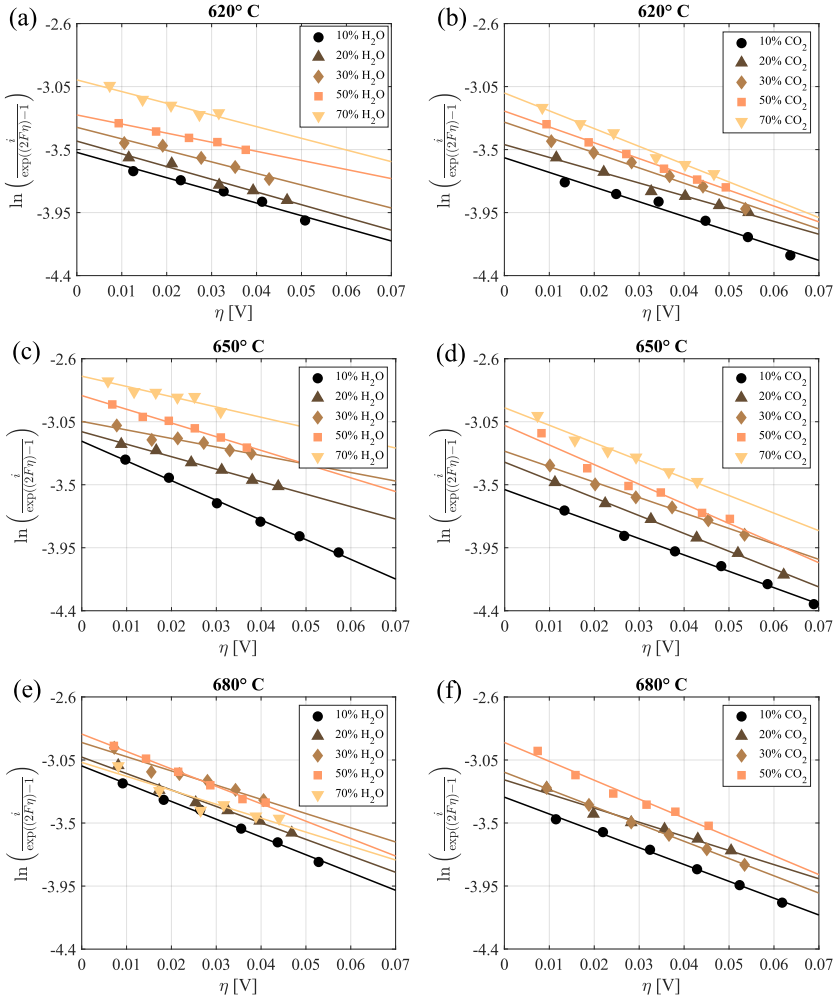

Figure 5.4. Allen-Hickling polarization curves from iR-corrected overpotentials at 620, 650, and 680 °C varying $\%H_2O$ (a),(c),(e) and $\%CO_2$ (b),(d),(f). The data were fitted to straight lines to calculate i_0 as the intercept and α_c as the slope. The low-overpotential data, i.e. $\eta < 70$ mV, were used for the calculation.

From the intercept at zero overpotential, evaluated from the Allen-Hickling plots in Fig. 5.4, exchange current densities values were estimated for each set of operating conditions. The value of i_0 as a function of temperature for different Ni electrode inlet compositions are presented in Fig. 5.5. The values are generally higher for the tests with varying $\%H_2O$ compared with those with varying $\%CO_2$. Higher values of i_0 are generally observed when the concentration of the reactant, either H_2O or CO_2, increases - except for the data at 680 °C at 70% H_2O (blue square in Fig. 5.5a). In this case, i_0 is lower compared to the values estimated at 20, 30, and 50% H_2O at the same temperature. The result can be attributed to changes in the electrode's wettability properties. In a molten carbonate cell, the active surface area depends on the electrolyte distribution inside the electrode pores and, consequently, on the wettability of the electrode [152]. Therefore, any change in the active surface area will affect the electrolysis reaction rate.

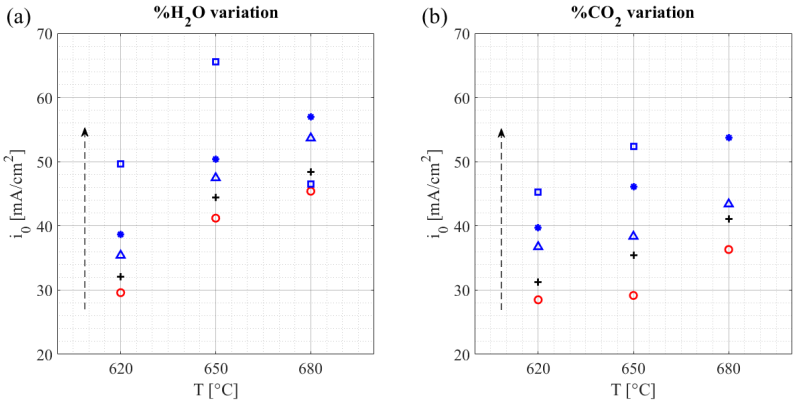

Figure 5.5. Exchange current densities derived from the intercepts of the Allen-Hickling plots in Fig. 5.4, shown as function of temperature with varied gas composition, H_2O (a) and CO_2 (b). The dotted arrow indicates increasing percentages of H_2O/CO_2.

The wetting properties of different materials in alkali carbonate mixtures have been studied by several researchers [125, 153, 154]. It has been concluded that on the oxygen side, NiO is perfectly wetted, with a wetting angle close to zero[153]. For the hydrogen side, the wetting angle is higher, around $50 - 60°$, and depends on the gas composition, polarization, temperature, and the material. Increasing the temperature enhances the electrode wettability [154] (reducing the contact angle), thereby increasing the contact surface area between the gas and liquid electrolyte phases. However, an excessive rise in temperature could increase the reaction surface area in larger pores while flooding the smaller pores of the electrode, thus decreasing the overall available active surface area for the reaction [125]. Therefore, the lower i_0 value observed at 70% H_2O in Fig. 5.5a can be explained by a combination of effects. On one hand, the increase in temperature excessively enhanced the electrode's wettability, causing the smaller pores to flood, which hindered gas access to the reactive sites at the three-phase-boundary (TPB). On the other hand, at 680 °C, the rWGS reaction becomes more favorable, which could mean the actual water content in the system exceeded 70% (see Tab. 5.1). This higher water concentration would similarly obstruct the diffusion of reactants within the electrode pores. These observations, of course, require further experimental testing to be confirmed.

Returning to the analysis of the data shown in Fig. 5.5, at 620 °C the exchange current densities range from 30 to 50 mA/cm^2 under all measured gas compositions. In Fig. 5.5a, increasing H_2O concentration results in exchange current densities approximately in the range of 40 to 70 mA/cm^2 at 650 °C. In contrast, these values lies in a slightly lower range, $30 - 55$ mA/cm^2, when CO_2 is increased from 10 to 70%, as shown in Fig. 5.5b. A similar trend is observed at 680 °C for variations from 10 to 50%, although the difference between the to composition groups is less pronounced. The ranges of i_0 are $45 - 55$ mA/cm^2 for increasing H_2O concentration, and $35 - 55$ mA/cm^2 for increasing CO_2 concentration in the inlet gas compositions.

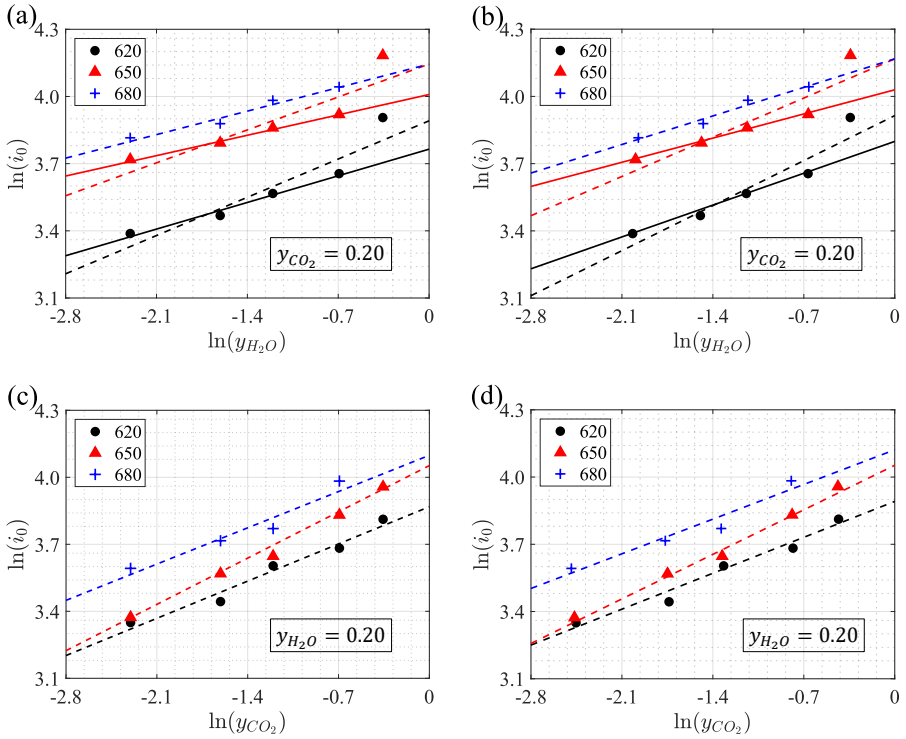

Figure 5.6. Effect of water (a)-(b) and carbon dioxide (c)-(d) concentrations on the exchange current density at 620 – 680 °C. (a)-(c) y_{H_2O} and y_{CO_2} from the inlet composition, (b)-(d) y_{H_2O} and y_{CO_2} from the gas composition calculated at equilibrium (see Tab. 5.1). The continuous line in (a)-(b) refers to the interpolation carried out without considering the data at 70% H_2O.

Estimate of reaction orders

Based on the exchange current densities obtained, the dependencies on the concentrations of carbon dioxide and water can be determined. Due to the uncertainty around whether gas compositions reach equilibrium in this study, two scenarios with different gas compositions are considered: (i) no shift reaction occurs (using the inlet gas compositions shown in Tab. 4.2), and (ii) complete equilibrium is established due essentially to the rWGS reaction (with gas compositions calculated in Tab. 5.1). Both scenarios are depicted in Figs. 5.6. The reaction orders can be determined from the slopes by fitting the parameters a and b in Eq. 5.5, while the standard current density, i_0^* is evaluated from the intercepts. The fitting results are shown in Tables 5.3 and 5.4 for the cases of the inlet gas compositions and the complete equilibrium gas compositions, respectively.

The dependence of the exchange current density on the concentration of water is analyzed in Fig. 5.6a. The evaluation is conducted in two ways. First, all the obtained data points are fitted to straight lines by means of a linear regression (dashed lines), resulting in values of 0.21 and 0.24 at 620 and 650 °C, respectively. The exchange current density obtained at 680 °C under 70% H_2O (Fig. 5.5a) is excluded from this analysis, as it deviates from the general trend observed in the other data points. This deviation suggests that the result is influenced by greater

Table 5.3. The standard exchange current densities and the dependency of exchange current densities on water and carbon dioxide molar fraction of the inlet Ni electrode gas compositions $i_0 = i_0^*(y_{H_2O})^a(y_{CO_2})^b$. The superscript † refer to the results obtained considering the exchange current density varying from 10 to 50% H_2O.

T [°C]	i_0^* [mA/cm^2]	$i_0^{*\dagger}$ [mA/cm^2]	a	$a^\dagger$	b
620	49.61	46.82	0.24	0.17	0.24
650	60.32	56.89	0.21	0.13	0.30
680	-	62.76	-	0.15	0.23

Table 5.4. The standard exchange current densities and the dependency of exchange current densities on water and carbon dioxide molar fraction of gas compositions calculated at rWGS equilibrium $i_0 = i_0^*(y_{H_2O})^a(y_{CO_2})^b$. The superscript † refer to the results obtained considering the exchange current density varying from 10 to 50% H_2O.

T [°C]	i_0^* [mA/cm^2]	$i_0^{*\dagger}$ [mA/cm^2]	a	$a^\dagger$	b
620	48.42	45.51	0.29	0.20	0.23
650	60.32	56.31	0.25	0.15	0.28
680	-	63.11	-	0.18	0.22

uncertainty, likely due to the combined effects of increased temperature and water concentration, which may impact the wettability and diffusion properties within the electrode. Secondly, only the data points referred to the range $10-50\%$ are fitted to straight lines, resulting in a reaction order ranging from 0.13 to 0.17. Regardless of the concentration intervals considered, the reaction order with respect to water shows minimal dependence on temperature. In Fig. 5.6b, the equilibrium conditions consider the potential formation of carbon monoxide in the gas compositions, yet similar dependencies on water concentration, as seen in Fig. 5.6a, are observed. Similarly, the reaction order of the carbon dioxide shows no significant dependence on temperature (see Fig. 5.6c and Tables 5.3 and 5.4), with values of 0.24, 0.30, and 0.23 at 620, 650, and 680 °C, respectively. In Fig. 5.6d, a minor impact of the reverse water-gas shift (rWGS) reaction is observed, with the reaction orders for gases at complete equilibrium ranging from 0.22 to 0.28.

Unlike the reaction orders, the standard exchange current density i_0^* is dependent on temperature. However, similar to the concentration dependencies, the equilibrium composition does not affect the i_0^* values. The values of $i_0^{*\dagger}$ referring to the $10-50\%$ H_2O and $10-50\%$ CO_2 ranges, can be correlated with temperature using an Arrhenius-type expression,

$$\ln\left(i_0^*\right) = -\frac{4169}{T} + 8.529 \tag{5.8}$$

with i_0^* in mA/cm^2 and T in K. The correlation between $i_0^{*\dagger}$ and temperature within the range of $620-680$ °C is illustrated in Fig. 5.7. The standard exchange current density values show good agreement with the Arrhenius expression for the temperature range and compositions tested. This result highlights the strong dependence of the hydrogen production reaction on temperature and, consequently,

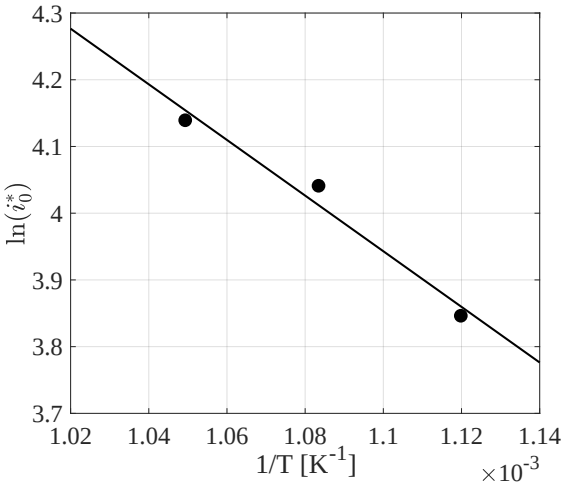

Figure 5.7. Trend of the standard exchange current density, $i_0^{*\dagger}$, as evaluated from Eq. 5.5, with respect to temperature.

the activation overpotential observed at the anode. According to the derived Arrhenius expression (Eq. 5.8), the activation energy for the reaction is approximately 72 kJ/mol. This value indicates that the Ni electrode is under a moderate kinetic or mixed control. This implies that the reaction rate may be limited not only by kinetic processes but also by the diffusion of reactants within the electrode porous structure. Notably, the value found is consistent with the findings reported by Hu et al. [111], reinforcing the validity of the observed behavior in similar systems

So far, the hydrogen production mechanism in a molten carbonate electrolyzer cell (MCEC) has been little studied, unlike the oxidation process, which has been extensively researched over the past decades. Assuming that the hydrogen production pathways occur as the reverse of hydrogen oxidation in molten carbonate cells, the theoretical partial pressure dependencies of the reactants would remain the same in both operating modes. When considering the hydrogen oxidation mechanisms proposed by [36, 155], the corresponding reactions for hydrogen production during electrolysis are expressed as Reactions 5.9-5.11 and Reactions 5.12,5.13 and 5.11, respectively.

$$\mathrm{H_2O + M + e^- \underset{k_{1b}}{\overset{k_{1f}}{\rightleftarrows}} MH + OH^-} \tag{5.9}$$

$$\mathrm{OH^- + CO_2 + M + e^- \underset{k_{2b}}{\overset{k_{2f}}{\rightleftarrows}} MH + CO_3^{2-}} \tag{5.10}$$

$$\mathrm{2MH \underset{k_{3b}}{\overset{k_{3f}}{\rightleftarrows}} H_2 + 2M} \tag{5.11}$$

$$\mathrm{H_2O + CO_3^{2-} \rightarrow 2OH^- + CO_2} \tag{5.12}$$

$$2\left(\mathrm{OH^- + CO_2 + M + e^- \rightarrow MH + CO_3^{2-}}\right) \tag{5.13}$$

$$2\mathrm{MH} \rightarrow \mathrm{H_2} + 2\mathrm{M} \tag{5.11}$$

The method for deriving theoretical reaction orders can be found in [36], where the authors assume that (i) Reaction 5.10 is the rate-determining step; (ii) Langmuir adsorption isotherm can be employed; and (iii) MH coverage, χ, is low (where M denotes metal). Considering Reactions 5.11 at equilibrium , the following expression can be obtained

$$\frac{\chi}{1-\chi} = \left(\frac{k_{3b}}{k_{3f}} C_{\mathrm{H_2}}\right)^{1/2} = K_3^{-1/2} C_{\mathrm{H_2}}^{1/2} \tag{5.14}$$

where K_3 is the equilibrium constant. For low coverage one obtain $\chi = K_3^{-1/2} C_{\mathrm{H_2}}^{1/2}$ and $1 - \chi \simeq 1$. Thus, for the electrochemical reactions 5.10 and 5.9, the net current can be expressed as

$$i_2 = \mathcal{F}\left[k_{2f} C_{\mathrm{OH^-}} C_{\mathrm{CO_2}} \exp\left(\frac{\beta_2 \mathcal{F} E}{RT}\right) - k_{2b} K_3^{-1/2} C_{\mathrm{H_2}}^{1/2} C_{\mathrm{CO_3^{2-}}} \exp\left(-\frac{(1-\beta_2)\mathcal{F} E}{RT}\right)\right] \tag{5.15}$$

$$i_1 = \mathcal{F}\left[k_{1f} C_{\mathrm{H_2O}} \exp\left(\frac{\beta_3 \mathcal{F} E}{RT}\right) - k_{1b} K_3^{-1/2} C_{\mathrm{H_2}}^{1/2} C_{\mathrm{OH^-}} \exp\left(-\frac{(1-\beta_3)\mathcal{F} E}{RT}\right)\right] \tag{5.16}$$

Here, β represents the symmetry factor and E is potential difference between the electrode and the electrolyte. At equilibrium ($i_1 = 0$), $C_{\mathrm{OH^-}}$ can be calculated from Eq.5.16. This value can then be substituted into Eq. 5.15, where E is also replaced by $E_0 + \eta$:

$$\begin{aligned} i_2 = \mathcal{F}\Bigg\{ & k_{2f} \frac{k_{1f}}{k_{1b}} K_3^{1/2} C_{\mathrm{H_2}}^{-1/2} C_{\mathrm{CO_2}} C_{\mathrm{H_2O}} \left[\frac{k_{2b}}{k_{2f}} \frac{k_{1b}}{k_{1f}} \frac{C_{\mathrm{H_2}}}{K_3} \frac{C_{\mathrm{CO_3^{2-}}}}{C_{\mathrm{H_2O}} C_{\mathrm{CO_2}}}\right]^{\frac{1+\beta_2}{2}} \exp\left(\frac{\beta_2 \mathcal{F}\eta}{RT}\right) + \\ & -k_{2b} K_3^{-1/2} C_{\mathrm{H_2}}^{1/2} C_{\mathrm{CO_3^{-2}}} \left[\frac{k_{2b}}{k_{2f}} \frac{k_{1b}}{k_{1f}} \frac{C_{\mathrm{H_2}}}{K_3} \frac{C_{\mathrm{CO_3^{2-}}}}{C_{\mathrm{H_2O}} C_{\mathrm{CO_2}}}\right]^{\frac{-1+\beta_2}{2}} \exp\left(\frac{(-1+\beta_2)\mathcal{F}\eta}{RT}\right)\Bigg\} \end{aligned} \tag{5.17}$$

When comparing this with the general relationship for activation polarization (Eq. 5.3), and assuming $\beta_2 = 0.5$, the authors in [36] found theoretical reaction orders of 0.25 for hydrogen, carbon dioxide, and water. The same reaction orders are obtained when considering the second reaciton mechanism described earlier (Reactions 5.12, 5.13 and 5.11), under the assumption that Reaction 5.13 is the rate-determining step.

The theoretical values derived from these two mechanisms for CO_2 and H_2O closely align with the experimental data presented in this study (see Tables 5.3 and 5.4). This agreement reinforces the validity of adopting hydrogen oxidation mechanisms to describe the reverse reaction in electrolysis mode. However, some discrepancies can be observed between the theoretical and experimental values, which may be attributed to several factors. For instance, previous studies reported above on MCFC kinetics used flag electrodes, while in this work data from a lab

scale cell were used. Additionally, the theoretical model employed in this study is relatively simplified. To enhance the accuracy of the predictions, it is advisable to account for the current distribution along the depth of the electrode and for the effective electrolyte conductivity variations under different operational conditions.

Resume

In summary, the investigation of the Ni electrode under varying operating conditions underscores the critical role of reactant concentrations and temperature in influencing the performance of the hydrogen production reaction. The polarization curves demonstrate that lower molar fractions of CO_2 and H_2O lead to increased overpotentials at high current densities. Notably, concentration polarization is more pronounced when the CO_2 content is lower than when there is a reduction in H_2O. This can be attributed to the reverse water-gas shift (rWGS) reaction, which further decreases the CO_2 concentration in the system while producing H_2O. The analysis of the polarization curves temperature dependency reveales a significant performance improvement between 620 and 650 °C, while further increases in temperature showed only marginal gains, consistent with the findings of Hu et al. work [111]. This trend underscores the importance of optimizing operational conditions to achieve efficient electrolysis, as the gains in performance may diminish beyond certain temperature thresholds.

Additionally, the analysis of the exchange current density values derived from the Allen-Hickling plots, generally indicate higher current densities for tests with increased $\%H_2O$ compared to those with varying $\%CO_2$. Notably, the observed decrease in i_0 at 680 °C with 70% H_2O highlights the complex interplay between wettability and reactant diffusion, suggesting that elevated temperatures can lead to flooding of smaller pores, which hinders reactant accessibility at the three-phase boundary (TPB). The findings also indicate that exchange current densities range from 30 to 50 mA/cm^2 at 620 °C and increase to approximately 40 to 70 mA/cm^2 at 650 °C with higher H_2O concentrations. In contrast, increasing $\%CO_2$ results in slightly lower values, ranging from 30 to 55 mA/cm^2. These results confirm the predominant role of CO_2 in the electrode kinetics. The reaction orders for water and carbon dioxide were evaluated from the i_0 values obtained earlier. The analysis indicates that the dependencies on the concentrations of carbon dioxide and water largely remain consistent across different scenarios. Even when considering the rWGS reaction, the variation in reaction order values is minimal, with the coefficients only slightly elevated in the equilibrium conditions scenario. This suggests that the equilibrium state, even if influencing the inlet gas composition, does not dramatically alter the overall kinetics in the system. The reaction mechanism based on the reverse of hydrogen oxidation in molten carbonate cells appears to be fairly consistent with the reaction orders estimated in this study.

The activation energy for the reaction, estimated at approximately 72 kJ/mol, points to a mixed control scenario, where both kinetic factors and mass transport limitations impact the overall reaction rate. This observation is consistent with experimental findings and supports the proposed mechanism for hydrogen production during electrolysis.

Future work should focus on experimentally verifying the impact of the reverse

water-gas shift reaction on gas compositions at the Ni electrode, as well as exploring the influence of electrode microstructure and wettability on electrochemical performance. Additionally, expanding the temperature range and gas composition variations could help in refining the understanding of the kinetic parameters governing the hydrogen production reaction in molten carbonate electrolyzer cells.

5.2 DRT-based impedance study

In this section, the DRT analysis of the impedance spectra data (operating conditions detailed in Sec 4.2.1) is presented. The discussion begins with an examination of the hydrogen electrode's impedance and its impact on cell polarization during electrolysis mode. Subsequently, the most significant processes occurring within the electrode identified and analyzed under a broad range of operating conditions.

5.2.1 Identification of the DRT function peaks during electrolysis operation

Fig. 5.8 illustrates the impedance spectra obtained for the cell and the electrodes at 650°C (hydrogen electrode composition VI from Tab. 5.5) both at OCV (a) and in electrolysis mode at 100 mA/cm^2 (c). The dashed line represents the sum of the values obtained for the single electrodes. It indicates that the effect of each electrode is additive if the experimental conditions are maintained steady. Fig. 5.8b and 5.8d show the respective DRT analysis results, revealing five distinct peaks for the cell: two distinct peaks at high frequency (P1-P2, $30 - 1000$ Hz), one main contribution at medium frequency (P3, $2 - 30$ Hz), followed by other two distinct peaks at lower frequency (P4-P5, $0.05 - 2$ Hz). Every peak is correlated with at least one process occurring in either one or both electrodes, and the amplitude represents their contribution to the cell polarization. A possible explanation for the similar frequencies of the peaks appearing in both electrodes DRT analysis is the comparable thickness and porosity of the two electrodes, as reported in [64]. The DRT results confirm the electrodes additive contribution to the cell impedance. Henceforth, the analysis will focus on the data acquired from the individual electrodes, with the inclusion of the suffixes "HE" and "OE" denoting peaks associated with the hydrogen and oxygen electrodes, respectively.

Table 5.5. Test matrix containing the molar percentages of the inlet gas for the hydrogen electrode of the button cell.

	Test	%H_2	%H_2O	%CO_2	%N_2
Reference composition	**I**	**10**	**20**	**20**	**50**
%H_2O variation	II	10	**10**	20	**60**
	III	10	**30**	20	**40**
	IV	10	**50**	20	**20**
	V	10	**70**	20	**0**
%CO_2 variation	VI	10	20	**10**	**60**
	VII	10	20	**30**	**40**
	VII	10	20	**50**	**20**
	IX	10	20	**70**	**0**

Note that the cell polarization decreases significantly in electrolysis mode compared with OCV operation. This feature can be explained by observing the OE behavior, as at OCV it exhibits a bigger impedance than during electrolysis operation. This result is in line with the findings of Hu et al. [101], who showed that

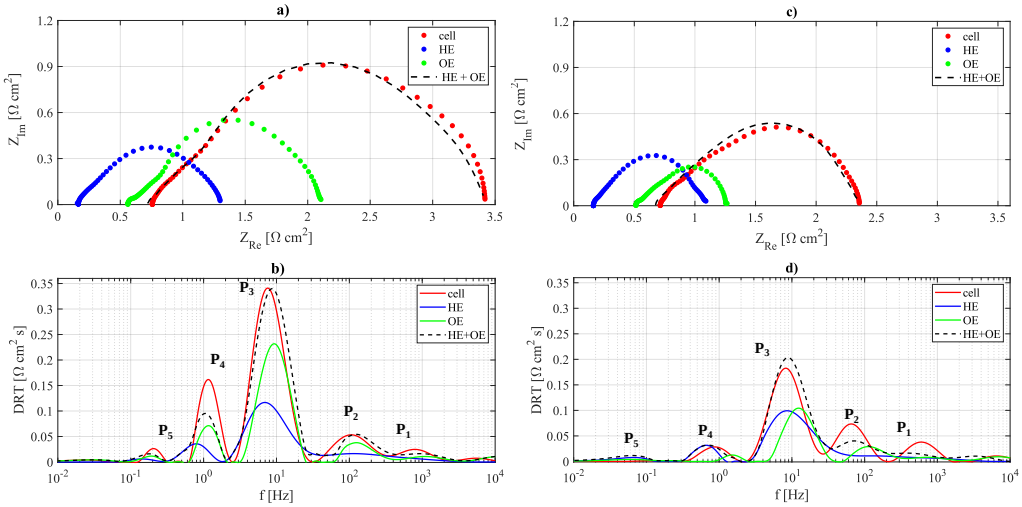

Figure 5.8. Full cell and single electrodes impedance spectra for the MCEC operated at 650° C, with 10/20/10/60% $H_2/H_2O/CO_2/N_2$ as HE composition, at OCV (a) and at 100 mA/cm^2 (c), and the corresponding DRT plots, (b) and (d). Both the experimental data and the DRT results shows that HE and OE contributions are additive. Five distinct peaks are visible, indicating at least five different physical phenomena characterizing the MCEC operation.

OE exhibits better performance when acting as an anode in MCEC rather than as a cathode in MCFCs. It is noteworthy that the HE polarization also decreases when the cell operates as an electrolyzer, albeit not to the extent observed for the OE. While the latter exhibits a significantly higher impedance at OCV compared with electrolysis operation, the contributions of the two electrodes are comparable during electrolysis under the operating conditions tested (Fig. 5.8c). The above observations are valid independently of the HE gas composition and temperature tested in this study and reported in Tab. 5.5. Additional results are provided in Fig. 5.9.

Given that during electrolysis operation the contribution of the two electrodes to the overall cell polarization become comparable, and that the production of carbonate ions occurs at the hydrogen electrode, it is crucial to thoroughly investigate and analyze the phenomena occurring at this electrode. Therefore, only variations in composition at the HE have been considered to identify the controlling resistances of the process and potentially determine the optimal operating conditions for this electrode. Henceforth, the results will be mainly related to the impedance data obtained for the HE.

Fig. 5.10 presents the Nyquist plots and the relative DRT plots of the hydrogen electrode, comparing the OCV operation with the electrolysis operation at 100 mA/cm^2. All the measurements were carried out at 650°C and with a HE gas composition of 10/20/30/40% $H_2/H_2O/CO_2/N_2$. The Nyquist plot (a) clearly shows the existence of two discernable arcs at low-medium ($0.01 - 10$ Hz) and high frequencies ($10 - 1000$ Hz). Note that in electrolysis mode only the low frequency part of the impedance shrinks a bit, but no additional features are visible in comparison

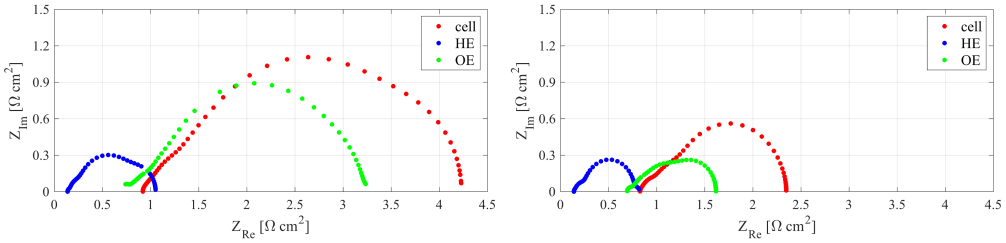

(a) MCEC operated at 620°C, 10/20/20/50% $H_2/H_2O/CO_2/N_2$, at OCV (left) and at 100 mA/cm^2 (right).

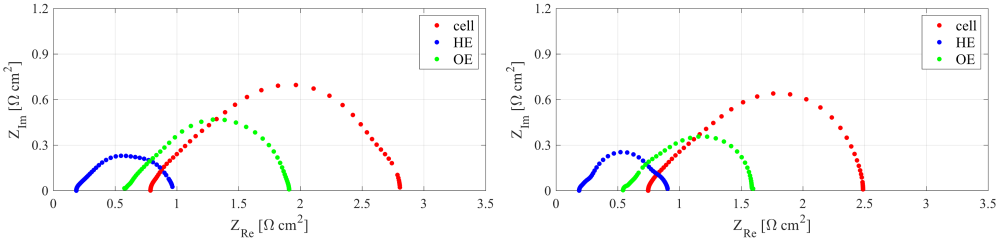

(b) MCEC operated at 680°C, 10/20/20/50% $H_2/H_2O/CO_2/N_2$, at OCV (left) and at 100 mA/cm^2 (right).

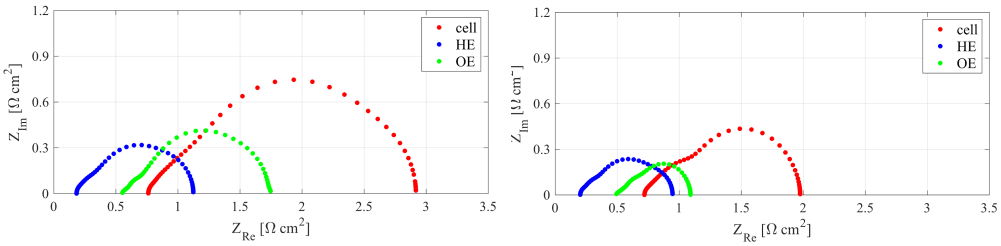

(c) MCEC operated at 650°C, 10/20/30/40% $H_2/H_2O/CO_2/N_2$, at OCV (left) and at 100 mA/cm^2 (right).

Figure 5.9. Full cell and single electrodes impedance spectra for the MCEC at different operating conditions and temperatures.

with the OCV measurement. Both impedance arcs are divided into several peaks, four in total, in the DRT spectrum. The associated DRT function (Fig. 5.10 c) shows that during electrolysis operation, the peak $P5_{HE}$ completely vanishes, $P4_{HE}$ and $P3_{HE}$ are considerably reduced, whereas the peak located at high frequency, $P2_{HE}$, is comparable to the corresponding OCV result. P1 summitting at about 1000 Hz is considered significant only for the OE, as it is not possible to distinguish between P1 and P2 for the HE under the tested conditions. $P3_{HE}$ can be reasonably associated with the water reduction reaction since in electrolysis mode it is both reduced and accelerated. In fact, kinetic losses decrease with increasing current density, which is explained by the Butler-Volmer equation (Eq. 2.31). Since 100 mA/cm^2 is still in a region where the polarization curve is dominated by activation and ohmic losses (Fig. 5.10 b), a limitation by mass transport seems unlikely. Thus, $P4_{HE}$ and $P5_{HE}$, located at low frequencies, suggest the existence of either an additional chemical reaction or diffusion limitations within the electrolyte. Regarding the highest

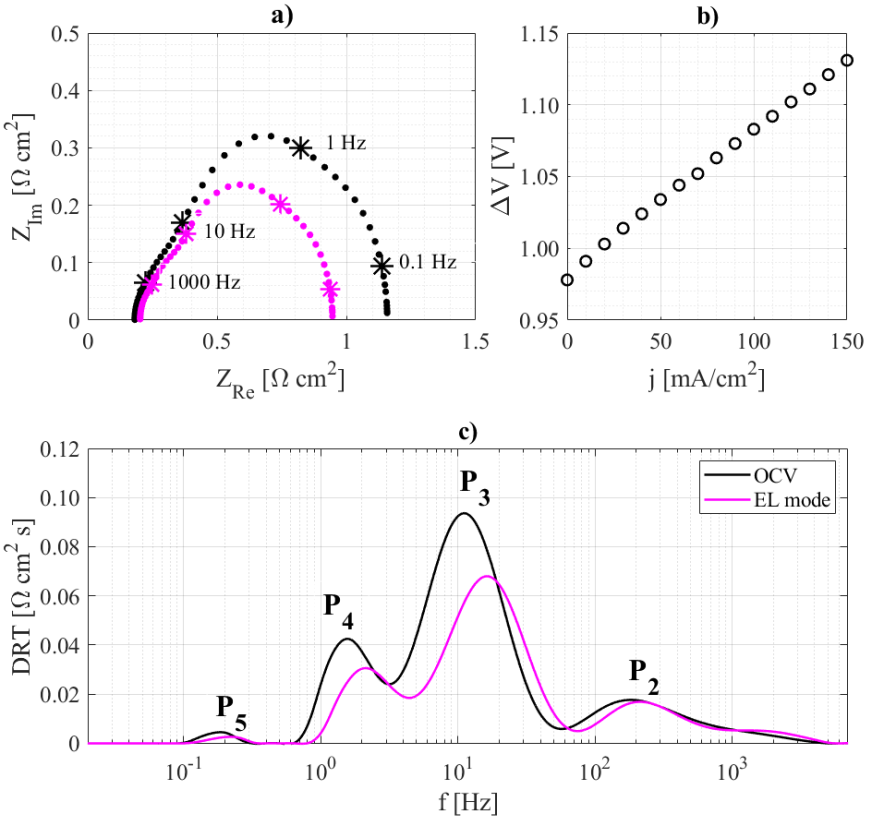

Figure 5.10. Nyquist plot (a) for the HE at 650° C, 10/20/30/40% $H_2/H_2O/CO_2/N_2$ as HE composition, 100 mA/cm^2 (pink data) and OCV (black data). The * symbol indicates frequencies of 1000, 10, 1, and 0.1 Hz. The polarization curve (b) shows that there is no concentration overpotential. The corresponding DRT plot (c) elucidates the presence of four peaks, among which only two at medium frequencies are mainly affected by electrolysis operation.

frequency peak, $P2_{HE}$, additional data in different operating conditions are needed to make a valid hypothesis on the related phenomenon occurring. The considerations made are broadly applicable to tests conducted under different operating conditions as well, as shown in Fig. 5.11, where some representative examples are provided.

5.2.2 DRT Analysis of parameter variation during cell operation and HE peaks assignment

To investigate the nature of each peak identified for the HE using the DRT method, various operating parameters were systematically adjusted. The cell was tested under several predefined conditions, with one parameter altered at a time, including the HE water content, HE carbon dioxide content, and temperature. The molar fractions of gas species in the HE for all the tests are shown in Tab.5.5, which were performed at 620, 650, and 680°C. The impedance data collected during each test were deconvoluted using the DRT method. DRT analysis was applied to the EIS spectra collected at each operating condition. Each peak obtained from the DRT

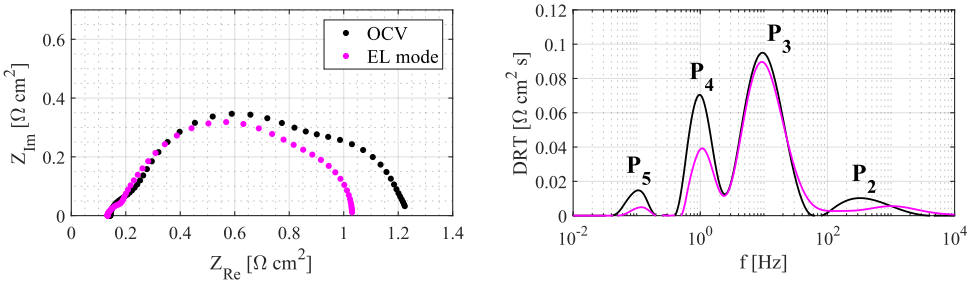

(a) MCEC operated at 620°C, 10/10/20/60% $H_2/H_2O/CO_2/N_2$ at HE.

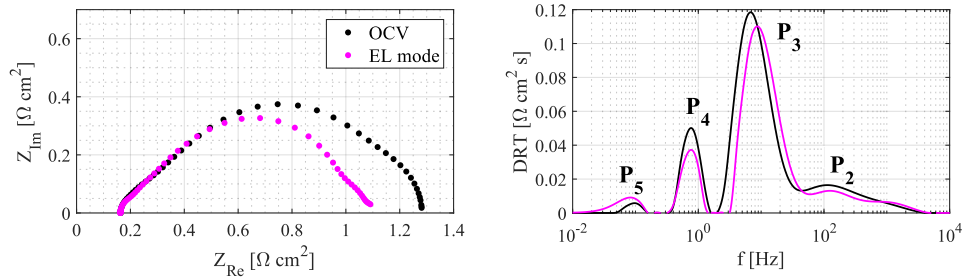

(b) MCEC operated at 650°C, 10/20/10/60% $H_2/H_2O/CO_2/N_2$ at HE.

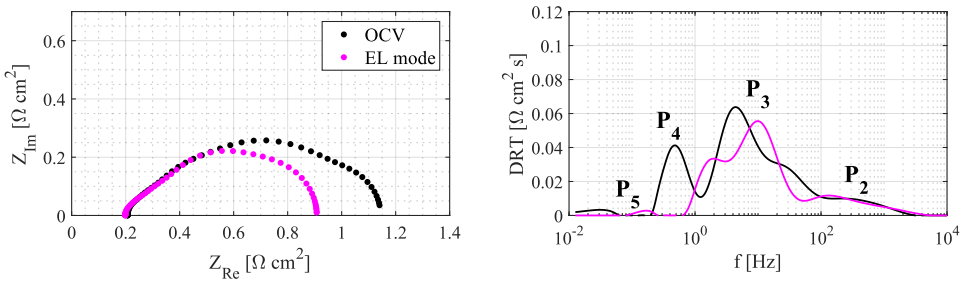

(c) MCEC operated at 680°C, 10/20/30/40% $H_2/H_2O/CO_2/N_2$ at HE.

Figure 5.11. Nyquist plots (on the left) and corresponding DRT spectra (on the right) for the HE electrode. OCV measurement and electrolysis mode results are compared.

deconvolution was associated with a specific process occurring within the hydrogen electrode by analyzing the results from the various tests conducted.

Fig. 5.12 and Fig. 5.13 illustrate some DRT results. Fig. 5.12 presents the DRT analysis of the hydrogen electrode for variation in water and carbon dioxide fractions at 650°C, both at OCV and 100 mA/cm^2. Fig. 5.13 shows the effect of CO_2 variation under electrolysis operation at 620 and 680 °C. The nature of the peaks identified in the relaxation times distribution for the hydrogen electrode will be discussed in detail in the following paragraphs.

High characteristic frequencies

The peak in the high-frequency region (> 300 Hz), $P2_{HE}$, is not easily attributable to a specific process because it does not vary linearly with $\%CO_2$ and $\%H_2O$ (Fig. 5.12

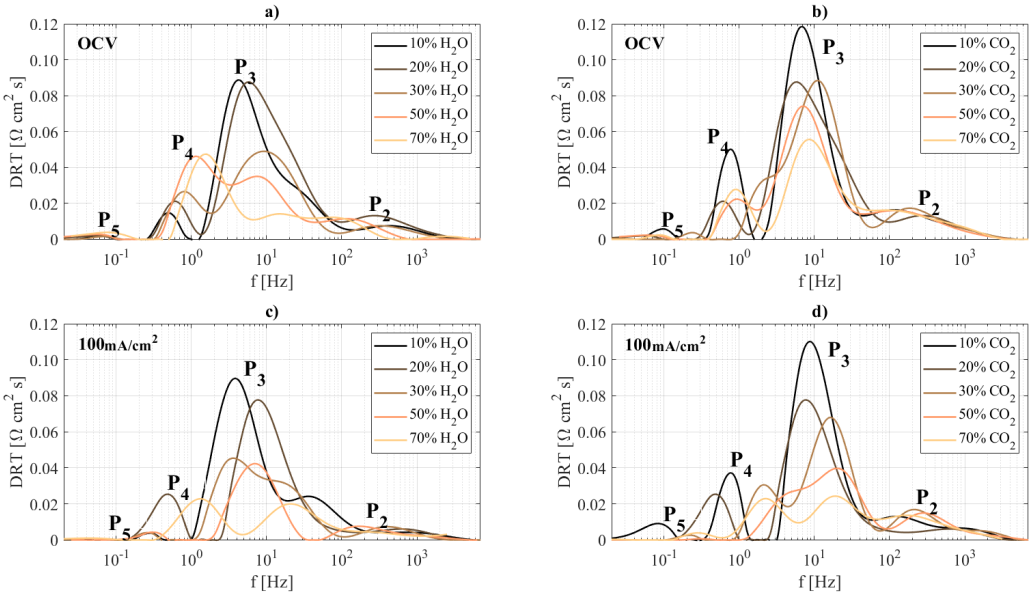

Figure 5.12. DRT spectra of the hydrogen electrode for $\%H_2O$, (a)-(c), and $\%CO_2$ variation, (b)-(d), at 650 °C. The overall gas composition is reported in Tab. 4.2. Both OCV and electrolysis data at 100 mA/cm^2 were analyzed.

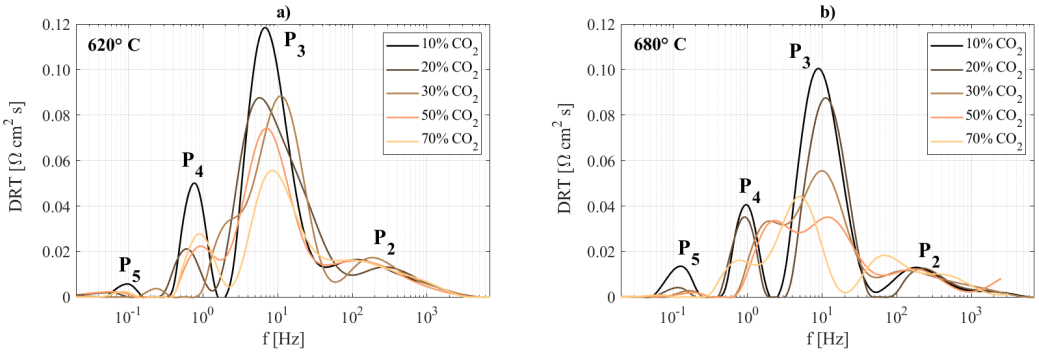

Figure 5.13. DRT spectra of the hydrogen electrode at 100 mA/cm^2 for $\%CO_2$ variation, (test I,VI-XI according to Tab. 4.2), at 620 (a) and 680 °C (b).

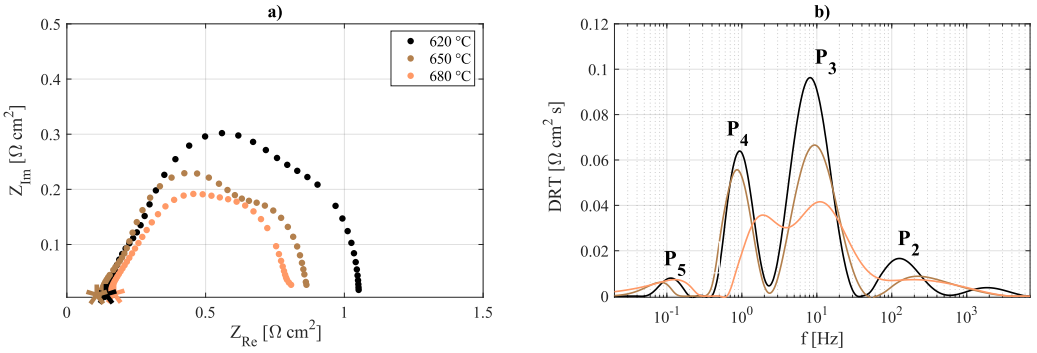

Figure 5.14. HE Nyquist plot (a) at OCV and at 10/20/20/50% $H_2/H_2O/CO_2/N_2$ (test I from Tab. 4.2), and corresponding DRT spectra (b) for temperature variations. The * symbol indicates frequencies of 1000 Hz, denoting the internal resistance of the MCEC.

and 5.13). This suggests that it may not be related to a mass transport process. Additionally, as can be seen in Fig. 5.14b, which compares data at fixed composition while varying the temperature, there is a marked decrease in the highest frequency peak intensity when moving from 620 to 650 °C, but this decrease does not occur when moving from 650 to 680 °C. Observing the behavior of the internal resistance in Fig. 5.14a, it follows the trend of the $P2_{HE}$ peak. Typically, the resistance observed at frequencies below 1 kHz is regarded as the 'internal resistance' of the MCEC [125, 156]. This internal resistance is influenced by several factors, including the effective conductivity of the electrolyte in the matrix pores, the contact resistance between materials, and the effective conductivity of the electrolyte in the pores of the electrode [125] These considerations suggest that $P2_{HE}$ is associated with ion transport resistance within the electrolyte, more precisely with the electrolyte effective conductivity in electrode pores.

As reported in the Sec. 2.3, the balance between OH^- and CO_3^{2-}, governed by hydrolisis equilibrium (Eq. 2.24), influences the kinetics of the water reduction reaction. Moreover, the presence of OH^- affects the internal resistance of the cell by altering the electrolyte composition and thus its conductivity. Specifically, hydroxides have a higher conductivity compared to the corresponding carbonate [157]. Therefore, a decrease in CO_2/H_2O ratio in the atmosphere, corresponding to an increase in hydroxide concentration within the electrolyte melt, is expected to reduce the internal resistance of the cell. Comparing the effects of variations in CO_2 and H_2O in Fig. 5.12, it can be observed that, at a constant H_2O percentage, higher CO_2 levels correspond to higher $P2_{HE}$ intensity. However, as previously mentioned, a linear trend is not evident, likely due to other phenomena coming into play at the frequencies considered.

The active surface area and effective conductivity of an MCFC are directly dependent on how the electrolyte is distributed within the electrode pores [52]. Therefore, any change in the active-surface area will also affect the hydrolysis equilibrium reaction, which occurs at the gas-electrolyte interface, and thus affect the amount of hydroxides present in the carbonates. Several researchers have investigated the

wetting characteristics of various materials in different alkali carbonate mixtures [125, 153, 154]. Their findings indicate that NiO on the oxygen side exhibits complete wetting, with a wetting angle near zero [153]. On the hydrogen side, however, the wetting angle is larger, typically ranging from 50° to 60°, and is influenced by factors such as gas composition, polarization, temperature, and the specific material used.

Increasing the temperature enhances the electrode wettability [154] (reducing the contact angle), thereby increasing the contact surface area between the gas and liquid electrolyte phases. However, an excessive rise in temperature could increase the reaction surface area in larger pores while flooding the smaller pores of the electrode, thus decreasing the overall available active surface area for the reaction [125]. Regarding the effect of gas composition on wettability, it is important to note that the studies here reported pertain to MCFCs, which primarily involve reducing gas mixtures. In contrast, MCECs are fed with more oxidizing mixtures (water and carbon dioxide). The most widely accepted result in the literature is that hydrogen electrode wettability increases in reducing atmospheres. Kawase et al. [152] demonstrated that it enhanced with higher content of H_2 and CO_2. Nonetheless, the gas composition also depends on the rWGS as well as the faradaic reaction, making it difficult to determine the precise composition of the atmosphere in contact with the electrolyte.

In summary, the no-linear behavior of $P2_{HE}$ with temperature variations can be attributed to the fact that temperature not only affects the hydroxide ion concentration but also influences the wettability and the composition of the gas in contact with the electrolyte, due to the reverse rWGS reaction. These combined effects result in multiple factors that influence the effective conductivity of the electrolyte, which in turn affects the internal resistance of the cell, making the relationship between $P2_{HE}$ and temperature complex. However, the strong dependence of $P2_{HE}$ on CO_2 concentration can be explained by the role of CO_2 in affecting the hydroxide ion concentration, which in turn determines the effective conductivity of the electrolyte and, consequently, the internal resistance. Therefore, this peak could reasonably correspond to an ionic transport step in the hydrogen production reaction. Obviously, this hypothesis requires verification through dedicated tests with additional temperature and gas composition variations.

Intermediate characteristic frequencies

The peak $P3_{HE}$ summitting in the intermediate frequencies region ($3 - 300$ Hz) accounts for most of the electrode polarization, as evident in all the figures presented earlier. As discussed in sec. 5.2.1, Fig. 5.10 shows that the height of $P3_{HE}$ clearly decreases when operating in electrolysis mode. This behavior is also visible in Fig. 5.12 and 5.13. Moreover, Figures 5.12 and 5.13 clearly demonstrate that the peak intensity is significantly affected by both CO_2 and H_2O content, irrespective of whether the measurement was taken at open-circuit voltage or under current. As illustrated in Figures 5.13 and 5.14, there is also a noticeable dependence on temperature, although this effect is less pronounced than concentration influence. So, the phenomena occurring at intermediate frequencies must be mainly affected by current and gas composition. Due to the strong dependence on H_2O and CO_2 concentrations, $P3_{HE}$ may be related to a mass transfer process.

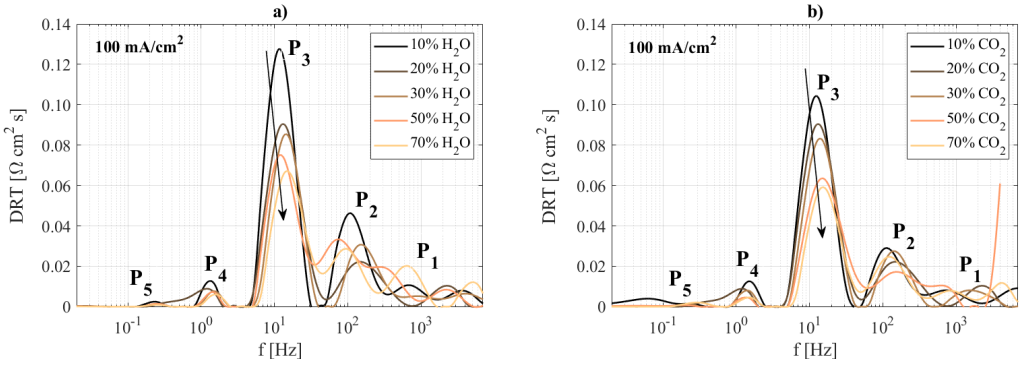

Figure 5.15. DRT spectra of the oxygen electrode for $\%H_2O$, (a), and $\%CO_2$ variation at the hydrogen electrode, (b), at 650 °C and at 100 mA/cm^2. The overall gas composition is reported in Tab. 4.2. The results show a clear dependence of the intermediate frequencies peak from the HE gas composition.

Considering the reactions 5.10 and 5.12,

$$H_2O + M + e^- \rightarrow MH + OH^- \tag{5.10}$$

$$OH^- + CO_2 + M + e^- \rightarrow MH + CO_3^{2-} \tag{5.12}$$

which, as previously discussed in the polarization data analysis (Sec. 5), could both potentially be rate-determining steps of the water reduction reaction, it is plausible that $P3_{HE}$ corresponds to the transport of reactants to the triple-phase boundary (TPB), where the water reduction reaction occurs.

However, given the poor wettability of the hydrogen electrode compared to the oxygen electrode [107, 156], the electrolyte film thickness inside the HE pores can be negligible, and, as a consequence, the HE may not show liquid phase transport resistance. Many assume that in an MCFC hydrogen electrode, the diffusion of reactants in the liquid phase within the electrolyte is negligible compared to that in the gas phase [108, 156, 158]. These considerations lead to the conclusion that $P3_{HE}$ is associated with reactant gas diffusion within the pores, as increased CO_2 and H_2O flow rate reduce mass transfer resistance in the gas phase. Additionally, during electrolysis operation both reactions 5.10 and 5.12 are enhanced, favoring H_2O and CO_2 diffusion, thereby explaining the peak reduction observed when a current is applied (see Fig. 5.10c and 5.11).

In connection with this, it is interesting to observe the oxygen electrode DRT results shown in Fig. 5.15, obtained with the same H_2O and CO_2 variations at the HE. Examining the intermediate frequency peak, $P3_{OE}$, a clear decreasing trend can be observed in correlation with increasing $\%H_2O$ and $\%CO_2$. Such a result is explainable only by assuming that the electrochemical reaction occurring at the OE, reaction 2.13,

$$CO_3^{2-} \rightarrow CO_2 + \frac{1}{2}O_2 + 2e^- \tag{2.13}$$

is strictly dependent on the amount of CO_3^{2-} produced at the hydrogen electrode. This confirms the correlation between $P3_{HE}$ and the CO_3^{2-} production, and more precisely, with the rate-determining steps of the hydrogen production reaction.

Low characteristic frequencies

Changes occurring in the electrolyte distribution inside the pores can be responsible for the presence of the two crests, $P4_{HE}$ e $P5_{HE}$, observed in the low-frequency range ($0.05 - 3$ Hz). The quality of the low-frequency experimental data is poorer compared to that of the high-frequency data, as confirmed by the Kramers-Kronig test (see Fig. 3.5). This can lead to distortions in the appearance of the DRT, making it difficult to interpret. Nevertheless, in the Figures 5.12 and 5.13, it can still be observed that the low-frequency peaks are influenced by changes in gas composition. In contrast, the effect of temperature is comparatively minor (see Fig. 5.13 and 5.14). However, it is difficult to single out $P4_{HE}$ e $P5_{HE}$ trend with the operating conditions variations considered.

Under equilibrium conditions, the local capillary pressures are balanced resulting in the electrolyte distribution among the matrix and the two electrodes. Capillary pressure depends on the diameter of the last filled pore, D_{pore}, and the wetting angle ϕ according to the following expression [52, 152]:

$$P_{\text{cap}} = \frac{4\sigma_{\text{lg}} \cos(\theta)}{D_{\text{pore}}} \tag{5.18}$$

Here σ_{lg} represents the electrolyte surface tension. When the cell voltage changes, the local composition of the electrolyte also changes. This, along with variations in gas composition, affects the wetting angle, leading to a migration of the electrolyte to balance the capillary pressure. Additionally, cation segregation within the electrolyte may occur, leading to a variation in the electrolyte composition. Variations in the local carbonate salts can impact the kinetics of electrochemical reactions, affect the solubility of Ni, and influence the rates of vaporization and corrosion of the current collector [32, 52]. Boden et al. [159] evaluated the characteristic timescales of electrolyte distribution and segregation phenomena for MCFC conditions, concluding that the characteristic time of the electrolyte composition change is at least four orders of magnitude smaller than that for the movement of bulk electrolyte. Obviously, if the temperature or gas composition changes, affecting the contact angle, the time constants change. However, they found that the most significant effect is due to variations in the degree of electrolyte filling. A smaller electrolyte filling degree will reduce the time constant difference, but the time constants will only approach each other in magnitude for an almost totally drained system and that is not of practical interest.

There are no similar studies conducted under electrolysis conditions, but, also in this case HE gas composition variation will affect the electrolyte wettability, causing the displacement of the electrolyte within the pores. Additionally, changing the current direction will not prevent the migration of the electrolyte cations. Therefore, observing the results reported before, it is plausible to associate $P4_{HE}$ with electrolyte distribution and $P5_{HE}$ with ion segregation, even though the latter does not appear at all the operating conditions tested and has a very low intensity, making it less significant compared to $P4_{HE}$. At constant temperature and gas composition, $P4_{HE}$ intensity under current, Fig. 5.12c-d, is lower than in OCV Fig. 5.12a-b. In fact, imposing a current facilitates the movement of the electrolyte within the pores, which is why the peak decreases. To clarify the effect of composition and temperature on

the low-frequency peaks, it is required to carry out specific studies under electrolysis operation. On one side, it is necessary to more precisely evaluate the dependence of the wetting angle on temperature and HE gas composition and, on the other, to delve into the cations migration mechanism.

Resume

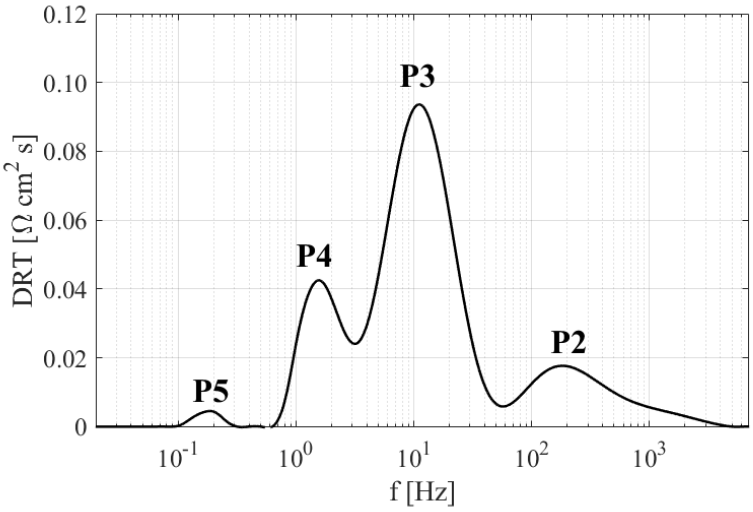

Figure 5.16. Example of DRT spectra for the hydrogen electrode, highlighting the four peaks observed during the experimental campaign.

Table 5.6. Resume of physicochemical processes occurring in the MCEC hydrogen electrode and their corresponding peaks in the DRT spectra.

Peaks	Dependecies			Process description
	$\%CO_2$	$\%H_2O$	Temperature	
$P2_{HE}$	Medium	Low	Low	ionic charge transfer
$P3_{HE}$	High	High	Medium	gas diffusion
$P4_{HE}$	Medium	Medium	Medium	electrolyte redistribution
$P5_{HE}$	Low	Low	No	electrolyte segregation

Fig. 5.16 depicts a relaxation-time distribution spectrum for the MCEC hydrogen electrode, showcasing peaks corresponding to various physicochemical processes within the electrode. Table 5.6 gives an overview of the processes identified by the DRT analysis together with their characteristic frequency range, gas partial pressure and temperature dependencies. The peak appearing around 10 Hz, $P3_{HE}$, accounts for most of the hydrogen electrode polarization and is significantly influenced by CO_2 and H_2O content. This peak corresponds to the mass transfer process of reactants to the triple-phase boundary where the water reduction reaction occurs, which is

connected to the rate-determining step of hydrogen production. The reduction in peak intensity during electrolysis mode suggests enhanced reactant gas diffusion. Additionally, the oxygen electrode results indicate a correlation between $P3_{HE}$ and CO_3^{2-} production, reinforcing the link to the rate-determining step of the reaction. The high-frequency peak, $P2_{HE}$, correlates with trends in internal resistance and likely reflects changes in electrolyte conductivity, which are linked to variations in hydroxide ion concentrations, with the latter being influenced by operating conditions (H_2O and CO_2 molar fractions and temperature) Studies conducted under MCFC conditions demonstrate that alterations in gas composition and temperature impact electrolyte wettability, thereby affecting the gas-electrolyte interface and potentially influencing the carbonate-hydroxide equilibrium. Even though in electrolysis only the gas composition changes, it is plausible that this effect persists, but dedicated tests are needed to confirm it. Finally, low-frequency peaks show an unclear dependency on gas composition, while temperature variations play a secondary role. It is important to emphasize that this is the first work conducted applying DRT on MCEC impedance spectra, and especially, peaks at low frequencies may be subject to different interpretations based on the results obtained in this study. Therefore, further investigation with specific tests is needed to confirm or refute the hypothesis made regarding these dependencies at certain frequencies.

5.3 Post-mortem analysis

To investigate the effects of temperature and gas composition variations during electrolysis operation, the sample tested has been analyzed by means of SEM/EDS analysis. This examination provided detailed insights into the microstructural and compositional changes induced by the operating conditions. The SEM images revealed structure morphology modifications, while the EDS analysis identified elemental distribution changes, particularly at the hydrogen electrode. These results were compared with those from a reference cell, which was shut down after the initial start-up and stabilization phase. The comparison highlighted differences in degradation patterns and material composition, shedding light on the impact of 1440 h of electrolysis operation under varying conditions on the hydrogen electrode.

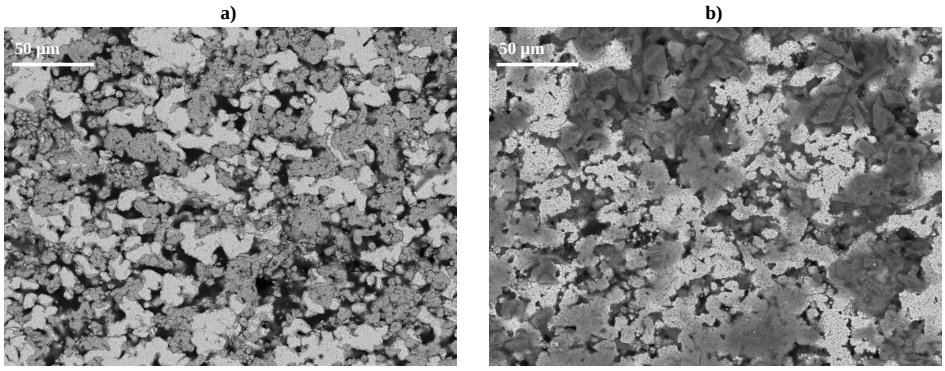

Figure 5.17. SEM images of the hydrogen electrode cross-section of (a) the reference sample and (b) the BC-MCEC used in the parametric variation campaign.

Fig. 5.17 shows a comparison between the hydrogen electrode cross sections of the reference sample (a) and the BC-MCEC (b), the sample used for the experimental campaigned reported in this chapter. The comparison between the two samples highlights distinct morphological changes in the electrode due to operational conditions. The reference sample (a), which comes from a cell that was shut down shortly after the start-up and stabilization phase, exhibits a relatively uniform surface morphology with well-defined pores and consistent particle distribution. Its open structure suggests minimal degradation, maintaining the porosity essential for efficient gas diffusion and electrochemical reactions. In contrast, the electrolysis sample (b) shows significant structure densification, accompanied by particle growth and a reduction in pore size. These structural changes imply a reorganization of the nickel particles, likely caused by the extended exposure to varying electrolysis conditions.

Fig. 5.18 presents the EDX mapping of the BC-MCEC hydrogen electrode cross-section, showing that both Ni and electrolyte (K) particles have formed large aggregates. The darker regions in the image correspond to the electrolyte, while the lighter areas are associated with the electrode material. The aggregation of nickel particles indicates possible sintering during operation, while the potassium formations could result from the high-temperature operation (680 °C) where electrolyte mobility is increased, allowing the molten carbonate to migrate and accumulate in specific

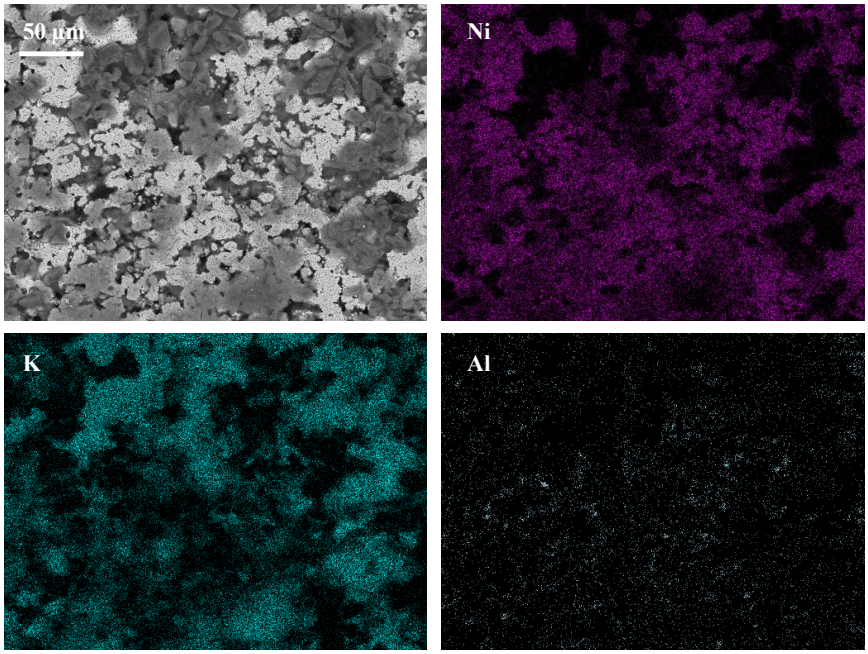

Figure 5.18. EDX analysis of the hydrogen electrode cross section: only Nickel, Potassium and Aluminum are shown.

regions. Such aggregates may block active electrode sites and disrupt gas transport, negatively affecting the overall electrochemical performance. It is challenging to draw conclusions regarding the presence of aluminum (Al) from the mapping, as it is initially present in both the electrode and the matrix. This makes it difficult to distinguish its role in the observed structures or its contribution to material degradation.

Finally, in Fig. 5.19 is reported a close-up view of the BC-MCEC electrode structure. An EDX analysis was performed to determine the composition of four different spots, confirming the previous observations, as reported in Tab. 5.7. Additionally, the presence of carbon alongside potassium further supports the conclusion that regions 1 and 2 correspond to the electrolyte. In conclusion, the post-mortem analysis indicates that the electrolysis operation significantly affects the structure of the nickel electrode. However, to accurately determine whether specific structural changes, such as nickel oxidation or potassium precipitation, have occurred, further targeted analyses are necessary. Techniques like X-ray diffraction (XRD) will be essential for confirming the presence of new phases or structural alterations in the electrode material.

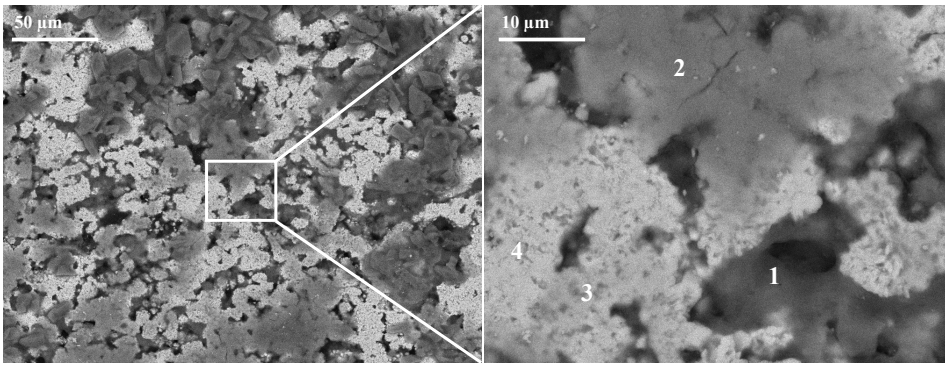

Figure 5.19. SEM image of cross-section hydrogen electrode (left). Magnification of some particles (right); numbers indicate the spots where EDS analysis has been carried out, and the compositions obtained are reported in Tab. 5.7 below.

Table 5.7. Elementary composition obtained from EDX analysis. Numbers refer to different spots located on the surface of the electrod section, as shown in Fig. 5.19.

Elements	1 (wt%)	2 (wt%)	3 (wt%)	4 (wt%)
C	8.0	7.3	8.9	0.6
O	32.9	30.8	14.5	24.4
Al	1.8	1.0	4.6	1.1
K	27.6	41.4	9.0	0.9
Ni	29.7	19.5	63.0	73.0

Chapter 6

Planar single MCEC performance evaluation

This chapter focuses on the performance analysis of a planar single MCEC. Although this configuration is on a laboratory scale (with an active area between 80 and 100 cm^2), it closely resembles industrial setups. Therefore, the performance obtained with this system, and the resulting conclusions, can reasonably be used as an indication of what to expect on an industrial scale.

The first part describes the development of a 2D model for the cell's cross-section, implemented in COMSOL Multiphysics, and validated against experimental data. This model was used to predict the heat distribution within the cell, evaluating the thermal contributions of the electrolysis reaction, Joule effect, and rWGS reaction, given that the cell is likely to operate in an adiabatic environment within a stack. Moreover, the 2D model was used to assess the various contributions to overpotential, showing that the distribution of these contributions between the two electrodes differs in MCEC operation compared to MCFC. These findings have been published in a scientific article [128].

The temperature profiles obtained from the model highlighted the importance of temperature control within the cell and emphasized the need to understand how the progression of electrochemical and chemical reactions influences this parameter. To gain deeper insights, it is essential not only to monitor the temperature but also to track the composition of the outlet gases. Building on these consideration, the experimental data obtained from the campaign described in Sec. 4.2.2 are then presented and discussed. In addition to polarization curves and EIS measurements, gas analysis was performed at the hydrogen electrode (HE) outlet. The gas composition results, together with the polarization data, allowed for a quantitative assessment of hydrogen and carbon monoxide production. Based on these findings, new observations regarding the contribution of rWGS reaction were made, given the lack of literature data on gas analysis in MCEC. Evaluating the rWGS contribution is essential for understanding how much hydrogen is converted to CO and how much additional CO_2 is consumed beyond what is required for electrolysis. The experimental results presented in the second section of this chapter are also detailed in a manuscript that has been submitted for publication [160].

6.1 Two-dimensional modeling

In this section, the 2D model developed to describe the behavior of a MCEC within the temperature range of $570 - 650$ °C is presented. Since the experimental data used for model validation were obtained from a separate study and are not part of the original work conducted in this thesis, a brief overview of the experimental setup is provided for context. Following this, a detailed description of the model is given, and finally, the results, along with the model validation using experimental data, are discussed. Additionally, the thermal effects within an adiabatic cell are predicted.

6.1.1 Experimental

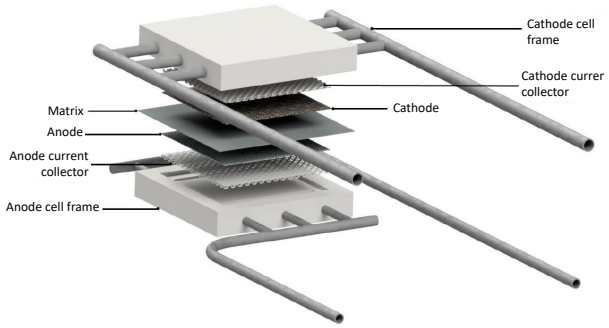

Figure 6.1. Single cell assembling for MCEC employed by Pérez Trujillo et al. [103], where "anode" refers to the hydrogen electrode and "cathode" denotes the oxygen electrode.

The experimental data used in this study were partially taken from previous work by Pérez Trujillo et al. [103] and obtained using a 80 cm^2 planar single cell at the ENEA Casaccia Research Center. Additional tests were conducted on a similar cell with a slightly larger area of 100 cm^2. The key characteristics of the materials used for the cell components remained consistent and are summarized in Tab. 6.1. Fig. 6.1 illustrates the single cell assembling. It should be noted that the main difference from the setup used in this thesis is the shape of the casing, which here results in a cross-flow configuration instead of the co-flow setup. The experimental station featured a customized test bench, equipped with gas flow meters, a controlled evaporation and mixing system (CEM) for water, and thermocouples for temperature monitoring. Gas composition at the cathode outlet was analyzed using a Clarus 680-PerkinElmer gas chromatograph, while the electrochemical performance of the cell was monitored using a Solartron SI-1287 for electrochemical impedance spectroscopy (EIS) and an Agilent power supply for polarization curves.

The data analyzed in this work come from three experimental campaigns: (i) the original work by Pérez Trujillo et al. [103], (ii) new tests performed on the same cell under different gas compositions, and (iii) tests on a newly fabricated cell that had different dimensions and distinct operating conditions. The latter cell used components similar to those in the single cell from the experimental work in this thesis, while the cell used by Pérez Trujillo et al. featured a distinct matrix and electrolyte morphology.

Table 6.1. Characteristics of the components used in the molten carbonate cell.

Hydrogen electrode	
Material	Ni+5% wt. Al
Porosity [%]	$52 - 65$
Thickness [mm]	$0.6 - 0.7$
Oxygen electrode	
Material	NiO+2% wt. Li
Porosity [%]	$60 - 65$
Thickness [mm]	$0.6 - 0.7$
Electrolyte	
Material	Li_2CO_3/K_2CO_3
Mole ratio	68:32
Matrix	
Material	γ-$LiAlO_2$
Current collector	
Material	SUS-316L

The main parameters for each set of experiments are summarized in Tab. 6.2, referred to "base case", "validation 1", and "validation 2", respectively. In the table, u_0 represents the inlet gas velocity, while s and H denote the gas channel and width, respectively. All experiments were conducted under atmospheric pressure conditions.

Table 6.2. Model parameters for the gas channels.

Parameter	Base case		Validation 1		Validation 2	
	HE	OE	HE	OE	HE	OE
u_0 [m/s]	0.3	0.6	1.5	6	0.1	0.35
T [K]	$843 - 923$		883		923	
$y^0_{N_2}$ [-]	0.25	0.50	-	0.75	-	-
$y^0_{CO_2}$ [-]	0.25	0.25	0.475	0.05	0.45	0.66
$y^0_{CO_2}$ [-]	-	-	-	-	-	-
$y^0_{H_2}$ [-]	0.25	-	0.06	-	0.10	-
$y^0_{H_2O}$ [-]	0.25	-	0.574	-	0.45	-
H [mm]	90	90	90	90	100	100
s [mm]	0.7	0.7	0.7	0.7	2.5	2.5

6.1.2 Modeling

The cell described in this work uses a cross-flow configuration for the anodic and cathodic gases (see Fig. 6.1), which would typically require a 3D model due to the increased complexity. However, in this case, a 2D model was developed by assuming a co-current gas flow. This simplification was justified by the uniformity of the gas composition in the oxygen electrode (OE) channel under the experimental conditions, which was achieved by feeding either an inert gas mixture (for the "base

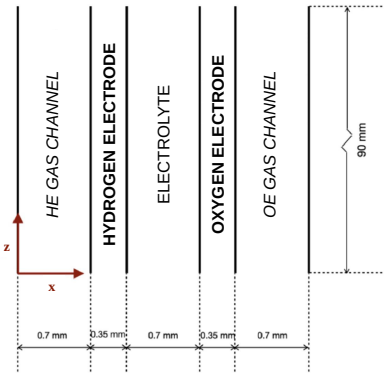

Figure 6.2. Schematic representation of the cell described in the model, designated as the "base case" in Tab. 6.2. Gas flows in the z-direction, while the x-direction is perpendicular to the electrode surface.

case" and "validation 1") or using the same composition as the gas produced during electrolysis (for "validation 2"). To validate this assumption, polarization curves were compared for both co-current and counter-current flow, and the results were identical, indicating that the 2D model with co-current flow is sufficient to describe the cell's performance.

Fig. 6.2 illustrates the representation of the cell for which the mathematical model was developed. The five defined domains are:

1. Hydrogen electrode gas channel
2. Hydrogen electrode
3. Electrolyte matrix
4. Oxygen electrode
5. Oxygen electrode gas channel

The electrochemical reactions occurring at the cathode and anode are shown in Eqs. 2.12 and 2.13, respectively. Additionally, the reverse water gas shift reaction, is assumed to occur in the HE gas channel under local equilibrium conditions. The primary balance equations for each domain are explained in the following sections. Initially, the model was developed under isothermal conditions, as the cell was held at a constant temperature inside a furnace.

Gas channels

The following phenomena were considered in the gas channels domains:

1. convective mass transport of all components in the direction parallel to the main gas flow;
2. diffusive mass transport of all components in both parallel and transverse directions relative to the main gas flow;

3. rWGS reaction occurring in the hydrogen electrode gas channel;

4. absence of chemical reactions in the oxygen electrode gas channel.

The mass balance equation can be expressed as

$$\nabla \cdot \mathbf{j}_k + \rho \mathbf{u} \nabla \omega_k = \mathcal{R}_k \tag{6.1}$$

taking into account the continuity equation:

$$\nabla \cdot (\rho \mathbf{u}) = 0 \tag{6.2}$$

In these equations, $\mathbf{j}_k$, $\mathcal{R}_k$ and ω_k represent the diffusive flux, rate of production and mass fraction, respectively of the kth components, while ρ denotes the gas density and $\mathbf{u}$ is the velocity vector.

Given the operational conditions regarding temperature, composition, and flow rates, it is reasonable to assume that local equilibrium conditions are achieved for the rWGS reaction. To include this condition in the simulations, the CO production rate from the rWGS was modeled using a first-order rate expression in relation to water and carbon dioxide:

$$\mathcal{R}_k = k p_{\mathrm{H_2O}} p_{\mathrm{CO_2}} (1 - \beta) \tag{6.3}$$

Here k represents the rate constant, while $p_{\mathrm{H_2O}}$ and $p_{\mathrm{CO_2}}$ denote the partial pressures of water and carbon dioxide, respectively. The term $(1 - \beta)$, which varies between 0 and 1, reflects the deviation from equilibrium and is defined as

$$1 - \beta = 1 - \frac{1}{K_{eq}} \frac{p_{\mathrm{H_2O}} p_{\mathrm{CO}}}{p_{\mathrm{H_2}} p_{\mathrm{CO_2}}} \tag{6.4}$$

where K_{eq} is the equilibrium constant for the rWGS reaction, evaluated using the correlation presented in [161]. The kinetic constant k was assigned a sufficiently high value to ensure that local equilibrium is achieved at all points within the HE gas channel. For convective transport, the gas velocity was assumed to be uniform and was calculated based on the inlet volumetric flow rate and the channel's entrance area. Diffusive transport was described using the Stefan-Maxwell equation for multi-component mixtures:

$$\mathbf{j}_k = -\rho \omega_k \sum_i \mathcal{D}_{ki} \left(\nabla y_i + \frac{1}{P} [(y_i - \omega_k) \nabla P] \right) \tag{6.5}$$

where $\mathcal{D}_{\mathrm{ki}}$ represents the binary diffusion coefficients, y_i is the molar fraction of the ith component, and ω_k is the mass fraction of the kth component. Gas density was determined using the ideal gas equation of state.

The boundary condition at the channel inlet ($z = 0$) maintained a fixed composition

$$\omega_k = \omega_{0k} \tag{6.6}$$

with no diffusive flux at the cell outlet ($z = H$),

$$\mathbf{j}_k \cdot \mathbf{n}_1 = 0 \tag{6.7}$$

The outer walls were considered impermeable to any fluxes,

$$(\mathbf{j}_k + \rho \mathbf{u} \omega_k) \cdot \mathbf{n}_2 = 0 \tag{6.8}$$

whereas continuity conditions were applied at the interface between the gas channel and the electrode, represented by the following equation:

$$(\mathbf{j}_k + \rho \mathbf{u} \omega_k) \cdot \mathbf{n}_3\big|_{s^-} = (\mathbf{j}_k + \rho \mathbf{u} \omega_k) \cdot \mathbf{n}_3\big|_{s^+} \tag{6.9}$$

where $\mathbf{n}_1$, $\mathbf{n}_2$, $\mathbf{n}_3$ are the vectors normal to the surfaces where boundary conditions are applied, and H denotes the length channel. The main parameters used in the electrode channels, which correspond to the experimental conditions, are labeled as "base case" in Tab. 6.2.

Electrodes

The phenomena modeled in the electrodes domain are:

1. electron transport within the solid fraction of the electrode;
2. ionic transport in the electrolyte phase present in the electrode pores;
3. electrochemical reaction occurring at the three-phase boundary between electrode, electrolyte and gas;
4. gas diffusion.

Charge conservation is expressed as

$$\nabla \cdot \mathbf{i}_s = -A_v \cdot i_{v,TOT} \tag{6.10}$$

where $\mathbf{i}_s$ represents the current density, A_v is the specific reaction surface area, set to 10^7 m^{-1}, and $i_{v,TOT}$ is the rate of the electron generation due to the electrochemical reaction, described through the Butler-Volmer equation:

$$i_{v,TOT} = i_0^* \left(\exp\left(\alpha_a n \mathcal{F} \eta^*\right) g_a - \exp\left(-\alpha_c n \mathcal{F} \eta^*\right) g_c\right) \tag{6.11}$$

The transfer coefficients were set to be equal, with $\alpha_a = \alpha_c = 0.5$. This is a standard approach when there is no evidence suggesting asymmetry in the polarization curve. Additionally, the influence of values that differ from 0.5 is minimal when the activation overpotential is low relative to other contributions to the overall overpotential [162], as will be demonstrated later for this cell. In the aforementioned equation, * denotes the reference conditions, which occur when the activities of all species involved in the electrochemical reaction are equal to unity. The terms g_a and g_c reflect deviations in gas composition from the reference conditions and are defined by

$$g_m = \prod_{k=1}^{n_c} \left(\frac{p_k}{p_k^*}\right)^{\nu_k} \tag{6.12}$$

where the subscript m is used to generically indicate an electrode, and ν_k represent the stoichiometric coefficient of the kth component in each of the semi-reactions. Electron transport is expressed using Ohm's law:

$$\mathbf{i}_s = -\kappa_s \nabla \phi_s \tag{6.13}$$

where ϕ_s is the solid-phase potential and κ_s is the electronic conductivity of the solid electrode. The electronic conductivities were assumed to be independent of temperature, with values of 10^3 S/m for the anode and 10^5 S/m for the cathode. Gas diffusion was described using the Stefan-Maxwell relation, similar to that in the gas channel. However, the diffusion coefficient was corrected using the Bruggeman correlation to account for the volumetric fraction of gas actually occupied by the electrode:

$$\mathcal{D}_{ki,eff} = \epsilon_g^{1.5} \mathcal{D}_{ki} \tag{6.14}$$

where ϵ_g is the volumetric fraction of gas in the electrode.

Electrolyte

The electrolyte is present both within matrix and electrodes pores and its aim is to transport the carbonate ions. Hence, the balance equations applied to the electrolyte phase are valid both within the electrolyte matrix and the porous electrodes. The primary difference lies in the values of the effective ionic conductivity used in the two domains, which will be discussed in greater detail in the following paragraphs.

In this domain the charge conservation is expressed as

$$\nabla \cdot \mathbf{i}_s + \nabla \cdot \mathbf{i}_l = 0 \tag{6.15}$$

with the current density within the electrolyte (liquid) phase named as $\mathbf{i}_l$. By combining Eqs. 6.10 and 6.15, the following is obtained

$$\nabla \cdot \mathbf{i}_l = A_v \cdot i_{v,\mathrm{TOT}} \tag{6.16}$$

Charge transport is once again linked to the potential by Ohm's law:

$$\mathbf{i}_l = -\kappa_{l,eff} \nabla \phi_l \tag{6.17}$$

Here, ϕ_l represents the liquid-phase potential, while $\kappa_{l,eff}$ denotes the effective ionic conductivity within the electrolyte. The value of this parameter is influenced by the intrinsic ionic conductivity of the electrolyte, its volumetric fraction, and the tortuosity of the phase in which it is embedded. The effective conductivity can be determined using a Bruggeman-type expression or by applying a correction factor, as will be detailed in the next section.

6.1.3 Results

The model developed in this work was first used to simulate the cell's behavior over the range of temperatures experimentally explored . Initial findings show that, in the tested operating conditions, the cathodic reaction does not limit performance ($i^*_{0,\mathrm{HE}} \to +\infty$). This result is consistent with other studies on MCFC, where it has been reported that the resistance of the oxygen reduction reaction is significantly greater than that of the hydrogen oxidation ($i^*_{0,\mathrm{OE}} << i^*_{0,\mathrm{HE}}$) [124, 159]. This suggests that in the electrolysis cell (MCEC), where the reactions occurring are the reverse of those in MCFC, the same principle may apply. However, it is important to note that the data analyzed in this work were obtained by feeding an equimolar mixture

Table 6.3. Effective ionic conductivities and anodic exchange current density at different temperatures, as obtained from the preliminary 1D model.

T [K]	$\kappa_{l,eff}^{\mathrm{HE}}$ [S/m]	$\kappa_{l,eff}^{\mathrm{OE}}$ [S/m]	$\kappa_{l,eff}^{mat}$ [S/m]	$i_{0,\mathrm{OE}}^{*}$ [mA/cm^2]
843	3.61	1.52	3.96	0.62
863	3.95	1.63	4.35	0.80
883	4.29	1.74	4.75	0.92
903	4.65	1.86	5.13	1.23
923	5.02	1.98	5.53	1.62

of $H_2/CO_2/H_2O/N_2$, and therefore this assumption may not hold for different composition values.

Here, the model was solved using the effective ionic conductivity values for the HE, OE, and electrolyte matrix, as well as the OE exchange current density, which were previously obtained from the 1D analysis. These values are summarized in Tab 6.3. It is essential to emphasize that the parameters used are specific to the materials employed, as they are closely dependent on porosity and specific surface area.

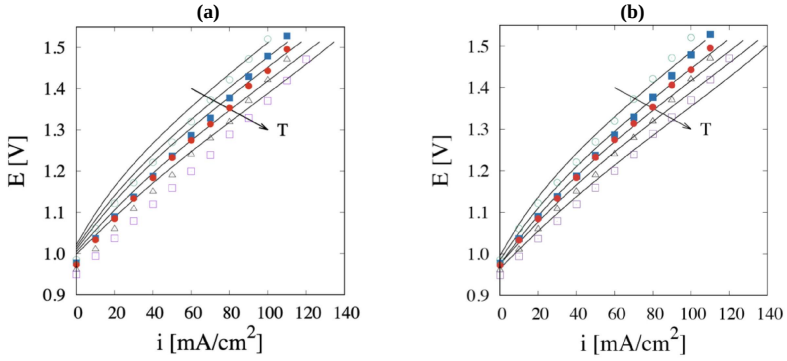

Figure 6.3. Comparison of experimental data (indicated by symbols) and calculated results (depicted by solid lines) for polarization curves at temperatures of 843, 863, 883, 903, and 923 K, shown before (a) and after (b) the correction of the OCV.

Fig. 6.3a displays the polarization curves obtained under specific conditions and operating parameters detailed in Tabs. 6.3 and 6.2. As observed in the earlier analysis using the 1D model, a discrepancy exists between the experimental and predicted OCV, defined by the Nernst equation (2.29). The observed discrepancy in OCV is small enough to be attributed to minor inaccuracies in the evaluation of equilibrium constants for the chemical and electrochemical reactions or to the presence of impurities in the gas feed. Previous studies has also noted discrepancies of approximately 0.05 V between experimental and calculated OCV values [117]. The results shown in Fig. 6.3 reflect the data after correcting the OCV, revealing excellent agreement between the two datasets, especially considering that all model parameters were derived from literature or earlier analyses using the 1D model. The

parameters derivation from the 1D model is described in Appendix A.

To distinguish between the effects of the rWGS reaction and the electrochemical reaction, concentration profiles of various gaseous species were examined. Fig. 6.4 presents the concentration profiles of hydrogen and carbon monoxide along the gas flow direction for the cell operating at 863 K with an applied potential of 1.5 V. The different symbols indicate concentrations at varying distances from the electrode surface, with the close overlap suggesting negligible concentration gradients perpendicular to the main gas flow. Additionally, a sharp change in gas composition occurs immediately after the inlet section due to the rWGS reaction quickly reaching equilibrium conditions. The concentration of CO remains nearly constant because the electrolysis processes consumes CO_2 and produces H_2, both reactants of the rWGS reaction. This explains why the CO concentration stays stable even as the hydrogen concentration continues to rise during the progression of the electrolysis process.

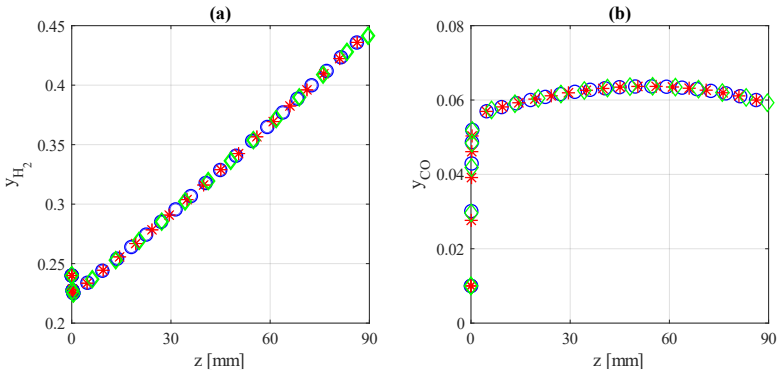

Figure 6.4. Concentration profiles of H_2 (a) and CO (b) along the cathodic gas channel of a cell operating at 863 K and 1.5 V. Different symbols represent various distances from the electrode interface in the x-direction.

Weights of overpotential contributions

Table 6.4. Estimated activation and Ohmic overpotentials at 883 K.

i	η_{act}	η_{ohm}	η_{tot}
[mA/cm^2]	[V]	[V]	[V]
20	0.02	0.09	0.11
40	0.04	0.17	0.21
60	0.06	0.26	0.32
80	0.08	0.34	0.42
100	0.09	0.43	0.52
120	0.11	0.52	0.63

The model has been developed and solved under the assumption that the only significant overpotentials are related to OE activation and ohmic resistance. To gain

further insight into the relative contributions of these two factors, we approximate the activation overpotential as

$$\eta_{act} = \frac{RT}{\mathcal{F}} \operatorname{arcsinh}\left(\frac{i/s_{\mathrm{OE}}}{2i^*_{0,\mathrm{OE}}A_v}\right) \tag{6.18}$$

and the Ohmic overpotential as

$$\eta_{ohm} = \left[\frac{s_{el}}{\kappa^{mat}_{l,eff}} + \frac{s_{\mathrm{HE}}}{\kappa^{\mathrm{HE}}_{l,eff}} + \frac{s_{\mathrm{OE}}}{\kappa^{\mathrm{OE}}_{l,eff}}\right] i \tag{6.19}$$

where s_{el}, s_{HE}, and s_{OE} represent the thickness of the electrolyte layer, hydrogen electrode , and oxygen electrode, respectively. All other symbols have been defined previously.

It is important to note that these expressions are approximations. Specifically, Eq. 6.18 does not consider the influence of gas composition on the activation overpotential, while Eq 6.19 would only be strictly valid if the current decreased linearly across the cell's thickness. Tab. 6.4 presents the values of the two contributions to the overpotential obtained at 883 K across the measured current densities, along with the total overpotential (η_{tot}). A key observation is that the total overpotentials estimated in this way align with the values derived from the complete model, suggesting that the simplifying assumptions used are sufficient for an order-of-magnitude analysis. Thus, while the results indicate that the ohmic overpotential is the primary contributor, it is crucial to note that the activation overpotential becomes increasingly important at higher current densities, reaffirming the need to consider gas composition effects in specific scenarios.

Model validation

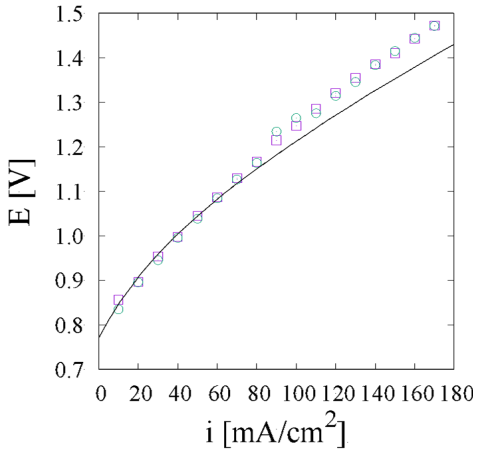

Figure 6.5. Comparison of the predicted polarization curves (solid lines) with the experimental data (points) for the cell operating under the conditions specified in Tab. 6.3 ("validation 1").

The model was first validated using data obtained from the same cell under different flow rates and gas compositions, as summarized in Tab. 6.3 ("validation 1").

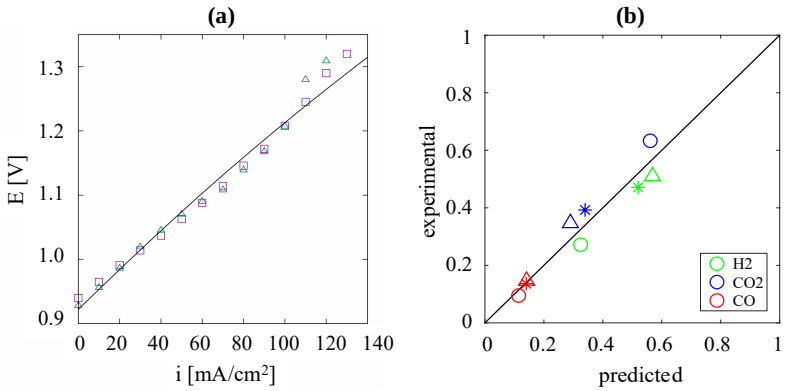

Figure 6.6. Comparison between experimental and predicted polarization curves (a), and molar fraction on dry basis (b) under the experimental conditions listed in Tab. 6.3 ("validation 2") with inlet $H_2O/CO_2/H_2$ molar ratios of 45/45/10. In (b) the data are at OCV (open circuit, circle), 80 mA/cm^2 (asterisk), and 100 mA/cm^2 (triangle).

Fig. 6.5 shows excellent agreement between predicted and experimental polarization curves, particularly at lower current densities. However, the model slightly underestimates the overpotential at higher current densities. It is worth noting that (i) the new experimental results span a broader range of current densities than those previously examined, and (ii) a slight underestimation of the overpotential at high current densities was already observed in earlier data sets (see Fig. 6.3), although it was less pronounced. These findings suggest that a more precise description of the concentration overpotential, specifically the diffusive transport from the gas bulk to the electrode surface, is necessary for accurately modeling the cell over a wider range of operating conditions. Nonetheless, these results underscore the value of a 2D model in quantifying the impact of concentration gradients on overall cell performance.

Additional tests were conducted using a cell with different dimensions from the one used in previous experiments. The geometric properties and operating conditions for this set of tests are provided in Tab. 6.2 under "validation 2". During this experimental campaign, the gas composition at the outlet of the HE gas channel was also measured to further validate the model. Fig. 6.6a compares the experimental (points) and calculated (solid lines) polarization curves under inlet hydrogen electrode gas compositions $H_2O/CO_2/H_2$ molar ratios of 45/45/10. Different symbols represent repeated experiments, demonstrating the excellent reproducibility of the experimental results. Fig. 6.6b presents a comparison between experimental and predicted gas compositions measured at the outlet of the cathodic gas channel, after water removal, under different current conditions: OCV (open circuit, circle), 80 mA/cm^2 (asterisk), and 100 mA/cm^2 (triangle). Red, green, and blue symbols correspond to the molar fractions of CO, H_2, and CO_2 on a dry basis, respectively. The strong alignment between the experimental data and model predictions in both the polarization curves and gas compositions underscores the model's excellent predictive capabilities. As for the oxygen gas channel, since the feed gas contained O_2 and CO_2 in the same proportions produced by the electrochemical reaction, the outlet gas composition was

expected to remain unchanged from the inlet, a fact confirmed by the experimental results.

Thermal effects

The previous results relate to a cell operating under controlled, isothermal conditions, where the temperature was regulated by placing the cell in a furnace. However, a cell operating in a stack would be under adiabatic conditions instead of isothermal. This could lead to a non-uniform temperature distribution due to the thermal effects caused by the chemical and electrochemical reactions taking place. Specifically, these effects include:

1. Heat consumption due to the endothermic rWGS reaction.
2. Heat absorption during the endothermic electrochemical water-splitting process.
3. Joule heating generated by the flow of current through the cell's electrodes.

To investigate the potential temperature variations in an adiabatic cell, the model was expanded to account for all these thermal phenomena. The energy balance in the gas channels, which incorporates heat transfer through both convection and conduction, as well as heat absorption from the rWGS reaction in the cathodic gas, Q_0, is described by:

$$\rho c_p u \nabla T + k_g \nabla^2 T = Q_0 \tag{6.20}$$

Here, ρ, c_p, and k_g represent the gas phase's density, specific heat, and thermal conductivity, respectively. The gas density was calculated using the ideal gas law, while the specific heat and thermal conductivity were taken as constants (1.2 kJ/(kg·K) and 0.06 W/(m·K), respectively) and were assumed to be independent of the gas composition. Eq. 6.20 is solved under the boundary condition of a fixed temperature at the gas inlet

$$T = T_{in} \tag{6.21}$$

At the outlet and on the outer solid walls, a zero conductive heat flux is considered

$$-k_g \nabla T \cdot \mathbf{n}_1 = 0 \tag{6.22}$$

$$-k_g \nabla T \cdot \mathbf{n}_1 = 0 \tag{6.23}$$

Within the electrodes, the energy balance considers Joule heating, Q_{JH}, and the heat produced by the electrochemical reaction, Q_{rxn}. Since heat is transferred solely by conduction in this region, the equation governing the temperature distribution is:

$$-k_s \nabla^2 T = Q_h \tag{6.24}$$

where k_s is the effective conductivity of the electrode, and the total heat source is given by

$$Q_h = Q_{JH} + Q_{rxn} \tag{6.25}$$

Similarly, in the electrolyte, where temperature increases due to Joule heating from current flow, the heat balance equation is:

$$-k_e \nabla^2 T = Q_{JH} \tag{6.26}$$

where k_e represents the thermal conductivity of the electrolyte. The thermal conductivities of the electrolyte, hydrogen, and oxygen electrode were set equal to $0.07, 90$, and $6\ \mathrm{W/(m \cdot K)}$, respectively.

All other balance equations remain unchanged, but the temperature dependence of key model parameters has been incorporated. The effective ionic conductivity of the electrolyte matrix was fitted using the parameter values from Tab. 6.2, and is expressed as:

$$\kappa_{l,eff}^{mat} = -0.1256 + 1.960 \times 10^{-4} T \tag{6.27}$$

where T is in K and κ is in S/cm. It was also observed from Tab. 6.2 that the ratio between the effective ionic conductivities in the electrodes and the electrolyte matrix remains constant with temperature. The effective ionic conductivities in the hydrogen electrode and oxygen electrode were obtained by multiplying the matrix conductivity by 0.91 and 0.37, respectively. An Arrhenius-type expression can be used to correlate the exchange current density at the HE,

$$\ln\left(i_{0,\mathrm{HE}}^{*}\right) = 8.025 - 9126\frac{1}{T} \tag{6.28}$$

with T in K and $i_{0,\mathrm{HE}}^{*}$ in $\mathrm{A/m^2}$. The temperature dependence of the equilibrium constant for the rWGS reaction, K_{eq}, was instead taken from the literature [161] and is expressed as:

$$\begin{aligned} \ln\left(K_{eq}\right) = \frac{1}{RT}\Big(&-3.9412 \times 10^4 - 54.15156T - 5.5642 \times 10^{-2}T^2 \\ &+ 2.5760 \times 10^{-5}T^3 \\ &-7.6594 \times 10^{-9}T^4 + 1.1061 \times 10^{-12}T^5 + 18.429T\ln T\Big) \end{aligned} \tag{6.29}$$

Fig. 6.7 illustrates the temperature profiles in an adiabatic cell, where gas is supplied at 883 K, and the cell operates at an applied voltage of 1.5 V. Panels (a) and (b) show the results without and with the rWGS reaction, respectively. In panel (b) The temperature profile near the inlet section is represented by a dashed line for clarity.

The temperature profiles in Fig. 6.7a show a rise in temperature, confirming that the cell is operating at a potential higher than the thermoneutral voltage, which is 1.3 V given that the heat of the electrolysis reaction is approximately 250 kJ/mol:

$$E_{TN} = \frac{\Delta H_{rxn}}{n\mathcal{F}} \tag{6.30}$$

In contrast, the presence of the rWGS reaction leads to a temperature decrease, which is only partially compensated by Joule heating. These findings emphasize the critical role of temperature control in a cell stack and the need to monitor chemical reactions, as they can significantly affect cell temperature and, in turn, the overall system performance.

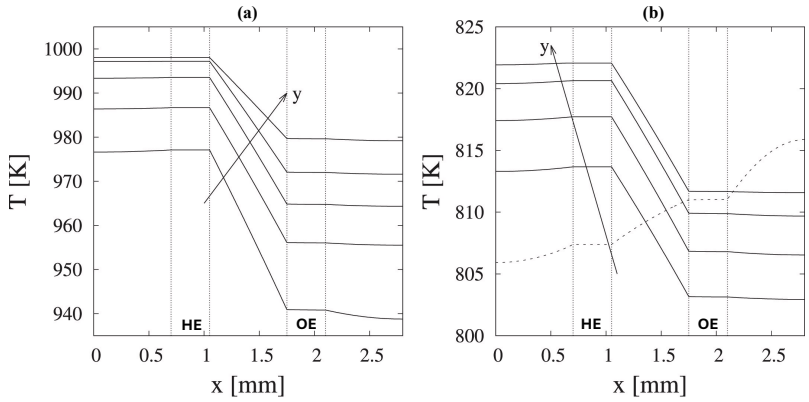

Figure 6.7. Temperature profiles in an adiabatic cell fed with gas at 883 K and operating under an applied voltage of 1.5 V. The profiles are shown for two cases: (a) without the rWGS reaction and (b) with the rWGS reaction. Curves were obtained at distances of 10, 20, 40, 60, and 90 mm from the gas inlet section. The figures are presented on different scales.

Fig. 6.8 presents the polarization curves for the isothermal cell and the adiabatic cell, both in the absence of the rWGS reaction, as well as the adiabatic cell in the presence of the rWGS reaction. The gas feed temperature was set at 883 K. It is important to note that the open circuit potential was evaluated theoretically and not adjusted. From the analysis of the reported results, several conclusions can be drawn. First, the rWGS reaction has minimal impact on the polarization curve of the isothermal cell. However, for both the isothermal and adiabatic cells, the inclusion of the rWGS reaction leads to an increase in the overpotential at a given current density. In the case of the isothermal cell, this small change is attributed to the slight consumption of hydrogen by the rWGS reaction. Conversely, in the adiabatic cell, the effect of the rWGS reaction is more significant because, in addition to consuming hydrogen, the thermochemical reaction induces a temperature decrease that negatively impacts cell performance by reducing both the rate of the electrochemical semi-reactions and the conductivity of the charged species.

It is noteworthy that, in the absence of the rWGS reaction, the primary differences in the behavior of the isothermal and adiabatic cells become apparent above the thermoneutral potential of 1.3 V. At lower potentials, the performance of the cell remains largely unaffected by whether it operates under adiabatic or isothermal conditions. This is attributed to the fact that the temperature within the cell does not vary significantly, as illustrated in Fig. 6.9. Additionally, the reduced overpotential observed when operating under adiabatic conditions and above the thermoneutral voltage is just one factor to consider when evaluating cell performance. Operating conditions that lead to increased cell temperatures may also result in thermal runaway failure.

These observations underscore the critical importance of temperature control when operating the cell stack. In the absence of an effective method to monitor temperature within the cell, analyzing the gas composition may serve as a valuable

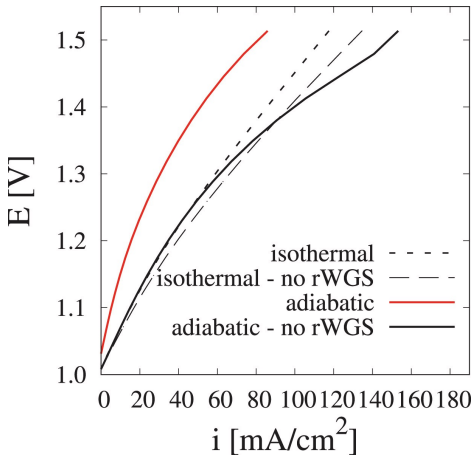

Figure 6.8. Polarization curves for the cell under isothermal conditions are shown with dashed lines, both with and without the rWGS reaction. Additionally, polarization curves for adiabatic conditions are represented by solid lines: the red solid line corresponds to the case with the rWGS reaction, and the black solid line to the case without it.

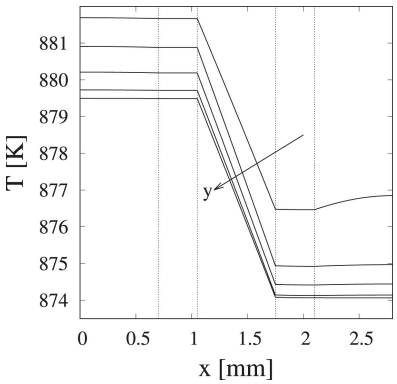

Figure 6.9. Temperature profiles in an adiabatic cell supplied with gas at 883 K and operating at an applied voltage of 1.2 V, in the absence of rWGS reactions. The profiles were recorded at distances of 10, 20, 40, 60, and 90 mm from the gas inlet section.

tool to determine if the electrochemical process is accompanied by chemical reactions, which can release heat and influence the temperature profile. The next section will indeed present the results of the experimental work conducted on the planar single cell, along with an analysis of the gas composition data obtained across a wide range of operating conditions.

6.2 Experimental study on the effect of operating conditions

This section presents the results of the first experimental campaign on the single cell focused on the systematic variation of temperature and gas composition at the hydrogen electrode (see Sec. 4.2.2). The objective of the study is to observe how changes in temperature and concentration of water and carbon dioxide at the hydrogen electrode affect the performance of the cell, including H_2 production rate, CO_2 conversion and CO formation. Specifically, starting from the reference condition 10/20/20/50% $H_2/H_2O/CO_2/N_2$, the molar fraction of water and carbon dioxide has been varied one at the time ranging from 10% to 40%, according to the test matrix detailed in Tab. 4.3. All the tests under these different compositions were repeated at 620, 650 and 680 °C. Higher temperatures can enhance gas molecule kinetics, improving mass transport and reactant distribution within the inlet channels, and decrease ohmic resistance, facilitating the electrolysis reaction. However, elevated temperatures also impact secondary reactions, including the rWGS reaction, which becomes more favorable at higher temperatures. The rWGS reaction is not only influenced by temperature but also by the composition of the gases, particularly high concentrations of CO_2 and H_2. This means that controlling the production of CO requires careful adjustment of both the temperature and the gas composition. The fact that part of the hydrogen produced by electrolysis is converted into CO represents an inefficiency in the process if the primary goal is hydrogen production. However, the scenario changes if syngas production is the desired outcome, where both hydrogen and CO are valuable products. Therefore, this study can help understand how to optimize operating conditions to either minimize CO formation for pure hydrogen production or maximize syngas yield.

Understanding the effects of both gas composition and temperature variations is not straightforward and requires a thorough evaluation of their broader influence on cell mechanisms. To achieve this, galvanostatic polarization and EIS measurements have been performed to evaluate the electrochemical performance of the cell under various operational conditions. Additionally, an in-depth analysis of the gas composition at the hydrogen electrode has been carried out to better understand the underlying reactions and their contributions to overall cell efficiency in H_2 production.

In the following sections, the results of the polarization curves and EIS measurements will first be presented. Subsequently, the gas analysis data will be discussed in light of the considerations raised before, offering a deeper understanding of the interconnection between hydrogen production and CO formation.

6.2.1 Polarization curves and EIS

The experimental campaign lasted approximately 984 hours, during which the several combinations of gas compositions and temperatures were tested. Given the prolonged duration of the experiments and the challenging conditions imposed, it was crucial to continuously monitor the electrochemical stability of the cell. To achieve this, polarization curves and EIS spectra were recorded periodically under reference conditions at 650 °C. As shown in Fig. 6.10 no significant differences were detected

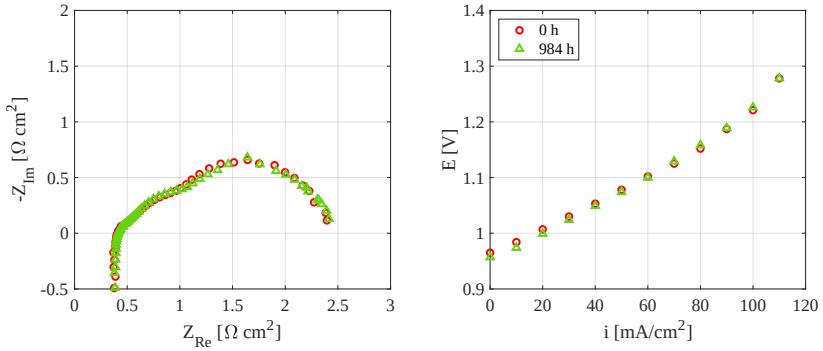

Figure 6.10. Comparison of EIS spectra (left) and polarization curve (right) before and after the experimental campaign. The electrochemical data were collected at 650 °C and reference composition (10/20/20/50% $H_2/H_2O/CO_2/N_2$).

between the initial and final moment of the experimentation, confirming the stability of cell's performance during the measurements, and validating the comparability of the experimental data.

Temperature variations

Fig. 6.11 illustrates the effect of temperature on both the EIS spectra (a)-(c)-(e) and the polarization curves (b)-(d)-(f) at constant hydrogen electrode composition. Examining the EIS spectra, it is evident that increasing temperature results in a slight reduction in the internal resistance, R_0, and a more significant decrease in the polarization resistance, R_{pol}, as detailed in Tab. 6.5. These observations indicate improvements in both charge and mass transfer processes at higher temperatures.

Table 6.5. Internal resistance (R_0) and polarization resistance (R_{pol}) of the EIS spectra reported in Fig. 6.11.

$H_2O/CO_2/H_2/N_2$		620 °C	650 °C	680 °C
20/20/10/50 %	R_0 [Ω· cm^2]	0.44	0.41	0.38
	R_{pol} [Ω· cm^2]	2.7	2.4	2.3
40/20/10/30 %	R_0 [Ω· cm^2]	0.45	0.40	0.36
	R_{pol} [Ω· cm^2]	2.5	2.3	2.1
20/**40**/10/30 %	R_0 [Ω· cm^2]	0.44	0.40	0.35
	R_{pol} [Ω· cm^2]	2.5	2.2	2.1

A similar trend is observed in the polarization curves, where the cell voltage at equivalent current densities decreases as the temperature increases. This behavior is consistent across all tested compositions. The lower cell voltages at higher temperatures suggest that operating under elevated temperature conditions enhances the electrochemical efficiency of the cell, likely due to increased ionic mobility and decreased internal resistance. Among the tested scenarios, the cell operates most efficiently at 680 °C, achieving lower voltages at the same current densities compared to the lower temperature conditions. These findings imply that MCEC

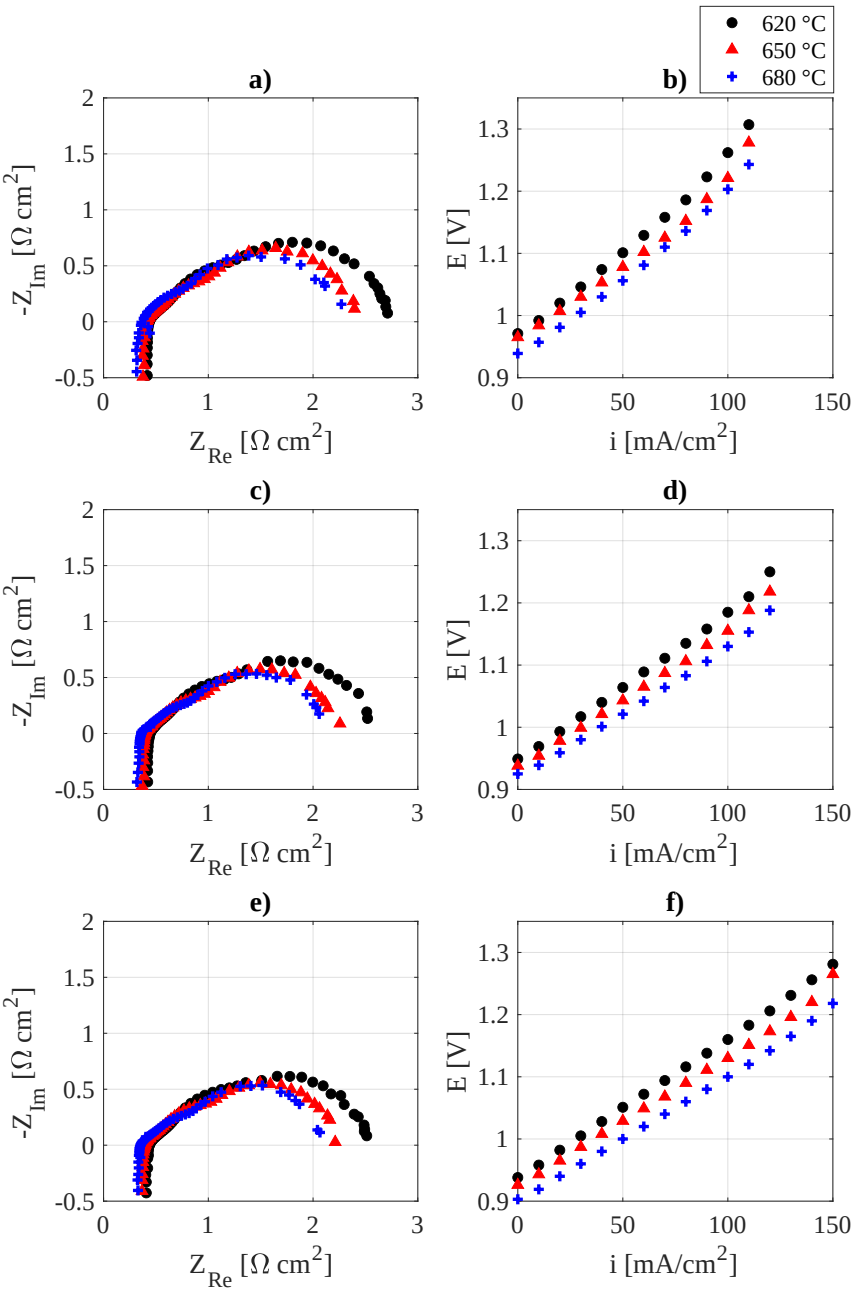

Figure 6.11. EIS spectra at OCV and polarization curves at 620, 650, 680 °Cat different hydrogen electrode composition $H_2O/CO_2/H_2/N_2$: (a)-(b) 20/20/10/50 %, (c)-(d) **40**/20/10/30 %, and (e)-(f) 20/**40**/10/30 %.

performs better under elevated temperature conditions, supporting the hypothesis that temperature is a critical factor influencing the efficiency of the cell.

However, it is important to note that the rWGS reaction is also more favorable at higher temperatures, impacting the overall gas composition at the hydrogen

electrode and, in turn, the hydrogen yield. Therefore, while the results in Fig. 6.11 suggest that molten carbonate electrolysis is favored at high temperatures, this must be evaluated in conjunction with the gas chromatography results presented later. These results will assess whether the lower potential observed at higher temperatures also corresponds to an increased hydrogen production rate at equivalent current densities.

Gas composition variations

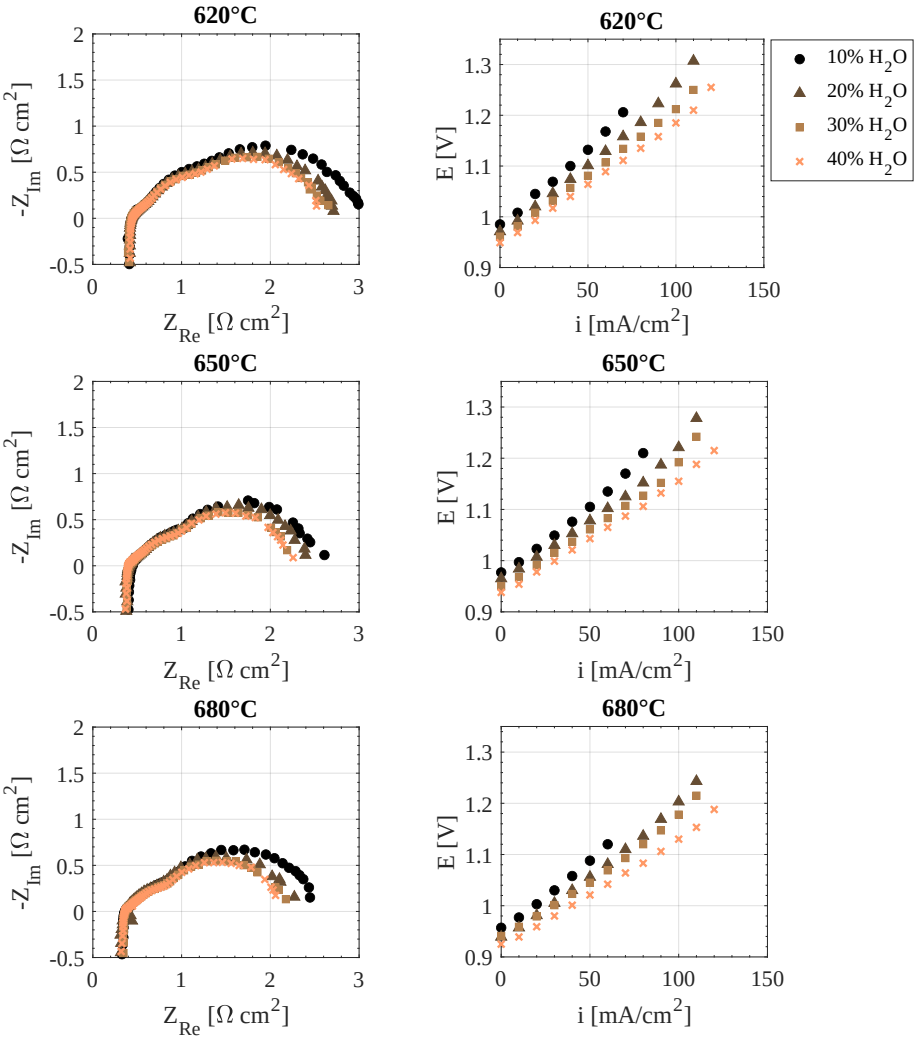

Figure 6.12. EIS spectra recorded at OCV and polarization curves for %H_2O variation, at 620, 650 and 680 °C.

Figure 6.12 and 6.13 illustrate the effects of varying H_2O and CO_2 content on electrochemical performance, respectively. In general, both the EIS spectra and polarization curves show that an increase in the molar fraction of either H_2O or CO_2, at a fixed temperature, leads to improved electrochemical performance of the

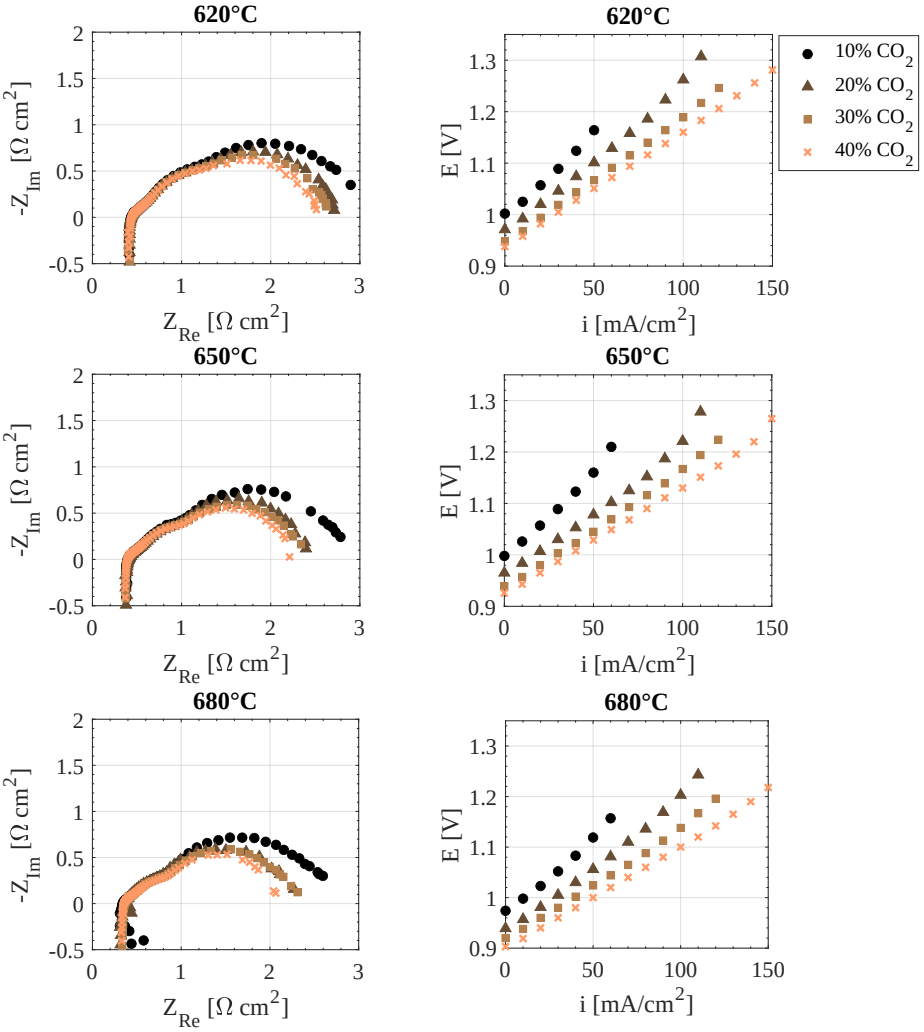

Figure 6.13. EIS spectra recorded at OCV and polarization curves for $\%CO_2$ variation, at 620, 650 and 680 °C.

cell in terms of polarization. This is reasonable, as both reactants are essential for the electrolysis reaction.

Regarding the EIS results, the graphs show that variations in gas composition do not appear to have a notable effect on the internal resistance, and thus do not significantly influence the effective conductivity of the electrolyte. It is important to note, however, that the EIS measurements were conducted on the full cell, making it impossible to isolate the contributions of the individual electrodes in this case, unlike the analysis performed on the button cell in Sec. 5.2. In contrast, R_{pol} is significantly affected by the gas composition. Specifically, the variation in CO2 content leads to a larger range of R_{pol} values compared to the variation in H2O content. For instance, at 650 °C, R_{pol} ranges from 2.21 to 2.78 $\Omega{\cdot}cm^2$ for different CO2 concentrations, whereas at the same temperature, R_{pol} varies from 2.25 to 2.61 $\Omega{\cdot}cm^2$ for different H_2O concentrations. As seen in Fig. 6.12 and 6.13, this trend can be confirmed also

at the other temperatures.

At low reactant concentrations, comparing 10% CO_2 and 10% H_2O data at constant temperature, a limited supply of CO_2 results in a more pronounced deterioration in performance. For instance, as shown in Fig.6.13 at 650 °C, the OCV value and R_{pol} are noticeably higher at 10% CO_2, measuring 0.998 V and 2.8 $\Omega{\cdot}cm^2$, respectively, compared to the other conditions tested at the same temperature, where OCV ranges from 0.938 to 0.965 V and R_{pol} varies from 2.39 to 2.21 $\Omega{\cdot}cm^2$. These findings indicate that under the given operating conditions, the concentration of CO_2 is the limiting factor for the advancement of the electrochemical reaction in a MCEC.

It is interesting to analyze what happens at high CO_2 concentrations $(30-40\%)$. Under these conditions, the water flow rate, corresponding to 20 mol% of the total, is 88 sccm. Since both CO_2 and H_2O are reactants in the hydrogen production reaction, in this case, water becomes the limiting factor. Therefore, according to Faraday's law, the maximum current applicable to the cell is approximately 110 mA/cm^2, which corresponds to a 100% conversion of the available water. However, as shown by the results in Fig. 6.13, it is possible to apply even higher currents, reaching up to 150 mA/cm^2 for cases with 40% CO_2. Thus, it is possible to achieve current densities higher than those predicted by Faraday's law and higher than those achievable in the reverse scenario, where the water content is 40%. In this latter case, while it is still possible to exceed the 110 mA/cm^2 limit (see Fig. 6.12), the slope of the polarization curve increases significantly at higher current densities, indicating a shortage of reactants in the cell.

This phenomenon can be explained by two possible mechanisms or a combination of both: i) the hydrogen produced recombines with the excess carbon dioxide via rWGS reaction, generating steam necessary to sustain the electrolysis reaction; ii) CO_2 electrolysis takes place alongside with water electrolysis, sustaining the cell's electrochemical performance,

$$2CO_2 + 2e^- \rightarrow CO + CO_3^{2-} \tag{6.31}$$

It is likely that the contribution from the rWGS reaction is the most significant due to the favorable conditions of composition, temperature, and the presence of nickel, which acts as a catalyst. Understanding whether CO_2 electrolysis also occurs is more complicated, as this reaction is inherently slow and occurs within a specific potential range, typically above 1.3 V [16, 105, 117]. Furthermore, CO_2 electrolysis is favored under well-controlled conditions characterized by a high concentration of CO_2 and H_2O, along with low concentrations of CO and H_2. However, the conditions investigated in this study do not align precisely with these requirements. The experimental results presented here are consistent with those reported by Audasso et al. [105], who concluded that the phenomenon could be explained solely by the rWGS reaction supplying additional water. However, their work does not support this conclusion with experimental gas analysis data, which is an important aspect addressed in this study. The most likely scenario is that both mechanisms contribute simultaneously, with the rWGS reaction playing a predominant role. In the following paragraph, gas chromatographic analysis data will be presented and discussed to support these findings.

6.2.2 Gas analysis results

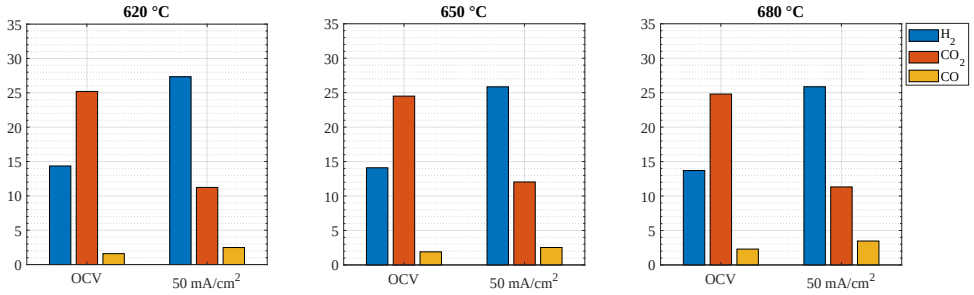

Figure 6.14. Gas composition on a dry basis of the hydrogen outlet stream measured at OCV and 50 mA/cm^2 at three different temperatures: 620, 650, and 680 °C. The inlet gas composition is $H_2O/CO_2/H_2/N_2$ 20/20/10/50 %. The nitrogen percentage is not shown in the graphs to simplify the representation.

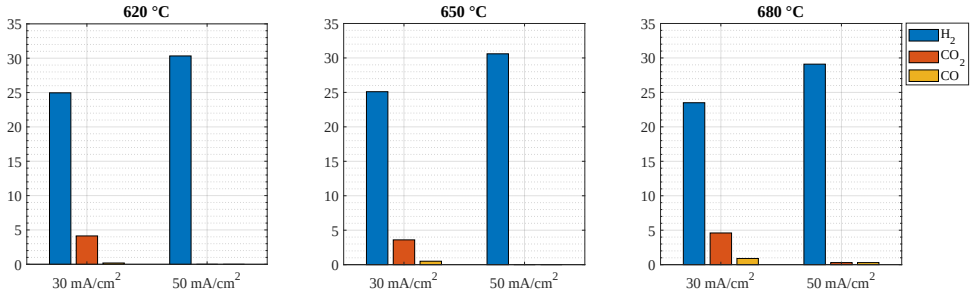

Figure 6.15. Gas composition on a dry basis of the hydrogen outlet stream measured at 30 and 50 mA/cm^2 at three different temperatures: 620, 650, and 680 °C. The inlet gas composition is $H_2O/\mathbf{CO_2}/H_2/N_2$ 20/**10**/10/60 %. The nitrogen percentage is not shown in the graphs to simplify the representation.

The gas composition of the hydrogen electrode outlet was evaluated through gas chromatography analysis as detailed in Section 4.2.2. Gas chromatography analysis was conducted on the hydrogen electrode outlet stream for all tested gas compositions and temperatures at OCV and at 50 mA/cm^2. In cases where both H_2O and CO_2 concentrations exceeded 20%, the analysis was also performed at 100 mA/cm^2. Additionally, for the cases with 40% CO_2, the analysis was conducted at 150 mA/cm^2.

Fig. 6.14 shows the dry gas composition measured at 620, 650, and 680 °C for the hydrogen outlet stream, with an inlet gas mixture of $H_2O/CO_2/H_2/N_2$ in a ratio of 20/20/10/50%. For each temperature, the graphs compare the data obtained at OCV with those at 50 mA/cm^2, corresponding to a conversion rate of 43% based on Faraday's law. The presence of CO in the outlet stream, even when no current is applied to the cell, regardless of the temperature, confirms that the rWGS reaction is occurring. Notably, the CO molar fraction increases with temperature, both at OCV and during electrolysis operation, rising from 1.6% to 2.3% at OCV and from 2.5% to 3.5% during electrolysis. Conversely, the H_2 molar fraction slightly decreases as the temperature increases, indicating that hydrogen is participating in the rWGS

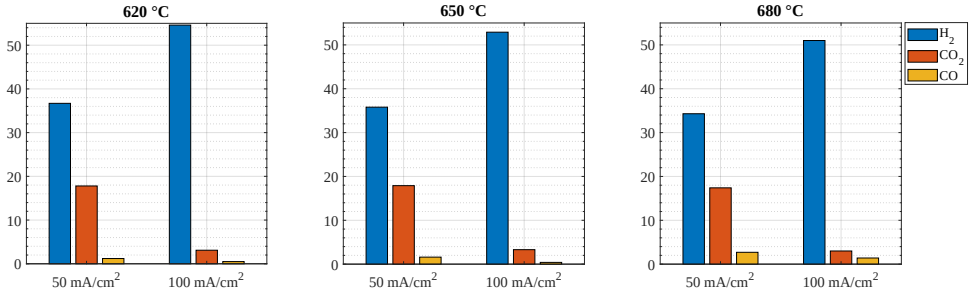

Figure 6.16. Gas composition on a dry basis of the hydrogen outlet stream measured at 50 and 100 mA/cm^2 at three different temperatures: 620, 650, and 680 °C. The inlet gas composition is $\mathbf{H_2O}/CO_2/H_2/N_2$ **40**/20/10/30 %. The nitrogen percentage is not shown in the graphs to simplify the representation.

reaction to produce CO.

In Fig. 6.15 the results obtained by feeding the hydrogen electrode with a lower CO_2 content, specifically 10%, are presented. The graphs show the gas composition at 30 and 50 mA/cm^2. In both cases, CO is nearly absent, and the hydrogen concentration is higher compared to the data in Fig. 6.14, about 30% as dry molar fraction, consistent with the earlier hypothesis regarding the rWGS reaction. Interestingly, at 620 and 650 °C, when the cell operates at 50 mA/cm^2, the CO_2 concentration drops to zero. This suggests that, under certain conditions, all the CO_2 supplied to the hydrogen electrode can be converted to carbonate ions and transported to the oxygen electrode. Consequently, the output at the hydrogen electrode is a mixture of water and hydrogen. Since water can be easily separated by condensation, the MCEC process not only facilitates CO_2 sequestration at the oxygen electrode but also allows for the production of pure hydrogen.

For the compositions containing 40% of H_2O, gas analysis was performed also at 100 mA/cm^2, as depicted in Fig. 6.16 where the data are presented alongside those obtained at 50 mA/cm^2. Once again, the CO molar dry fraction increases with higher temperatures, reaching a maximum 1.4% at 680 °C and 100 mA/cm^2. It is evident that at fixed temperature and elevated current densities, the CO decreases lower. Since the same trend is observed for CO_2, primarily due to the electrolysis reaction, it is likely that under these conditions the rWGS reaction is no longer favored, as CO_2 is also consumed as a reactant in that process. Nevertheless, these results are consistent with the findings presented before on hydrogen production trends. In this case, the H_2 dry fraction ranges between 49 and 55%, but still decreases as temperature rises. By combining the gas analysis results with the polarization curves and EIS spectra discussed earlier, it becomes clear that strong electrochemical performance in terms of polarization does not necessarily correspond to maximum hydrogen yield. Therefore, if the primary goal hydrogen production, operating at 650 °C would be more advantageous, as it offers a compromise between power consumption (linked to cell voltage) and effective hydrogen output.

Finally Fig. 6.17 presents the dry gas composition measured when the inlet gas to the HE contained 40% of CO_2. As discussed in the previous paragraph, in this case it was possible to apply current densities higher than 110 mA/cm^2, corresponding to the complete conversion of the inlet H_2O, which constituted 20% of the total

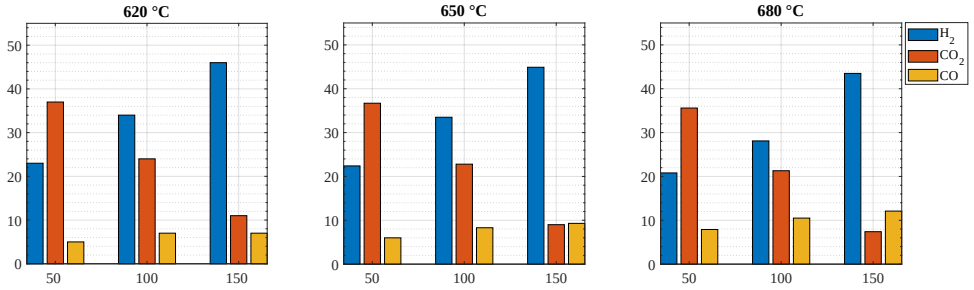

Figure 6.17. Gas composition on a dry basis of the hydrogen outlet stream measured at 50, 100 and 150 mA/cm^2 at three different temperatures: 620, 650, and 680 °C. The inlet gas composition is $H_2O/\mathbf{CO_2}/H_2/N_2$ 20/**40**/10/30 %. The nitrogen percentage is not shown in the graphs to simplify the representation.

gas mixture. Hence, the data were collected also at 150 mA/cm^2. From Fig. 6.17, increasing the current density from 100 to 150 mA/cm^2 leads to higher H_2 content and lower CO_2 percentage, indicating that electrolysis is proceeding and additional water is provided from rWGS reaction. This is further supported by the observed CO trend, which reaches 12% at 680 °C under these conditions.

The considerations here outlined were numerically validated by calculating the dry molar fractions under the assumption that both water electrolysis and the rWGS reaction occur. The reaction rate for electrolysis was determined using Faraday's law,

$$\mathcal{R}_{el} = \frac{I}{n\mathcal{F}} \tag{6.32}$$

The contribution of rWGS, denoted as $\mathcal{R}_r$, was calculated using the least squares method. The objective function is defined as:

$$\Theta(\mathcal{R}_r) = \sum_k \left(x_k^e - x_k^t\right)^2 \tag{6.33}$$

The goal is to resolve the following minimization problem:

$$\min \Theta(\mathcal{R}_r) = \sum_k \left(x_k^e - x_k^t\right)^2 = 0 \tag{6.34}$$

Here, x_k^e represents the experimentally measured dry molar fraction of the k component, while x_k^t denotes the theoretical dry molar fraction, calculated as follows:

$$x_{\mathrm{CO_2}} = \frac{F_{\mathrm{CO_2}}^{in} - \mathcal{R}_{el} - \mathcal{R}_r}{F_{dry}^{in} - \mathcal{R}_r} \tag{6.35}$$

$$x_{\mathrm{CO}} = \frac{\mathcal{R}_r}{F_{dry}^{in} - \mathcal{R}_r} \tag{6.36}$$

$$x_{\mathrm{H_2}} = \frac{F_{\mathrm{H_2}}^{in} + \mathcal{R}_{el} - \mathcal{R}_r}{F_{dry}^{in} - \mathcal{R}_r} \tag{6.37}$$

$$x_{\mathrm{N_2}} = \frac{F_{\mathrm{N_2}}^{in}}{F_{dry}^{in} - \mathcal{R}_r} \tag{6.38}$$

Table 6.6. Reverse water gas shift reaction rate calculated solving the minimization problem in Eq 6.34. The experimental data considered for the calculation were collected at 30 and 40% of CO_2, at 100 mA/cm^2 and at 620, 650 and 680 °C. The electrolysis reaction rate, $\mathcal{R}_r$, is equal to 76 sccm for all the cases.

T [°C]	$H_2O/CO_2/H_2/N_2$ % 20/**30**/10/40		20/**40**/10/30	
	$\mathcal{R}_r$ [sccm]	$\Theta(\mathcal{R}_r)$	$\mathcal{R}_r$ [sccm]	$\Theta(\mathcal{R}_r)$
620	11.7	2.5×10^{-3}	19.4	1.8×10^{-3}
650	16.4	2.5×10^{-3}	27.8	1.9×10^{-3}
680	22.56	2.4×10^{-3}	30.8	1.7×10^{-3}

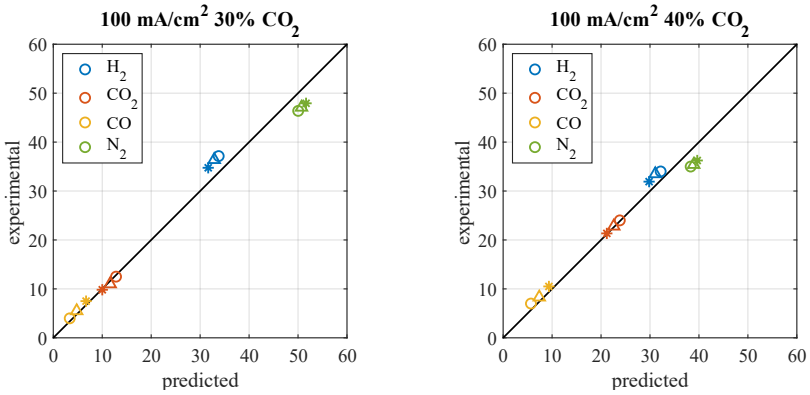

Figure 6.18. Comparison between the experimental and predicted molar fraction on dry basis of H_2 (sky blue), CO_2 (orange), CO (yellow), and N_2 (green) at 100 mA/cm^2. The left graph shows the data obtained with 30% CO_2, while the right graph represents the 40% CO_2 case. Both graphs include values measured at 620 °C(circles), 650 °C(triangles), and 680 °C(asterisks).

Table 6.6 reports the solution of the minimization problem (Eq. 6.34) for gas chromatography results obtained at 100 mA/cm^2, under two of the tested compositions: $H_2O/CO_2/H_2/N_2$% 20/**30**/10/40 and 20/**40**/10/30. The obtained value for the minimization is on the order of 10^{-3}, which is considered acceptable for this analysis. This order of magnitude remains consistent across all the cases examined. At a fixed temperature, comparing the two compositions shows that larger $\mathcal{R}_r$ values are obtained when the inlet gas contains 40% CO_2. This is expected, as the higher CO_2 concentration shifts the rWGS equilibrium towards the production of more CO. The reverse water gas shift reaction rate also increases with temperature, consistent with the observed CO percentage trend in the graphs of Fig. 6.17. Fig. 6.18 shows the comparison between the experimental and calculated molar fractions on a dry basis considering the $\mathcal{R}_r$ values reported in Tab. 6.6 and $\mathcal{R}_{el}$ according to the Faraday's law. The good agreement confirms the validity of the analysis. Obviously, with a higher concentration of CO_2, the increased contribution of the rWGS reaction reduces the effective hydrogen produced by the cell. This trend is confirmed by

the data shown in the graph, where the hydrogen output is lower for the 40% CO_2 composition compared to the 30% case. These results indicate that MCECs can be effectively used for syngas production, with the H_2/CO ratio being adjustable by modifying the inlet gas composition or operating temperature. This flexibility could be especially advantageous for coupling MCEC technology with hard to abate sectors, such as cement production or steel manufacturing. By integrating an MCEC system with such processes, the CO_2 produced could be efficiently converted into valuable products, offering a promising solution for CO_2 utilization and emission reduction.

Table 6.7. Reverse water gas shift reaction rate calculated solving the minimization problem in Eq 6.34. The experimental data considered for the calculation were collected at 40% of CO_2, at 150 mA/cm^2 and at 620, 650 and 680 °C.

T [°C]	$H_2O/CO_2/H_2/N_2$ % 20/**40**/10/30		
	$\mathcal{R}_r$ [sccm]	$\mathcal{R}_{el}$ [sccm]	$\Theta(\mathcal{R}_r)$
620	23.8	105.7	5×10^{-3}
650	31.8	114.0	2.5×10^{-3}
680	35.1	114.0	2×10^{-3}

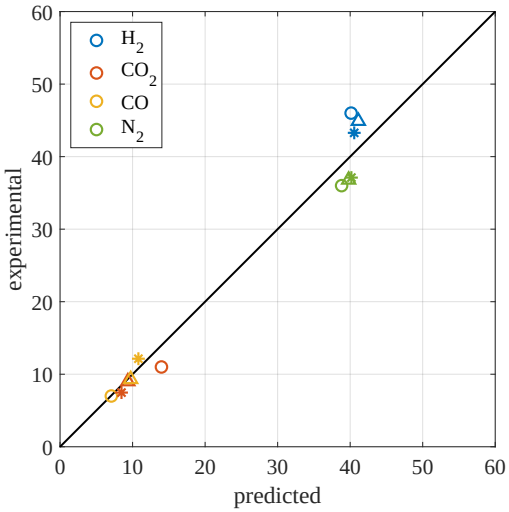

Figure 6.19. Comparison between the experimental and predicted molar fraction on dry basis of H_2 (sky blue), CO_2 (orange), CO (yellow), and N_2 (green) at 150 mA/cm^2. The graph shows the data obtained with 40% CO_2, and includes values measured at 620 °C(circles), 650 °C(triangles), and 680 °C(asterisks).

The same procedure was applied to analyze the gas compositions measured at 150 mA/cm^2 for the 40% CO_2 case. Table 6.7 provides the numerical results for each temperature. The low values of $\Theta(\mathcal{R}_r)$ indicate a good agreement between experimental and estimated molar fractions. According to Faraday's law, $\mathcal{R}_{el}$ should be equal to 114 sccm, which implies that an additional amount of water equal to 26

sccm is required for water electrolysis to occur. For the cases at 650 and 680 °C, this additional water is supplied by the rWGS reaction, at the expense of hydrogen production (see Fig. 6.19). However, at 620 °C, $\mathcal{R}_r$ is 23 sccm, meaning that a lower $\mathcal{R}_{el}$ was used for the calculations in this case. Examining the calculated molar fractions at 620 °C (circles) in Fig. 6.19, the predicted CO_2% is overestimated while the H_2 fraction is underestimated. This discrepancy could be explained by the fact that not all of the CO observed experimentally is produced by the rWGS reaction, but also by CO_2 electrolysis. In fact, according to the stoichiometry of the reaction (see Reaction 6.31), CO production via electrolysis would result in a greater consumption of CO_2, leading to an even lower CO_2 concentration than the calculated values in Fig. 6.19. In this scenario, the H_2 percentage would increase, as the contribution from the rWGS reaction would be reduced. These observations suggest that, under these conditions, CO_2 electrolysis may contribute to the overall reaction, and it is an oversimplification to assume that it cannot occur.

Resume

A 2D model for an MCEC planar cell was developed using experimental polarization curves obtained under constant composition and temperatures ranging from $570 - 650$ °C. The main assumptions were: (i) HE kinetic resistance is negligible compared to that of the OE, (ii) the exchange current density is independent of the gas composition within the electrode, (iii) the rWGS reaction occurs within the HE channel and reaches equilibrium conditions, and (iv) the cell operates at isothermal conditions. The model was validated using polarization curves and gas chromatography data obtained from a cell operated under different conditions than those used to fit the model parameters, demonstrating good predictive ability.

At this point, the model was modified to describe a cell operating under adiabatic conditions, accounting for the thermal contribution of the electrochemical reaction, the Joule effect, and the rWGS reaction. When the cell operates at a voltage higher than the thermoneutral value, the temperature can rise considerably, while at lower voltages, the endothermic contribution of the rWGS reaction causes the temperature to decrease. Moreover, the overpotential increases under adiabatic conditions compared to the isothermal case. It is due to the rWGS reaction that consumes H_2 and CO_2. These results highlight the importance of temperature control for a cell operating under adiabatic conditions and the need to explore the interdependence between electrochemical and chemical reactions.

As for this last point, the systematic experimental study conducted on the single planar cell demonstrates higher operating temperatures improve electrochemical behavior but also increase CO production and reduce H_2 yield. Generally, an increased supply of CO_2 and H_2O positively affects cell performance, resulting in lower polarization. However, higher CO_2 concentrations result in a substantial amount of CO generation, attributed to both the rWGS reaction and CO_2 electrolysis. The contribution of the rWGS reaction was confirmed by operation at higher current densities, facilitated by additional water production. In contrast, performance declined when CO_2 supply was limited, underscoring its crucial role in sustaining the electrolysis process. Nonetheless, the gas analysis indicated that complete CO_2 consumption is possible under these conditions, enabling pure hydrogen production.

Correlating electrochemical data with gas analysis is therefore fundamental for controlling MCEC operation and understanding how to maximize its efficiency, whether for pure hydrogen production or syngas generation.

Chapter 7

Integration of MCEC technology in industrial processes

This chapter delves into both experimental and theoretical analyses to explore the potential of integrating molten carbonate electrolysis with renewable energy systems and hydrogen production processes. The chapter is divided into two sections: The first part presents the results from the second phase of the experimental campaign conducted on the single cell (see Sec. 4.2.2). These tests were designed to assess the feasibility of directly coupling an MCEC with a photovoltaic (PV) system, analyzing its performance under variable load conditions. The second part provides a preliminary theoretical analysis of a potential plant scheme integrating the molten carbonate electrolyzer with the separation of the cathodic output to produce pure hydrogen. The study builds on the findings obtained in Chapter 6 on a 100 cm^2 planar cell.

7.1 MCEC coupled with PV

This section presents the results of the second part of the experimental campaign conducted on the single cell (see Sec. 4.2.2). The aim of these tests was to investigate the behavior of an MCEC directly coupled with a PV system, operating under variable load conditions. In the experimental section 4.2.2, the method for identifying the twelve typical daily power profiles, one for each month, for a 1 kW PV system has been explained. To correlate the PV power production profile with the power experimentally delivered to the cell, a polarization curve under reference conditions (i.e., 650 °C, 10/20/20/50% $H_2/CO_2/H_2O/N_2$ at the hydrogen electrode and 15/30/55% $O_2/CO_2/N_2$ at the oxygen electrode) was used as a model.

Since the PV power profiles are based on a peak power of 1 kW, these were scaled selecting a peak power value specific to match the laboratory cell requirements. The peak power was determined based on the polarization curve obtained under reference conditions (see Fig. 7.1), identifying an operating point in the ohmic region (the linear section of the curve). Thus 13 W is determined to be the maximum power deliverable by the MCEC single cell, which serves as the peak power for all subsequent experiments. The right panel in Fig. 7.1 shows the twelve PV power profiles corresponding to 13 W as peak power, which were used to power the

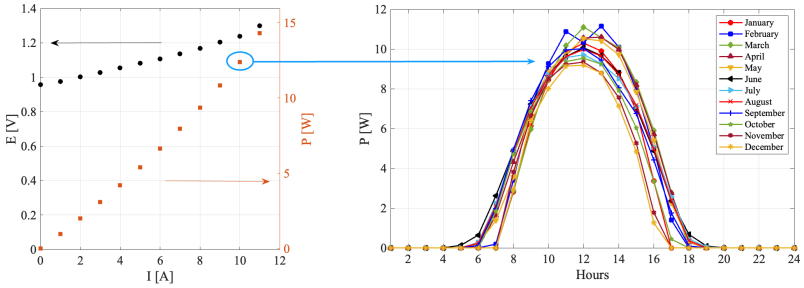

Figure 7.1. Polarization and power curves under reference conditions (left). Power profiles from twelve typical PV days, scaled down with a maximum power of 13 W for the cell (right).

single cell in electrolysis mode. In the following paragraphs, the results of the two designed experimental campaigns will be presented and analyzed. Hereafter, the first experimental campaign will be referred to as LTT1, and the second one as LTT2, where LTT stands for *Long Term Test*.

7.1.1 Results

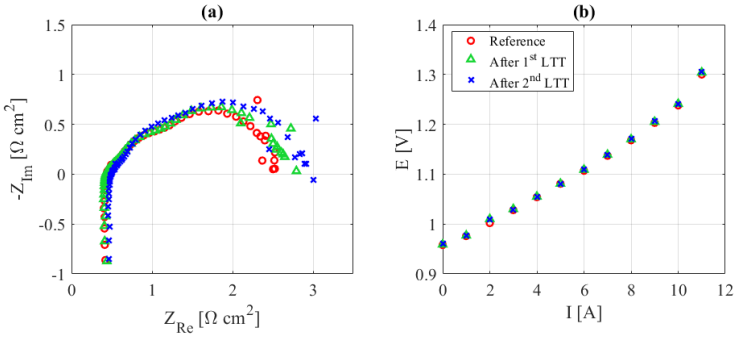

Figure 7.2. Comparison of the cell's electrochemical performance: (a) EIS and (b) polarization curves, before and after LTT1 and LTT2. Note that for the second campaign, only data from before the CO_2 shortage are reported.

The two experimental campaigns lasted overall for about 600 hours. Since the extended duration of the experiments and the stressful conditions imposed, to constantly monitor the electrochemical stability of the cell has been of primary importance. For the purpose, polarization curves and EIS spectra were recorded periodically when the no load was provided to the cell according to the simulation of the PV profile. The comparison of EIS spectra and polarization curves taken at the start and at the end of the two experimental campaigns is reported in Fig. 7.2. Note that the end of LTT2 was considered just before the simulation of the November and December load profile, due to a CO_2 shortage that occurred during the test, which compromised the cell's performance. The open-circuit voltage and the voltage recorded at 10 A are respectively 0.959 V and 1.238 V for the reference case, 0.960 V and 1.240 V, and 0.961 V and 1.241 V, at the end of LTT1 and LTT2, respectively.

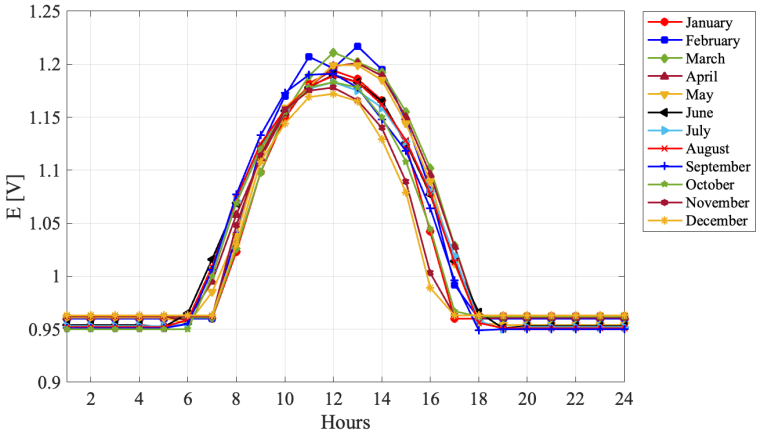

Figure 7.3. Potential profiles corresponding to LTT1, where the power profiles depicted in Fig. 7.1 were applied to the cell. These curves illustrate the cell's voltage response under varying power input conditions throughout the experiment.

Referring to the EIS spectra, the internal resistance and total resistance were at the beginning 0.43 $\Omega{\cdot}cm^2$ – 2.17 $\Omega{\cdot}cm^2$, while the corresponding values for LTT1 and LTT2 were respectively 0.43 – 2.27 $\Omega{\cdot}cm^2$ and 0.49 – 2.4 $\Omega{\cdot}cm^2$. Although a slight increase in polarization resistance is observed from the EIS spectra, this does not correspond to a significant degradation in cell performance during electrolysis, as the voltage at 10 A remains practically unchanged. This suggests that the electrochemical performance under operational conditions is stable and validates the comparability of the experimental data.

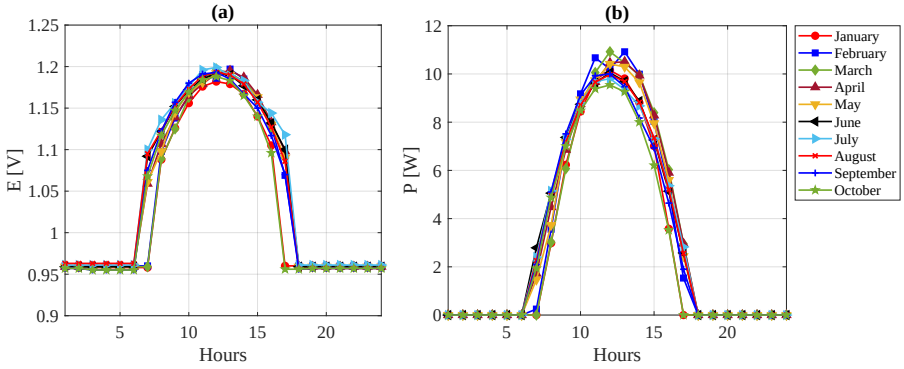

Figure 7.4. Results of LTT2: a) voltage profiles and b) power profiles. Data for November and December have not to be considered due to a shortage of CO_2 occurred during that period of testing.

Fig. 7.3 depicts the voltage profiles obtained during LTT1 providing the cell with the power profiles reported in Fig. 7.1. These results highlights minimal deviation among the monthly profiles, suggesting robust electrochemical stability under the tested conditions. This behavior is particularly notable in light of the high operational demands, as it indicates that the cell can effectively manage load

Table 7.1. The current I column shows the LTT1 results obtained for a typical day of March. Using these current values, the reaction rate was determined based on Faraday's law. Assuming a 70% conversion efficiency, the corresponding molar flow rates were then calculated and used as input for LTT2. When no current supply is expected, the flow rate is maintained constant at 400 sccm with a composition of 10/20/20/50% $H_2/H_2O/CO_2/N_2$.

Time	Results LTT1		Input LTT2			
	I [A]	Reaction rate [sccm]	$F^{c,in}_{H_2O}$ [sccm]	$F^{c,in}_{CO_2}$ [sccm]	$F^{c,in}_{N_2}$ [sccm]	$F^{c,in}_{H_2}$ [sccm]
00:00	-	-	80.00	80.00	200.00	40.00
01:00	-	-	80.00	80.00	200.00	40.00
02:00	-	-	80.00	80.00	200.00	40.00
03:00	-	-	80.00	80.00	200.00	40.00
04:00	-	-	80.00	80.00	200.00	40.00
05:00	-	-	80.00	80.00	200.00	40.00
06:00	-	-	80.00	80.00	200.00	40.00
07:00	2.77	21.09	30.13	30.13	75.31	15.06
08:00	5.40	41.02	58.60	58.60	146.50	29.30
09:00	7.42	56.38	80.55	80.55	201.37	40.27
10:00	8.50	64.64	92.34	92.34	230.86	46.17
11:00	9.12	69.36	99.09	99.09	247.72	49.54
12:00	8.77	66.69	95.28	95.28	238.19	47.64
13:00	8.42	64.02	91.45	91.45	228.63	45.73
14:00	7.21	54.77	78.25	78.25	195.62	39.12
15:00	5.36	40.71	58.16	58.16	145.39	29.08
16:00	2.71	20.61	29.44	29.44	73.60	14.72
17:00	-	-	80.00	80.00	200.00	40.00
18:00	-	-	80.00	80.00	200.00	40.00
19:00	-	-	80.00	80.00	200.00	40.00
20:00	-	-	80.00	80.00	200.00	40.00
21:00	-	-	80.00	80.00	200.00	40.00
22:00	-	-	80.00	80.00	200.00	40.00
23:00	-	-	80.00	80.00	200.00	40.00

variations without significant degradation in performance over time.

As an example, the results for the month of March during LTT1 are presented in Tab. 7.1. The first column reports the current values, based on which the reaction rate was calculated according to Faraday's law. To carry out the second LTT at fixed conversion value of 70%, the hydrogen electrode inlet flow rates were calculated based on the reaction rates obtained from LTT1. During LTT2, the current and inlet flow rates for each month were selected according to the current values obtained in LTT1, while maintaining the theoretical conversion at 70%. The new flow rates were chosen to ensure that the composition remained the same, with a constant flow rate of 400 sccm when no current supply is expected, using the reference composition of 10/20/20/50% $H_2/H_2O/CO_2/N_2$.

Finally, Fig. 7.4 shows the voltage profiles (a) and the corresponding power values (b) obtained from LTT2. As previously mentioned, a CO_2 shortage occurred during the test in correspondence of the month of November, leading to an irreparable decline in the cell performance. Even after restoring the CO_2 supply, the cell operation remained irreversibly compromised. For this reason, the data for November and December are not reported in Fig. 7.4. Nevertheless, the voltage profiles followed the expected behavior for the months from January to October, closely matching the dynamic load applied throughout these months, demonstrating the feasibility of operating under variable load and variable flow conditions.

7.1.2 Data Analysis

Despite comparing the results from LTT1 and LTT2, no immediately apparent significant differences can be observed in the electrochemical performance of the cell. However, subtle variations in performance over time may still be present, and these could potentially be critical in understanding the long-term stability and degradation processes of the cell. For this reason, the CUSUM (Cumulative Sum Control Chart) technique was adopted [163]. CUSUM is particularly suited for detecting small shifts in the data that might go unnoticed in a straightforward comparison. The CUSUM is widely known for its capability to accurately detect anomalies in a control variable, with respect to an expected value, while also having a faster response than other methods such as the Shewhart individuals control chart. The CUSUM is used in many sectors where a long time series of data has to be evaluated to be in control, such as in industrial energy management applications [164].

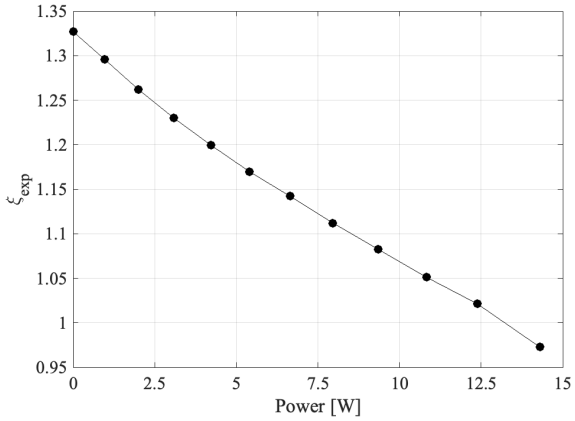

Figure 7.5. Expected efficiency of the cell as a function of the absorbed power, characterized at beginning of life.

Specifically, the CUSUM used in this work takes the cell efficiency as control variable and its definition is:

$$CUSUM(n) = \sum_{i=1}^{n} \left(\frac{\xi_M(i)}{\xi_{exp}(i)} - 1 \right) \tag{7.1}$$

where n is the progressive measurement. ξ_{exp} is the expected efficiency and is a function of the index i, depending on the cell operating set-point. The ξ_{exp} values

derive from the cell characterization at beginning of life, before the renewable-following operation (Fig. 7.5). Specifically ξ_{exp} reads:

$$\xi_{exp} = \frac{\left(\frac{I_{exp}}{2\mathcal{F}}\right) LHV}{P_{exp}} \tag{7.2}$$

where I_{exp} is the measured cell current before beginning the tests, $LHV = 2.44 \cdot 10^5$ J/mol is the hydrogen lower heating value, and P_{exp} is the measured cell absorbed power at beginning of the tests.

ξ_M is the measured cell efficiency and is defined as

$$\xi_M = \frac{\left(\frac{I_M}{2\mathcal{F}}\right) LHV}{P_M} \tag{7.3}$$

where I_M is the measured cell current during the tests of the twelve typical days, and P_M is the measured cell absorbed power during the tests. The sampling rate of the measurements consists of two samples per minute. If the measured efficiency is lower than the expected value, the CUSUM value will decrease (i.e. become more negative), indicating some degradation happening.

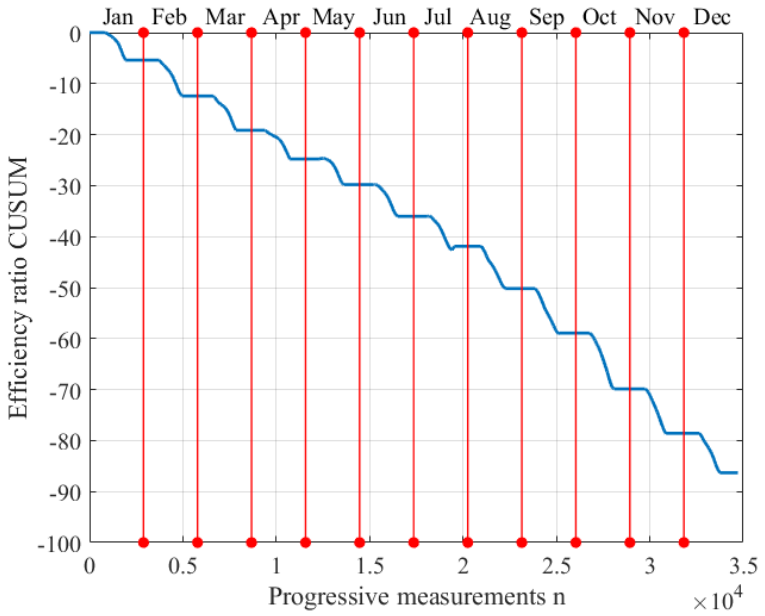

Figure 7.6. CUSUM chart obtained from the first LTT at constant flow rate.

The CUSUM was evaluated for both the long term tests carried out in this work. Figure 7.6 illustrates the the chart obtained from LTT1, where the flow rate was kept constant while changing the electric power supplied to the cell. The CUSUM exhibits a progressively negative trend, indicating a reduction in cell efficiency relative to the initial values. This steady decrease in efficiency suggests ongoing degradation over time. In the first eight months, the reduction in efficiency is gradual, with a relatively constant cumulative decline. However, in the last four months, the decline in the

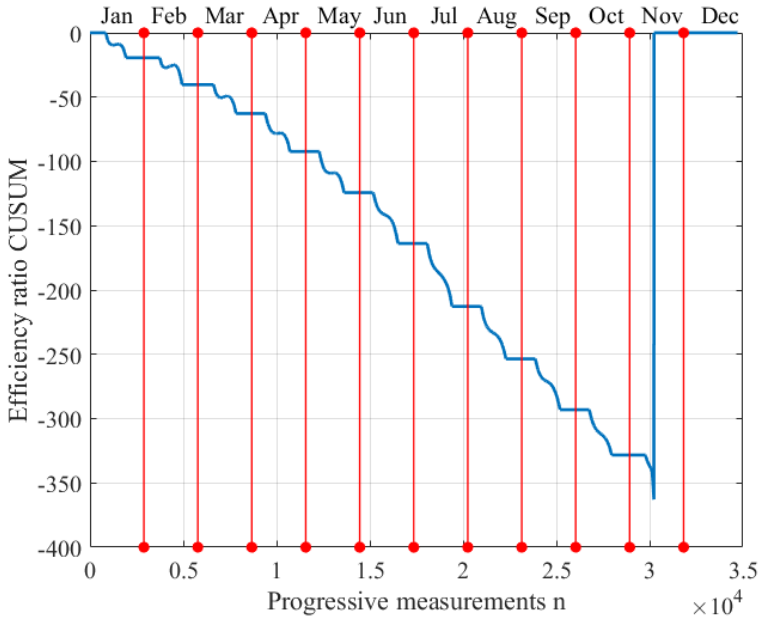

Figure 7.7. CUSUM chart obtained from the second LTT at fixed conversion. A shortage of CO_2 occurred during the test, in correspondence of the typical day of November, as indicated by the spike in the graph.

CUSUM curve becomes more pronounced, with the efficiency loss during this period being roughly equivalent to the entire drop recorded over the first eight months. This suggests that while the degradation is initially slow and uniform, it accelerates toward the end of the test. It is difficult to definitively justify this behavior, but one possible explanation lies in the power profile associated with the months from June to October, which represent the longest periods of continuous cell operation with a consistent power supply (see Fig. 7.1). This extended power input may have affected the system's stability, leading to the more pronounced performance decline observed in Fig. 7.6.

The CUSUM chart obtained from LTT2 results is depicted in Fig. 7.7. The chart clearly shows a progressive decrease in the CUSUM value as the test advances, reflecting a consistent drop in efficiency. This trend continues until mid-November, when the CO_2 shortage occurred, significantly impacting the system's performance. The CUSUM value reaches a low of -400, indicating a much wider variation range compared to the LTT1 results (see Fig. 7.6), where the CUSUM variation was limited to a smaller range. The quadruple difference in the CUSUM range indicates that the system during LTT2 faced more severe challenges in maintaining stable efficiency over time. Qualitatively analyzing the trend of the CUSUM value in Fig. 7.7, from January to May it exhibits a gradual decline, suggesting more stable conditions during the initial phase of testing. However, starting in June, the degradation accelerates more abruptly, indicating that the operational mode with variable inlet flow rates had a progressively negative impact on performance.

In conclusion, this work demonstrates that the direct coupling of a PV plant with the molten carbonate electrolyzer (MCE) is feasible, enabling the system to

absorb energy dynamically in a load-following strategy. This integration allows for optimal utilization of renewable energy sources. It has been observed that using a fixed gas composition while varying the power input is the most effective approach to maintain optimal cell efficiency over time. In contrast, employing a variable gas flowrate in line with the variable power input can negatively impact the cell's efficiency. However, this strategy may yield positive results when considering the entire Balance of Plant (BoP), as it could help balance other system components. Looking ahead, future long-term tests should focus on maintaining the cell at its thermoneutral voltage, applying the same variable power input as in previous long term tests. It would be interesting to evaluate the operation at the thermoneutral voltage because it represents the optimal operating point for an electrolysis cell, where the endothermic and exothermic contributions of the electrolysis reaction and the Joule effect balance each other out. Finally, continuous monitoring of the gases produced during the tests is essential, as it could provide a more accurate assessment of the cell's efficiency and potential degradation over time in terms of hydrogen yield.

7.2 Process analysis

This section reports a preliminary analysis of a possible plant scheme integrating the electrolysis process with the separation of the cathodic flowrate to produce pure hydrogen, and the recycling of part of the anode outlet stream. Fig. 7.8 shows the

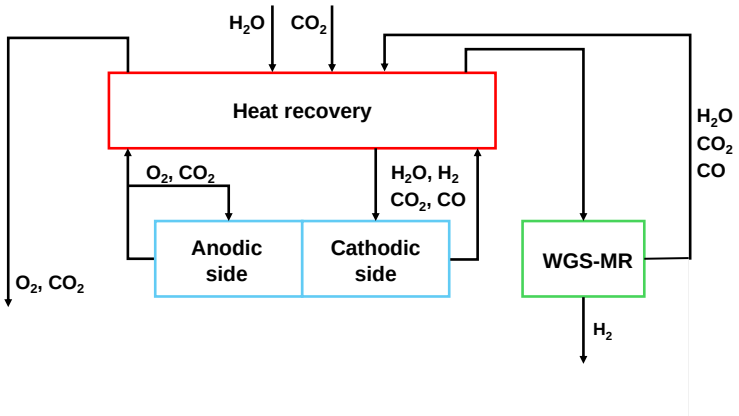

Figure 7.8. Block diagram of the analyzed process for the production of pure hydrogen by molten carbonate electrolysis.

block diagram of the analyzed process. In molten carbonate cells, besides the primary electrochemical reactions, the reverse rWGS reaction can also occur under typical operating conditions. This means that CO can be produced alongside hydrogen at the cathode. To ensure the production of pure hydrogen, it is necessary to separate not only unreacted CO_2 and H_2O, but also CO from the cathodic gas stream. The proposed process addresses this by sending the cathode gas exiting the electrolyzer to a water-gas shift membrane reactor (WGS-MR) to convert the CO present in the cathode gas into CO_2. Membrane reactors operate by selectively removing one of the reaction products as the reaction progresses, thus shifting the chemical equilibrium to favor product formation. These reactors typically use palladium-based membranes, which offer high permeability and near-perfect selectivity for hydrogen [165, 166]. This setup provides the additional benefit of producing pure hydrogen downstream of the membrane. The gas stream exiting the shift reactor can then be recycled back to the electrolysis cell after being reconditioned to the desired temperature and supplemented with CO_2 and H_2O. In addition, a small amount of CO is introduced into the cathode feed along with hydrogen to maintain a reducing environment at the cathode. Meanwhile, the anodic outlet flowrate can be split into two streams: one to be recirculated to the electrolyzer, and the other potentially directed to a process for separating O_2 and CO_2, or to an oxy-combustion process. However, the treatment of the cathodic outlet flowrate is beyond the scope of the present study.

The process flowsheet was implemented using AVEVA PRO/II software in order to identify suitable operating conditions to achieve pure hydrogen production while minimizing external energy demand. Specifically, simulations have been carried out by varying the operating potential of the electrolyzer. The implemented flowsheet is shown in Fig. 7.9. In the following two sections, the flowsheet will be explained in

Table 7.2. Operating conditions of the molten carbonate electrolyzer.

	Cathode inlet	Anode inlet
T [°C]	590	
P [atm]	3	
F [kmol/h]	15	30
y_{CO_2}	0.4	0.67
y_{CO}	0.01	-
y_{H_2}	0.19	-
y_{H_2O}	0.4	-
y_{O_2}	-	0.33

detail. The first section will focus on the electrolysis process, while the second section will address the treatment of the cathodic outlet stream, including the membrane shift reactor, to produce pure hydrogen.

7.2.1 Electrolysis process

The molten carbonate electrolyzer has been modeled using a fixed conversion reactor (R1 in Fig. 7.10) to represent the electrolysis reaction, coupled with an equilibrium Gibbs reactor (R2) to simulate the rWGS reaction that occurs on the cathode side in practice. Table 7.2 summarizes the operating conditions proposed for the electrolyzer. The anode feed consists of a mixture of oxygen and carbon dioxide in a 1:2 molar ratio, which corresponds to the ratio in which they are produced in the anodic half-reaction. Thus, part of the anodic outlet flowrate can be directly recycled to the electrolyzer. In reactor R1 the water conversion for the electrolysis reaction has been fixed according to the Faraday law,

$$X_{el} = \frac{I}{\mathcal{F} n F^{in}_{H_2O}} \tag{7.4}$$

For each operating potential considered in the simulations, the corresponding current value I was evaluated through the 2D model described in Section 6.1.2, considering a stack constituted by 140 cells of 8100 cm^2. Fig. 7.11 illustrates the polarization curve generated by the model under the operating conditions outlined in Tab. 7.2. It also presents the potential values at which the simulations were conducted, along with the respective conversion values for the electrolysis reaction, evaluated according to Equation 7.4.

Returning to the flowsheet in Fig. 7.10, the *stream calculator* SC1 functions as the matrix that separates the anodic gas (F_AN in Fig. 7.10) from the cathodic gas (F_CAT). Additionally, the calculator evaluates the flow rates of CO_2 and O_2 in the cathodic outlet stream, based on the inlet water flow rate and the conversion X_{el} fixed in R1, on the basis of the following relationships

$$F^{a}_{O_2} = F^{a,in}_{O_2} + \frac{X_{el}}{2} \cdot F^{c,in}_{H_2O} \tag{7.5}$$

$$F^{a}_{CO_2} = F^{a,in}_{CO_2} + X_{el} \cdot F^{c,in}_{H_2O} \tag{7.6}$$

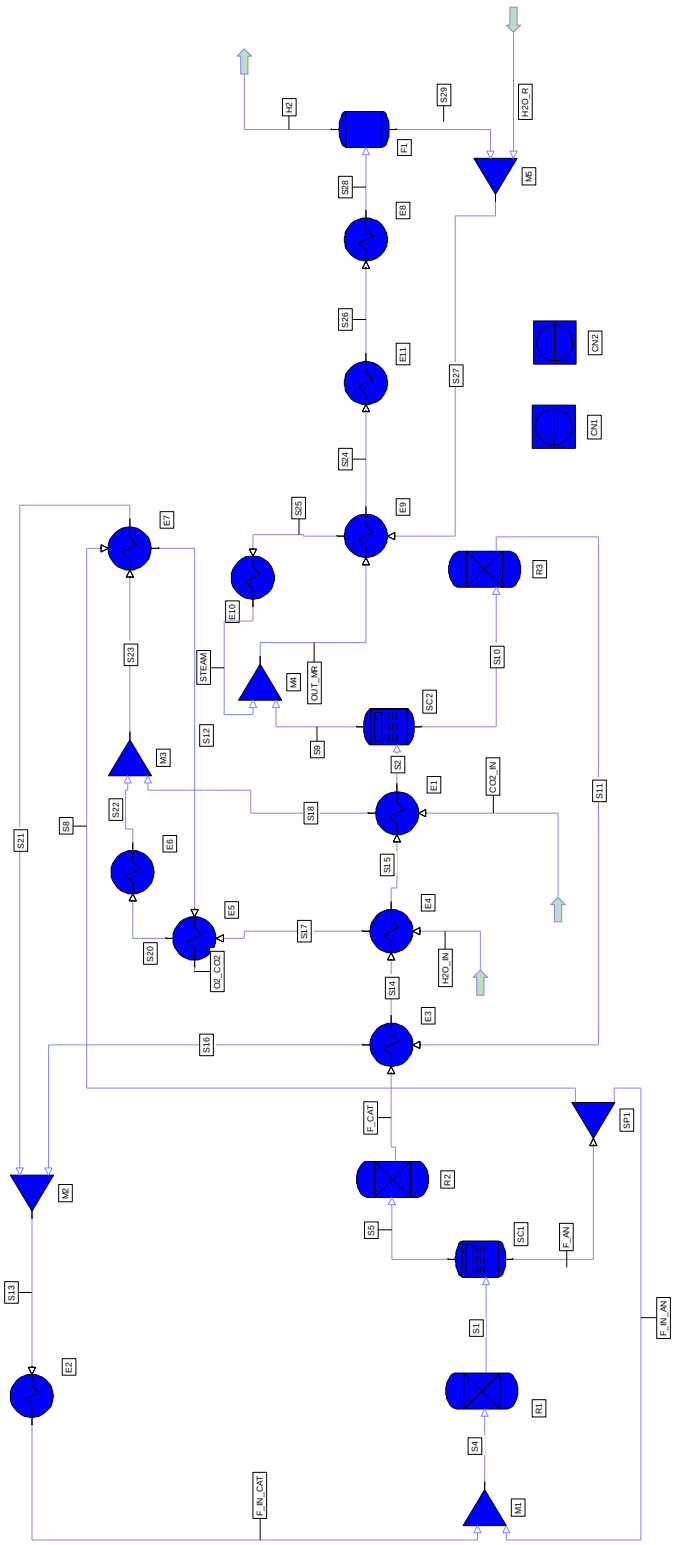

Figure 7.9. Flowsheet developed using AVEVA PRO/II software to investigate pure hydrogen production through molten carbonate electrolysis.

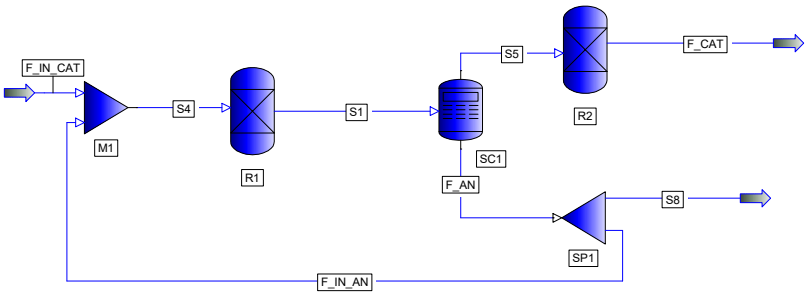

Figure 7.10. Simulation in PRO/II of the electrolyzer, where R1 simulates the water electrolysis reaction and R2 simulates the rWGS reaction occurring only on the cathodic side.

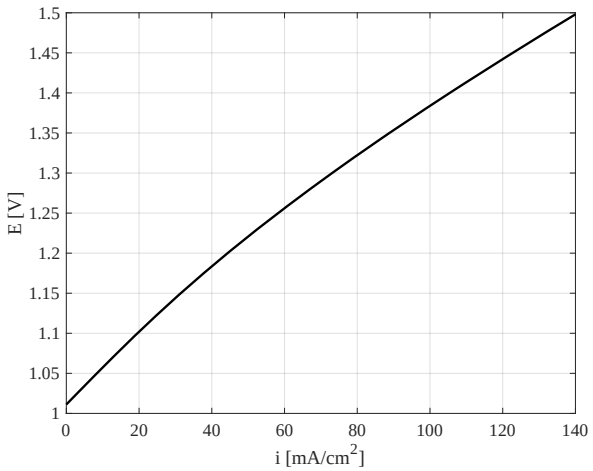

E [V]	X_{el}
1.5	0.496
1.475	0.464
1.45	0.427
1.4	0.372
1.35	0.312
1.3	0.258

Figure 7.11. Simulated polarization curve under the operating conditions detailed in Table 7.2, obtained using the model described in Section 6.1.2. The table shows the potential values at which the simulations were conducted and the respective conversion values evaluated according to Equation 7.4.

Table 7.3. Equilibrium conversion values for rWGS reaction evaluated through Gibbs reactor (R2 in Fig. 7.10) in AVEVA/PROII software.

E [V]	X_{rWGS}
1.5	0.144
1.475	0.144
1.45	0.143
1.4	0.140
1.35	0.136
1.3	0.131

where the superscript a indicates the flowrate specifically at the anode, distinguishing from the CO_2 cathodic flowrate.

As explained before, part of the anode gas is recirculated to the electrolyzer inlet, while the remaining portion is subjected to heat recovery. The other stream exiting from SC1, representing the cathode gas, is sent to a Gibbs reactor (R2), which is designed to simulate the reverse water-gas shift reaction that, in practice, takes place in the cathode gas channel of the electrolyzer. It is reasonable to assume that under these conditions, the rWGS reaction reaches equilibrium. The resulting stream, F_CAT, represents the cathode gas leaving the cell, and its composition can be determined through the following mass balances:

$$F^{c}_{\mathrm{H_2}} = F^{c,in}_{\mathrm{H_2}} + X_{el} \cdot F^{c,in}_{\mathrm{H_2O}} - X_{rWGS} \cdot F^{c,in}_{\mathrm{CO_2}} \tag{7.7}$$

$$F^{c}_{\mathrm{CO_2}} = F^{c,in}_{\mathrm{CO_2}} - X_{el} \cdot F^{c,in}_{\mathrm{H_2O}} - X_{rWGS} \cdot F^{c,in}_{\mathrm{CO_2}} \tag{7.8}$$

$$F^{c}_{\mathrm{H_2O}} = F^{c,in}_{\mathrm{H_2O}} - X_{el} \cdot F^{c,in}_{\mathrm{H_2O}} + X_{rWGS} \cdot F^{c,in}_{\mathrm{CO_2}} \tag{7.9}$$

$$F^{c}_{\mathrm{CO}} = F^{c,in}_{\mathrm{CO}} + X_{rWGS} \cdot F^{c,in}_{\mathrm{CO_2}} \tag{7.10}$$

where X_{rWGS} is defined as

$$X_{rWGS} = \frac{F^{in,c}_{\mathrm{CO}} - F^{c}_{\mathrm{CO}}}{F^{c,in}_{\mathrm{CO_2}}} \tag{7.11}$$

Tab. 7.3 shows the equilibrium conversion values obtained for the different potential values considered in the simulations.

7.2.2 WGS Membrane reactor

To recirculate the cathodic stream directly into the electrolyzer, it is necessary to remove the produced carbon monoxide and recover the hydrogen. For this purpose, the cathodic stream is sent to a water gas shift membrane reactor. This type of reactor combines a chemical reaction with product separation, providing significant advantages. The membrane enables very high conversions since the removal of one product shifts the reaction equilibrium to the right, favoring further conversion.

Fig. 7.12 depicts the flow sheet section related to the WGS-MR, to which the cathodic gas is fed after being cooled. Inside the reactor, the WGS reaction takes

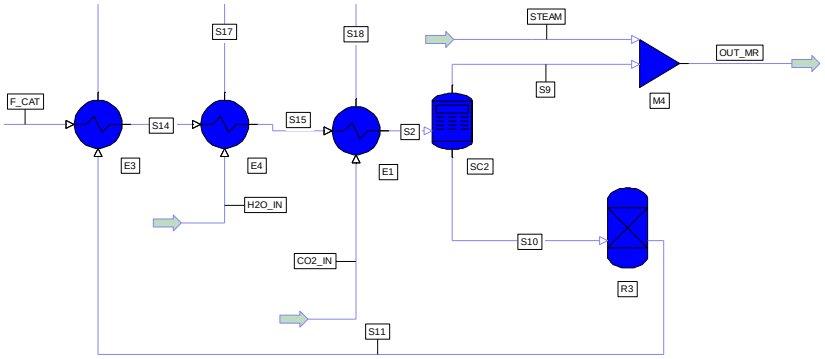

Figure 7.12. Part of the flow sheet related to treating of the cathodic stream for CO conversion and hydrogen recovery through the membrane-based WGS process. S11 is the stream recirculated to the electrolyzer, while OUT_MR, is the permeate stream containing hydrogen.

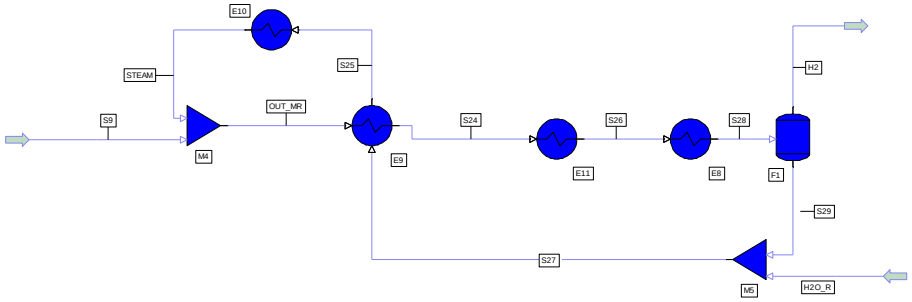

Figure 7.13. Part of the flow sheet related to the steam cycle, used as sweep gas into the WGS-MR. OUT_MR is the permeate stream exiting the WGS-MR.

place, converting CO into CO_2. Hydrogen is recovered within the reactor using palladium-based membranes, which are capable of selectively removing H_2 with high efficiency. The reaction is simulated through another Gibbs reactor (R3 in Fig. 7.12), where the temperature is set to 350 °C. The output stream is then brought back to the electrolyzer operating temperature, with water and carbon dioxide added to compensate for the consumed reactants, and recirculated into cathode inlet. The makeup streams of CO_2 and H_2O are assumed to be available at 25 °C and 3 atm.

The SC2 calculator functions as the membrane, separating hydrogen from the rest of the mixture. It also regulates the flow rate of hydrogen to be removed (the S9 stream in the diagram) so that, at equilibrium, all the carbon monoxide previously produced in the electrolyzer is converted. This allows the retentate stream from the shift reactor (S11) to be recirculated to the cathode inlet of the electrolyzer without reducing its performance due to the presence of CO. The total flow rate of pure hydrogen that can be theoretically produced is therefore equal to

$$F_{\mathrm{H_2}} = X_{el} \cdot F^{in}_{\mathrm{H_2O}} \tag{7.12}$$

Steam has been selected as the sweep gas due to its easy separation from hydrogen by condensation. Fig. 7.13 illustrates the sweep gas cycle flow diagram. The stream

OUT_MR, containing the hydrogen permeated through the membrane along with the sweep gas, is cooled to 10 °C to condense the water. The condensed water is then separated from the hydrogen via a flash drum, and after replenishment, it is vaporized and recirculated back to the WGS-MR.

7.2.3 Results and discussion

Table 7.4. Data relative to gas flow when the elctrolyzer operates at 1.5 V.

Stream	T [°C]	Flow rate [kmol/h]	CO [%]	CO_2 [%]	H_2O [%]	H_2 [%]	O_2 [%]
F_IN_CAT	590	15	1	40	40	19	-
F_CAT	590	12.04	8.45	17.95	32.35	41.25	-
F_IN_AN	590	30	-	66.67	-	-	33.33
F_AN	590	34.46	-	66.67	-	-	33.33
S8	590	4.46	-	66.67	-	-	33.33
F_AN_COLD	350	4.46	-	66.67	-	-	33.33
CO2_O2	150	4.46	-	66.67	-	-	33.33
S14	475	12.04	8.45	17.95	32.35	41.25	-
S15	419	12.04	8.45	17.95	32.35	41.25	-
F_CAT_COLD	350	12.04	8.45	17.95	32.35	41.25	-
H2O	25	2.98	-	-	100	-	-
S3	132	2.98	-	-	100	-	-
S22	137	2.98	-	-	100	-	-
CO2	25	2.98	-	100	-	-	-
S1	259	2.98	-	100	-	-	-
S21	395	5.96	-	50	50	-	-
S13	452	15	1	40	40	10	-
OUT_WGS	350	9.05	1.56	33.42	33.42	31.6	-
OUT_MR	248	5.04	-	-	41	59	-
STEAM	130	2.07	-	-	100	-	-
H2	10	3	-	-	1	99	-
S29	10	2.04	-	-	100	-	-
H2O_R	25	3×10^{-2}	-	-	100	-	-

Figure 7.14 shows a simplified scheme of the entire process and the characteristics of the main streams for the case at 1.5 V are detailed in Tab. 7.4. Table 7.5 reports the energy consumption of the electrolyzer, along with the hydrogen production rate for each of the cases considered. Note that P_{el} represents the electric power required by the electrolyzer, calculated as:

$$P_{el} = n\mathcal{F}EF_{\mathrm{H_2}} \tag{7.13}$$

$P_{el}^{\text{PRO II}}$, on the other hand, is the duty of the electrolyzer (R1) obtained from the simulations, accounting for the fact that the electrolysis reaction is overall exothermic (the considered potential values are above the thermoneutral point, i.e. about 1.28 V).

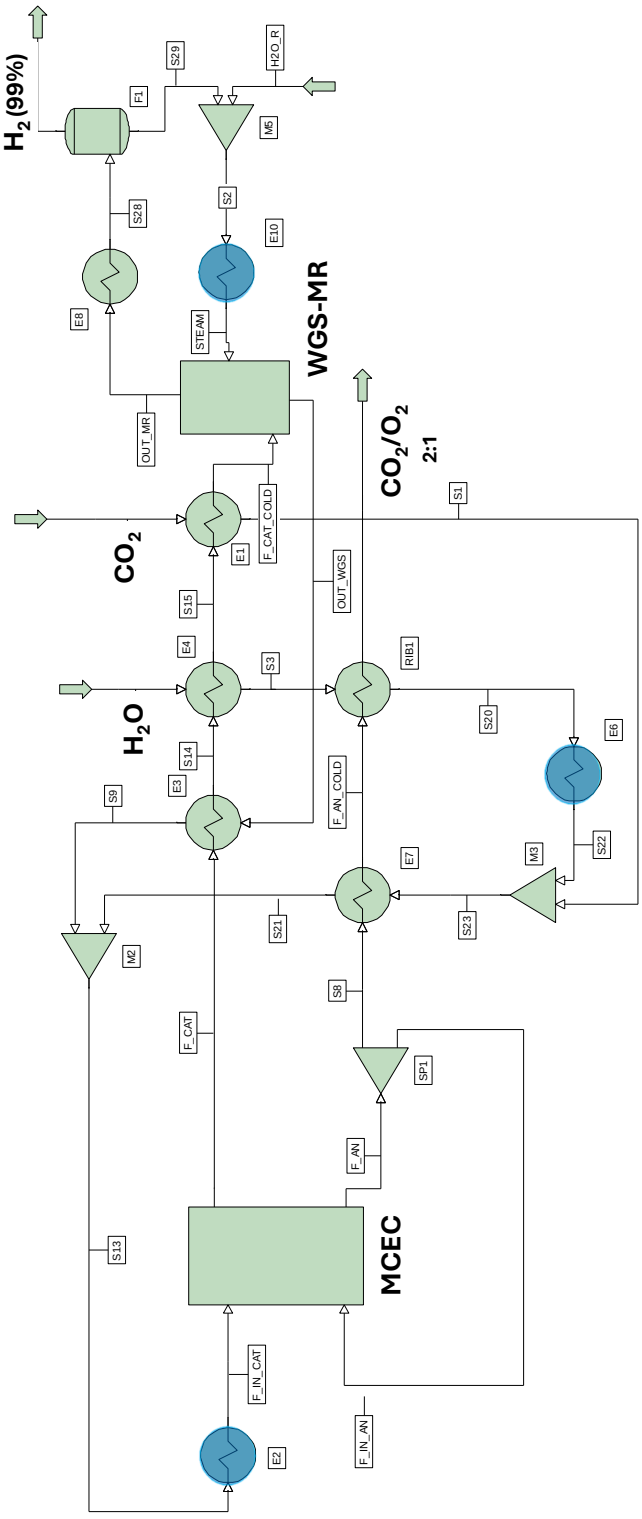

Figure 7.14. Simplified flow sheet of the process. The blue-marked heat exchangers represent the heat sources of the process (see Tab. 7.6).

In the heat balance for the electrolyzer, the contribution of the rWGS reaction, which is endothermic and occurs in the cathodic compartment, must also be considered. This has been evaluated considering the duty of reactor R2. Therefore, the heat balance for the electrolyzer can be expressed as follows:

$$\Delta Q_{el} = P_{el} - P_{el}^{\text{PRO II}} - Q_{rWGS} \tag{7.14}$$

From the results in Tab. 7.5, it can be observed that Q_{rWGS} decreases only slightly with the reduction in voltage. Consequently, for lower values, such as 1.35 V and 1.3 V, ΔQ_{el} becomes negative, meaning that additional heat must be supplied to the electrolyzer to maintain a constant temperature.

Table 7.5. Energy consumption of the electrolyzer and corresponding hydrogen production rate at different potentials. A positive or negative ΔQ_{el} indicates exothermic or endothermic behavior, respectively, considering electrolysis and rWGS reactions, as well as the Joule effect.

E [V]	P_{el} [kW]	$P_{el}^{\text{PRO II}}$ [kW]	Q_{rWGS} [kW]	ΔQ_{el} [kW]	F_{H_2} [kmol/h]
1.50	239.28	204.31	8.69	26.28	2.98
1.475	219.96	191.14	8.69	20.13	2.78
1.45	199.52	175.83	8.64	15.05	2.57
1.40	168.14	153.25	8.42	6.47	2.24
1.35	136.06	128.53	8.14	−0.61	1.88
1.30	108.43	106.28	7.83	−5.68	1.56

Referring back to the diagram in Fig. 7.14, the heat exchangers marked in blue represent the external heat source of the process: E2 compensates for the heat that cannot be provided to the cathodic feed by thermal recovery, while the other two are intended to complete the vaporization of water. E6 is necessary for the replenishment intended for the electrolyzer, and E10 is required to generate the steam used as sweep gas in the WGS-MR. It should be noted that heating the cathodic feed up to 590 °C will require the use of a furnace, an electric heat exchanger, or coupling the process with a solar concentrating plant. The corresponding heat duties are listed in Table 7.6. The table also reports the energy input required to cool the outlet stream from the membrane reactor to achieve 99% pure hydrogen and the value of ΔQ_{el} in the case where the electrolysis process is endothermic.

A brine refrigeration cycle has been hypothesized for thes cooling process. The work required by the cycle was calculated using the coefficient of performance (COP):

$$COP = \frac{Q_1}{L} = \frac{T_1}{T_2 - T_1} \tag{7.15}$$

where Q_1 is the heat adsorbed by the refrigeration cycle, L is the required work, T_1 is the outlet temperature (10 °C), and T_2 is the inlet temperature (83 °C in this case). The COP expression in Eq. 7.15 refers to ideal conditions, and in this work, an efficiency factor of 0.75 has been applied. From the values reported in Tab. 7.5 and 7.6 it is possible to calculate the gross efficiency of the hydrogen production

Table 7.6. Required power of the heat exchangers highlighted in Fig. 7.14, power required by the refrigeration cycle, and the amount of thermal energy required by the electrolyzer.

E [V]	E2 [kW]	E6 [kW]	E10 [kW]	ΔQ_{el} [kW]	Q_{tot} [kW]	L [kW]	$Q_{tot}+ L$ [kW]
1.50	23.97	22.34	23.56	-	69.86	14.52	84.38
1.475	22.47	20.97	22.00	-	65.44	13.58	79.02
1.45	20.72	19.22	20.33	-	60.28	12.51	72.79
1.40	18.08	16.83	17.78	-	52.69	10.93	63.62
1.35	15.25	14.14	14.92	0.61	44.92	9.18	54.09
1.30	12.67	11.72	12.33	5.68	42.40	7.56	50.00

process:

$$\xi = \frac{F_{\mathrm{H_2}} HHV}{Q_{tot} + L + P_{el}} \tag{7.16}$$

where HHV is the higher heating value of H_2, equal to 283.4 MJ/kmol. Similarly, it is possible to evaluate a thermodinamic efficiency, considering the higher value of electricity compared to thermal energy, assuming an electrical efficiency ξ_e of 40%:

$$\xi_{tc} = \frac{F_{\mathrm{H_2}} HHV}{Q_{tot} + L + \dfrac{P_{el}}{\xi_e}} \tag{7.17}$$

Finally, Tab. 7.7 and Fig. 7.15 shows the values of the efficiencies calculated at different operating voltages with the corresponding hydrogen production rate.

Table 7.7. Gross and thermodynamic efficiencies evaluated according to Eq. 7.16 and 7.17.

E [V]	ξ [%]	ξ_{tc} [%]	$F_{\mathrm{H_2}}$ [kmol/h]
1.50	72.4	34.3	2.98
1.475	73.3	34.9	2.78
1.45	74.1	35.3	2.57
1.40	76.1	36.5	2.24
1.35	77.9	37.6	1.88
1.30	77.3	38.2	1.56

The results shown demonstrate that the gross efficiency of the hydrogen production process increases as the operating voltage decreases. This trend is primarily due to the reduced electrical input required at lower voltages, which directly impacts the overall energy consumption of the process. However, the thermodynamic efficiency exhibits a slightly different behavior. While it also increases with decreasing voltage, the difference between the gross efficiency and the thermodynamic efficiency becomes more pronounced. This is because the contribution of electricity, which is considered more valuable than thermal energy, becomes more significant at lower voltages.

This analysis highlights the importance of carefully balancing the electrical nd thermal inputs to maximize efficiency in hydrogen production processes. Operating

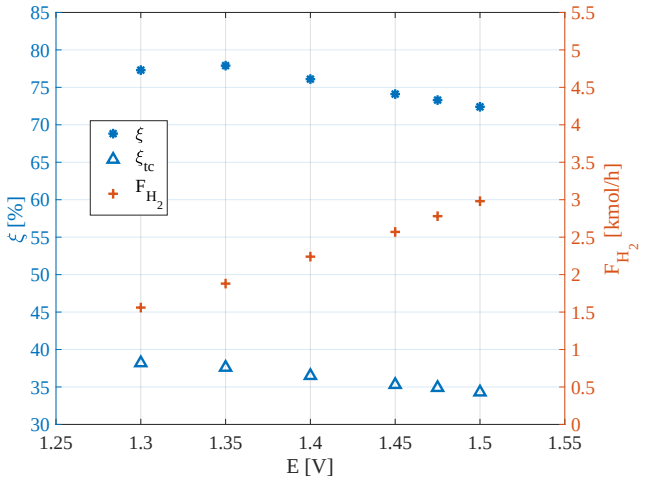

Figure 7.15. Gross and thermodynamic efficiencies detailed in Tab. 7.7.

at lower voltages can improve both gross and thermodynamic efficiencies, though additional heat must be supplied to maintain the electrolyzer's temperature, as evidenced by the endothermic behavior at 1.35 V and below. A potential optimal choice could be to find a compromise between achieving high efficiency and the ability to operate the electrolyzer isothermally, thereby simplifying the overall process. This balance could help reduce operational complexities and enhance the sustainability of hydrogen production.

Chapter 8

Fuel-assisted electrolysis in molten carbonate cells: first attempts

In this chapter, the results of the experimental campaign conducted at the Royal Institute of Technology (Stockholm) will be presented. The campaign aimed to investigate the concept of fuel-assisted electrolysis in molten carbonate cells, a mechanism that, to date, has only been demonstrated in solid oxide electrolysis cells. The first section will introduce and explain the principle of fuel-assisted electrolysis in detail. Following this, a brief description of the experimental setup and the campaign itself will be provided. Finally, the results will be presented and analyzed, offering insights into the potential of this approach for MCECs.

8.1 Introduction to fuel-assisted electrolysis

Water is best electrolyzed at high temperatures ($700 - 900$ °C) where the chemical potential necessary to separate the water into hydrogen and oxygen is lower. In addition, the high temperature accelerates the reaction kinetics, reducing the energy loss due to electrode polarization and increasing the overall system efficiency. However, despite these advantages, the cost of electricity remains a significant challenge. Around $50 - 70\%$ of the total cost of hydrogen production via electrolysis comes from electricity [167]. To make electrolytic hydrogen competitive with steam methane reforming process, it is crucial to reduce the electrolyzer power consumption. Unfortunately, this is limited by the thermodynamics of water decomposition, which sets a high baseline for the energy required in the process. As a result, innovations or alternative solutions are needed to address this constraint.

In conventional SOECs, the cathode side, where water is decomposed, is typically fed with a steam-hydrogen mixture, while the anode side is supplied with air. At zero current, the system reaches an open-circuit voltage of approximately $0.8 - 0.9$ V, though this value can vary based on the hydrogen-to-steam ratio and the operating temperature. To initiate electrolysis, a voltage greater than the open-circuit voltage must be applied to pump the oxygen from the steam side (cathode) to the oxygen side (anode). A significant portion of the electrical power is consumed in overcoming

the high chemical potential gradient for oxygen. Reducing power requirement is, therefore, a key challenge for improving process efficiency.

One strategy to reduce the open-circuit voltage and, consequently, the electricity consumption, is to circulate natural gas on the anode side. The reducing properties of natural gas lower the chemical potential difference between the two sides of the electrolyzer, thus decreasing the energy needed to drive the reaction. Considering a solid oxide electrolyzer, the half cell reaction in the cathode side in both conventional and fuel-assisted (FA) electrolysis process is:

$$H_2O + 2e^- \rightarrow H_2 + O^{2-} \tag{8.1}$$

The half cell reaction in anode of SOEC is:

$$O^{2-} \rightarrow \frac{1}{2}O_2 + 2e^- \tag{8.2}$$

As for FA electrolysis operation using CH_4 as assisting-fuel, the half cell reaction in anode (when fully oxidized) is:

$$\frac{1}{4}CH_4 + O^{2-} \rightarrow \frac{1}{4}CO_2 + \frac{1}{2}H_2O + 2e^- \tag{8.3}$$

While if considering the partial oxidation,

$$CH_4 + O^{2-} \rightarrow CO + 2H_2 + 2e^- \tag{8.4}$$

It is necessary to point out that any other fuel or compound that can be oxidized can be envisaged, including no hydrogen-containing gas such as CO or NH_3.

The introduction of fuel to the anode of solid oxide electrolysis cells (SOECs) was pioneered by Pham et al. [168], who demonstrated that methane as a reducing gas could reduce the operating potential by nearly 50%. Subsequent experiments showed even larger reductions, with decreases in operating potential reported to reach up to one order of magnitude. Additionally, these studies uncovered the potential for co-generation of hydrogen and electricity, or even synthesis gas, further highlighting the versatility of FASOECs [169, 170].

The stability and performance of different electrode materials have been extensively studied under various reducing gases, including hydrogen, carbon monoxide, and methane. Control over fuel supply has emerged as a key factor for optimizing performance. For instance, in hydrogen-assisted systems, an insufficient fuel supply can negate the advantages of fuel-assisted operation, while in methane-assisted electrolysis, the electro-oxidation of hydrogen governs at high methane conversion ratios, and direct methane oxidation dominates at lower ratios [171]. In a study by Cui et al. [172], gas composition measurements showed that methane conversion at temperatures between 750 ℃ and 850 ℃ remained relatively low, around 5%, even at high current densities. Interestingly, the study revealed that at a low electrolysis current density of 250 mA/cm^2, significant hydrogen was produced due to methane cracking reactions. However, as the electrolysis current density increased above 1000 mA/cm^2, CO_2 began to dominate in the anode effluent, indicating a shift in reaction pathways.

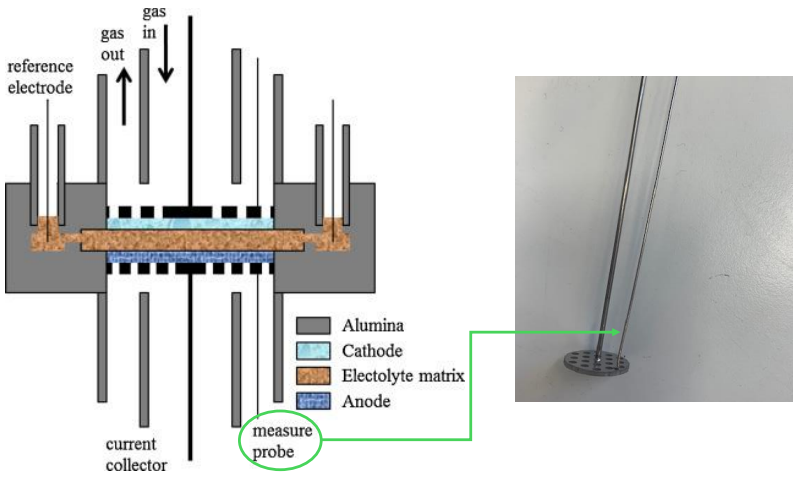

Figure 8.1. Cross-sectional view of the button MCEC (left), used in the experimental campaign at KTH, adapted from [65]. This is the same cell employed in the tests at ENEA, with the only modification being the addition of a probe to the current collectors, as shown in the photograph on the right.

While these findings have laid the groundwork for the development of FA-SOECs, there remains a lack of understanding about how the specific reaction pathways—whether electrochemical or chemical—impact the performance limits of these systems. Moreover, the majority of these experiments have been carried out on single-component, radial button cells, raising concerns about the scalability and relevance of the results to larger FASOEC stacks or systems operating with multi-component fuel mixtures.

Although significant research has been conducted on fuel-assisted electrolysis in SOECs, this approach has never been tested in MCECs. A key distinction between the two systems is the presence of molten carbonates, which require a supply of CO_2 to maintain stable operation. Additionally, MCECs operate at lower temperatures, typically below 700 °C, to avoid excessive volatility of the electrolyte, in contrast to the higher operating temperatures in SOECs. These factors introduce challenges when applying the fuel-assisted concept to molten carbonate cells. Nonetheless, in this study it has been hypothesized that introducing a fuel at the anode could similarly reduce the operating potential, as observed in SOECs, potentially increasing the efficiency of MCECs in hydrogen production. To address this gap in the literature, an experimental investigation was carried out to assess the feasibility of FA electrolysis in molten carbonate cells. The following section will provide an overview of the experimental setup and describe the testing conditions employed in this study.

8.2 Experimental

The experimental study was performed on a 3 cm^2 molten carbonate button cell. The cell was assembled with the state-of-the-art materials detailed in Chapter 4 (see Tab. 4.1). The experimental set-up was also the same as that used for the campaign at the ENEA laboratories, as described in Chapter 4, although some slight

Table 8.1. Inlet anode gas composition in mol%.

	O_2	N_2	CO_2	H_2	CH_4
Std	15	55	30	-	-
	-	100	-	-	-
	-	90	-	10	-
	-	95	5	-	-
	-	90	5	-	5

differences were present between the two. Notably, the current collectors used in this experimental campaign were equipped with probes, allowing for more accurate electrochemical measurements compared to the ENEA set-up. Additionally, unlike the previous set-up where water was supplied via a controlled evaporator mixer (CEM), in this campaign a humidifier is employed to control water vapor content. Fig. 8.1 presents a simplified schematic of the KTH set-up, along with a picture of one of the current collector used.

In this experimental campaign, the cathode (Ni electrode) gas composition was kept constant for all tests, with a mixture of 25/25/25/25% $H_2O/CO_2/N_2/H_2$. In contrast,the gas composition at the anode (NiO electrode) was varied throughout the experiments. The standard anode gas mixture consisted of 55/30/15% $N_2/CO_2/O_2$. All tests were conducted with a total flow rate of 200 ml/min and at a constant operating temperature of 650 °C, which has been identified as the optimal operating temperature for molten carbonate cells [173].

The anode gas compositions tested for electrolysis operations are summarized in Tab. 8.1. To evaluate the feasibility of fuel-assisted electrolysis in MCECs, the first step involved verifying that such an approach could be implemented by supplying a 90/10 mol% N_2/H_2 mixture to the anode, using H_2 as the fuel. While this test served to demonstrate the feasibility of the process, it is ultimately impractical from a real-world perspective, as it would be quite meaningless to use pure hydrogen in FA electrolysis in practice. Therefore, subsequent tests were conducted to assess the viability of using CH_4 as the fuel. The flow rate was maintained at 200 ml/min throughout the tests, with the composition adjusted in steps to assess the contribution of each component added. Initially, the cell was fed with pure nitrogen (100% N_2). Next, a mixture of nitrogen and CO_2 (95/5% N_2/CO_2) was introduced, and finally, methane was added, resulting in a 90/5/5% $N_2/CO_2/CH_4$ mixture, as summarized in Tab. 8.1.

This stepwise approach was chosen to evaluate the impact of each component on the cell performance and to determine whether the presence of methane improved performance. Unlike SOECs, fuel-assisted operation in MCECs poses additional challenges, primarily due to the need to maintain a minimum amount of CO_2 in the atmosphere to preserve the stability of the carbonate electrolyte. It is governed by the following equilibrium reaction:

$$\begin{aligned} M_2CO_3 &\leftrightarrow 2M^+ + CO_3^{2-} \\ CO_3^{2-} &\leftrightarrow CO_2 + O^{2-} \end{aligned} \tag{8.5}$$

where M stands for either Na, Li or K. If insufficient CO_2 is supplied, the equilibrium

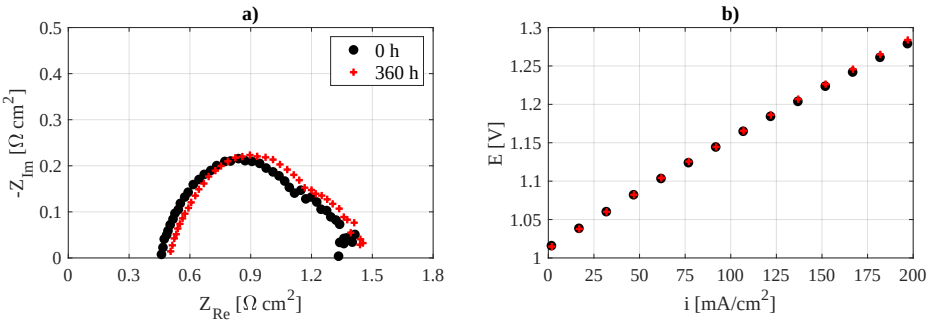

Figure 8.2. Electrochemical data for the cell at the start and end of the experimental campaign obtained at 650 °C under standard composition: a) EIS at 100 mA/cm^2; b) polarization curves.

shifts to the right leading to the decomposition of the molten salts. This not only destabilizes the electrolyte but also increases the volatility of the molten carbonates, potentially resulting in electrolyte loss over time. Furthermore, CO_2 is crucial for preventing the reduction of the NiO anode, which could occur under certain conditions (see Sec. 2.2.4).

The amount of methane was selected based on calculations indicating that, theoretically, it would be fully oxidized at a current density of about 400 mA/cm^2, referred to as the current density turning point. This value is significantly higher than the current densities typically achievable with button MCECs. Consequently, under these conditions, all the O^{2-} ions generated from the electrolysis reaction should, in theory, react completely with methane, preventing any excess oxygen from being produced at the anode. In this scenario, methane would act as the primary oxidizable species, ensuring that the electrochemical oxidation reaction consumes all available O^{2-} ions, rather than them contributing to oxygen evolution.

For each gas composition, as detailed in Tab. 8.1, the electrochemical performance of the cell was evaluated by measuring EIS and polarization curves. EIS are recorded from 1 MHz to 0.01 Hz at 100 mA/cm^2. These measurements were conducted using the potentiostat-frequency response analyzer Zahner ZENNIUM X.

8.3 Results and discussion

Fig. 8.2 shows the impedance spectra at 100 mA/cm^2 and the polarization curves obtained under the standard anodic composition at both the beginning and the end of the experimental campaign. There are no significant differences between the measurements. As for the EIS data, the red curve (representing the end of the experimental campaign) has the same shape as the initial curve but is slightly shifted. This indicates that while the cell polarization remained consistent, there was a slight increase in internal resistance. As for the polarization curves, they overlap, showing no significant differences. These results confirm that during the fuel-assisted electrolysis tests, the cell did not experience any drastic modifications or performance deterioration.

Fig. 8.3 summarizes the polarization curves obtained under the other anodic gas

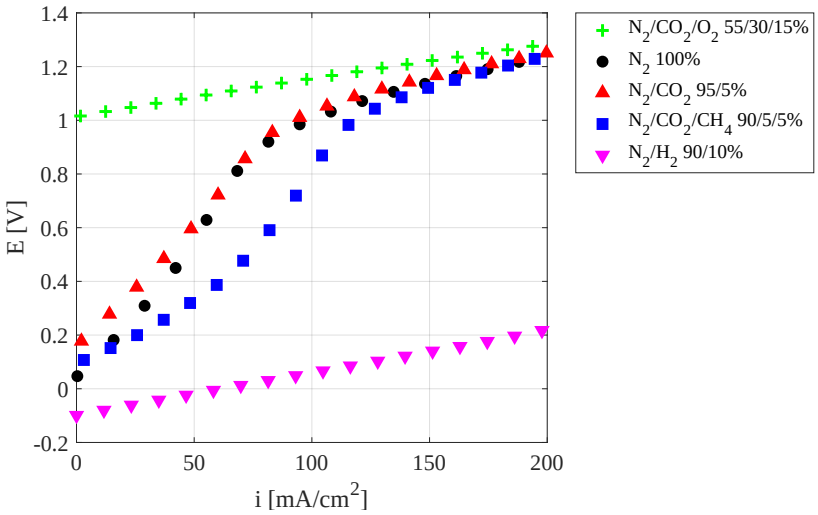

Figure 8.3. Cell polarization curves as a function of anodic composition at 650 °C. Gas composition detailed in Tab. 8.1.

compositions tested. In all cases, the absence of O_2 causes the OCV to be very low than the standard $0.9 - 1$ V, even negative for the case with 10% hydrogen. The negative OCV suggests that electrolysis occurs spontaneously with the assistance of hydrogen oxidation in the anode. For the hydrogen case the comparison with the curve in Fig. 8.2 shows that a much lower voltage is required to produce the same amount of electrolysis current. For instance, while the conventional process requires 1.15 V to achieve a current density of 100 mA/cm^2, this voltage drops by nearly an order of magnitude to 0.1 V when the cell operates in FA mode using H_2. The fact that the voltage remains consistently low up to 200 mA/cm^2 indicates that all O^{2-} ions are oxidized by the available hydrogen, preventing any gaseous oxygen production.

Aside from the OCV values, the curves at 100% N_2 and 95/5% N_2/CO_2 show a similar trend. Under these conditions the reaction taking place at the anode is the standard oxygen evolution from the oxidation of the carbonate ions. The voltage increases almost linearly from OCV to about 1 V, likely due to a large concentration overpotential. In contrast to typical MCEC operation, this overpotential becomes relevant even at low current densities due to the small amount of CO_2 and the absence of O_2. Once the potential approaches 1 V, the slope of the curves decreases significantly. At this point, CO_2 and O_2 are present in sufficient amounts to stabilize cell operation and lower the concentration overpotential. Notably, at high current densities, these two oxygen-deficient compositions exhibit voltage behavior similar to that of the cell under standard conditions. Comparing these results with Fig. 8.2, the potential required to achieve a current density of 200 mA/cm^2 is 1.25 V for both the standard composition and the 100% N_2 and 95/5% N_2/CO_2 mixtures.

When methane is introduced, the open circuit voltage (OCV) remains very low, around 0.1 V, and the polarization curve can be divided into two regions with different slopes: one at low potential and another at higher overpotential. The shape of the curve suggests a transition between two regimes. Up to a current

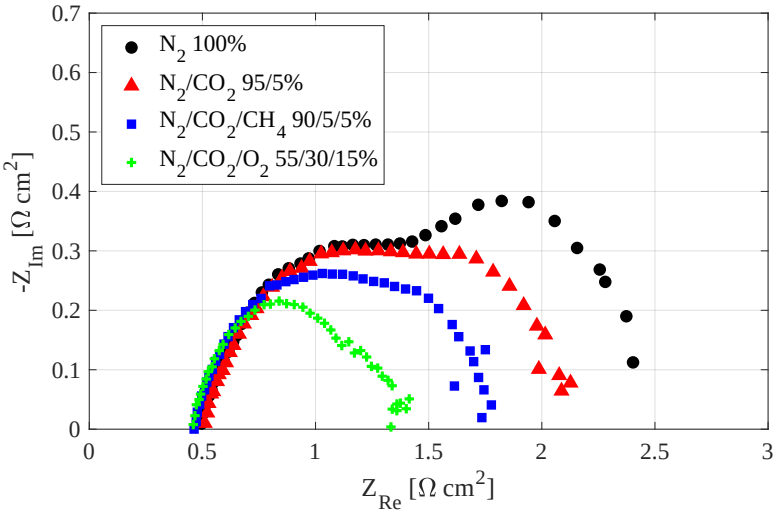

Figure 8.4. Impedance spectra in electrolysis mode at 100 mA/cm^2 at different anodic composition at 650 °C. Cathodic composition: 25/25/25/25% $H_2O/CO_2/N_2/H_2$.

density of 60 mA/cm^2, the electrochemical oxidation of methane seems to occur, lowering the operating voltage. However, as the current density increases beyond 100 mA/cm^2, the system begins to produce oxygen, similar to standard MCEC operation. Interestingly, at higher current densities, the polarization curve (blue squares in Fig. 8.3) converges with the other curves obtained without methane. This suggests that methane conversion decreases as the current density increases. Given the amount of methane fed to the anode, i.e. 10 ml/min, the cell should theoretically have been able to operate in fuel-assisted mode up to current densities of 400 mA/cm^2. However, this transition does not occur as expected, and several potential explanations can be considered. While methane electrochemical oxidation appears to occur up to a certain current density, the oxygen evolution reaction takes over beyond that point. This indicates that the kinetics of methane oxidation may become slower compared to oxygen production at higher current densities. The gas composition could play a crucial role, for instance, the CO_2 concentration changes due to ongoing reactions, potentially affecting the rates of these processes. Multiple chemical reactions, including but not limited to the partial oxidation of methane ($CH_4 + O^{2-} \rightarrow CO + 2H_2$), complete oxidation of methane ($CH_4 + 4O^{2-} \rightarrow CO_2 + 2H_2O$), methane decomposition ($CH_4 \rightarrow C + 2H_2$), and the reverse water-gas shift reaction ($CO_2 + H_2 \rightarrow CO + H_2O$), may contribute to the equilibrium gas composition, further influencing reaction kinetics.

Finally, Fig. 8.4 displays the impedance spectra measurements performed at different gas compositions. The curve at 100% N_2 shows the highest polarization, nearly double that of the standard composition. The spectra for 100% N_2 and 95/5% N_2/CO_2 present the same trend up to medium frequencies, but the polarization for pure N_2 becomes noticeably higher at low frequencies. This confirms the previously discussed concentration overpotential effect, which becomes significant compared to the standard composition due to the substantial reduction in CO_2. Additionally,

this result confirms that mass transfer limitations also become relevant under these conditions. The spectrum for the 90/5/5% $N_2/CO_2/CH_4$ composition shows a different shape. Generally, both the height and width of this spectrum are smaller compared to the spectra without oxygen but larger than that of the standard composition. This intermediate level of polarization suggests that the methane oxidation reaction is occurring to some extent, influencing the impedance response. The results indicate that while methane oxidation may contribute to the overall polarization, its effect is not as pronounced as the standard operation but still noteworthy.

In conclusion, the experimental investigation of fuel-assisted electrolysis in molten carbonate cells presented in this chapter is a pioneering effort in exploring this novel approach. The results obtained provide valuable insights into the behavior of the system under various anodic gas compositions, with a notable emphasis on methane and its interactions with the electrochemical processes. Given that this is one of the first attempts to investigate fuel-assisted electrolysis in this context, it is crucial to continue expanding this research. Future studies should focus on testing additional gas compositions and fuels, such as carbon monoxide, to further understand their impact on the electrochemical performance. Additionally, conducting experiments with larger cells could provide a more comprehensive analysis of gas behavior and utilization factors. Exploring the effects of different electrode materials and temperatures will also be essential to optimize performance and gain a deeper understanding of the underlying mechanisms. Moreover, fuel-assisted electrolysis holds significant potential for energy savings and process efficiency. It can be particularly advantageous in upgrading syngas from gasification processes or exhaust streams, contributing to more sustainable energy solutions. This work provides a basis for further research and development, suggesting the need for continued exploration in this promising field.

Chapter 9

Conclusions

This thesis aims to contribute understanding the operation of Molten Carbonate Electrolysis Cells as a viable solution for hydrogen production and CO_2 utilization. It helps to clarify the dependency of key mechanisms on operational conditions, pointing out specific areas that require further investigation to optimize performance and stability. The research presented addresses both theoretical and applied aspects of MCEC technology, from experimental investigations to numerical modeling and process integration.

The analysis of electrochemical data obtained from the button cell demonstrates that, under electrolysis conditions, the polarization associated with the Ni electrode has a greater impact than in fuel cell mode and, therefore, it cannot be considered negligible in studying the electrochemical mechanisms of an MCEC. This analysis confirms findings reported in the literature, showing that kinetic and mass transport mechanisms control hydrogen production reaction at the Ni electrode.

The study performed on the polarization curves revealed that the advancement of the rWGS reaction, dependent on operating conditions, affects the overpotentials at high current densities. By examining the exchange current density values estimated from the Allen-Hickling plots, higher H_2O concentrations result in increased exchange current densities compared to variations in CO_2. However, a significant decrease in the exchange current density at elevated temperatures and elevated $H_2O\%$ suggests that smaller pores flooding may impede reactant access at the three-phase boundary. Overall, these findings highlight the dominant influence of CO_2 on Ni electrode kinetics, affecting both electrochemical and chemical reactions.

The DRT analysis performed on the EIS spectra aligns with the results from the polarization curves. Among the four polarization loss mechanisms identified at the hydrogen electrode, the peak at approximately 10 Hz accounts for the majority of the hydrogen electrode polarization, influenced by variations in CO_2 and H_2O concentrations. From the deconvolution of the EIS spectra, it can be inferred that the crucial mechanism for the reaction rate-determining step is the mass transfer of reactants at the triple-phase boundary, where the water reduction reaction occurs. Results obtained from the oxygen electrode confirm this assumption. Notably, this research represents a pioneering application of DRT to MCEC impedance spectra.

The experimental campaign carried out on the single cell validates the CO_2 essential role in sustaining the electrolysis process. Notably, variations in CO_2

concentration lead to more pronounced changes in overpotentials compared to alterations in H_2O content. Gas analysis at the hydrogen electrode outlet reveals that CO production increases with elevated temperatures, while H_2 level decreases. Furthermore, with higher CO_2 inlet concentrations, the cell achieves greater current densities, significantly increasing CO generation (approximately 12% on a dry molar basis). This effect is driven by the rWGS reaction and CO_2 electrolysis, with the former producing additional water that further supports electrolysis. Conversely, it was observed that, at low temperatures and high water content, complete CO_2 consumption is possible, enabling pure hydrogen production from the MCEC. This experimental work thus demonstrates the importance of correlating electrochemical data with gas analysis to maximize efficiency, whether for pure hydrogen production or syngas generation.

The 2D model developed for the planar single cell enabled the prediction of the thermal effects on the electrolyzer operating in adiabatic conditions, which are close to the conditions experienced by the cell when operating within a stack. The results indicate that in the absence of proper control, the cell temperature could increase significantly at voltages higher than the thermoneutral point, due to the Joule effect overcoming the endothermic contribution of electrochemical and rWGS reaction. Besides, the latter is enhanced by high temperature and elevated hydrogen content. Thus, the model results emphasize the need to control the chemical reaction progression, which can hinder the faradaic cell efficiency.

The process study, developed using AVEVA PRO/II based on single-cell results, indicates that operating at lower voltages improves both the gross and thermodynamic efficiencies, albeit at the expense of hydrogen production. For this analysis, the cathode gas exiting the electrolyzer is sent to a water-gas shift membrane reactor, which converts the CO present into CO_2 while separating the produced hydrogen. The heat sources identified in the process are the heat exchangers required to vaporize the inlet water stream and to raise the retentate stream temperature exiting the membrane reactor to the electrolyzer operating temperature. However, the majority of the power required by the process is the electricity needed to operate the MCEC. Additionally, the thermal balance analysis of the electrolyzer has shown that the rWGS reaction increases the thermoneutral voltage compared to the theoretically predicted value. By comparing the process efficiency at different operating voltages, it can be inferred that a good compromise between hydrogen production and low energy consumption would be to operate slightly above the effective thermoneutral voltage, identified under the analyzed conditions as 1.35 V.

The investigation of MCEC coupled with a photovoltaic system demonstrates that operating an MCEC with a load-following strategy is feasible. The CUSUM approach applied to analyze the experimental results, suggests that maintaining a fixed gas flow rate while varying the power input is more efficient than operating the cell at a fixed conversion rate, which involves modulating both the power input and the inlet flow rates. Although the latter operation mode results in a more pronounced decline in cell efficiency, it could help to operate the other system components efficiently, yielding positive outcomes when considering the entire Balance of Plant.

Finally, the exploration of the fuel-assisted operation mode on the button cell has yielded promising results. First, the negative open-circuit voltage, along with a close to zero operating voltage at 100 mA/cm^2, assesses the feasibility of sending a

fuel to the oxygen electrode to reduce the cell voltage. Substituting hydrogen with methane led to a lower voltage than normal operation but not to the same extent as the one observed using hydrogen, suggesting a slower decomposition rate of methane. The positive results obtained from these initial attempts to investigate fuel-assisted electrolysis in MCEC pave the way for testing different gas compositions and fuels, such as carbon monoxide, to gain insights into their impact on electrochemical performance. Moreover, conducting experiments with larger cells could facilitate a more comprehensive analysis of gas behavior, enabling the evaluation of conversion rates and providing insights into the underlying reactions.

In conclusion, this thesis offers a foundation for further delving into MCECs operation, clarifying the dependency of key mechanisms on operational conditions and highlighting specific areas that require further investigation to optimize performance and stability.

Appendix A

Parameters from 1D model

For a preliminary analysis of the system a 1D model was initially developed, accounting only for gradients in the x direction [174]. The model domains and main equations are those reported in Sec. 6.1.2. Regarding the gas composition, which affects the rate of the electrochemical reactions, the outlet concentrations were used. These values were evaluated from mass balances considering the inlet flow rate of each component and the rate of production deriving from the measured current density. For instance, the rate of hydrogen production from the electrochemical reaction was evaluated as

$$F_{H_2}^{el} = \frac{iS}{2\mathcal{F}} \tag{A.1}$$

where S is the surface area of the electrode. The experimental data reported in Tab.6.3 where analyzed with the 1D model. The data at each temperature was analyzed separately.

The bulk conductivity of the liquid electrolyte was taken from the literature [38]. The effective conductivity was taken from a Bruggemantype equation

$$\kappa_{l,eff}^{\text{mat}} = \kappa_l \varepsilon_l^d \tag{A.2}$$

where ε_l is the matrix porosity, equal to 0.5, and the exponent d was found by fitting the experimental data to be equal to 4.7, regardless of the temperature. The effective ionic conductivity in the two porous electrodes was instead evaluated by introducing the corrective factors, f_h and f_o for the cathode and anode, respectively

$$\kappa_{l,eff}^{\text{HE}} = f_h \kappa_l \tag{A.3}$$

$$\kappa_{l,eff}^{\text{OE}} = f_o \kappa_l \tag{A.4}$$

The corrective factors were found to be independent of temperature and equal to 0.91 for the cathode and 0.37 for the anode. Finally, the exchange current density at the anode was also determined by fitting the experimental data.

The final parameters that were obtained are those reported in Tab. 6.2. Fig. A.1 shows a comparison between the experimental and calculated polarization curves, obtained from the above-described correlation after having corrected the open circuit potential. The comparison between experimental and modeling results is very good, and suggests that the assumption of negligible cathodic activation overpotential enforced is in fact valid. The model parameters obtained were therefore employed in the subsequent 2D model.

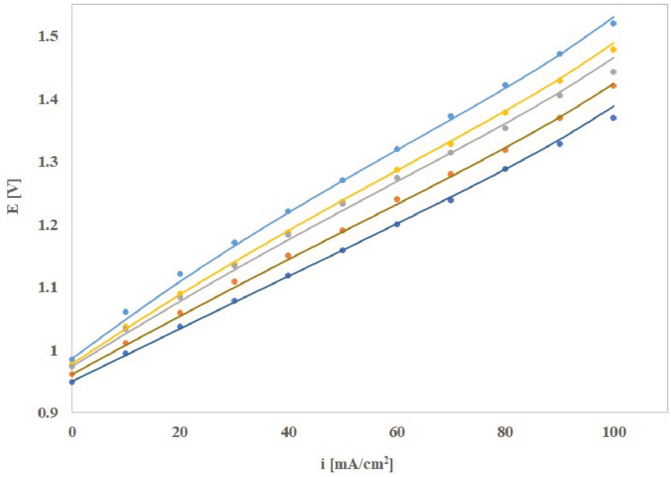

Figure A.1. Comparison between experimental (points) and calculated (solid lines) polarization curves obtained from the 1D model with parameter fitting.

Appendix B

Nomenclature

Latin Symbols

0D	Zero-dimensional
1D	One-dimensional
2D	Two-dimensional
COP	Coefficient of performance
$CUSUM$	Cumulative Sum Control Chart
$\mathcal{D}$	Binary diffusion coefficient
D	Pore diameter
E	Electric potential
F	Molar flowrate
$\mathcal{F}$	Faraday constant
f	Frequency
HHV	Higher heating value of hydrogen
H	Gas channel length
I	Current
i	Current density
$\mathbf{j}$	Diffusive flux vector
K_{eq}	Equilibrium constant
L	Refrigeration cycle work
LHV	Lower heating value of hydrogen
N	Molar flux

n	number of electrons
P	Electric power
p	Partial pressure
Q	Heat
$\mathcal{R}$	Production molar rate
R_0	Internal resistance
R_{pol}	Polarization resistance
s	Gas channel width
T	Temperature
u_0	Inlet gas velocity
$\mathbf{u}$	Velocity vector
X	Conversion
x	Dry molar fraction
y	Molar fraction
Z	Impedance

Greeks

α	Transfer coefficient
γ	Distribution function
ϵ	Volumetric porosity
η	Overpotential
θ	Contact angle
Θ	Objective function
κ	Conductivity
ξ	Process efficiency
ρ	Density
σ	Superficial tension

τ	Time constant
ϕ	Local potential
χ	Reactive sites coverage
ω_k	Mass fraction
ω	Frequency

Subscripts

el	Electolysis reaction
exp	Expected
g	Gas
l	Liquid
M	Measured
$rWGS$	Reverse water gas shift reaction
s	Solid

Superscripts

a	anode
c	cathode
e	Experimental
t	Theoretical

Bibliography

[1] European Commission. *European Green Deal*. https://commission.europa.eu/strategy-and-policy/priorities-2019-2024/european-green-deal_en. Accessed: 2024-09-13.

[2] Torbjørn Egeland-Eriksen, Amin Hajizadeh, and Sabrina Sartori. "Hydrogen-based systems for integration of renewable energy in power systems: Achievements and perspectives". In: *International journal of hydrogen energy* 46.63 (2021), pp. 31963–31983. DOI: 10.1016/j.ijhydene.2021.06.218.

[3] Alexander Buttler and Hartmut Spliethoff. "Current status of water electrolysis for energy storage, grid balancing and sector coupling via power-to-gas and power-to-liquids: A review". In: *Renewable and Sustainable Energy Reviews* 82 (2018), pp. 2440–2454. DOI: 10.1016/j.rser.2017.09.003.

[4] Immanuel Vincent and Dmitri Bessarabov. "Low cost hydrogen production by anion exchange membrane electrolysis: A review". In: *Renewable and Sustainable Energy Reviews* 81 (2018), pp. 1690–1704. DOI: 10.1016/j.rser.2017.05.258.

[5] Anne Hauch et al. "Recent advances in solid oxide cell technology for electrolysis". In: *Science* 370.6513 (2020), eaba6118. DOI: 10.1126/science.aba611.

[6] M Cassir et al. "Molten carbonate fuel cells". In: *Compendium of hydrogen energy*. Elsevier, 2016, pp. 71–87. DOI: 10.1016/B978-1-78242-363-8.00003-7.

[7] Gabor Kiss et al. "CO_2 Capture From Natural Gas Combined Cycle Power Generation Using Carbonate Fuel Cells". In: *Abu Dhabi International Petroleum Exhibition and Conference*. SPE. 2019. DOI: 10.2118/197377-ms.

[8] FuelCell Energy, Inc. *ExxonMobil to Build CCS Pilot Plant with FuelCell Energy Using Carbonate Fuel Cell Technology*. Accessed: 2024-09-13. 2023. URL: https://investor.fce.com/press-releases/press-release-details/2023/ExxonMobil-to-Build-CCS-Pilot-Plant-with-FuelCell-EnergyUsing-Carbonate-Fuel-Cell-Technology/default.aspx.

[9] Timothy A Barckholtz et al. "Molten carbonate fuel cells for simultaneous CO2 capture, power generation, and H2 generation". In: *Applied Energy* 313 (2022), p. 118553. DOI: 10.1016/j.apenergy.2022.118553.

[10] A Kulkarni and S Giddey. "Materials issues and recent developments in molten carbonate fuel cells". In: *Journal of Solid State Electrochemistry* 16 (2012), pp. 3123–3146. DOI: 10.1007/s10008-012-1771-y.

[11] JR Selman. "MOLTEN SALT FUEL CELLS: Diversity and convergence, cycles and recycling". In: *International Journal of Hydrogen Energy* 46.28 (2021), pp. 15078–15094. DOI: 10.1016/j.ijhydene.2020.05.197.

[12] S. Frangini and A. Masi. "Molten carbonates for advanced and sustainable energy applications: Part I. Revisiting molten carbonate properties from a sustainable viewpoint". In: *International Journal of Hydrogen Energy* 41.41 (2016), pp. 18739–18746. ISSN: 0360-3199. DOI: 10.1016/j.ijhydene.2015.12.073.

[13] Michelle Cassir and C Belhomme. "Technological applications of molten salts: the case of the molten carbonate fuel cell". In: *Plasmas & Ions* 2 (1999). DOI: 10.1016/S1288-3255(99)80006-9.

[14] Huayi Yin et al. "Capture and electrochemical conversion of CO2 to value-added carbon and oxygen by molten salt electrolysis". In: *Energy Environ. Sci.* 6 (5 2013), pp. 1538–1545. DOI: 10.1039/C3EE24132G.

[15] D Chery et al. "Thermodynamic and experimental approach of electrochemical reduction of CO2 in molten carbonates". In: *international journal of hydrogen energy* 39.23 (2014), pp. 12330–12339. DOI: 10.1016/j.ijhydene.2014.03.113.

[16] H Meskine et al. "Electrochemical investigations on CO_2 reduction mechanism in molten carbonates in view of H_2O/CO_2 co-electrolysis". In: *International Journal of Hydrogen Energy* 46.28 (2021), pp. 14944–14952. DOI: 10.1016/j.ijhydene.2020.07.008.

[17] Stephen H. Clarke et al. "Catalytic aspects of the steam reforming of hydrocarbons in internal reforming fuel cells". In: *Catalysis Today* 38.4 (1997). Fuel Cells and Catalysis, pp. 411–423. ISSN: 0920-5861. DOI: 10.1016/S0920-5861(97)00052-7.

[18] C.-G. Lee. "Overpotential Behavior of Carbon Monoxide Fuel in a Molten Carbonate Fuel Cell". In: *Fuel Cells* 12.4 (2012), pp. 550–556. DOI: 10.1002/fuce.201100149.

[19] J. R. Selman. "Research, Development, and Demonstration of Molten Carbonate Fuel Cell Systems". In: *Fuel Cell Systems*. Ed. by Leo J. M. J. Blomen and Michael N. Mugerwa. Boston, MA: Springer US, 1993, pp. 345–463. ISBN: 978-1-4899-2424-7. DOI: 10.1007/978-1-4899-2424-7_10.

[20] Stephen J. McPhail et al. *International Status of Molten Carbonate Fuel Cells Technology*. Annex 23 - MCFC. Accessed: 2024-08-06. Advanced Fuel Cells Implementing Agreement, 2015.

[21] P. Iora, S. Campanari, and A. Salogni. "Off-Design Analysis of a MCFC-Gas Turbine Hybrid Plant". In: *Journal of Fuel Cell Science and Technology* 7.3 (Mar. 2010), p. 031022. ISSN: 1550-624X. DOI: 10.1115/1.4000679.

[22] José Luz Silveira, Elisangela Martins Leal, and Luiz F Ragonha Jr. "Analysis of a molten carbonate fuel cell: cogeneration to produce electricity and cold water". In: *Energy* 26.10 (2001), pp. 891–904. DOI: 10.1016/S0360-5442(01)00038-X.

[23] FuelCell Energy, USA. *FuelCell Energy*. http://www.fce.com/. Accessed: 2024-08-06.

[24] M. Genovese V. Cigolotti. *Stationary Fuel Cell Applications: Tracking Market Trends*. https://www.ieafuelcell.com/fileadmin/publications/2021/2021_AFCTCP_Stationary_Application_MarketTrend.pdf. Accessed: 2024-08-13. 2021.

[25] S Frangini. "Corrosion of structural materials in molten carbonate fuel cells: an overview". In: *Molten Salt Forum*. Vol. 7. 2003, pp. 135–154.

[26] "Corrosion of anode current collectors in molten carbonate fuel cells". In: *Journal of Power Sources* 160.2 (2006). Special issue including selected papers presented at the International Workshop on Molten Carbonate Fuel Cells and Related Science and Technology 2005 together with regular papers, pp. 782–788. ISSN: 0378-7753. DOI: 10.1016/j.jpowsour.2006.04.069.

[27] Stefano Frangini. "Corrosion of metallic stack components in molten carbonates: Critical issues and recent findings". In: *Journal of Power Sources* 182 (2 Aug. 2008), pp. 462–468. ISSN: 0378-7753. DOI: 10.1016/J.JPOWSOUR.2007.11.100.

[28] H Morita et al. "Degradation mechanism of molten carbonate fuel cell based on long-term performance: long-term operation by using bench-scale cell and post-test analysis of the cell". In: *Journal of Power Sources* 195.20 (2010), pp. 6988–6996. DOI: 10.1016/j.jpowsour.2010.04.084.

[29] S McPhail et al. "Molten carbonate fuel cells". In: Elsevier, 2008, pp. 248–279. DOI: 10.1533/9781845694838.248.

[30] S Majid Hassanizadeh and William G Gray. "Thermodynamic basis of capillary pressure in porous media". In: *Water resources research* 29.10 (1993), pp. 3389–3405. DOI: 10.1029/93WR01495.

[31] Kazumi Tanimoto et al. "Cell performance of molten-carbonate fuel cell with alkali and alkaline-earth carbonate mixtures". In: *Journal of Power Sources* 39.3 (1992), pp. 285–297. ISSN: 0378-7753. DOI: 10.1016/0378-7753(92)80002-S.

[32] Stephen J. McPhail, Ping-Hsun Hsieh, and Jan Robert Selman. "Molten Carbonate Fuel Cells". In: *Materials for High-Temperature Fuel Cells*. John Wiley & Sons, Ltd, 2013. Chap. 9, pp. 341–371. ISBN: 9783527644261. DOI: 10.1002/9783527644261.ch9.

[33] Charles E. Baumgartner. "Solubility and Transport of NiO Cathodes in Molten Carbonate Fuel Cells". In: *Journal of the American Ceramic Society* 69 (2 1986), pp. 162–168. ISSN: 15512916. DOI: 10.1111/j.1151-2916.1986.tb04722.x.

[34] S. Yoshioka and H. Urushibata. "Simulation of Cathode Dissolution and Shorting for Molten Carbonate Fuel Cells". In: *Journal of The Electrochemical Society* 144.3 (1997), p. 815. DOI: 10.1149/1.1837494.

[35] Andrew L Dicks. "Molten carbonate fuel cells". In: *Current Opinion in Solid State and Materials Science* 8.5 (2004), pp. 379–383. DOI: 10.1016/j.cossms.2004.12.005.

[36] PGP Ang and AF Sammells. "Influence of electrolyte composition on electrode kinetics in the molten carbonate fuel cell". In: *Journal of the Electrochemical Society* 127.6 (1980), p. 1287. DOI: 10.1149/1.2129873.

[37] H Morita et al. "Performance analysis of molten carbonate fuel cell using a Li/Na electrolyte". In: *Journal of Power Sources* 112.2 (2002), pp. 509–518. DOI: 10.1016/S0378-7753(02)00468-8.

[38] Toshikatsu Kojima et al. "Electrical conductivity of molten Li2CO3-X2CO3 (X: Na, K, Rb, and Cs) and Na2CO3-Z2CO3 (Z: K, Rb, and Cs)". In: *Journal of The Electrochemical Society* 154.12 (2007), F222. DOI: 10.1149/1.2789389.

[39] M. Yoshikawa et al. "NiO Cathode Dissolution and Ni Precipitation in Li/Na Molten Carbonate Fuel Cells: Distribution of Ni Particles in the Matrix". In: *Journal of The Electrochemical Society* 148 (11 2001), A1230. ISSN: 00134651. DOI: 10.1149/1.1407830.

[40] Yoji Fujita et al. "Degradation of the components in molten carbonate fuel cells with Li/Na electrolyte". In: *Electrochemistry* 71.1 (2003), pp. 7–13. DOI: 10.5796/electrochemistry.71.7.

[41] S.H. White and U.M. Twardoch. "The electrochemical behaviour of solutions of molten ternary alkali carbonate mixture equilibrated with carbon dioxide-water mixtures at 460°C". In: *Electrochimica Acta* 29.3 (1984), pp. 349–359. ISSN: 0013-4686. DOI: https://doi.org/10.1016/0013-4686(84)87074-7.

[42] T. Kudo et al. "X-ray diffractometric study of in situ oxidation of Ni in Li/K and Li/Na carbonate eutectic". In: *Journal of Power Sources* 104.2 (2002), pp. 272–280. ISSN: 0378-7753. DOI: 10.1016/S0378-7753(01)00962-4.

[43] M Mohamedi, Y Hisamitsu, and I Uchida. "Ternary alkali carbonate composition-oxygen solubility relationship under atmospheric and pressurized conditions–a utility model for MCFC". In: *Journal of applied electrochemistry* 32 (2002), pp. 111–117. DOI: 10.1023/A:1014225725716.

[44] Silvera Scaccia. "Investigation on NiO solubility in binary and ternary molten alkali metal carbonates containing additives". In: *Journal of Molecular Liquids* 116.2 (2005), pp. 67–71. DOI: 10.1016/j.molliq.2004.07.078.

[45] Seung-Goo Kim, Jae-ho Jun, and Joonghwan Jun. "Predictions of the optimum ternary alkali-carbonate electrolyte composition for MCFC by computational calculation". In: *Journal of power sources* 160.2 (2006), pp. 805–810. DOI: 10.1016/j.jpowsour.2006.04.067.

[46] Toshikatsu Kojima et al. "Density, surface tension, and electrical conductivity of ternary molten carbonate system Li2CO3-Na2CO3-K2CO3 and methods for their estimation". In: *Journal of the Electrochemical Society* 155.7 (2008), F150. DOI: 10.1149/1.2917212.

[47] K. Tanimoto et al. "Optimization of the electrolyte composition in a $(Li_{0.52}Na_{0.48})_{2-2x}AE_xCO_3$ (AE=Ca and Ba) molten carbonate fuel cell". In: *Journal of Power Sources* 131.1 (2004), pp. 256–260. ISSN: 0378-7753. DOI: 10.1016/j.jpowsour.2003.11.085.

[48] Toshikatsu Kojima et al. "The electrical conductivity of molten Li_2CO_3 – K_2CO_3 and Li_2CO_3 – Na_2CO_3 containing alkaline earth (Ca, Sr and Ba) carbonates". In: *Denki Kagaku oyobi Kogyo Butsuri Kagaku* 64.6 (1996), pp. 471–477. DOI: 10.5796/kogyobutsurikagaku.64.471.

[49] S. Giddey et al. "A comprehensive review of direct carbon fuel cell technology". In: *Progress in Energy and Combustion Science* 38.3 (2012), pp. 360–399. ISSN: 0360-1285. DOI: 10.1016/j.pecs.2012.01.003.

[50] Robert Baron et al. "Manufacturing of γ-$LiAlO_2$ matrix for molten carbonate fuel cell by high-energy milling". In: *International Journal of Hydrogen Energy* 43.13 (2018), pp. 6696–6700. ISSN: 0360-3199. DOI: 10.1016/j.ijhydene.2018.02.085.

[51] SH Hyun et al. "Reinforcement of molten carbonate fuel cell matrixes by adding rod-shaped γ-$LiAlO_2$ particles". In: *Journal of materials science* 36 (2001), pp. 441–450. DOI: 10.1023/A:1004884730628.

[52] Andreas Bodén, Masahiro Yoshikawa, and Göran Lindbergh. "Influence of anode pore-size distribution and total electrolyte filling degree on molten carbonate fuel cell performance". In: *Journal of The Electrochemical Society* 155.2 (2007), B172. DOI: 10.1149/1.2816213.

[53] Asrar A. Sheikh et al. "A review on MCFC matrix: State-of-the-art, degradation mechanisms and technological improvements". In: *Heliyon* 10.4 (2024), e25847. ISSN: 2405-8440. DOI: 10.1016/j.heliyon.2024.e25847.

[54] Yu-Jeong Kim et al. "Performance analysis with various amounts of electrolyte in a molten carbonate fuel cell". In: *Journal of Electrochemical Science and Technology* 7.3 (2016), pp. 234–240. DOI: 10.5229/JECST.2016.7.3.234.

[55] Jin-Eok Kim et al. "Mechanical properties of the lithium aluminate matrix for MCFC reinforced with metal oxide materials". In: *Current Applied Physics* 10.2 (2010), S73–S76. DOI: 10.1016/j.cap.2009.11.046.

[56] Jin Y Cho, Sang H Hyun, and Seong A Hong. "Fabrication and Characterization of γ-LiAlO2 Matrices Using an Aqueous Tape-Casting Process". In: *Journal of the American Ceramic Society* 84.5 (2001), pp. 937–40. DOI: 10.1111/j.1151-2916.2001.tb00771.x.

[57] M Della Pietra et al. "Accelerated test for MCFC button cells: First findings". In: *International Journal of Hydrogen Energy* 41.41 (2016), pp. 18807–18814. DOI: 10.1016/j.ijhydene.2016.07.021.

[58] E Bergaglio, A Sabattini, and P Capobianco. "Research and development on porous components for MCFC applications". In: *Journal of power sources* 149 (2005), pp. 63–65. DOI: 10.1016/j.jpowsour.2005.01.033.

[59] E Gürbüz et al. “Reinforcement of the MCFC matrix by Al-based additives: Effect of lithiation”. In: *Ceramics International* 48.6 (2022), pp. 7448–7455. DOI: 10.1016/j.ceramint.2021.11.142.

[60] K Kinoshita, JW Sim, and JP Ackerman. “Preparation and characterization of lithium aluminate”. In: *Materials Research Bulletin* 13.5 (1978), pp. 445–455. DOI: 10.1016/0025-5408(78)90152-6.

[61] Jin-Eok Kim et al. “Using aluminum and Li2CO3 particles to reinforce the α-$LiAlO_2$ matrix for molten carbonate fuel cells”. In: *International journal of hydrogen energy* 34.22 (2009), pp. 9227–9232. DOI: 10.1016/j.ijhydene.2009.08.069.

[62] Kailash Yashvant Patil et al. “The effect of lithium addition on aluminum-reinforced α-LiAlO2 matrices for molten carbonate fuel cells”. In: *International journal of hydrogen energy* 36.10 (2011), pp. 6237–6247. DOI: 10.1016/j.ijhydene.2011.01.161.

[63] Jong-Jin Lee et al. “Characteristics of aluminum-reinforced γ-LiAlO2 matrices for molten carbonate fuel cells”. In: *Journal of Power Sources* 179.2 (2008), pp. 504–510. DOI: 10.1016/j.jpowsour.2007.12.110.

[64] F. Santoni et al. “Accurate in-operando study of molten carbonate fuel cell degradation processes -part I: Physiochemical processes individuation”. In: *Electrochimica Acta* 291 (Nov. 2018), pp. 343–352. ISSN: 0013-4686. DOI: 10.1016/J.ELECTACTA.2018.08.100.

[65] I. Rexed et al. “Molten carbonate fuel cells for CO2 separation and segregation by retrofitting existing plants – An analysis of feasible operating windows and first experimental findings”. In: *International Journal of Greenhouse Gas Control* 35 (2015), pp. 120–130. ISSN: 1750-5836. DOI: https://doi.org/10.1016/j.ijggc.2015.01.012. URL: https://www.sciencedirect.com/science/article/pii/S1750583615000286.

[66] PA2 Finn. “The effects of different environments on the thermal stability of powdered samples of $LiAlO_2$”. In: *Journal of The Electrochemical Society* 127.1 (1980), p. 236. DOI: 10.1149/1.2129626.

[67] K Takizawa and A Hagiwara. “The transformation of LiAlO2 crystal structure in molten Li/K carbonate”. In: *Journal of power sources* 109.1 (2002), pp. 127–135. DOI: 10.1016/S0378-7753(02)00045-9.

[68] N Tomimatsu et al. “Phase stability of $LiAlO_2$ in molten carbonate”. In: *Journal of the Electrochemical Society* 144.12 (1997), p. 4182. DOI: 10.1149/1.1838163.

[69] Mihui Lee et al. “Mechanical strength improvement of aluminum foam-reinforced matrix for molten carbonate fuel cells”. In: *International Journal of Hydrogen Energy* 42.25 (2017), pp. 16235–16243. DOI: 10.1016/j.ijhydene.2017.03.096.

[70] Hoang Viet Phuc Nguyen et al. “Nano Ni layered anode for enhanced MCFC performance at reduced operating temperature”. In: *International journal of hydrogen energy* 39.23 (2014), pp. 12285–12290. DOI: 10.1016/j.ijhydene.2014.03.253.

[71] Dohwon Jung et al. “On the high creep resistant morphology and its formation mechanism in Ni–10 wt.% Cr anodes for molten carbonate fuel cells”. In: *Journal of materials chemistry* 13.7 (2003), pp. 1717–1722. DOI: 10.1039/B300745F.

[72] Gyubeom Kim, Youngjoon Moon, and Dokyol Lee. “Preparation of creep-resistant Ni–5 wt.% Al anodes for molten carbonate fuel cells”. In: *Journal of power sources* 104.2 (2002), pp. 181–189. DOI: 10.1016/S0378-7753(01)00910-7.

[73] Dokyol Lee, Insung Lee, and Sookhee Chang. “On the change of a Ni_3Al phase in a Ni–12 wt.% Al MCFC anode during partial oxidation and reduction stages of sintering”. In: *Electrochimica acta* 50.2-3 (2004), pp. 755–759. DOI: 10.1016/j.electacta.2004.01.122.

[74] M Farooque and HC Maru. “Carbonate fuel cells: Milliwatts to megawatts”. In: *Journal of Power Sources* 160.2 (2006), pp. 827–834. DOI: 10.1016/j.jpowsour.2006.04.127.

[75] T Tagawa et al. “Ceramic anode catalyst for dry methane type molten carbonate fuel cell”. In: *Journal of Power Sources* 126.1 (2004), pp. 1–7. ISSN: 0378-7753. DOI: 10.1016/j.jpowsour.2003.08.005.

[76] Grazia Accardo et al. “Performance and properties of anodes reinforced with metal oxide nanoparticles for molten carbonate fuel cells”. In: *Journal of Power Sources* 370 (2017), pp. 52–60. DOI: 10.1016/j.jpowsour.2017.10.015.

[77] Hary Devianto et al. “The effect of a ceria coating on the H2S tolerance of a molten carbonate fuel cell”. In: *Journal of Power Sources* 159.2 (2006), pp. 1147–1152. DOI: 10.1016/j.jpowsour.2005.11.092.

[78] K Tanimoto et al. “Long-term operation of small-sized single molten carbonate fuel cells”. In: *Journal of power sources* 72.1 (1998), pp. 77–82. DOI: 10.1016/S0378-7753(97)02673-6.

[79] S Yoshioka and H Urushibata. “Simulation of cathode dissolution and shorting for molten carbonate fuel cells”. In: *Journal of the Electrochemical Society* 144.3 (1997), p. 815. DOI: 10.1149/1.1837494.

[80] M Yoshikawa et al. “NiO cathode dissolution and ni precipitation in Li/Na molten carbonate fuel cells: Distribution of Ni particles in the matrix”. In: *Journal of the Electrochemical Society* 148.11 (2001), A1230. DOI: 10.1149/1.1407830.

[81] ZP Liu, PY Guo, and CL Zeng. “Effect of Dy on the corrosion of NiO/Ni in molten (0.62 Li, 0.38 K) 2CO3”. In: *Journal of power sources* 166.2 (2007), pp. 348–353. DOI: 10.1016/j.jpowsour.2007.01.063.

[82] Jung-Ho Wee and Kwan-Young Lee. “Overview of the effects of rare-earth elements used as additive materials in molten carbonate fuel cell systems”. In: *Journal of materials science* 41 (2006), pp. 3585–3592. DOI: 10.1007/s10853-005-5551-2.

[83] Prabhu Ganesan et al. “Performance of La0. 8Sr0. 2CoO3 coated NiO as cathodes for molten carbonate fuel cells”. In: *Journal of power sources* 115.1 (2003), pp. 12–18. DOI: 10.1016/S0378-7753(02)00621-3.

[84] Bo Huang et al. “Study of NiO cathode modified by ZnO additive for MCFC”. In: *Journal of power sources* 128.2 (2004), pp. 135–144. DOI: 10.1016/j.jpowsour.2003.10.008.

[85] H Okawa et al. “Performance of NiO/MgFe2O4 composite cathode for a molten carbonate fuel cell”. In: *Journal of power sources* 131.1-2 (2004), pp. 251–255. DOI: 10.1016/j.jpowsour.2003.11.092.

[86] Stefano Frangini. “Corrosion of metallic stack components in molten carbonates: critical issues and recent findings”. In: *Journal of Power Sources* 182.2 (2008), pp. 462–468. DOI: 10.1016/j.jpowsour.2007.11.100.

[87] RA Donado et al. “Corrosion of the Wet-Seal Area in Molten Carbonate Fuel Cells: I. Analysis”. In: *Journal of the Electrochemical Society* 131.11 (1984), p. 2535. DOI: 10.1149/1.2115354.

[88] M Cassir and C Belhomme. “Technological applications of molten salts: the case of the molten carbonate fuel cell”. In: *Plasmas & ions* 2.1 (1999), pp. 3–15. DOI: doi.org/10.1016/S1288-3255(99)80006-9.

[89] C Yuh et al. “Status of carbonate fuel cell materials”. In: *Journal of power sources* 56.1 (1995), pp. 1–10. DOI: 10.1016/0378-7753(95)80001-W.

[90] Piotr Tomczyk. “MCFC versus other fuel cells—Characteristics, technologies and prospects”. In: *Journal of Power sources* 160.2 (2006), pp. 858–862. DOI: 10.1016/j.jpowsour.2006.04.071.

[91] Beomjoo Kim et al. “The operation results of a 125 kW molten carbonate fuel cell system”. In: *Renewable Energy* 42 (2012), pp. 145–151. DOI: 10.1016/j.renene.2011.08.044.

[92] Elisabetta Arato et al. “Optimisation of the cell shape for industrial MCFC stacks”. In: *Journal of Power Sources* 86.1-2 (2000), pp. 302–308. DOI: 10.1016/S0378-7753(99)00463-2.

[93] Joon-Ho Koh and Byoung Sam Kang. “Theoretical study of a molten carbonate fuel cell stack for pressurized operation”. In: *International journal of energy research* 25.7 (2001), pp. 621–641. DOI: 10.1002/er.709.

[94] Franco Cotana, Federico Rossi, and Andrea Nicolini. “A new geometry high performance small power MCFC”. In: *Journal of Fuel Cell Science and Technology* 1 (2004), pp. 24–29. DOI: 10.1115/1.1782924.

[95] Federico Rossi and Andrea Nicolini. “A cylindrical small size molten carbonate fuel cell: experimental investigation on materials and improving performance solutions”. In: *Fuel Cells* 9.2 (2009), pp. 170–177. DOI: 10.1002/fuce.200800064.

[96] Federico Rossi and Andrea Nicolini. “Experimental investigation on a novel electrolyte configuration for cylindrical molten carbonate fuel cells”. In: *Journal of Fuel Cell Science and Technology* (2011). DOI: 10.1115/1.4003773.

[97] Makoto Kawase. "Manufacturing method for tubular molten carbonate fuel cells and basic cell performance". In: *Journal of Power Sources* 285 (2015), pp. 260–265. DOI: 10.1016/j.jpowsour.2015.03.117.

[98] Makoto Kawase. "Durability and robustness of tubular molten carbonate fuel cells". In: *Journal of Power Sources* 371 (2017), pp. 106–111. DOI: 10.1016/j.jpowsour.2017.10.024.

[99] Si-Won Kim et al. "Reactions and mass transport in high temperature co-electrolysis of steam/CO2 mixtures for syngas production". In: *Journal of Power Sources* 280 (2015), pp. 630–639. DOI: 10.1016/j.jpowsour.2015.01.083.

[100] Zhengshan Yang et al. "Electrolyte engineering for efficient molten-carbonate electrolysis of CO_2". In: *Chemical Engineering Journal* 473 (2023), p. 145146. DOI: 10.1016/j.cej.2023.145146.

[101] Lan Hu et al. "Electrochemical performance of reversible molten carbonate fuel cells". In: *International Journal of Hydrogen Energy* 39 (23 Aug. 2014), pp. 12323–12329. ISSN: 03603199. DOI: 10.1016/j.ijhydene.2014.02.144.

[102] Lan Hu, Göran Lindbergh, and Carina Lagergren. "Performance and Durability of the Molten Carbonate Electrolysis Cell and the Reversible Molten Carbonate Fuel Cell". In: *Journal of Physical Chemistry C* 120 (25 June 2016), pp. 13427–13433. ISSN: 19327455. DOI: 10.1021/ACS.JPCC.6B04417/SUPPL_FILE/JP6B04417_SI_001.PDF.

[103] Juan Pedro Perez-Trujillo et al. "A numerical and experimental comparison of a single reversible molten carbonate cell operating in fuel cell mode and electrolysis mode". In: *Applied Energy* 226 (2018), pp. 1037–1055. ISSN: 0306-2619. DOI: 10.1016/j.apenergy.2018.05.121.

[104] Stefano Frangini et al. "Degradation of MCFC materials in a 81 cm2 single cell operated under alternated fuel cell/electrolysis mode". In: *Frontiers in Energy Research* 9 (2021), p. 653531. DOI: 10.3389/fenrg.2021.653531.

[105] Emilio Audasso et al. "Investigation of molten carbonate electrolysis cells performance for H2 production and CO2 capture". In: *Journal of Power Sources* 523 (Mar. 2022), p. 231039. ISSN: 0378-7753. DOI: 10.1016/J.JPOWSOUR.2022.231039.

[106] S. H. Lu and J. R. Selman. "Electrode Kinetics of Fuel Oxidation at Copper in Molten Carbonate". In: *Journal of The Electrochemical Society* 131 (12 Dec. 1984), pp. 2827–2833. ISSN: 0013-4651. DOI: 10.1149/1.2115427.

[107] C. Y. Yuh and S. R. Selman. "Polarization of the molten carbonate fuel cell anode and cathode". In: *Proceedings - The Electrochemical Society* 84-13 (9 Sept. 1984), pp. 465–487. ISSN: 01616374. DOI: 10.1149/1.2116020/XML.

[108] C. Y. Yuh and J. R. Selman. "The Polarization of Molten Carbonate Fuel Cell Electrodes: I . Analysis of Steady-State Polarization Data". In: *Journal of The Electrochemical Society* 138 (12 Dec. 1991), pp. 3642–3648. ISSN: 0013-4651. DOI: 10.1149/1.2085473/XML.

[109] Göran Lindbergh, Marie Olivry, and Mari Sparr. "Experimental Investigation of the Porous Nickel Anode in the Molten Carbonate Fuel Cell". In: *Journal of The Electrochemical Society* 148.5 (2001), A411. DOI: 10.1149/1.1359195.

[110] Lan Hu, Göran Lindbergh, and Carina Lagergren. "Electrode kinetics of the NiO porous electrode for oxygen production in the molten carbonate electrolysis cell (MCEC)". In: *Faraday Discuss.* 182 (0 2015), pp. 493–509. DOI: 10.1039/C5FD00011D.

[111] Lan Hu, Göran Lindbergh, and Carina Lagergren. "Electrode Kinetics of the Ni Porous Electrode for Hydrogen Production in a Molten Carbonate Electrolysis Cell (MCEC)". In: *Journal of The Electrochemical Society* 162.9 (July 2015), F1020. DOI: 10.1149/2.0491509jes.

[112] H. R. Kunz, L. J. Bregoli, and S. T. Szymanski. "A Homogeneous/Agglomerate Model for Molten Carbonate Fuel Cell Cathodes". In: *Journal of The Electrochemical Society* 131.12 (1984), p. 2815. DOI: 10.1149/1.2115415. URL: https://dx.doi.org/10.1149/1.2115415.

[113] Stefano Frangini, Claudio Felici, and Pietro Tarquini. "A novel process for solar hydrogen production based on water electrolysis in alkali molten carbonates". In: *ECS Transactions* 61.22 (2014), p. 13. DOI: 10.1149/06122.0013ecst.

[114] Paul Claes, Dominique Moyaux, and Daniel Peeters. "Solubility and Solvation of Carbon Dioxide in the Molten $Li_2CO_3 - Na_2CO_3 - K_2CO_3$ (43.5: 31.5: 25.0 mol%) Eutectic Mixture at 973 K I. Experimental Part". In: *European journal of inorganic chemistry* 1999.4 (1999), pp. 583–588. DOI: 10.1002/(sici)1099-0682(199904)1999:4<583::aid-ejic583>3.0.co;2-y.

[115] W Peelen, K Hemmes, and JHW De Wit. "The CO_2 reduction in the molten 62/38 mol% Li/K carbonate mixture". In: *Proceedings of the Fourth International Symposium on Carbonate Fuel Cell Technology.* Vol. 97. 4. The Electrochemical Society. 1997, p. 274.

[116] D Chery, V Lair, and M Cassir. "CO2 electrochemical reduction into CO or C in molten carbonates: a thermodynamic point of view". In: *Electrochimica Acta* 160 (2015), pp. 74–81. DOI: 10.1016/j.electacta.2015.01.216.

[117] H Meskine et al. "CO_2 electrolysis in a reversible molten carbonate fuel cell: Online chromatographic detection of CO". In: *International Journal of Hydrogen Energy* 46.28 (2021), pp. 14913–14921. DOI: 10.1016/j.ijhydene.2020.08.028.

[118] Dayan Monzer and Chakib Bouallou. "Production of synthetic gas by the co-electrolysis of H_2O and CO_2 in the molten carbonate electrolyzer". In: *International Journal of Hydrogen Energy* 52 (2024), pp. 152–166. ISSN: 0360-3199. DOI: 10.1016/j.ijhydene.2023.03.402.

[119] Dayan Monzer and Chakib Bouallou. "Dynamic exploration of a 1 MW molten carbonate electrolyzer: A modeling study approach". In: *International Journal of Hydrogen Energy* 56 (2024), pp. 989–997. ISSN: 0360-3199. DOI: 10.1016/j.ijhydene.2023.12.194.

[120] Maria Anna Murmura. "Modelling High-Temperature Electrochemical Cells: An Engineering Perspective". In: *ChemElectroChem* 11.1 (2024), e202300313. DOI: doi.org/10.1002/celc.202300313.

[121] Juan Pedro Perez-Trujillo et al. "Preliminary theoretical and experimental analysis of a Molten Carbonate Fuel Cell operating in reversible mode". In: *Applied Energy* 263 (Apr. 2020), p. 114630. ISSN: 0306-2619. DOI: 10.1016/J.APENERGY.2020.114630.

[122] Maria Anna Murmura et al. "Analysing the Performance of MCECs over a Wide Range of Operating Temperatures". In: *Chemical Engineering Transactions* 96 (2022), pp. 421–426. DOI: doi.org/10.3303/CET2296071.

[123] Barbara Bosio, Paola Costamagna, and Filippo Parodi. "Modeling and experimentation of molten carbonate fuel cell reactors in a scale-up process". In: *Chemical engineering science* 54.13-14 (1999), pp. 2907–2916. DOI: doi.org/10.1016/S0009-2509(98)00414-X.

[124] N Subramanian et al. "Full cell mathematical model of a MCFC". In: *Journal of the Electrochemical Society* 150.10 (2003), A1360. DOI: 10.1149/1.1604786.

[125] Masahiro Yoshikawa et al. "Experimental determination of effective surface area and conductivities in the porous anode of molten carbonate fuel cell". In: *Journal of Power Sources* 158 (1 July 2006), pp. 94–102. ISSN: 03787753. DOI: 10.1016/j.jpowsour.2005.09.038.

[126] Lan Hu et al. "A Model for Analysis of the Porous Nickel Electrode Polarization in the Molten Carbonate Electrolysis Cell". In: *Journal of The Electrochemical Society* 164.8 (May 2017), H5197. DOI: 10.1149/2.0311708jes.

[127] Vittorio Verda and Adriano Sciacovelli. "Design improvement of circular molten carbonate fuel cell stack through CFD Analysis". In: *Applied Thermal Engineering* 31.14-15 (2011), pp. 2740–2748. DOI: 10.1016/j.applthermaleng.2011.04.046.

[128] MA Murmura et al. "Two-dimensional modeling and experimental investigation of an inverse molten carbonate fuel cell". In: *Journal of Power Sources* 573 (2023), p. 233103. DOI: 10.1016/j.jpowsour.2023.233103.

[129] Allen J Bard, Larry R Faulkner, and Henry S White. *Electrochemical methods: fundamentals and applications*. New York: John Wiley & Sons, 2022.

[130] Barsoukov Evgenij and J Ross Macdonald. "Impedance spectroscopy theory, experiment, and applications". In: *New Jersy: Wiley* (2005).

[131] Vadim F Lvovich. *Impedance spectroscopy: applications to electrochemical and dielectric phenomena*. John Wiley & Sons, 2012.

[132] M. Schönleber, D. Klotz, and E. Ivers-Tiffée. "A Method for Improving the Robustness of linear Kramers-Kronig Validity Tests". In: *Electrochimica Acta* 131 (2014). Electrochemical Impedance Spectroscopy, pp. 20–27. ISSN: 0013-4686. DOI: 10.1016/j.electacta.2014.01.034.

[133] Lan Hu, Goran Lindbergh, and Carina Lagergren. "Operating the nickel electrode with hydrogen-lean gases in the molten carbonate electrolysis cell (MCEC)". In: *International Journal of Hydrogen Energy* 41.41 (2016), pp. 18692–18698. DOI: 10.1016/j.ijhydene.2016.06.037.

[134] Bernard A. Boukamp. "A Linear Kronig-Kramers Transform Test for Immittance Data Validation". In: *Journal of The Electrochemical Society* 142.6 (1995), p. 1885. DOI: 10.1149/1.2044210. URL: https://dx.doi.org/10.1149/1.2044210.

[135] M. Schönleber and E. Ivers-fée. "Approximability of impedance spectra by RC elements and implications for impedance analysis". In: *Electrochemistry Communications* 58 (Sept. 2015), pp. 15–19. ISSN: 13882481. DOI: 10.1016/j.elecom.2015.05.018.

[136] Bernard A. Boukamp. "Electrochemical impedance spectroscopy in solid state ionics: recent advances". In: *Solid State Ionics* 169.1 (2004). Proceedings of the Annual Meeting of International Society of Electrochemistry, pp. 65–73. ISSN: 0167-2738. DOI: https://doi.org/10.1016/j.ssi.2003.07.002. URL: https://www.sciencedirect.com/science/article/pii/S016727380400058X.

[137] Andrey N. Tikhonov and Vasiliy Y. Arsenin. *Solutions of ill-posed problems*. Washington, D.C.: John Wiley & Sons, New York: V. H. Winston & Sons, 1977.

[138] D Calvetti et al. "Tikhonov regularization and the L-curve for large discrete ill-posed problems". In: *Journal of computational and applied mathematics* 123.1-2 (2000), pp. 423–446. DOI: 10.1016/S0377-0427(00)00414-3.

[139] Christian Hansen. "The L-curve and its use in the numerical treatment of inverse problems". In: 2000. URL: https://api.semanticscholar.org/CorpusID:9665185.

[140] Jane Cullum. "The effective choice of the smoothing norm in regularization". In: *Mathematics of computation* 33.145 (1979), pp. 149–170. DOI: 10.1090/S0025-5718-1979-0514816-1.

[141] Carlos Boigues Muñoz et al. "More accurate macro-models of solid oxide fuel cells through electrochemical and microstructural parameter estimation – Part I: Experimentation". In: *Journal of Power Sources* 294 (2015), pp. 658–668. ISSN: 0378-7753. DOI: 10.1016/J.JPOWSOUR.2015.06.118.

[142] Alexandra Weib et al. "Distribution of Relaxation Times Analysis of High-Temperature PEM Fuel Cell Impedance Spectra". In: *Electrochimica Acta* 230 (2017), pp. 391–398. ISSN: 00134686. DOI: 10.1016/j.electacta.2017.02.011.

[143] Pietro Iurilli et al. "EIS2MOD: A DRT-based modeling framework for li-ion cells". In: *IEEE Transactions on Industry Applications* 58.2 (2021), pp. 1429–1439.

[144] André Leonide et al. "Evaluation and modeling of the cell resistance in anode-supported solid oxide fuel cells". In: *Journal of The Electrochemical Society* 155.1 (2007), B36.

[145] Alexander Kromp. *Model-based interpretation of the performance and degradation of reformate fueled solid oxide fuel cells*. Vol. PhD Thesis. KIT Scientific Publishing, 2014.

[146] Photovoltaic Geographical Information System (PVGIS). *PVGIS: Solar Radiation Database*. https://pvgis.com/. Accessed: 2023-05-04.

[147] Andrea L Facci and Stefano Ubertini. "Analysis of a fuel cell combined heat and power plant under realistic smart management scenarios". In: *Applied Energy* 216 (2018), pp. 60–72. DOI: 10.1016/j.apenergy.2018.02.054.

[148] International Energy Agency. *Heating degree days in Italy, 2000-2020*. 2022. URL: https://www.iea.org/data-and-statistics/charts/heating-degree-days-in-italy-2000-2020.

[149] Silvia Lo Conte et al. "Drt-Based Electrochemical Investigation on the Fuel Electrode in a Molten Carbonate Electrolysis Cell". In: (2024). Submitted, under review. Pre-print available at SSRN: https://ssrn.com/abstract=5018817.

[150] Carina Lagergren and Daniel Simonsson. "The effects of oxidant gas composition on the polarization of porous $LiCoO_2$ electrodes for the molten carbonate fuel cell". In: *Journal of the Electrochemical Society* 144.11 (1997), p. 3813. DOI: 10.1149/1.1838097.

[151] Mohammadamin Alizadeh Jarchlouei et al. "Gibbs energy minimization using Lagrange method of undetermined multipliers for electrochemical and thermodynamic modeling of a MCFC with internal steam reforming". In: *Energy Conversion and Management* 228 (2021), p. 113594. DOI: 10.1016/j.enconman.2020.113594.

[152] Makoto Kawase, Yoshihiro Mugikura, and Takao Watanabe. "An Electrolyte Distribution Model in Consideration of the Electrode Wetting in the Molten Carbonate Fuel Cell". In: *Journal of The Electrochemical Society* 147 (3 2000), p. 854. ISSN: 00134651. DOI: 10.1149/1.1393282.

[153] Y Mugikura and JR Selman. "Meniscus behavior of metals and oxides in molten carbonate under oxidant and reducing atmospheres: I. Contact angle and electrolyte displacement". In: *Journal of The Electrochemical Society* 143.8 (1996), p. 2442. DOI: 10.1149/1.1837028.

[154] Suk-Gi Hong and J. Robert Selman. "Wetting Characteristics of Carbonate Melts under MCFC Operating Conditions". In: *Journal of The Electrochemical Society* 151 (1 2004), A77. ISSN: 00134651. DOI: 10.1149/1.1629094.

[155] J Jewulski and L Suski. "Model of the isotropic anode in the molten carbonate fuel cell". In: *Journal of applied electrochemistry* 14.2 (1984), pp. 135–143. DOI: 10.1007/BF00618732.

[156] C. Y. Yuh and J. R. Selman. "The Polarization of Molten Carbonate Fuel Cell Electrodes: II . Characterization by AC Impedance and Response to Current Interruption". In: *Journal of The Electrochemical Society* 138 (12 Dec. 1991), pp. 3649–3656. ISSN: 0013-4651. DOI: 10.1149/1.2085474.

[157] Timothy A. Barckholtz et al. “Experimental and Modeling Investigation of CO3=/OH– Equilibrium Effects on Molten Carbonate Fuel Cell Performance in Carbon Capture Applications”. In: *Frontiers in Energy Research* 9 (2021). ISSN: 2296-598X. DOI: 10.3389/fenrg.2021.669761.

[158] Choong Gon Lee. “Analysis of impedance in a molten carbonate fuel cell”. In: *Journal of Electroanalytical Chemistry* 776 (Sept. 2016), pp. 162–169. ISSN: 1572-6657. DOI: 10.1016/J.JELECHEM.2016.07.005.

[159] Andreas Bodén and Göran Lindbergh. “A Model for Mass Transport of Molten Alkali Carbonate Mixtures Applied to the MCFC”. In: *Journal of The Electrochemical Society* 153 (11 2006), A2111. ISSN: 00134651. DOI: 10.1149/1.2338653.

[160] Simone Mataloni et al. “Effect of operating conditions on Molten Carbonate Electrolysis Cell performance: an experimental study”. In: (2024). Submitted, under review.

[161] Geert H Graaf and Jozef GM Winkelman. “Chemical equilibria in methanol synthesis including the water–gas shift reaction: a critical reassessment”. In: *Industrial & Engineering Chemistry Research* 55.20 (2016), pp. 5854–5864. DOI: 10.1021/acs.iecr.6b00815.

[162] Edmund JF Dickinson and Andrew J Wain. “The Butler-Volmer equation in electrochemical theory: Origins, value, and practical application”. In: *Journal of Electroanalytical Chemistry* 872 (2020), p. 114145. DOI: 10.1016/j.jelechem.2020.114145.

[163] ES Page. “Controlling the standard deviation by CUSUMS and warning lines”. In: *Technometrics* 5.3 (1963), pp. 307–315. DOI: 10.1080/00401706.1963.10490100.

[164] Barney L Capehart, Wayne C Turner, and William J Kennedy. *Guide to energy management*. River Publishers, 2020.

[165] FR Garcia-Garcia et al. “Catalytic hollow fibre membrane micro-reactor: High purity H2 production by WGS reaction”. In: *Catalysis today* 171.1 (2011), pp. 281–289. DOI: 10.1016/j.cattod.2011.03.083.

[166] D Mendes et al. “The water-gas shift reaction: from conventional catalytic systems to Pd-based membrane reactors—a review”. In: *Asia-Pacific Journal of Chemical Engineering* 5.1 (2010), pp. 111–137. DOI: 10.1002/apj.364.

[167] Hua Liu et al. “Pathway toward cost-effective green hydrogen production by solid oxide electrolyzer”. In: *Energy & Environmental Science* 16.5 (2023), pp. 2090–2111. DOI: 10.1039/D2EE01023B.

[168] Ai-Quoc Pham, P Henrik Wallman, and Robert S Glass. *Natural gas-assisted steam electrolyzer*. US Patent 6,051,125. 2000.

[169] Joel Martinez-Frias, Ai-Quoc Pham, and Salvador M Aceves. “A natural gas-assisted steam electrolyzer for high-efficiency production of hydrogen”. In: *International Journal of Hydrogen Energy* 28.5 (2003), pp. 483–490. DOI: 10.1016/S0360-3199(02)00135-0.

[170] Yao Wang et al. “A novel clean and effective syngas production system based on partial oxidation of methane assisted solid oxide co-electrolysis process”. In: *Journal of Power Sources* 277 (2015), pp. 261–267. DOI: 10.1016/j.jpowsour.2014.11.092.

[171] Giovanni Cinti, Gianni Bidini, and Kas Hemmes. “An experimental investigation of fuel assisted electrolysis as a function of fuel and reactant utilization”. In: *International Journal of Hydrogen Energy* 41.28 (2016), pp. 11857–11867. DOI: 10.1016/j.ijhydene.2016.05.205.

[172] Changsong Cui et al. “Syngas production through CH4-assisted co-electrolysis of H2O and CO2 in La0. 8Sr0. 2Cr0. 5Fe0. 5O3-δ-Zr0. 84Y0. 16O2-δ electrode-supported solid oxide electrolysis cells”. In: *International Journal of Hydrogen Energy* 46.39 (2021), pp. 20305–20312. DOI: 10.1016/j.ijhydene.2021.03.177.

[173] Fumihiko Yoshiba. “Kawagoe 300 kW class MCFC/TCG compact system: Thermal efficiency and endurance test results”. In: *J. Fuel Cell Sci. Technol.* (2008). DOI: 10.1115/1.2784281.

[174] Maria Anna Murmura, Luca Turchetti, and Maria Cristina Annesini. “Multi-scale modelling of low-temperature electrolysis of steam in molten carbonate cells”. In: *2022 AIChE Annual Meeting*. AIChE. 2022.